September 2014

Optimal Sizing and Power Management Strategies of Islanded Microgrids for Remote Electrification Systems

Faruk A. Bhuiyan
The University of Western Ontario

Supervisor
Dr. Amirnaser Yazdani
The University of Western Ontario

Graduate Program in Electrical and Computer Engineering
A thesis submitted in partial fulfillment of the requirements for the degree in Doctor of Philosophy

OPTIMAL SIZING AND POWER MANAGEMENT STRATEGIES OF ISLANDED MICROGRIDS FOR REMOTE ELECTRIFICATION SYSTEMS

(Thesis format: Monograph)

by

Faruk Bhuiyan

Graduate Program in Electrical and Computer Engineering

A thesis submitted in partial fulfillment

of the requirements for the degree of

Doctor of Philosophy

The School of Graduate and Postdoctoral Studies

The University of Western Ontario

London, Ontario, Canada

Abstract

Over the past few years, electrification of remote communities with an efficient utilization of on-site energy resources has entered a new phase of evolution. However, the planning tools and studies for the remote microgrids are considered inadequate. Moreover, the existing techniques have not taken into account the impact of reactive power on component sizes. Thus, this thesis concentrates on optimal sizing design of an islanded microgrid (IMG), which is composed of renewable energy resources (RERs), battery energy storage system (BESS), and diesel generation system (DGS), for the purpose of electrifying off-grid communities. Owing to the utilization of both BESS and DGS, four power management strategies (PMSs) are modeled upon analyzing the impacts of reactive power to chronologically simulate the IMG. In this work, two single-objective optimization (SOO) and two multiobjective optimization (MOO) approaches are developed for determining the optimal component sizes in an IMG. Chronological simulation and an enumeration-based search technique are adopted in the first SOO approach. Then, an accelerated SOO approach is proposed by adopting an improved piecewise aggregate approximation (IPAA)-based time series and a genetic algorithm (GA). Next, an adaptive weighted sum (AWS) method, in conjunction with an enumeration search technique, is adopted in a bi-objective optimization approach. Finally, an elitist non-dominated sorting GA-II (NSGA-II) technique is proposed for MOO of the IMG by introducing three objective functions.

The enumeration-based SOO approach ensures a global optimum, determines the optimal sizes and PMSs simultaneously, and offers a realistic solution. The accelerated SOO approach significantly reduces the central processing unit (CPU) time without largely deviating the life cycle cost (LCC). The bi-objective optimal sizing approach generates a large number of evenly spread trade-off solutions both in regular and uneven regions upon adopting the LCC and renewable energy penetration (REP) as the objective functions. Using the MOO approach, one can produce a diversified set of Pareto optimal solutions, for both the component sizes and PMSs, at a reduced computational effort. The effectiveness of the proposed approaches is demonstrated by simulation studies in the MATLAB/Simulink software environment.

Keywords: Remote Microgrid, Islanded Microgrid, Off-grid, Simulation, Optimal Sizing, Single-objective, Bi-objective, Multiobjective, Optimization, Enumeration, Genetic Algorithm, Non-Dominated Sorting GA-II, Adaptive Weighted Sum, Improved Piecewise Aggregate Approximation, Time Series, Loss of Power Supply Probability, Net Present Value, Life Cycle Cost, Renewable Energy Penetration, Power Management Strategy, Pareto set, and Pareto Front.

Acknowledgements

First and foremost, I would like to express my sincere gratitude to my supervisor, Professor Amirnaser Yazdani, for his invaluable supervision, encouragement, enthusiasm, contributions, and continuous support, throughout this research.

My thanks and appreciations also go to my co-supervisor, Professor Serguei L. Primak, for his inspiration, guidance, supervision, and valuable technical suggestions.

This research work would not have been possible without the financial support from my supervisor, the Western University, Ministry of Training, College, and Universities, Ontario, and Natural Science and Engineering Research Council (NSERC), Canada.

I would also like to thank all the member of my group for their friendship and help.

Furthermore, I wish to thank my wife, Fardous Fatama, for her care, support, and patience during the extent of this work. Last but not the least, I wish to thank my kids, Farzan Ahmed and Mehjabin Ahmed, for having made my life happier and having relieved my stress with their innocent smiles and laughters.

Contents

List of Figures

List of Tables

List of Appendices

Acronyms

AC	Alternating current
ARES	Autonomous renewable energy systems
AWS	Adaptive weighted sum
BESS	Battery energy storage subsystem
CPU	Central-processing unit
DAL	Daily average load
DC	Direct current
DER	Distributed energy resources
DES	Distributed energy storage
DG	Distributed generator
DGS	Diesel generator subsystem
DOD	Depth of discharge
DM	Decision maker
EA	Evolutionary algorithm
EMS	Energy management system
GA	Genetic algorithm
HOGA	Hybrid optimization by genetic algorithm
HOMER	Hybrid optimization model for electric renewables
IG	Induction generator
iHOGA	Improved hybrid optimization by genetic algorithm
IMG	Islanded microgrid
INSEL	Integrated simulation environment language
IPAA	Improved piecewise aggregate approximation
LCC	Life-cycle cost
LCE	Levelized cost of energy
LPSP	Loss of power supply probability
MATLAB	Matrix laboratory

MCDA	Multicriteria decision analysis
MIP	Mixed-integer programm
MOEA	Multiobjective evolutionary algorithm
MOGA	Multiple objective GA
MOO	Multiobjective optimization
MOP	Multiobjective optimization problem
NBI	Normal boundary intersection
NL	Newfoundland and Labrador
NPGA	Niched Pareto GA
NPV	Net present value
NSGA	Non-dominated sorting genetic algorithm
NT	Northwest Territories
NU	Nunavut
ON	Ontario
PAA	Piecewise aggregate approximation
PCC	Point of common coupling
PDF	Probability density function
PMS	Power management strategy
PSO	Particle swarm optimization
PV	Photovoltaic
PVS	Photovoltaic subsystem
QC	Quebec
RAP-Sim	Remote area power simulator
REP	Renewable energy penetration
RER	Renewable energy resource
RETScreen	Renewable technologies (RETS) covering energy
SA	Simulated annealing
SD	Standard deviation

SOC	State of charge
SOE	State of energy
SOMES	Simulation and optimization model for renewable energy systems
SOP	Single-objective problem
SOO	Single-objective optimization
SPEA	Strength Pareto evolutionary algorithm
STATCOM	Static synchronous compensator
SVC	Static var compensator
TMY	Typical meteorological year
TRNSYS	Transient energy system simulation program
VEGA	Vector evaluated GA
WBGA	Weight-based GA
WPS	Wind power subsystem
WS	Weighted sum

Symbols

Symbol	**Explanation**	**Unit**
a, b, c	Wind power coefficient	
A_p	Area of a PV module	[m^2]
c_f	Fuel price	[currency/L]
c_1	Scale parameter Weibull PDF	
C_f^{di}	Fuel consumption cost of DGS	[currency/kWh]
$C_c^{(.)}$	Capital cost of a component	[currency]
$C_{om}^{(.)}$	Operation and maintenance cost of a component	[currency]
$C_s^{(.)}$	Salvage value of a component	[currency]
E^w	Year-round energy of WPS	[kWh]
E^{pv}	Year-round energy of PVS	[kWh]
E^{dl}	Year-round dump energy	[kWh]
E^l	Year-round primary-load energy	[kWh]
E^b	Battery bank instantaneous SOE	[kWh or p.u.]
E^b_{rat}	Rated capacity of battery bank	[kWh or p.u.]
E^b_{max}	Maximum allowed SOE of battery bank	[kWh or p.u.]
E^b_{min}	Minimum allowed SOE of battery bank	[kWh or p.u.]
$f(.)$	Probability density function	
$f_{(.)}$	Individual objective function	
$\bar{f}_{(.)}$	Normalized individual objective function	
$\mathbf{F}$	Objective function vector	
$F_{(.)}$	Weighted average objective function	
F_c^{di}	Fuel consumption of DGS	[L/h]
g_1	Fuel consumption coefficient	[L/kW^2h]
g_2, g_3	Fuel consumption coefficient	[L/kWh]
k	Shape parameter of Weibull PDF	
K	Compression ratio of time series	

N_{lp}	Project life	[year]
N_{pv}	Number of PV module	
$p_{(.)}$	Parent/child/individual	
$q_{(.)}$	Parent/child/individual	
$P_{(.)}$	Population for GA technique	
P^{w}	Instantaneous WPS power	[kW or p.u.]
P^{w}_{rat}	Rated wind power	[kW or p.u.]
P^{pv}_{rat}	Rated PV power	[kW or p.u.]
P^{con}_{ava}	Allowed real-power component of the BESS converter	[kW or p.u.]
P^{di}_{max}	Maximum allowed real-power component of DGS	[kW or p.u.]
P^{di}	Instantaneous real-power component of DGS	[kW or p.u.]
P^{b}	Instantaneous battery bank power	[kW or p.u.]
P^{b}_{rat}	Rated power of bank power	[kW or p.u.]
P^{pv}	Instantaneous PVS power	[kW or p.u.]
P^{l}	Load real-power component	[kW or p.u.]
P^{dl}	Dump load	[kW or p.u.]
Q^{l}	Load reactive-power component	[kVar or p.u.]
Q^{pv}	Instantaneous reactive-power of the PVS converter	[kVar or p.u.]
Q^{con}	Reactive-power component of the BESS converter	[kVar or p.u.]
Q^{di}	Reactive-power component of the DGS	[kVar or p.u.]
r_1	Discount rate	[%]
r_2	Market interest rate	[%]
r_3	Inflation rate	[%]
$\mathcal{R}$	Feasible region	
S^{pv}_{con}	Rated power of the PVS converter	[kVA or p.u.]
S^{con}_{rat}	Rated power of the BESS converter	[kVA or p.u.]
S^{di}_{max}	Maximum operating power of DGS	[kVA or p.u.]
S^{di}_{min}	Minimum operating power of DGS	[kVA or p.u.]

S_{rat}^{di}	Rated power of DGS	[kVA or p.u.]
T_{cref}	Reference temperature for PV array	[° C]
T_c	PV array temperature on PV array	[° C]
v_w	Wind speed	[m/s]
V_{ci}	Cut-in wind speed	[m/s]
V_{co}	Cut-out wind speed	[m/s]
V_r	Rated wind speed	[m/s]
w_1	Weighting factors for forming a weighted sum	
X	Decision variable vector	
$x_{..}$	Individual decision variable	
x_θ	Power factor of the primary load power	
ϕ_s	Solar insolation	[W/m^2]
γ	Temperature coefficient of PV array	[/ ° C]
δ	Self-discharge coefficient of battery bank	[%]
η_c^b	BESS converter charging-time efficiency	[%]
η_d^b	BESS converter discharging-time efficiency	[%]
β_{fl}^{di}	Fuel consumption cost of per unit power generation	[currency/kWh]
$\beta_c^{(.)}$	Capital cost for per unit component	[currency/(kW or kVA)]
$\beta_{om}^{(.)}$	Operation and maintenance cost for component	[currency/(kW or kVA)/year]
$\beta_s^{(.)}$	Salvage value for per unit component	[currency/(kW or kVA)]
γ_{re}	Renewable energy penetration	[%]

Chapter 1

Introduction

1.1 Statement of Problem and Thesis Objectives

Providing electricity to an off-grid community through a power grid is prohibitive due to large investments required for transmission lines, right of way, towers, and construction materials [1–3]. On the other hand, power generation using only diesel generator systems/subsystems (DGSs) is also expensive due to the high fuel transportation and inventory holding costs [4]. A more cost-effective approach of electrifying an off-grid community could then be to use a stand-alone power generation system that utilizes the available renewable energy resources (RERs) [5–7]. Such isolated power generation and distribution systems, which embed distributed energy resources (DERs), are known as islanded microgrids (IMGs). An IMG energized mainly by RERs not only reduces the life-cycle cost (LCC) but it also enhances renewable energy penetration (REP) and thus decreases greenhouse gas emissions. To fulfill the load-power demand in an off-grid community with a large REP, an appreciable number of RERs (e.g., wind power subsystem (WPS), photovoltaic subsystem (PVS)) and large energy storage (ES) capacity need to be embedded. Amongst the ES technologies, battery banks are widely available, have a proven track record, and are independent of the site geography [8], [9]. Thus, battery banks are substantially used in the grid-connected systems [10] and their trend of use in the off-grid power systems is increasing [11]. Considering both economical and technical criteria, the selection of DERs for an IMG, during the planning phase, is challenging. Thus, the issues of planning, operations, and maintenances (i.e., the issues related with economical and technical criteria) of a few projects in different off-grid communities of Canada have limited their lifetimes, and most projects have been abandoned and left un-operational [1]. To achieve the benefits of a RER-based IMG (used IMG in this thesis), feasibility of the RERs, REP, cost, and reliability of the IMG must be carefully evaluated. The cost, REP, and reliability of an IMG depend on the control strategy, i.e., the power management strategy (PMS), of the IMG. Thus, the simultaneous optimization of the PMS and component sizes of an IMG is required for a cost-effective design. An appropriate optimal sizing approach guarantees the lowest LCC, the maximum REP, and the highest reliability. However, optimization of an IMG is challenging due to the complexities of operation, stochastic nature of the RERs, variability of the load, nonlinear characteristics of the components, and the number of design constraints and optimization variables. The perceived economical and environmental benefits of IMGs have encouraged research and development efforts towards resolving the design, planning, and operational issues. Nonetheless, continued research and development efforts are needed to make IMGs economically feasible and technically reliable.

The objective of this thesis is to investigate the PMSs and to propose a few optimal sizing approaches for an IMG so that the component optimal sizes, i.e., the appropriate DER combinations considering economics, reliability, environmental measures subject to physical, and operational constraints can be achieved. This thesis also addresses a few concerns regarding the optimal sizing design of an IMG that can be used in a large off-grid community. Thus, the objectives of this thesis are broadly classified as:

- To collect site-specific weather data of the renewable resources (e.g., wind speeds and solar irradiations) and to investigate the statistical characteristics (e.g., mean, standard deviation, seasonal and diurnal variations, and parameters (estimated) of the Weibull probability density function) of the data such that the renewable resource models, which will facilitate to study the impacts of stochastic behavior of wind speed on life-cycle cost (LCC), can be developed.

- **To analyze the impacts of reactive power (variable demand) on component sizes and reliability (i.e., LPSP) evaluation**.
- To investigate the PMSs of an IMG that is comprised of the BESS, DGS, along with, RERs, and **to develop the aforementioned PMSs' algorithmic flowcharts** that enable simulating the IMG, studying the performances, calculating the loss of power supply probability (LPSP), and incorporating the constraints of the IMG.
- To develop a mathematical model for an IMG by combining the subsystem's mathematical models that are formulated based on both real and reactive powers such that the IMG can be simulated by utilizing both the mathematical model and PMSs.
- To develop a detailed economic model (i.e., the LCC) and **to propose an SOO approach employing an enumeration technique in order to simultaneously optimize the component sizes and PMSs of an IMG upon incorporating the impacts of reactive power on component sizes**, and subsequently to investigate the impacts of REP, LPSP, and stochastic characteristics of the renewable resource on LCC.
- **To develop an accelerated single objective optimal sizing approach** both for two cases in order to substantially reduce the central processing unit (CPU) time of the optimization process.
- **To develop a bi-objective optimization algorithm** and to present the related mathematical model of the technique, i.e., the adaptive weighted sum (AWS) such that an evenly spread and a large amount of Pareto optimal solutions can be generated in non-convex and uneven regions, along with, an integer decision variable environment.
- To develop a multiobjective optimization problem (MOP) for an IMG by incorporating LCC, LPSP, and REP as objective functions and formulating a decision variable vector by considering the PMS as a decision variable too.
- **To propose an MOO approach** for the aforementioned MOP utilizing an elitist non-dominated sorting genetic algorithm-II (NSGA-II) such that a diversified and a large

number of Pareto optimal solutions with less computational complexity can be produced.

1.2 IMGs, DERs, and Off-Grid Communities

The electricity infrastructure in off-grid communities are diverse and vary depending on the access of energy resources, remoteness of location, and impact of climates. Considering geographical characteristics and availability of RERs in an off-grid community, various kinds of DER can be used [12] in an IMG. The DERs are generally be classified as distributed generators (DGs) (e.g., wind turbine, solar PV, small hydro, ocean tidal, fuel cell, gas turbine, and microturbine) and distributed energy storages (DESs) (e.g., battery bank, compressed air, hydrogen, flywheel, and supercapacitor). Among the RERs, the PV and wind sources have gained much attention in recent years due to their omnipresence and environment-friendly characteristics. Few of the RERs are highly site specific, i.e., they cannot be utilized in all remote communities. Based on the demand and nature of load, availability of RERs, desired reliability, and targeted REP, the IMGs can be constructed at different installation sizes and configurations. An IMG can be comprised of only the DGS. However, the RER-based IMGs are called IMG in this thesis. The following subsections describe the categories and configurations of IMGs.

1.2.1 Categories of IMGs

Until now the IMGs are categorized based on a number of factors such as installation capacity, peak load, and daily average load (DAL) [5], [13], [14]. Among the IMGs in off-grid systems, the communication tower, satellite earth station, desert agriculture, and single house (e.g., hotel, motel, lodge, and resort) are the smallest in terms of load demand as their average consumptions remain around 20 kWh/day. Some other IMGs in off-grid systems such as irrigation project, remote sea-port, desalination plant, and remote community with less than five houses (i.e., less than 15 people) are also small as they consume on average 250 kWh/day. The rest of the remote systems are the remote communities where a group of people live. There are many remote communities in Canada and around the world where several hundreds to several thousands of people live. Thus, the installation capacity of an IMG in a remote community depends on usages, i.e., the number of people, geographical region, and nature of load. Considering all kinds of off-grid system/remote community, reference [13] has divided the IMGs based on their installation capacity and the categories are presented in Table 1.1. As shown in Table 1.1, when the installed capacity of an IMG remains between 100−10,000 kW, the system is described as island power system. The estimated daily average consumptions for the installations of Table 1.1 are also estimated. However, a system that incorporates a set of RERs with installed power greater than 10,000 kW, is considered a grid connected system. The installation capacity of an island power system of Table 1.1 depends on load size of the remote community and level of reliability. The island power systems of Table 1.1 are occasionally sub-categorized by their yearly peak load demand [14]. A remote community that has less than 500 kW of peak load is considered a small island power system and the remote communities with 501-1000 kW of peak load are considered the large island power systems. This thesis however takes into account all the island power systems as large off-grid systems.

Table 1.1: Categories of IMG Based on Installed Power

Installed Power(kW)	Estimated DAL (kWh)	Types	Descriptions	Remarks
<1	1-20	Micro power system	Single point DC based system	Mostly energy storage and PV system
1-100	21-400	Village power systems	Small power system both DC and alternating current (AC) bus	The diesel generators are helped by wind and PV system
101-10,000	401-50,000	Island power systems	Isolated grid systems mostly AC bus	Mostly augmented the diesel generators by wind power and/or PV power integrated with energy stoarge
>10,000	–	Large interconnected systems	Large remote power system	Big wind and/or solar farm integrated with BES

1.2.2 Configurations of DERs in an IMG

The configurations of an IMG depend on the types of DER, number of buses, direction of power flow, and types of load. Different combinations of component can be utilized in an IMG based on availability and potentiality. For an example, Table 1.2 illustrates various combinations of DER, which can be used in an IMG. The categories/combinations in the second column of Table 1.2 are generally utilized in the very small off-grid systems, i.e., not in island power systems of Table 1.1. As hydrogen and pump energy storages (ESs) are capable to store energy for a long time [9], i.e., they can be used for load leveling in grid-connected systems, the combinations in the third column are expected to provide a high level of reliability [5] in off-grid systems. However, the combinations in the first column are used for low REP off-grid system while the fourth column of Table 1.1 are mostly utilized in large off-grid communities due to incorporating both DGS and BESS, which are mainly responsible for maintaining a high level of reliability. The DERs in an IMG can be connected in various topologies depending on their types, sizes, and nature of loads, i.e., the components can be connected either a direct current (DC) bus system or an alternating current (AC) bus system or both. The choices of connection are mainly depended on the size and nature of loads. Figure 1.1 illustrates a few topologies of the IMGs. As shown in Figure 1.1(d), the RERs and load are connected in a single DC bus, as the load is DC only. The classical IMGs contain both DC and AC buses for the battery bank and DERs (shown in Figure 1.1(c)), as the off-grid community contains both AC and DC loads. The fast-growing technologies of power electronics and controls have allowed the DC-producing renewable DERs to include dedicated power electronic converter with them,

Table 1.2: Types of IMG Based on the Combination of Components

With DGS	With battery	With other ES	With battery/ES and DGS
PV-DGS	PV-battery	PV-hydrogen/ES	PV-DGS-battery/ES
Wind-DGS	WPS-battery	WPS-hydrogen/ES	WPS-DGS-battery/ES
PV-WPS-DGS	PV-WPS-battery	PV-wind-hydrogen/ES	PV-WPS-DGS-battery/ES

and thus to make an AC-bus system more cost effective [15]. In addition to that, when an off-grid power system becomes large, then an AC-bus system is more suitable. Thus, considering the types of buses and sizes of microgrid, the configurations can further be identified as (i) series and (ii) parallel connected topologies. Owing to unidirectional flow of current, Figure 1.1(a) shows a series connected IMG, while, if the current flows in two directions then the IMG is called parallel connected (shown in Figure 1.1(b)). This thesis is intended to determine the optimal component sizes of an IMG that can be utilized in a large off-grid community. Thus, it is expected that the nature of load will be similar to that of grid-connected system. Considering the aforementioned facts, this thesis takes into account a configuration that is similar to Figure 1.1(b) for the study system.

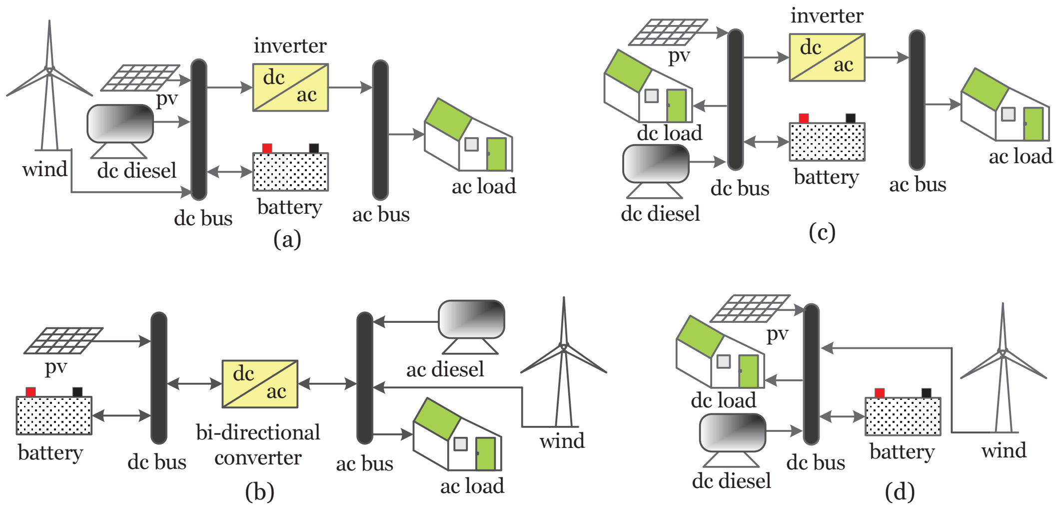

Figure 1.1: Island microgrid (a) series, (b) parallel, (c) double-bus, and (d) single-bus topologies.

1.2.3 Remote Communities in Canada

In Canada, there are 292 remote communities, where approximately two hundred thousand people have been living [16]. Among these remote communities, more than 160 enjoy low REP, along with, diesel generation mix and around 130 remote communities still solely depend on the DGS [1], [14]. The number of people in each of these remote communities vary from 25 to over 10,000. However, the number of people in majority of these off-grid communities are within 500-3,500. The energy consumption in an off-grid community also vary based on the condition of weather and seasons. The per capita national average energy consumption in Canada is 17,061 kWh/year, whereas, due to the limitation of energy resources the per capita energy consumption in these remote communities is 5,395 kWh/year, which is 70% less than that of national average. In Ontario only, there are thirty off-grid communities. Fuel logistics are cumbersome and costly due to the limited accessibility and fuels are transported either by winter road or air in the most communities. The average price of electricity in the communities that are based on diesel only system goes beyond \$1.3/kWh, while the price of electricity in the Ontario remote communities ranges between \$0.4/kWh and \$1.2/kWh. Though, some Canadian remote communities are blessed with high wind potential [14], the medium and high REP wind-diesel and/or PV-diesel systems are rare [1]. Presently, there is no remote community in Canada, where a high REP IMG is available. Over the past 20 years, many remote communities in Canada, such as, Big Trout Lake (ON), Cambridge Bay (NU), Ellesmere Island (NU), Fort Severn (ON), Igloolik (NT), Iqaluit (NU), Kasabonika Lake (ON), Kugkluktuk (formerly Coppermine) (NU), Kuujjuaq (QC), Omingmaktok (NT), Sachs Harbour (NT), Ramea (NL), Rankin Inlet (NU) and Winisk (ON) have been installed wind-diesel systems [14]. Owing to planning, operation, and maintenance problem most projects are abandoned. The background analyses of these remote communities indicate that they had been installed as low REP wind-diesel systems except Ramea and the projects were failed less than two years period of installation [14]. In spite of the past difficulties, there are renewed interests on wind-diesel options, especially in Quebec, Manitoba, and Northwest Territories.

1.3 REP and Reactive Power in IMGs

The REP in an IMG has great influence on costs and operating issues. The consideration of reactive power, especially in a large off-grid community is important due to using various kinds of load. Thus, the rationale for high REP IMG in the context of economies of scale and the necessity of reactive power in a large remote community are elaborated below.

1.3.1 Rationale for REP in IMGs

In a WPS-DGS based IMG, when the rated power of the WPS does not exceed the minimum load power of an off-grid community, then the IMG is called a low REP system where the WPS supplies load power to the off-grid community in the order of 10-15%, without incorporating any complex control scheme in the system. As an example of a low REP IMG, Figure 1.2(b)

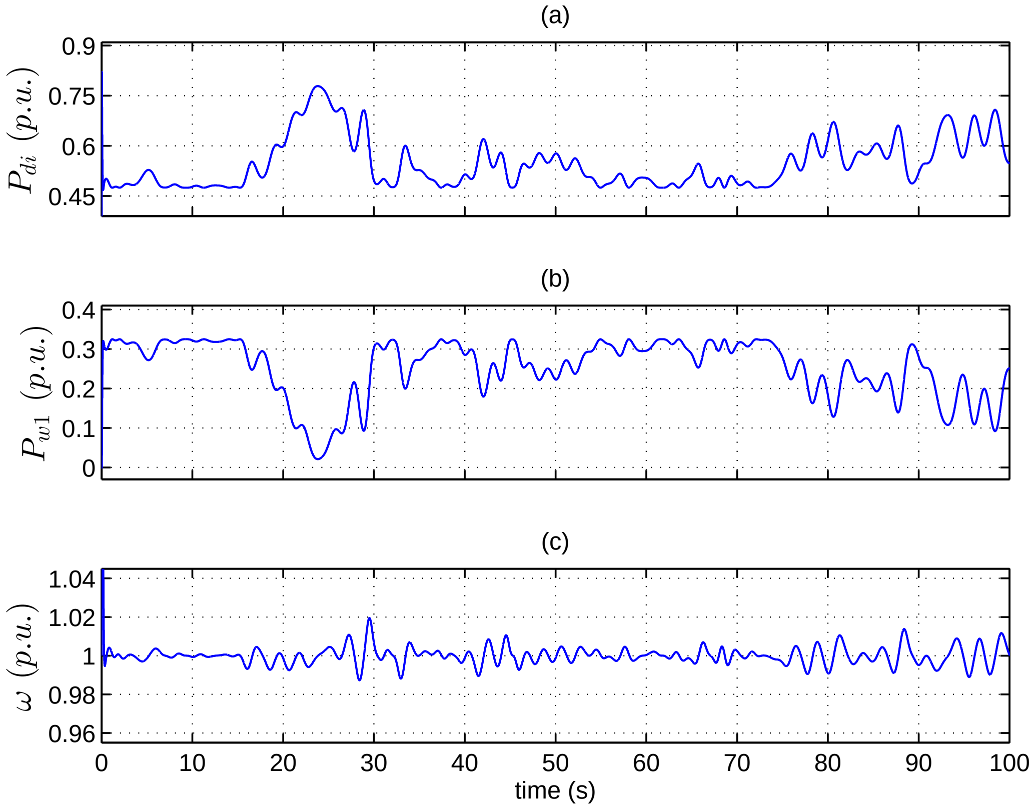

Figure 1.2: Example of low penetration system output

shows that the maximum output power of the WPS is $P_{w1} = 0.30$ p.u., while the load power demand is 0.75 p.u.. Thus, Figure 1.2(a) indicates that the DGS always operates and the output power of the DGS, P^{di}, does not drop below 0.45 p.u. though the system frequency deviates. The economies of scale for a low REP-based IMG is assumed high due to high capital costs of the RERs [5]. Alternately in a medium REP IMG, the DGS may not require to deliver power for a brief period of time (30 s - 5 min) [5], i.e., the DGS needs to be kept idle when the wind speed is too high and the community load is too low. Thus, when the minimum load demand

Table 1.3: IMG Classification Based of Renewable Power Penetration

Penetration class	**Characteristics**	**Instantaneous power penetration**	**Annual average penetration**
Low	Diesel runs full time. RER power reduces net load on diesel. All RER energy goes to primary load and no supervisory control	<50%	<20%
Medium	Diesel runs full time. At high RER power, diesel run at no load sometime or RER generation is curtailed. and requires simple control system.	50%-100%	20%-50%
High	Diesel may be shut down during high RER availability. Auxiliary components required to regulate voltage and frequency and requires sophisticated control system.	100%-400%	50%-150%

of a remote community and the rated output power of the WPS become equal, then the system is said to be a medium REP IMG. Table 1.3 [17], [18] illustrates briefly the various REP based IMG. Thus, annual average renewable power penetration of a medium REP IMG stays within 20%-50%. The DGS operation cost at no load is a disadvantage for the medium REP IMG. In a high REP IMG, the WPS output power frequently exceeds the demand of the load power and thus the DGS needs to be kept fully stop for a significant amount of time. The high REP system must be equipped with a complicated control system so that the voltage and frequency of the IMG can be maintained at a permissible limit. Moreover, a dump load might be required for the periods when the power output from the WPS exceeds the load power and charging power of the battery bank. The annual average renewable power penetration in a high REP IMG resides around 50%-150%. A significant amount of fuel savings is the advantage of such system and it is also expected to get a benefit from the economies of scale for the construction and maintenance.

1.3.2 Rationale for Reactive Powers in Large IMGs

The aspect of reactive power compensation in a power system is viewed from (i) load compensation and (ii) voltage support. The controls of voltage deviations in a distribution network by a reactive power management, especially in islanded mode of operation, are proposed in many studies [19]. In a grid-connected system, an induction generator (IG) can get reactive power from the grid system, such as, static var compensator (SVC), capacitor banks, synchronous condenser, and static synchronous compensator (STATCOM) system, whereas, the reactive power demand of an IMG need to be supplied from an arrangement, such as built-in capacitor bank with WPS or synchronous condenser or converter system. Many loads of a large remote community are inductive in nature and the power factor of a typical residential load varies around 0.92 while the same for the commercial/industrial loads ranges from 0.8 to 1.0. The high REP IMGs are expected to operate keeping the DGS idle for a substantial amount of time. In such a situation, the reactive power demand need to be supplied from a converter system. The mismatch in generation and consumption of the reactive power in an IMG can cause serious problems such as large voltage fluctuations at generator terminals [20]. Reference [21] proposes a centralized energy management system (EMS) for an isolated microgrid considering both real and reactive powers. Presently, due to integrating RERs in the existing DGS-based off-grid power systems, the reactive power demands of IG are supplied by a dedicated DGS that runs at no-load operation [1], [22]. Thus, the DGS can provide reactive power in a low REP IMG. If the sizes of component in a large REP IMG are insufficient for supplying reactive power, large voltage fluctuations in the IMGs are imminentness.

1.4 Control Strategies and Optimal Sizing of IMGs

The investigations on existing (i) operating strategies, and (ii) approaches of optimization for the IMGs are required at the outset of optimal sizing design. The already carried out studies and the remaining scopes on the topics are discussed below.

1.4.1 Control Strategies/Operating Policies for the IMGs

The economic performance of an IMG heavily relies on operating policies, i.e., the coordinated controls among the DERs of an IMG. The control strategies that pertain the energy flows among the components in an IMG is known as dispatch/energy menegement/power management strategy (PMS). An IMG that is comprised of DGS, BESS, and RERs offers many modes of operation. As such, Figure 1.3 signifies the energy-flow options of a high REP-based IMG. Figure 1.3 shows a dump load that is required in a high REP-based IMG in order to absorb the access generation, though few researchers [23] have proposed dynamic control schemes to regulate output power of a WPS during high wind and suggested to eliminate the use of dump load in the IMGs. The DGS of an IMG ensures reliability of power supply, as well as maintains the voltage and frequency. For an IMG, the operating strategies decide the sequences of start/stop and charge/discharge for the DGS and BESS, respectively. The PMS of an IMG also maintains a balance among costs, reliability, amount of dump energy, and REP.

However, the grid-connected microgrids integrated with BESS usually do not employ DGS and thus, the PMS of a grid-connected microgrid is straightforward and simple. Figure 1.4 represents a PMS for a grid-connected microgrid integrated with a BESS. Moreover, the PMS of an IMG that contains either DGS or BESS, along with RERs, does not generally provide many modes of operation. Therefore, the PMS of an IMG consisting of the components of Figures 1.3 is not as simple as grid-connected microgrid due to various possible modes of operation. The formulation of a PMS includes constraints associated with operational limits of the generating units, power balance, energy balance of energy storage systems, and spinning reserve. In numerous studies [21, 24–31], the PMS concepts, economic benefits, energy sav-

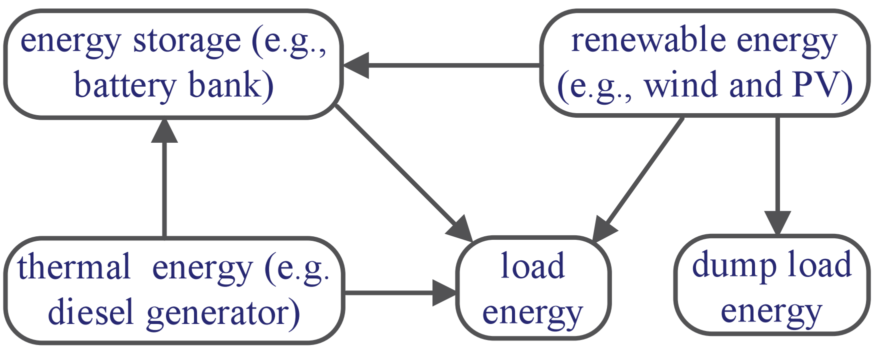

Figure 1.3: Energy flow options in a high REP IMG

ings by the PMSs, and optimization of the parameters of a PMS are focused. Considering a wind-PV-diesel-battery system, a few PMSs have been proposed and the effects of those PMSs

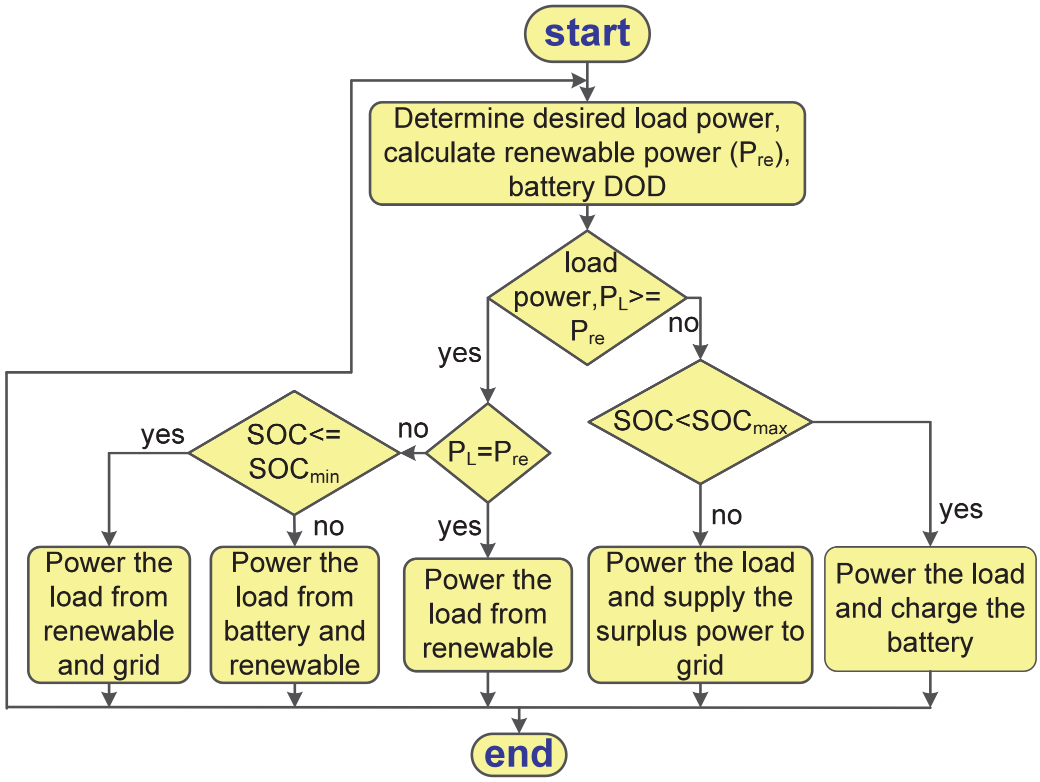

Figure 1.4: Grid-connected mode supervisory control

on LCC have been analyzed in [24]. The proposed four main PMSs of [24] are (i) *load following strategy*, (ii) *SOC setpoint dispatch strategy* (iii) *full power dispatch strategy*, and (iv) *frugal discharge dispatch strategy* that are explained in general, i.e., without considering the constraint of component sizes. Developing a typical PMS for a PV-diesel-battery system, reference [25] has optimized the PMS by means of the DGS starting and stopping set points. The state of charge (SOC) setpoint of the battery bank has been optimized using genetic algorithm (GA) in [26] upon analyzing and combining a few dispatch strategies of [24]. Reference [27] has reiterated that the performance of an IMG significantly relies on supervisory control and the reference has proposed a scheme accordingly for a PV-wind-battery system. Without taking the optimal sizes into account, a PMS for a stand-alone PV-wind-fuel energy system has been analyzed in [28]. Based on the combination of components, reference [29] has proposed optimal sizing method of a high REP wind-PV-battery system for three operating modes, which are the (i) RER and BESS, (ii) RER and DGS, and (iii) RER, DGS, and BESS. A centralized energy management system (EMS) for an optimal dispatch of energy has been introduced in [21] where the reactive power effect is adopted in the EMS design. The optimization of the operating states for a PMS of an IMG has been proposed in [30] based on battery life-cycle characteristics. Using predictions and controllable load, reference [32] has proposed a load management strategy for a wind-diesel-battery system so that the DGS use can be minimized. Reference [33] utilizes artificial neural network for the operation and control of PV-diesel-battery system under known insolation and load demand. Reference [34] proposes energy flow and dynamic power flow model for an autonomous wind-diesel system to investigate the daily and monthly performance of the system under various wind and load regime. Various power management strategies are proposed in [35] for a stand-alone hybrid power system integrated with hydrogen energy storage. The strategies describe the scheme of fuel cell based hydrogen energy storage operations at above or below residual power. The "*source following*" and "*grid-following*" dynamic control approaches are proposed in reference [36] in order to exchange the powers among the sources, and to manage energy for a grid integrated system. Using the combination of DGS and/or BESS with RERs, reference [31] has presented a sequential simulation technique for evaluating four operating modes of a stand-alone power system.

The aforementioned studies of PMS for the IMGs have either used both the DGS and BESS or any one of the DGS and BESS in their systems. The system consisting any one of BESS and DGS does not require to investigate many dispatch strategies and thus the related studies with the said configuration have not analyzed many PMS either. The above discussion further reveal that the studies with both BESS and DGS have mostly optimized the SOC set point strategy. In some of the studies, the comparisons of the PMSs have been performed based on diesel fuel savings only, i.e., not by adopting in any optimization scheme. The reliability evaluation aspects for IMGs by the use of the PMSs are avoided in the aforementioned studies. The most studies have not accounted in the reactive power effect in the PMSs. Above all, none of the studies have structurally modeled the PMSs, especially, in the context of incorporating any constraints of the components.

1.4.2 Optimal Sizing of IMGs

The general optimization problems, techniques to solve them, and various optimization studies for the IMGs are discussed below.

1) Optimization Problems and Techniques in General

The optimization theories, problems, and techniques comprise a large area of applied mathematics. Figures 1.5 and 1.6 respectively illustrate the numerous types of optimization problem and the techniques to solve the problems. Utilizing the Figures 1.5 and 1.6, an optimal sizing problem of an IMG can be categorized as constrained combinatorial optimization problem consisting of discrete/integer variables and the number of objectives can be single or multiple. The modality of the IMG sizing problem is assumed to be a multimodal and thus the global optimum solution is essential to investigate. As the wind speeds and solar irradiations are intermittent, the optimal sizing problem of an IMG involves stochastic parameters and constraints. Thus, the problem is expected to be solved by any one of probabilistic, iterative, enumerative, analytical, and stochastic techniques. Depending on the size of load, types of component, and numbers of objective function, optimal sizing problems of the IMGs can be numerous. To determine the optimal sizes of an IMG, evaluation must be carried out on the basis of power supply reliability and system LCC. In addition to that the REP or the greenhouse gas emission is another important criterion to be taken into account. The realistic optimal sizing output and

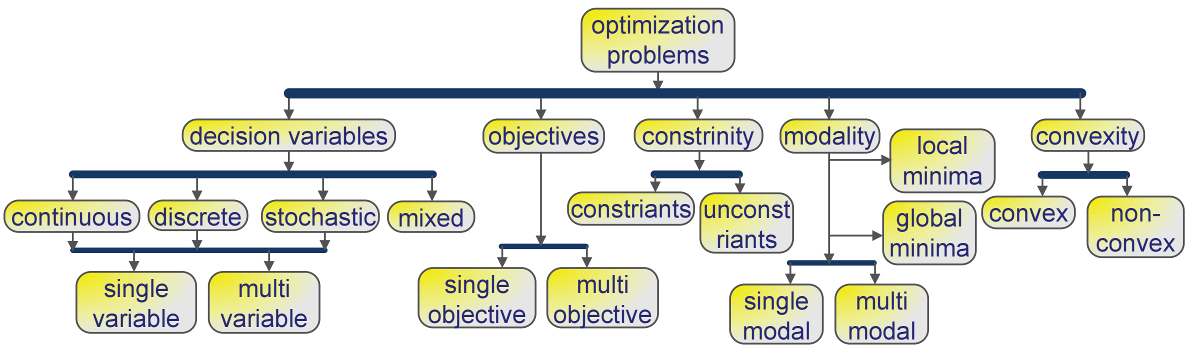

Figure 1.5: Types of optimization problems

the degree of accuracy vary with the adopted technique.

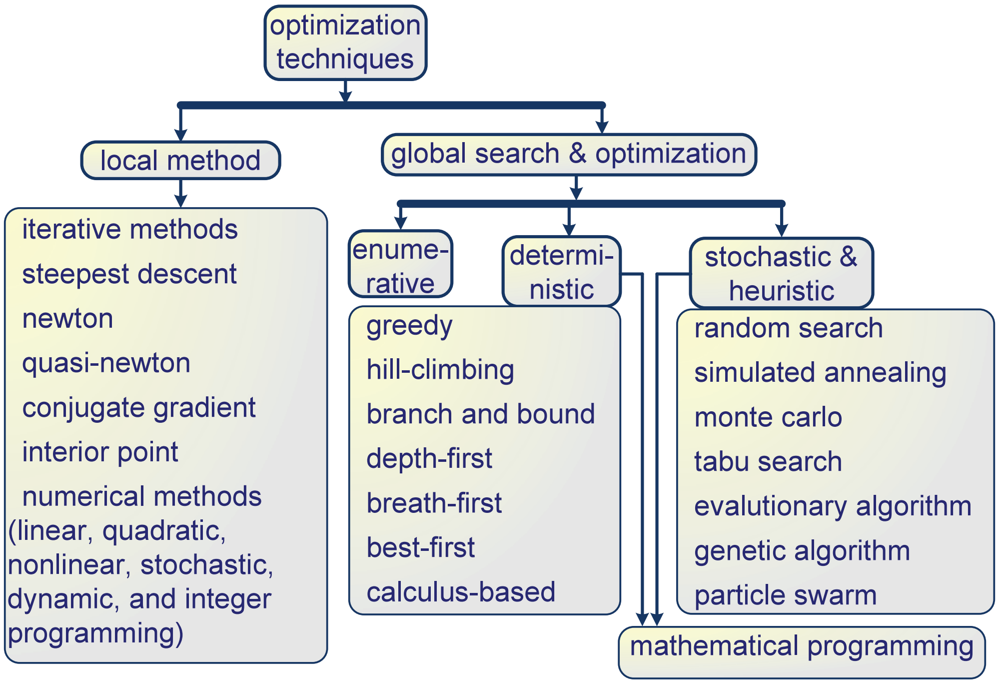

Figure 1.6: Some optimization techniques

2) Single-Objective Optimization of IMGs

Taking the reliability of power supply as a constraint and adopting the cost as an objective function, many researchers [37–45] have investigated and proposed various approaches for determining the optimal sizes of an IMG. Their recommended optimization techniques are mainly (1) graphical construction method, (2) probabilistic approaches, (3) enumerative/iterative technique, and (4) stochastic & heuristic techniques.

- Keeping one decision variable (e.g., size of WPS) fixed and varying the other (e.g., size of PVS), graphical construction method has been utilized to determine the sizes of a battery bank and a PV array [37] and to calculate the sizes of WPS and PVS [46]. This method has utilized only two decision variables in the optimization processes and the cost function of the IMG has been taken a linear function that combines the decision variables. This method is not effective for the problems that involve more than two decision variables.

- Probabilistic approaches have been proposed in [38] and [47] to determine the upper limit of a battery bank in a wind-PV-battery system and to asses the performances of a PV-wind system, respectively. Probabilistic methods are generally the simplest sizing methods. The disadvantage of the probabilistic approach is that the approach cannot represent the dynamic changing performances of the IMG. Thus, the obtained results by these methods are not generally be the most suitable solution.

- By minimizing production cost, linear programming approaches have been utilized to optimize the component sizes of IMGs [39], [48], [49] and to determine optimal design of a autonomous and grid-connected hybrid wind-PV power system [50]. Reference [40] has used a computer programming technique to calculate the maximum number of storage days and minimum areas of PV array for a PV-diesel-battery system. However, the linear programming approaches are not effective for a large and complicated IMG. The approaches may end up the optimization process in a suboptimal solution and have required a large computational effort.

- By employing enumeration and/or iterative schemes and minimizing costs upon maintaining the power supply reliability to a desired value, many researchers [41, 44, 51–58] have proposed the single objective optimal sizing approaches for numerous configurations of an IMG. Among the aforementioned studies, the most [41], [53], [54], [56], [58] have optimized the sizes of very small IMGs (e.g., a single house/motel) where the daily average load (DAL) is less than 75 kWh, some others [51], [52], [55] have determined the optimal sizes of small IMGs that have the DAL between 100 kWh and 700 kWh, and the rest [44], [55] have calculated the optimal sizes of medium IMGs that have the DAL between 800 kWh and 2000 kWh. Reference [41] has proposed a simple numerical algorithm to determine the optimum generation capacities and storage for a hybrid wind-PV-battery system. Based on loop iteration, reference [59] has presented a general methodology for technical-economic analysis of an autonomous renewable power system. Few of the aforementioned studies have utilized PV-wind-diesel-battery configuration while the rest have employed PV-wind-battery/fuel cell in the configurations. All of the aforementioned studies have neither utilized more than one PMSs for simulating the IMGs nor optimized the PMSs as well and they have accounted in small number (e.g., two to four) of decision variables. None of the above studies have adopted converter and/or battery charger size(s) as decision variable(s). In the aforementioned studies, the effect of reactive power on component sizes during the optimal sizing studies has not been taken into account, though the reactive power issues (e.g., the voltage deviations) in an IMG are investigated in many dynamic studies and control designs [12], [19]. Many researchers have proposed methods to minimize the intermittencies of solar irradiance [60] by analysis and wind speeds by utilization of BESS [61]. The aforementioned optimal sizing studies have not investigated the impact of RERs' intermittency on LCC.

- Among the stochastic and heuristic techniques, GA [3], [42], [62], [63], particle swarm optimization (PSO) [64], [65] simulated annealing (SA) [66], and tabu search [67] have been used for determining optimal sizes of an IMG. Assuming the total cost to be an objective function, GAs are utilized in [3] to determine the optimum number of PV modules, wind turbine generators, and battery banks and to develop a hybrid optimization GA (HOGA) program [26] for simultaneously determining the optimal sizes and control strategies of a PV-diesel system, while reference [62] has presented a methodology for the optimal sizing of a PV-wind-battery system. Reference [68] has employed GA to jointly optimize the sizes and operations of a hybrid-PV system while reference [69] has utilized GA for investigating optimal sizes and economical analysis of a wind-microturbine-PV-battery hybrid system. By ensuring a low LPSP and minimizing the annualized costs, reference [42] has suggested a GA to optimize the sizes of a PV-wind-battery system. Taking the total costs as an objective function and based on stochastic gradient search, reference [66] has used SA algorithm to optimize the sizes of PV-wind-battery system. Though the GAs are generally robust in finding global optimal solutions in multi-modal and multi-optimization process, the attainment of a global minimum with a small number of population is sometime uncertain. Reference [70] has proposed tabu search technique to optimize the sizes of a PV-wind-diesel-battery system with a large number of decision variables where the peak load has been 120 kW. Standard PSO has the shortcomings that the calculation time is too long and it is easy to fall into local optimal solution [64]. The most studies have utilized chronological simulation scheme for determining the optimal sizes. The aforementioned studies have either used typical meteorological year (TMY) or typical day or typical month time series weather data to simulate the IMG. The typical day or typical month time series cannot provide satisfactory solution due to avoiding the seasonal variations while the TMY time series needs large central processing unit (CPU) time. Therefore, the TMY-based methods are computational intensive as well as time consuming.

3) Multiobjective Objective Optimization (MOO) of IMGs

Most real-life search and optimization problems naturally involve multiple objectives, i.e., an MOOP deals with more than one objective functions. Two goals of MOO are (1) to find a set of solutions as close as possible to the Pareto-optimal front, and (2) to find a set of solutions as diverse as possible. The MOO approaches are proven effective for the objective functions that are conflicting with each other [71]. There are two general approaches in MOO for obtaining solution. One approach (priori) is used to get a single-point optimization solution that combines the individual objectives into a single one. The other approach (posteriori) generates an entire set of Pareto optimal solutions or a representative subset [72]. In this context, the MOO is performed by weighted sum approach [73] that is one of the earliest one. Although the approach is faster, it has disadvantage of selecting the weights [71], [74]. The WS approach can be used as posteriori to generate Pareto front upon adopting a vector of weights. However, the approach cannot find solution in the non-convex region. Thus, the adaptive weighted sum (AWS) approach is proposed in [75], [76] both for bi-objective and for multiobjective cases. Though the approaches are efficient in non-convex and multi-modal environment, they become computationally intensive with the increase of decision variables. The use of WS and AWS methods for determining the optimal sizes of an IMG is rare.

- The most popular method applied for MOO of an IMG is GA. In recent years, researchers have employed MOO by evolutionary algorithm (EA) for optimal sizing of an IMG [72]. Using a multiobjective evolutionary algorithm (MOEA) reference [77] has employed three objective functions (i.e., LCC, unmet load, pollutant emissions) for the optimization of a PVwind-diesel-hydrogen-battery system while reference [78] has utilized GA for two objective functions (i.e., LPSP and cost) such that the optimal sizes for the IMG can be determined; reference [79] has utilized both GA and monte carlo methods for optimizing a study system. Queuing multiobjective optimization (QMOO) method, which claims better than MOEA, is used by few researcher [80] in order to optimize economics and emission criteria of an off-grid system. Recently an intelligent Pareto-search genetic algorithm (IPGA) has been proposed in [81] for the optimization of India's electricity generation portfolio involving cost, emission, and risk as the criteria. It is worthwhile to mention that the MOEA is a population based non Pareto approach.

- The second popular method of MOO is the particle swarm optimization (PSO). In order to optimize the batteries and hydrogen storage, reference [82] has employed a PSO algorithm for minimizing cost and power exchange to a weak grid. To minimize the cost and maximize the energy index reliability, a modified PSO algorithm has been proposed in [83] for a hybrid power system and the algorithm is tested both for grid-connected and off-grid scenario. It is worthwhile to mention that the PSO methods are single point search technique.

- Other than the above, an ε state evolutionary algorithm based on ε-dominance has been utilized in [84] for four objective evaluation and then combines to a multicriteria decision analysis (MCDA) process, whereas [85] has dealt with optimal sizing of a grid-connected PV-wind system by adopting different MCDA optimization approaches. Their focus were mainly on MCDA instead of generating Pareto front.

The aforementioned literature review indicates that the employment of the elitist population Pareto based approach, i.e., NSGA-II, is not many for determining Pareto optimal solutions of an IMG.

1.4.3 Simulation and Optimization Softwares

Other than the optimization studies, there are some softwares [86–91] that are developed for designing and evaluating the performances of the IMGs. Table 1.4 recapitulates some features of the software tools [15, 18, 92–94]. Many software tools, shown in Table 1.4, are developed for simulating and thus for evaluating the performances of an IMG. Among the available soft-

Table 1.4: Tools for Hybrid System Optimization

Description	Control strategies	Simulation /Technical Analysis	Economic Optimization	Multi-objective Optimization	Economic Evaluation in Spreadsheet	Available (Free)
HYBRIDS		✓				unknown
HYBRID2	✓	✓				✓
INSEL		✓				priced
ARES		✓				unknown
HOMER	✓	✓	✓			✓
iHOGA/HOGA	✓	✓	✓	✓		✓
RAP-Sim		✓				unknown
SOMES		✓				unknown
SOLSIM		✓				unknown
TRNSYS		✓				priced
RETScreen					✓	✓
PROLOAD		✓∗				unknown
WINSYS					✓	
WDLTOOLS				✓∗∗		unknown
SimEnerg		✓				unknown
DER−CAM			✓			unknown

∗: probabilistic load flow analysis
∗∗: design tool for wind-diesel system

ware tools, HOMER (hybrid optimization model for electric renewables) and HOGA (hybrid optimization by GA) programs are utilized for optimizing the costs. Although HOGA can be used for MOO, the HOMER program provides single-point solution. Both the software tools employ two PMSs during the optimization scheme. In addition to that, the programs do not allow to access in the algorithms and thus, the users cannot intuitively choose the components.

The time step of simulation in HOMER and HOGA is 1-h interval, which makes the total process computational intensive and time consuming especially for the problem with large number of decision variables. The utilization of time varying load reactive power and subsequent impact on component sizes is not comprehensible in those programs. As can be seen in Table 1.4, most of the softwares are only used for simulating and evaluating techno-economic performances. The simulation that is performed by HYBRID2 is considered very precise, as the time interval inside the package can be changed from 1 hour to 10 minutes. Among the software tools, the DER-CAM is particularly applied to the power dispatch operation of pre-defined microgrid systems, while RETScreen is an excel worksheet-based cost analyzing tool that is applied for the purpose of techno-economic feasibility studies of a project. Though the lifespan of some components changes with operation, many of the above-mentioned softwares neglect the component lifespan-reduction cost during the optimization scheme.

1.4.4 Renewable Resource Data for Simulation

The accuracy of renewable resource data, i.e., wind speeds, solar irradiations, air temperatures, and so forth is important for determining the optimal sizes of an IMG. The intensity and the availability of the data depend on climatic conditions of a specific location. The long-term system performance is an important design criteria for an IMG. Some researchers have utilized long period weather data for studying the performances of an IMG. The hourly average weather data may not always be available in many areas. In such a situation, researchers use statistical weather data, which are synthetically generated either from monthly-average values or from extrapolating nearby sites values with some correction factors [92], [95]. The time consuming behavior of large historical data and the unavailability of the accurate time series put forth the researchers to use typical meteorological year (TMY)-based time series. Average TMY-based weather data is initially synthesize for twelve months where the monthly averages are determined from the long-term weather data. When the weather data for a long time is not available then hourly average year-round data can also be used as a representative of TMY time series. Many approaches [96–99] are proposed by the researchers to create TMY-based renewable resource data. The performances evaluation of an IMG and accuracy of an optimal sizing approach highly depend on the perfectness of the time series model or time series data and thus extra attention should be given on renewable resource data. Since the performances of a hybrid energy system depend on the environmental conditions, a site-specific analysis requires as much accurate as possible data in order to investigate the associated cost, component sizes, and overall economics [5].

1.5 Adopted Methods for the Optimization Problems

The sizing optimization problems of this thesis are non-linear, contain stochastic parameters, and involve cause and effect relations due to control aspects of the DERs. Thus, the sizing optimization problems are very complex to be solved by analytical means, i.e., by using gradient information upon formulating the problem with continuous variables. Therefore, the problems are studied via computer simulations utilizing hourly averaged time series of renewable resources and loads. Considering 'off-the-shelf' component sizes, the sizing optimization problems are dealt with combinatorial combinations of components. It can also be expected that the problems might have multi-modes and thus, the identification of global optimum is essential. Alternately, the gradient based methods are basically local search methods. Owing to the absence of gradient information and the presence of multi-modes, the decision spaces need to be searched either by enumeration method or intelligent-based, e.g., GA method. When the sizing optimization problem becomes a multiobjective optimization problem, then the classical way to solve the problem is the preference-based approach where the relative preferences are used to convert the multiobjective problems into single-objective ones. The selection of preferences are sometimes very difficult before optimization. Moreover, it is necessary to convert the task of finding multiple trade-off solutions in a multiobjective optimization problem.

In this connection, the field of search and optimization has significantly changed over the years by the use of evolutionary algorithm, e.g., genetic algorithm. The GA has the ability to simultaneously search different regions of decision space, subsequently generates a diverse set of solutions for the problems that involve non-convex, discontinuous, multi-modal solutions spaces, and multi-objective cases. Thus, this thesis takes advantage of both enumeration technique and intelligent-based methods, i.e., GA methods for solving the problems.

1.6 Thesis Outline

This thesis is organized as follows:

In **Chapter 1,** the general overview, concept of PMSs, and optimization aspects of an IMG are discussed. Problem statement, research objectives, categories of IMG, configurations, single and multiobjective optimization, simulation and optimization softwares, remote communities and their corresponding IMGs in Canada, and thesis outlines are also elaborated in this chapter.

In **Chapter 2,** the PMSs of an IMG are investigated, modified, and explained in the context of real- and- reactive power demand. Subsequently, the PMSs are structurally presented by flowcharts considering the constraints of the components. The illustrated flowcharts are used for simulating the IMG while the performances of an IMG for the PMSs can also be compared. Chapter 2 also identifies the most sensitive parameters that are responsible for the PMSs. With the long-time performance study, Chapter 2 further illustrates that the PMS-B (equivalent to SOC set point strategy) is the most effective strategy for the IMG.

Chapter 3 introduces an SOO approach for determining the component optimal sizes of the IMG. The mathematical models for the subsystems, reactive power effect on component sizes, and algorithm of the enumerative optimization are developed. The optimization is performed based on both technical and economic criteria. As a technical criterion, during optimization, power supply is ensured, i.e., the LPSP is maintained very low. The detailed economic evaluation model is also developed in this chapter. A global optimum identification, sensitivity analysis, comparison with standard method, impact of LPSP and REP on LCC are also demonstrated in this scope. Chapter 3 further demonstrates that the PMS-B (equivalent to SOC set point strategy) is the most cost-effective strategy for the IMG.

In **Chapter 4,** an accelerated single objective optimal sizing approach for the IMG is developed utilizing both GA technique and chronological simulation based on IPAA time series. The method allows to develop the mathematical models in the context of mixed-integer programming (MIP). The proposed approach is tested both for unconstrained and constrained objective functions under different stochastic environment of renewable power generation and load demand. Chapter 4 demonstrates that the CPU timing is significantly improved while the impact of LPSP on LCC is also demonstrated in this study.

In **Chapter 5,** a bi-objective optimal sizing approach is developed for determining Pareto optimal solutions where the approach takes advantage of the AWS method. The approach facilitates to generate evenly distributed and substantial number of solutions than that of traditional WS method. The approach is comparatively simpler, especially for the problems of two objective functions. Chapter 5 illustrates a comparison of the AWS and WS methods.

In **Chapter 6,** a comprehensive MOO approach, incorporating three objective functions, is developed. The approach takes benefit of the NSGA-II technique for solving the MOP and thus for generating Pareto front solutions. The approach is facilitated to produce a diversified and as much as possible solutions of Pareto front in a less computational complexity. The approach utilizes the elitism mechanism so that the potential solutions do not lost due to mutation.

Chapter 7 presents thesis conclusions and future work.

1.7 Contributions

The main contributions of the thesis are:

- **This thesis includes the impact of reactive power (variable demand) on component sizes and reliability (i.e., LPSP) evaluation of an IMG** that can be used for the purpose of electrifying a large off-grid community.

- **This thesis develops the algorithmic flowcharts for the PMSs of an IMG** that is comprised of both BESS and DGS, along with, RERs upon incorporating the constraints of the components such that the PMSs can be utilized to simulate and optimize the IMG.

- **This thesis proposes an enumeration-based SOO approach for determining the optimal sizes of the IMG. The approach enables the identification of global optimum, simultaneously optimizes both component sizes and PMSs, and offers realistic optimal sizes for the IMG components.** This study also contributes on developing the detailed mathematical models, finding the economies of scale for the IMG by the use of REP, and analyzing the sensitivities on LCC with stochastic characteristic of the wind speed. Compared to the similar types work, this study incorporates more decision variables, e.g., the sizes of the BESS converter and battery bank charger.

- **This thesis proposes an accelerated SOO approach such that the CPU timing can substantially be reduced**. It can be expected that the approach can deal a problem with a very large number of decision variables.

- Next, **this thesis presents simple bi-objective optimization approach adopting both the WS and AWS methods** for determining Pareto optimal solution of the IMG. To the best of author's knowledge, the utilization of the AWS method for generating Pareto optimal solutions of an IMG, especially in the context of discrete variable, is the first. The bi-objective optimization approach with the AWS method generates evenly spread and more solutions both non-convex and irregular regions of the objective space.

- Finally, **this thesis presents an MOO approach incorporating an elitist NSGA-II technique** for determining the Pareto optimal solutions for the IMG. The proposed approach enables to generate a large number of diversified Pareto optimal solutions at a low computational complexity. The use of REP as an objective function and the incorporation of PMSs as a decision variable are new compared to other similar types of work.

1.8 Conclusions

The thesis objective, statement of problem, types of off-grid system, configurations of IMGs, control and PMSs of IMGs, off-grid communities in Canada, single and multiobjective objective optimization studies, rationale of high REP and reactive power in IMGs, and a few optimization software tools at the advent of growing use of RERs are discussed in this chapter. In addition to that, the research outlines, contributions, and literature survey pertinent to the studies of this thesis are also presented in this chapter.

Chapter 2

Power Management Strategies For a DGS and BESS-Based IMG

2.1 Introduction

In Chapter 1, the power management strategies (PMSs) for different kinds of IMG were discussed. It was also elaborated that the long-term performances of an IMG can be investigated through simulation studies, which require some well-defined PMSs. When the component sizes of the IMG are not sufficient for fulfilling the year-round primary load demand, then the power system reliability of the IMG goes down. Thus to evaluate power system reliability and to determine optimal component sizes, the IMG is required to simulate by well defined PMSs. Chapter 1 also showed that the PMS of a grid-connected hybrid power generation system is simple and straightforward while the PMSs of an IMG is complex, especially if the IMG employs both the DGS and BESS along with RERs. Owing to technological advancement, the remote community load includes the appliances very similar to that of urban community load and thus the power factor of remote community load varies with time. The modeling of the PMSs of an IMG that is composed of the DGS, battery bank, RERs, and primary load with real-and reactive power components is challenging.

Upon utilizing both real and reactive powers of primary load demand, this chapter presents and modifies the algorithms of four main PMSs of the IMG, where the algorithms are constructed using flowcharts. The modified PMSs can be used for simulating the IMG and for studying the performances. Multiple simulations need to be performed to determine the optimal sizes of the IMG and thus the PMSs of this chapter can be used during optimization. The effectiveness of the modified PMSs is evaluated in MATLAB/Simulink environment through simulation studies.

2.2 Study System

Figure 2.1 shows a schematic diagram of an IMG whose main components are a DGS, a WPS, a PVS, a BESS, a primary load, and a dump load. Figure 2.1 illustrates that the PV array comprises multiple PV modules interfaced with the point of common coupling (PCC) through an inverter. Also, the BESS is composed of a bank of series-/parallel-connected batteries and a power-electronic converter. It is assumed that at steady state the WPS delivers power P^{w} at unity power factor to the PCC due to capacitor bank attached in WPS. Alternately, the WPS is generally considered a negative load in an IMG and the required reactive power of the WPS is assumed to be delivered from a converter system. The PV array also produces power at unity power factor. However, the PVS inverter has the capability of delivering reactive power if required by the load. Thus, the real- and reactive-power outputs of PVS are signified, respectively, by P^{pv} and Q^{pv}. The real- and reactive-power outputs of the DGS are denoted by P^{di}, and Q^{di}, respectively. The aggregate power delivered by the batteries is referred to as the discharge power and denoted by P^{b}, and the real- and reactive-power outputs of the BESS are denoted by P^{con} and Q^{con}, respectively; the typical high efficiency of the power-electronic converter implies that P^{b} and P^{con} are almost equal and, therefore, is treated the same in this paper until specified. The real- and reactive-power components of the primary load are represented by P^{l} and Q^{l}, respectively. The dump load is assumed to be resistive and draws the real-power P^{dl}. At any instant, stable operation of the IMG requires the following

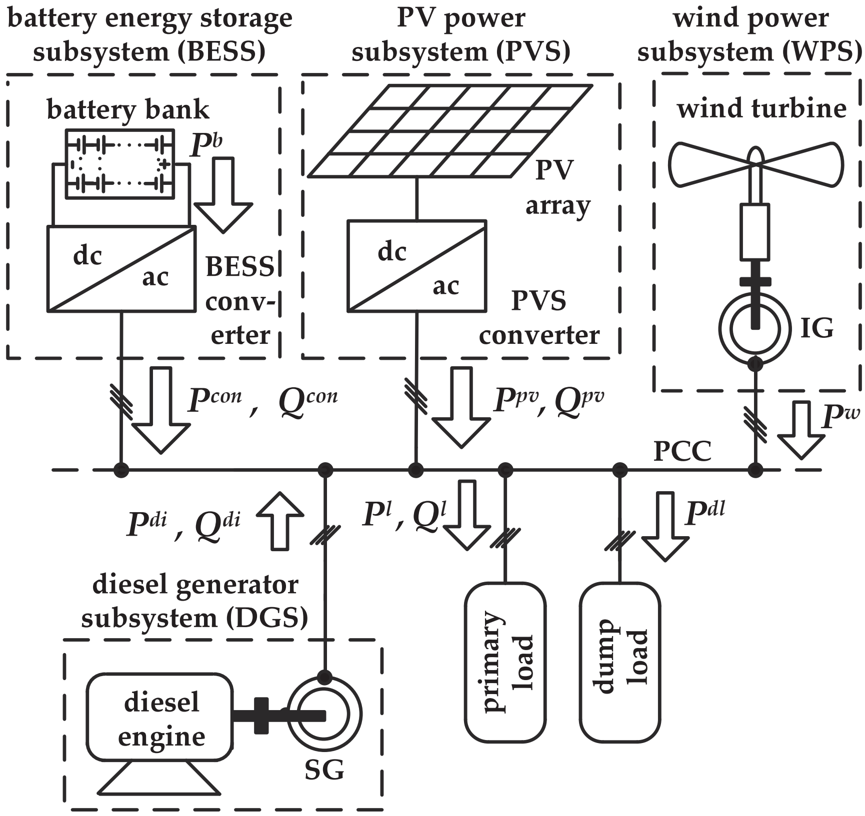

Figure 2.1: Schematic diagram of an islanded microgrid.

power-balance equations:

$$
\begin{aligned}
P^{w}(t) + P^{pv}(t) + P^{di}(t) + P^{con}(t) - P^{l}(t) - P^{dl}(t) &= 0 \\
Q^{di}(t) + Q^{pv}(t) + Q^{con}(t) - Q^{l}(t) &= 0
\end{aligned}
\tag{2.1}
$$

2.3 Effect of Reactive Power on Component Sizes

Based on power triangle concept, Figures 2.2(a) and (b) show the impacts of reactive power on component sizes. The load real- and reactive-power demands are represented by P^l and Q^l, respectively. Depending on the control strategy of the study system of Figure 2.1, the load reactive power, Q^l, is shared from the PVS converter, BESS converter, and DGS. To deliver the rated power of the PVS into PCC, the PVS converter apparent power rating, S^{pv}_{con}, should be the same as the rated power value of PV array, i.e., P^{pv}_{rat}. The PV array power generation usually falls below P^{pv}_{rat} in most of the time of a year due to diurnal variations. Thus, the PVS converter can be utilized for delivering the reactive power of the load. If the instantaneous active power of the PVS is $P^{pv}(t)$, then the PVS delivered reactive power is expressed as,

$$Q^{pv} = \sqrt{(S^{pv}_{con})^2 - (P^{pv})^2} \text{ where } (S^{pv}_{con})^2 \geq (P^{pv})^2 \tag{2.2}$$

Thus, Figures 2.2(a) and (b) indicate that a part of load reactive power is supplied from the PVS converter and the amount is Q^{pv}. The remaining load reactive power is supplied from the BESS converter and/or DGS. Figure 2.2(a) demonstrates that the effective size of the BESS converter decreases when the load reactive power is compensated by the BESS converter. When the PVS and BESS converters supply the load reactive power, the remaining size of the BESS converter, P^{con}_{ava}, is expressed as,

$$P^{con}_{ava} = \sqrt{(S^{con}_{rat})^2 - \big(\underbrace{\max\{0, (Q^{l} - Q^{pv})\}}_{Q^{l}_{rem}}\big)^2} \tag{2.3}$$

where S^{con}_{rat} is the apparent power rating of the BESS converter, and Q^{l}_{rem} is the remaining load reactive power demand. The value of S^{con}_{rat} need to be higher than the value of Q^{l}_{rem} at the time when the DGS does not run. Figure 2.2(b) illustrates that the sharing of reactive power occurs between the DGS and BESS converter by the amounts Q^{di} and Q^{con}, respectively. Thus, the remaining effective sizes of the BESS converter, P^{con}_{ava}, and the DGS, P^{di}_{max}, are expressed as,

$$P^{con}_{ava} = \sqrt{(S^{con}_{rat})^2 - (Q^{con})^2} \tag{2.4}$$

$$P^{di}_{max} = \sqrt{(S^{con}_{rat})^2 - (Q^{di})^2} \tag{2.5}$$

In this case, the DGS is able to deliver the maximum amount of P^{di}_{max} real power. The charging power of the battery bank depends on SOE (i.e., $E^{b}(t)$), energy capacity of the battery bank (i.e., E^{b}_{max}), power rating of the charge controller (i.e., P^{b}_{max}), and the value of P^{con}_{ava}. Thus, the

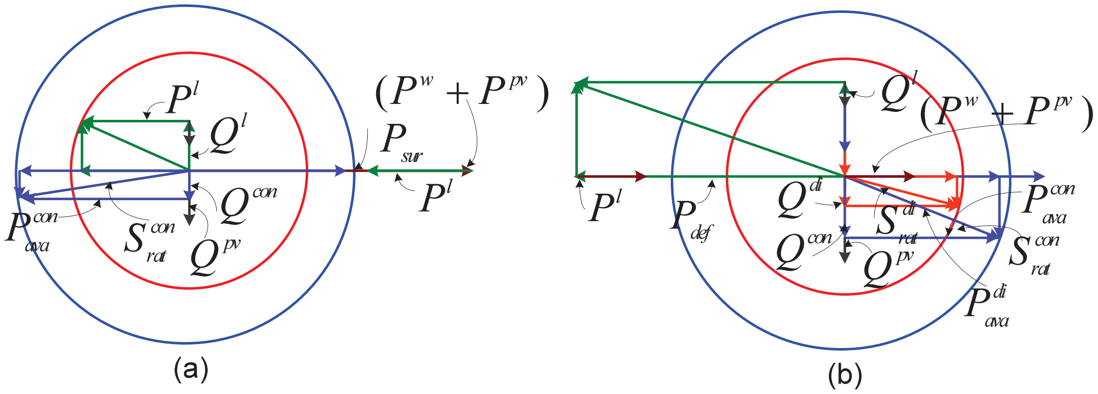

Figure 2.2: Power triangles (a) excess renewable generation, and (b) shortage of renewable generation.

actual charging power of the battery bank is expressed as,

$$P^b = -\min\left[P_{sur}, P^{con}_{ava}, \min\left\{P^b_{max}, \max\left(0, \frac{E^b_{max} - E^b(t)}{\Delta t}\right)\right\}\right] \tag{2.6}$$

where the surplus generation is $P_{sur} = P^w + P^{pv} - P^l$, when $(P^w + P^{pv}) > P^l$. Similarly, the actual discharging power of the battery bank is expressed as,

$$P^b = min\left[P_{def}, P^{con}_{ava}, \min\left\{P^b_{max}, \max\left(0, \frac{E^b(t) - E^b_{min}}{\Delta t}\right)\right\}\right] \tag{2.7}$$

where the deficient power is $P_{def} = P^l - P^w - P^{pv}$, when $(P^w + P^{pv}) < P^l$. Thus, the equations (2.6) and (2.7) indicate that both the charging and discharging powers of the battery bank are depend on the remaining size of the BESS converter, i.e., P^{con}_{ava}. Alternately, they are affected by the load reactive power.

2.4 Power Management Strategies

The two distinct types of control in an IMG are (i) dynamic control, which deals with the frequency and magnitude of voltage and (ii) PMS, which controls the energy resources of the IMG. This thesis has modeled four PMSs that were initially discussed in [24]. The models are formulated by considering both real and reactive powers such that the powers, i.e., the equations of (2.1) at each time step are tried to maintain balance among the components. Whenever, the equations of (2.1) become imbalance, the algorithms of the PMSs consider an event of power shortage and subsequently the reliability of the IMG is evaluated. The formulation of the PMSs are based on cause and effect relationships and the instantaneous output powers from the components are highly non-linear. Thus, the PMSs are not formulated by analytical means, rather than, the PMSs tested in discrete variable environment.

2.4.1 Power Management Strategy-A (PMS-A)

Figure 2.3 shows the algorithmic flowchart of the PMS-A. As can be seen in Figure 2.3, the load reactive power is compensated by the respective sources, i.e., the PVS converter, BESS converter, and DGS of the IMG. After delivering the output power of PV array, the remaining size of the PVS converter is utilized to compensate the load reactive power. When the total load reactive power cannot be supplied by the PVS converter, then the remaining load reactive power is shared by the BESS converter and the DGS. Consequently, the remaining sizes of the BESS converter and DGS are calculated based on 2.3 such that the load real power supplies can be performed with the help of them. The aforementioned algorithm is carried out in 'compare Q' block of Figure 2.3. Then, the aggregated output of the real power from the WPS and PVS is compared with the load real power. When there is a surplus generation from the RERs (i.e., $P^w + P^{pv} - P^l = P_{sur} > 0$), the surplus power is utilized for charging the battery bank. Actual charging of the battery bank, P^b, depends on the energy state, power rating of the battery bank, and the remaining size of the BESS converter. When the surplus power cannot be fully accommodated into the battery bank (i.e., $P_{sur} > P_1^b$), then the rest of the power is supplied to the dump load. Whenever the RERs cannot deliver the load real-power demand, i.e., there is net load demand, ($P^l - P^w - P^{pv} = P_{def} > 0$), then the battery bank (i.e., $P_2^b > P_{def}$) is employed to compensate the net load real-power demand. The DGS starts for delivering the load real-power demand, if BESS cannot deliver the net load demand. The power shortage block in Figure 2.3 indicates that the resource sizes are not sufficient to meet the load real power demand. According to the philosophy of this strategy, the DGS is not allowed for charging the battery bank. An exception of the philosophy occurs when the DGS is needed to operate for a low net load at a non-zero minimum setpoint, P^{di}_{min}. Thus, when the net load real-power demand reaches below the minimum setpoint of the DGS, the DGS starts to operate at its minimum operating value. Thus, the extra generation from the DGS is used for charging the battery bank, otherwise the extra amount need to be dumped. This strategy is a modified form of the load following strategy. The brief description of the strategy is given in Table 2.1.

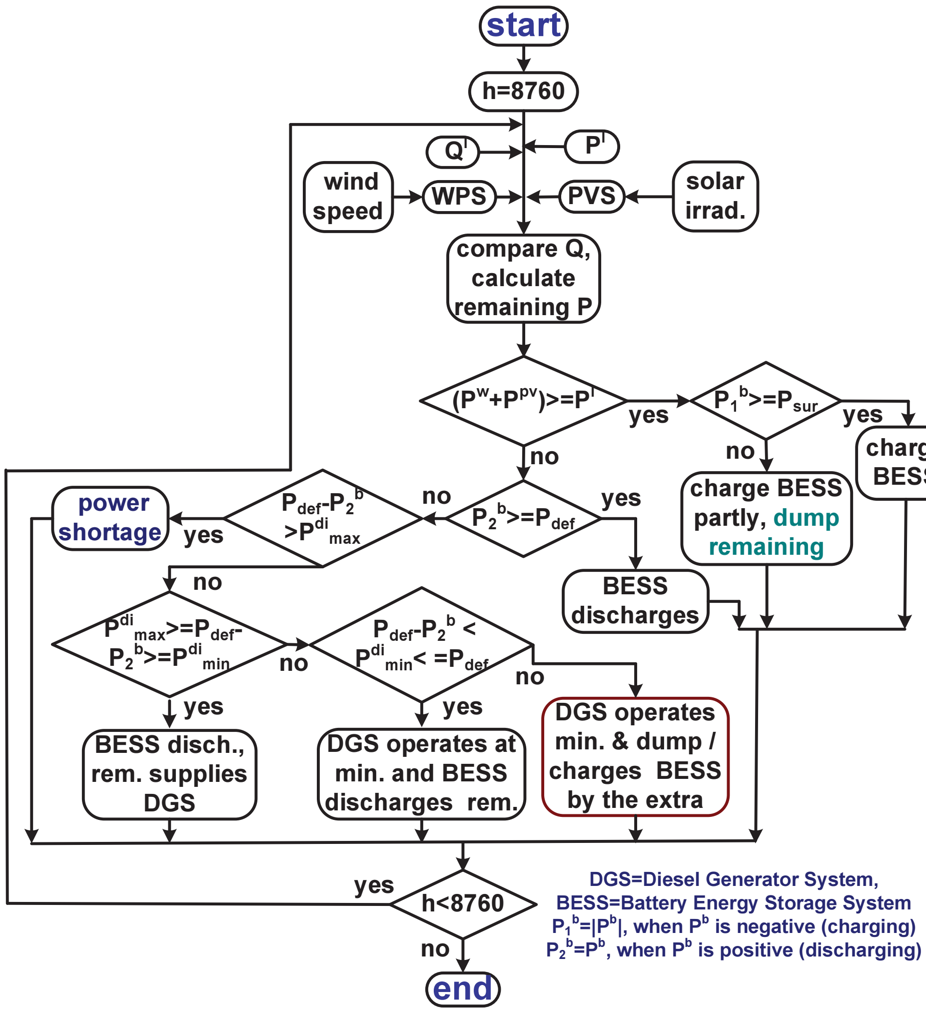

Figure 2.3: Flowchart of PMS-A.

Table 2.1: Brief Description of the PMS-A

Modes	Description of Operation
C0: Reactive power	Reactive load power is compared with the available resources and compute the remaining sizes of the components for the real power.
C1: Battery charging	Aggregated renewable power is larger than the load real-power demand.
C2: Dumping power	Surplus renewable power is larger than the actual charging power of the battery bank or the energy state of the battery bank does not allow to store more energy.
C3: Battery only	Battery bank supplies the net load real-power demand on priority and until exhausted.
C4: Battery and DGS	When the net load real-power demand is too high, then the battery bank discharges the maximum amount and the DGS provides the rest.
C5: DGS only	When battery bank does not have enough energy to deliver for net load demand,
C6: Power shortage	When all the resources of the IMG cannot supply the load real-power demand.

2.4.2 Power Management Strategy-B (PMS-B)

Figure 2.4 illustrates a flowchart that is applicable both for the PMS-B and PMS-C, where the DGS is allowed to charge the battery bank such that the state of energy (SOE) for the battery bank does not stay at minimum level for a long period of time. In PMS-B, the DGS is allowed for charging the battery bank up to a certain SOE level that must be below the maximum SOE level. As before the flowchart begins with the compensation of load reactive power by the available resources and the remaining sizes of those resources are calculated accordingly. Next, the aggregated renewable power is compared with the load real power. If there is surplus generation (i.e., $P^w + P^{pv} - P^l = P_{sur} > 0$) and this surplus generation is more than the actual charging power of the battery bank, P^b_1, then the battery bank begins charging at the rated/maximum value and the rest of the power passes to the dump load. When the surplus power is less than the actual charging power of the battery bank and the DGS has been running from the previous hours (i.e., $s = 1$), then the battery bank begins charging at a maximum possible value with the use of the DGS. Otherwise, only the surplus power is used for charging the battery bank. If there is deficit of renewable generation for load real-power demand, then the battery bank SOE level and the DGS operating condition are evaluated. In such a situation, when the SOE of the battery bank is $E^b(t) > E^b_{min}$ and the DGS is in off

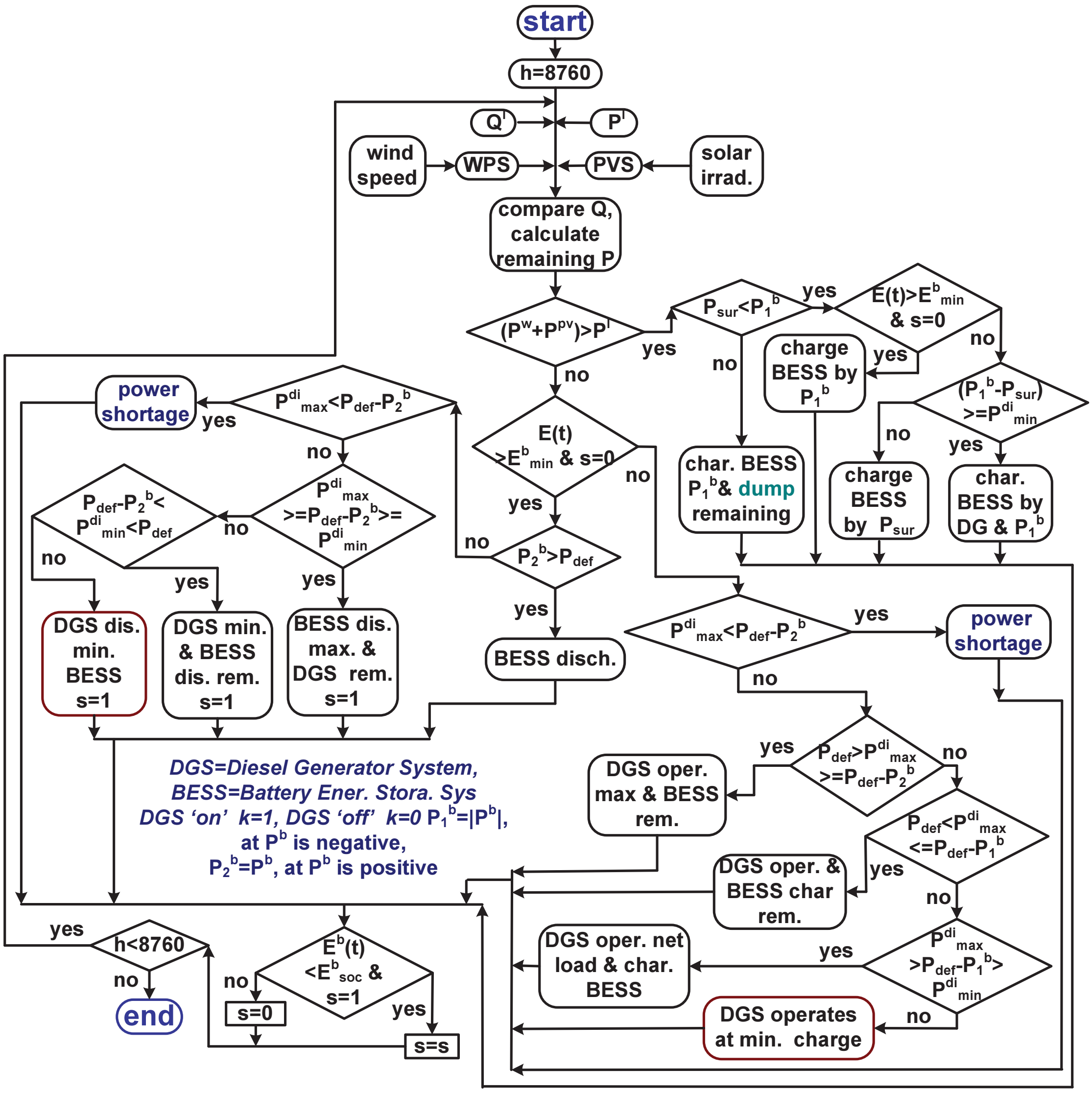

Figure 2.4: Flowchart of PMS-B and PMS-C.

status, i.e., $s = 0$, the deficit demand of the load real power is supplied by the battery bank only if the condition $P_2^b > P_{def}$ fulfill. Whenever the load real power deficit is too large and the DGS and battery bank cannot compensate the net load demand, then the power shortage occurs. Otherwise, putting the BESS into priority, the load real-power deficit is compensated with the help of battery bank and the DGS. Once the DGS goes into operation, i.e., $s = 1$, or the battery bank touches at minimum SOE level, the DGS is used for charging the battery bank. In this situation, to ensure the reliability of the power supply both the DGS and battery bank are evaluated. Whenever they fails to supply the net load demand, then the power shortage

Table 2.2: Concise Description of the PMS-B

States	Description of Operation
C0: Reactive power	Reactive load power is compared with the available resources and compute the remaining sizes of the components for the real power.
C1: Battery bank charges during the excess renewable power generation	
C11: Dumping power and charging battery	Surplus renewable power is larger than actual charging power of the battery bank or the energy state of the battery bank does not allow to store more energy.
C12: Battery bank charges by the surplus and DGS	The battery bank charges at maximum power that is more than the surplus and the DGS has been in operation and assists the charging of the battery bank.
C13: Battery bank charges by the surplus only	The surplus power is used for charging the battery bank due to being off the DGS or the extra amount of charging power is low for the DGS operation.
C2: Battery bank and DGS compensate load demand at $E^b(t) > E^b_{min}$, and $s = 0$ for previous hour	
C21: Power shortage	When all the resources of the IMG cannot supply the load real-power demand
C22: Battery only	Battery bank supplies the net load real power on priority and until exhausted.
C23: Battery and DGS	When the net load real-power demand is too high, then the battery bank discharges maximum and the DGS provides the rest.
C24: DGS only	When battery bank does not have enough energy, DGS supplies the net load
C3: DGS compensate net load and charges the battery bank when $E^b(t) \leq E^b_{min}$ or $s = 1$	
C31: Power shortage	When all the resources of the IMG cannot supply the load real-power demand
C32: DGS and battery	When the net load real-power demand is too high, then the DGS operates at maximum and the battery bank provides the rest.
C33: DGS only	The DGS operates at maximum power to supply the net load real-power demand and to charge the battery bank.

occurs. Otherwise, the DGS is utilized to compensate the net load demand and to charge the battery bank. During every time of operation, the DGS maintains its constraints. The DGS is commanded to stop (i.e., $s = 0$) when the SOE of the battery bank reaches at E^b_{soc} which is shown at an ending conditional block of Figure 2.4. This strategy is a modified form of the SOC setpoint dispatch strategy. The concise description of the strategy is given in Table 2.2.

2.4.3 Power Management Strategy-C (PMS-C)

According to the PMS-C, the DGS is permitted for charging the battery bank up to the maximum level, i.e., at E^b_{max}. The flowchart of Figure 2.4 is applicable for the PMS-C when the last conditional block is evaluated at E^b_{max}, instead of E^b_{soc}. This strategy is the modified form of the cycle charge strategy and it allows the DGS to continue the operation for a longer period of time than that of PMS-B. Both in PMS-B and PMS-C the DGS operates either at a rated power or at a power not exceeding the aggregate powers of the battery bank and net load demand. The flowchart also indicates that the dumping of power, generated from the DGS, may also be required sometimes. Figure 2.4 demonstrates further that the power shortage occurs under various conditions, especially with improper sizes of components in the IMG. Moreover, Figure 2.4 illustrates the ‘on’/‘off’ status of the DGS by a flag variable ‘s’.

2.4.4 Critical Load and Power Management Strategy-D (PMS-D)

The mathematical derivation of the critical load for the DGS is required in order to model the PMS-D.

1) Determination of Critical Load and Cycle Charge Load

The per unit costs of energy for a component (e.g., DGS, battery bank) include capital, operation, and maintenance. Capital costs depend on the power rating of the component and the running costs vary on the operations and maintenances.

The fuel consumption of the DGS is assumed a quadratic function with a cost at no-load operation and the fuel consumption [L/h] of the DGS for a load P^{di}, is expressed as [100],

$$F_c^{di} = g_1 (P^{di})^2 + g_2 P^{di} + g_3 P_{rat}^{di} \tag{2.8}$$

where g_1, g_2, and g_3 are the fuel consumption coefficients in L/kW^2h, L/kWh, and L/kWh, respectively and the values of the parameters for a 300 kW DGS are given in Table A.1. The apparent power rating of the DGS, S_{rat}^{di}, is the same as P_{rat}^{di} at unity power factor. The fuel consumption cost in $\$/kWh$ for the DGS is expressed as,

$$C_f^{di} = \left(g_1 P^{di} + g_2 + g_3 \frac{P_{rat}^{di}}{P^{di}} \right) c_f \tag{2.9}$$

where the coefficient c_f in $[\$/L]$ accounts for the fuel price, transportation cost, and inventory holding costs. Maintenance cost of the DGS varies at the output power and number of start-stop. This chapter adopts a constant maintenance cost for each hour of the DGS operation. The per kWh hourly maintenance cost, C^{di}_{mh}, is formulated as,

$$C^{di}_{mh} = \frac{C^{di}_{m}}{P^{di}_{rat}} \tag{2.10}$$

where the parameter C^{di}_{m} is the maintenance cost for the rated power of the DGS. The hourly running cost of the DGS for per kWh diesel generated energy is the sum of equations (2.9) and (2.10) expressed as,

$$C^{di}_{om} = \left(g_1 P^{di} + g_2 + g_3 \frac{P^{di}_{rat}}{P^{di}}\right) c_f + C^{di}_{mh} \tag{2.11}$$

where C^{di}_{om} is the aggregated hourly operation and maintenance costs of the DGS.

The capital cost of the battery bank depends on size. The battery bank wear cost is considered the sum of per unit energy cost and maintenance cost of the battery bank. Assuming a constant maintenance cost, the wear cost of the battery bank is expressed as,

$$C^{b}_{w} = \frac{C^{b}_{c}}{DOD_{eqc} E^{b}_{rat}} + C^{b}_{mh} \tag{2.12}$$

where C^{b}_{w}, C^{b}_{c}, DOD_{eqc}, E^{b}_{rat}, and C^{b}_{mh} are wear cost, capital cost, equivalent depth of discharge, energy rating of the battery bank, and hourly maintenance cost of the battery bank, respectively. Number of cycle to failure, N_{cf}, for the battery bank is formulated as [101],

$$N_{cf} = \frac{N_{ce} e^{-u_1(DOD-1)}}{DOD^{u_0}} \tag{2.13}$$

where N_{ce}, u_1, and u_0 are the parameters for the equation (2.13). The parameter DOD is the depth of discharge for the battery bank. Based on life cycles of a battery manufacturer, the equation (2.13) can be best fitted for the battery bank. As an example, manufacturer's life cycle data for NiCd battery is best fitted and the values of the parameter are achieved as $u_0 = 1.67$, $u_1 = -0.52$, and $N_{ce} = 2055$. Based on the best fitted values, the equivalent DOD for the battery bank is calculated as,

$$DOD_{eqc} = \frac{1}{M}\sum_{n=1}^{M}(N_{cf})_n(DOD)_n \tag{2.14}$$

where M is the total number of observations and the value of N_{cf} is obtained from equation (2.13). The value of DOD_{eqc} is used in (2.12).

Sometimes the DGS runs in excess to the net load for charging the battery bank and it requires an extra cost. If the round trip efficiency of the BESS and the charger is η_R, then, the sum of the wear cost and cycle charge cost for the battery bank is written as,

$$C_c^e = C_c^{di} + C_w^b = C_w^b + \frac{F_i^{di}c_f}{\eta_R} \tag{2.15}$$

where F_i^{di} is the extra fuel required for charging the battery bank.

The DGS optimum starting/stopping set-point occurs when the wear cost of the battery bank and the running cost of the DGS becomes equal. Thus, the equations (2.11) and (2.12) are equalized to determine the roots of P^{di} and the roots are expressed as,

$$P_d = \frac{C_w^b - g_2c_f - C_{mh}^{di}}{2g_1c_f} \pm \frac{\sqrt{(g_2c_f + C_{mh}^{di} - C_w^b)^2 - 4g_1g_3c_f^2P_{rat}^{di}}}{2g_1c_f} \tag{2.16}$$

The realistic value of P_d is called the critical load. By using equations (2.11) and (2.15), the cycle charge load, P_c, is calculated as,

$$P_c = \frac{C_c^e - g_2c_f - C_{mh}^{di}}{2g_1c_f} \pm \frac{\sqrt{(g_2c_f + C_{mh}^{di} - C_c^e)^2 - 4g_1g_3c_f^2P_{rat}^{di}}}{2g_1c_f} \tag{2.17}$$

Figure 2.5 shows a per unit energy cost curve of the DGS for a variable load power [24], where direct diesel energy cost represents the incurred cost by the generated power of the DGS alone. Figure 2.5 further illustrates that the horizontal line is the battery bank deterioration cost

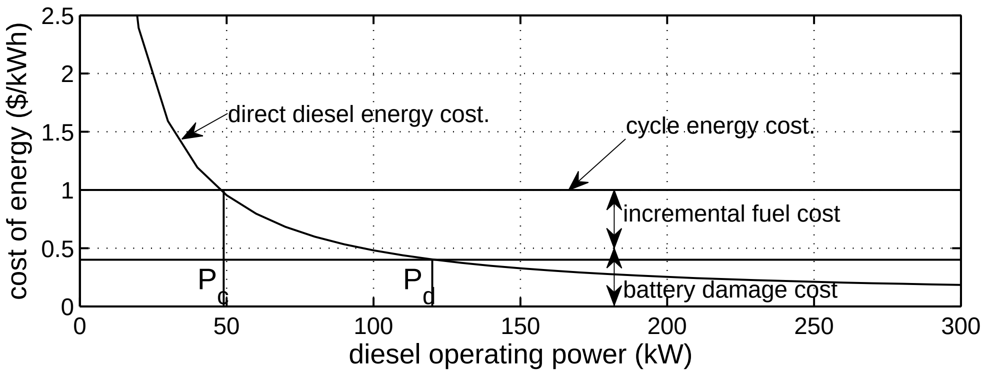

Figure 2.5: Load on DGS versus diesel energy cost curve

and it is assumed fixed. The aforementioned calculated value of P_d is the intersecting point of direct diesel cost and the battery bank deterioration cost. Similarly, the intersecting point of the direct diesel energy cost and cycle energy cost provide the cycle charge load P_c.

2) Description of PMS-D

Figure 2.5 illustrates that it is more economical to use the battery bank for the net load while the net load demand stays below the value of P_d. Alternately, the operation of the DGS is more cost-effective when the net load demand is higher than the value of P_d. Utilizing the aforementioned property, the modified algorithm of the frugal dispatch strategy (i.e., PMS-D) is developed. Figure 2.6 illustrates a flowchart of the PMS-D, where the load reactive power is compensated first by the available resources and the remaining size of the component are calculated. As can be seen in Figure 2.6, the battery bank starts charging when the total real-power output of the WPS and PVS is larger than the load real-power demand, i.e., ($P^w + P^{pv} \geq P^l$). Whenever, the total surplus power of the RERs cannot be stored in the battery bank (i.e., $P_{sur} > P_1^b$), the rest is delivered to a dump load. Power failure may occurs if both the DGS and BESS cannot meet the net load demand, due to improper design of component sizes. During insufficient generation of renewable energy, the critical load, P_d, is compared with the net load real-power demand ($P^l - P^w - P^{pv} = P_{def}$). Whenever the net load is less compared to the value of P_d (i.e., $P_{def} < P_d$), the BESS is given a priority to supply the net load demand. In the

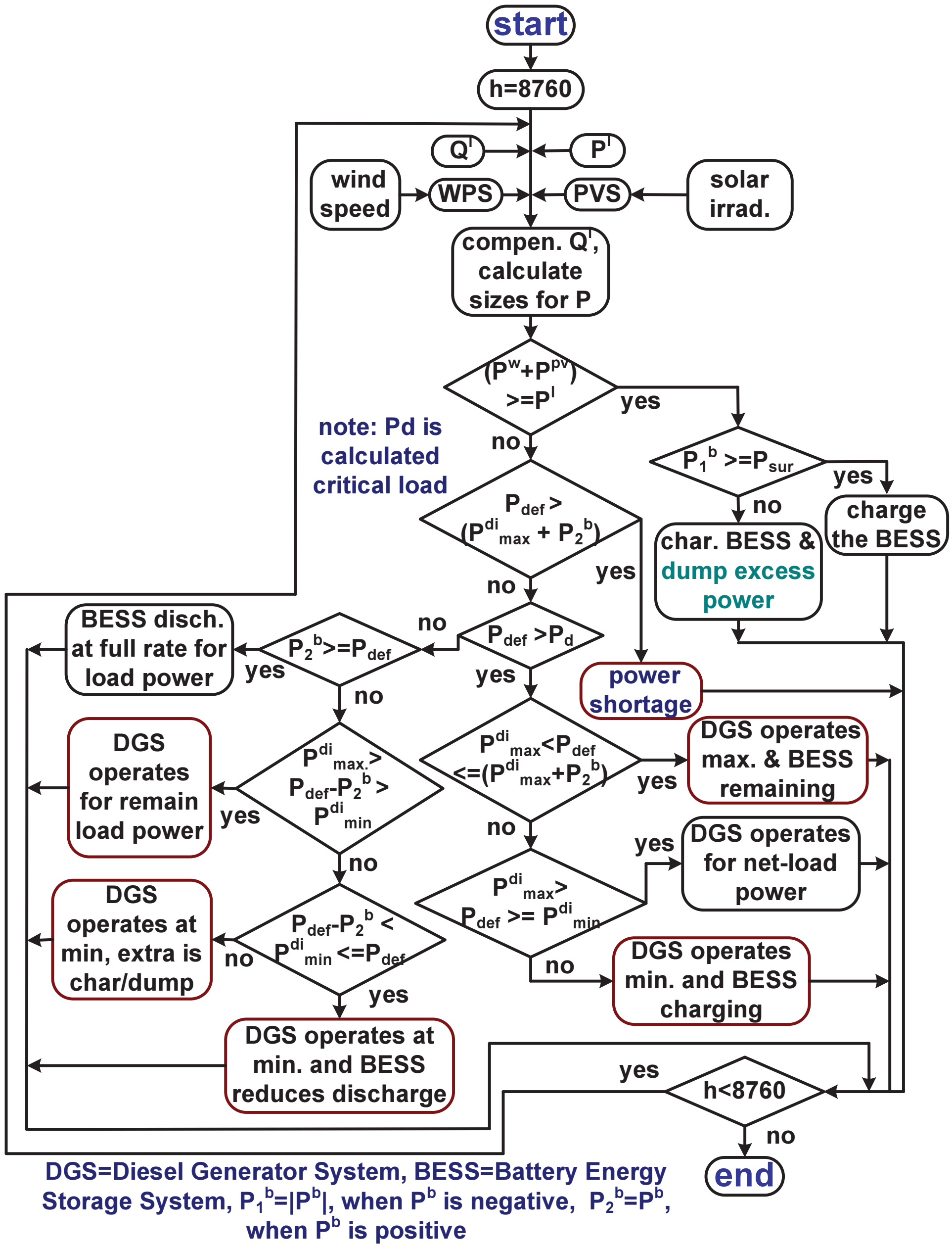

Figure 2.6: Flowchart of PMS-D.

aforementioned situation, if the stored energy/actual discharge power of the battery bank is not enough for the net load, the DGS supplies the deficit of the net load in order to ensuring the reliability of power supply and the operation of the DGS maintains its constraints. As can be seen in Figure 2.6, when the net load, P_{def}, is higher than the critical load, P_d, the DGS delivers the net load. In such a situation, if the DGS cannot deliver the total net load at any reason, the BESS compensates the remaining net load power such that the power supply reliability can be ensured. Utilizing the value of P_c (equation 2.17), the PMS-D can be explained. The brief description of the strategy is given in Table 2.3.

Table 2.3: Brief Description of the PMS-D

State	Description of Operation
C0: Reactive power	Reactive load power is compared with the available resources, then calculate the remaining sizes of the components for the real power.
C1: Battery charging	Aggregated renewable power is larger than the load real-power demand.
C2: Dumping power	Surplus renewable power is too large than the actual charging power of the battery bank and the energy state of the battery bank does not allow to store more energy.
C3: Power shortage	When all the resources of the IMG cannot supply the load real-power demand
	C4: when $P_{def} < P_d$
C41: Battery only	Battery bank supplies the net load real-power demand.
C42: Battery and DGS	When the stored energy of the battery bank is low the DGS provides the rest net load demand.
	C5: when $P_{def} > P_d$
C51: DGS only	The DGS delivers the net load demand
C52: DGS and battery	When the net load demand is too high then battery bank assists the DGS for supplying the net load demand.

2.5 Simulation Results

To demonstrate the performances of the PMSs, several case studies have been conducted in the MATLAB/Simulink environment by utilizing the values of parameter from Table A.2. The values of parameter from Table A.1 are used in equation (2.16) in order to determine the value of critical load, P_d, that is required to simulate the PMS-D. The value of parameter C_w^b in equation (2.16) has computed using (2.12) and (2.14). The hourly average wind speed time series, for a Canadian site (Argentia, Newfoundland), is obtained from [102]; and the hourly average solar irradiation time series is produced by using HOMER package based on latitude and longitude of the site. The wind power and PV power are produced by employing [103] and [104], respectively. The detail mathematical models of the subsystems are given in Chapter 3. To generate Figure 2.7, probabilistic treatment is included for 15 minutes interval on time series. For other figures, the hourly average time-series is utilized. In Figure 2.1, the P^b value is positive for the delivered power of BESS; however, in all the figures except Figure 2.7, the BESS output power is represented by $-P^b$. The real and reactive components of the load power are calculated by utilizing the IEEE RTS load model [105] and a time series of load power factor [106]. Different windows of hours for the following simulations are adopted in order to capture the harmful effects for the PMSs.

2.5.1 Impact of Converter Reactive Power on the Charging of Battery

This case study has been conducted to demonstrate the impact of converter reactive power on the charging of the battery bank. Thus, the study system, i.e., the IMG is simulated by adopting the PMS-A, where the PVS is excluded in the configuration of the IMG. The power rating of the BESS converter is taken 0.50 p.u.. As can be seen in Figure 2.7(a), the wind power P^w remains above 1.0 p.u. that is higher than the primary load real-power demand. Therefore, the DGS does not require to run and the output real power, P^{di}, and reactive power, Q^{di}, in Figure 2.7(a) are zero from 1520th to 1525th hour. Figure 2.7(b) indicates that the SOE of the battery bank has not reached to the maximum level until 1525th hour and thus the excess wind power could be stored in the battery bank. The reactive power demand is 0.50 p.u. at 1520.25th hour and is supplied by the BESS converter, as shown in Figure 2.7(a). Though, there is an excess wind power at 1520.25th hour and the battery bank has capacity for storing energy, the actual charging power P^b of the battery bank is zero due to providing reactive power by the BESS converter at that time.

2.5.2 A Few Hours Simulation of the IMG Using the PMS-A

Figure 2.8 illustrates the real powers, reactive powers, and SOE of the IMG components, where the IMG is simulated by utilizing the PMS-A. The generated total renewable power between 2171th and 2192th hour is more than the primary load demand shown in Figure 2.8(a) and thus the battery bank is charging by the surplus power. As can be seen in Figure 2.8(a), the aggregate

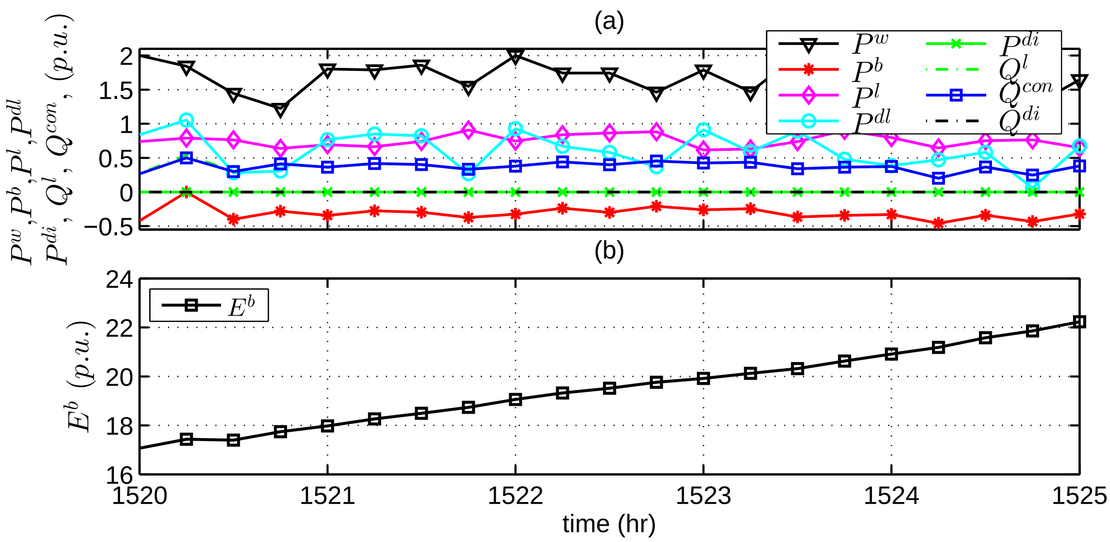

Figure 2.7: Impact of reactive power on the charging power of battery bank.

renewable power output from 2238th to 2285th hour is low to meet the primary load demand. Thus, the shortage is compensated by the BESS; when fails, the DGS runs, e.g., 2286th to 2378th hours. The operation of the IMG from 2114th to 2170th hour in Figure 2.8(b) indicates that the SOE of the BESS stays at minimum. Figure 2.8(a) further demonstrates that the short-term start/stop of the DGS (e.g., 2325th hour) may occur depending on the output power of WPS and PVS. The dump load, P^{dl}, of Figure 2.8(a) indicates that the excess renewable power output is there, especially when the battery bank cannot store the excess energy. As can be seen in Figure 2.8(c), the load reactive power is mostly delivered by the PVS converter and the rest is supplied by the BESS converter and/or DGS.

2.5.3 Performance Study of the PMS-B by Simulation

Figure 2.9 demonstrates the effectiveness of PMS-B by the SOE of battery, along with, the real and reactive powers of the IMG components. Figure 2.9(a) shows that the delivered power from the WPS is very low for various hours between 3300th and 3475th hour. The battery bank does not have enough stored energy (i.e., low SOE) for discharging from 3303th to 3318th hour as shown in Figure 2.9(b) and thus, the DGS delivers both the net load real power and charging power of the battery bank. Once the SOE of battery bank reaches at $E^b_{soc} \approx 16p.u.$ the DGS is

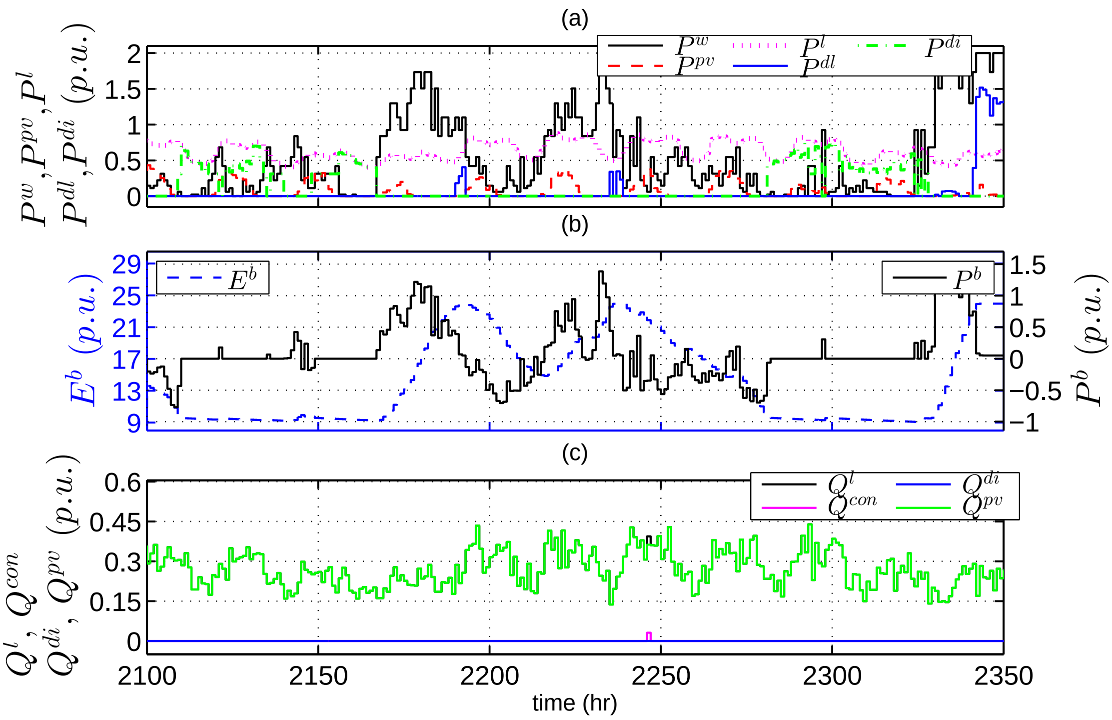

Figure 2.8: Performances of the IMG for the PMS-A.

commanded to stop. The battery bank delivers the net load until the SOE of the battery bank stays above E^b_{min}. Figure 2.9(b) illustrates that the DGS starts as soon as the SOE of the battery bank touches at E^b_{min}. The DGS mainly operates at the rated power as it delivers the net load demand and charges the battery bank as well; subsequently, the frequent start/stop of the DGS decreases. Figure 2.9(c) demonstrates further that the load reactive power is mainly supplied by the PVS converter and then the BESS converter delivers the remaining load reactive power; otherwise the DGS helps.

2.5.4 A Few Hours Simulation for the Performances of PMS-C

Figure 2.10 illustrates the productiveness of the PMS-C by the real power, reactive power, and SOE of the battery bank. The 3395th to 3410th hour simulation of the IMG, presented in Figure 2.10(b), indicates that the DGS operates for charging the battery bank until the energy level reaches at maximum. As can be seen in Figure 2.10(a), the DGS mostly operates at full load to charge the battery bank and to supply the net load demand. By comparing Figures 2.9

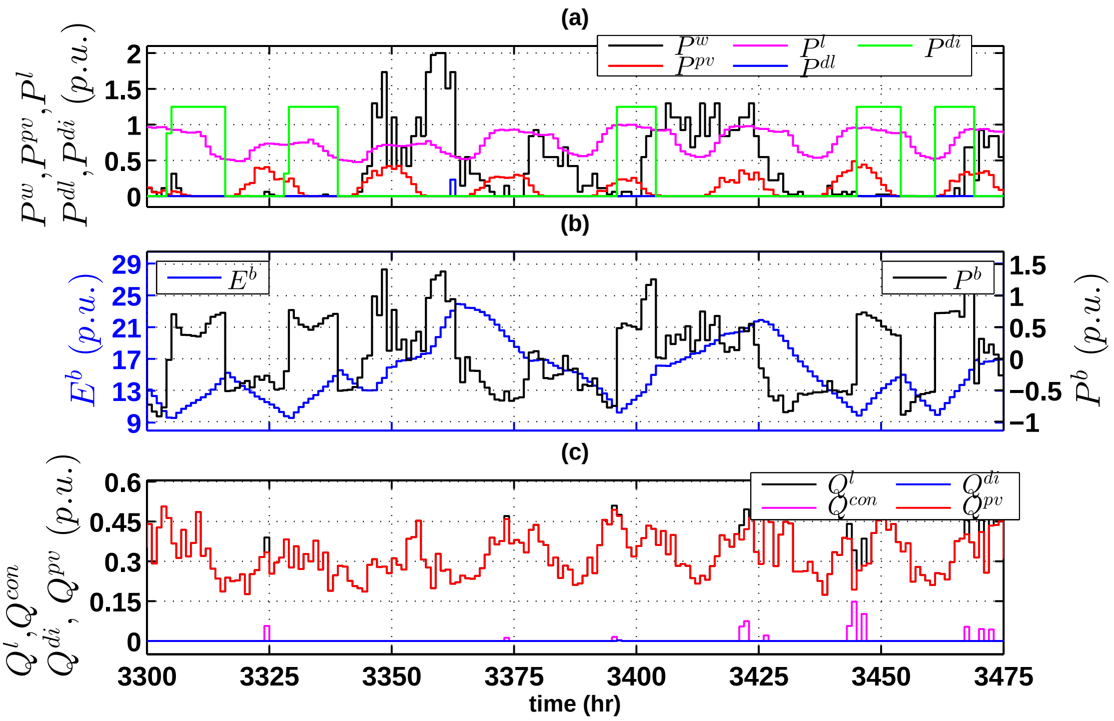

Figure 2.9: Power and energy of the IMG components for the PMS-B

and 2.10, it can be stated that the operating periods of the DGS by this strategy are longer than those of the PMS-B. As the SOE of the battery bank goes at maximum energy level by the DGS operation, Figure 2.10(a) illustrates that the dumping power is high (e.g., from 3350th to 3367th hour). Thus, the REP for the primary load is expected to decrease for this PMS.

2.5.5 Simulation Results of IMG for the PMS-D

Figure 2.11 demonstrates the performance of the IMG due to PMS-D and the performance is presented from 2105th to 2110th hour of operation. As can be seen in Figure 2.11(a), the DGS operates when the net load demand exceeds the value of P_d. Otherwise, the BESS delivers the net load demand, e.g., 2111th to 2117th hour. Thus, the operation of the DGS and battery bank is complementary for supplying the net load demand unless there is any constraints. Figure 2.11(a) further demonstrates that the DGS operation contains frequent start/stop and it can be inferred that this causes high maintenance costs for the DGS. Figure 2.11(b) illustrates that the decrease rate of SOE (i.e., discharging) in the battery is low compared to other strategies.

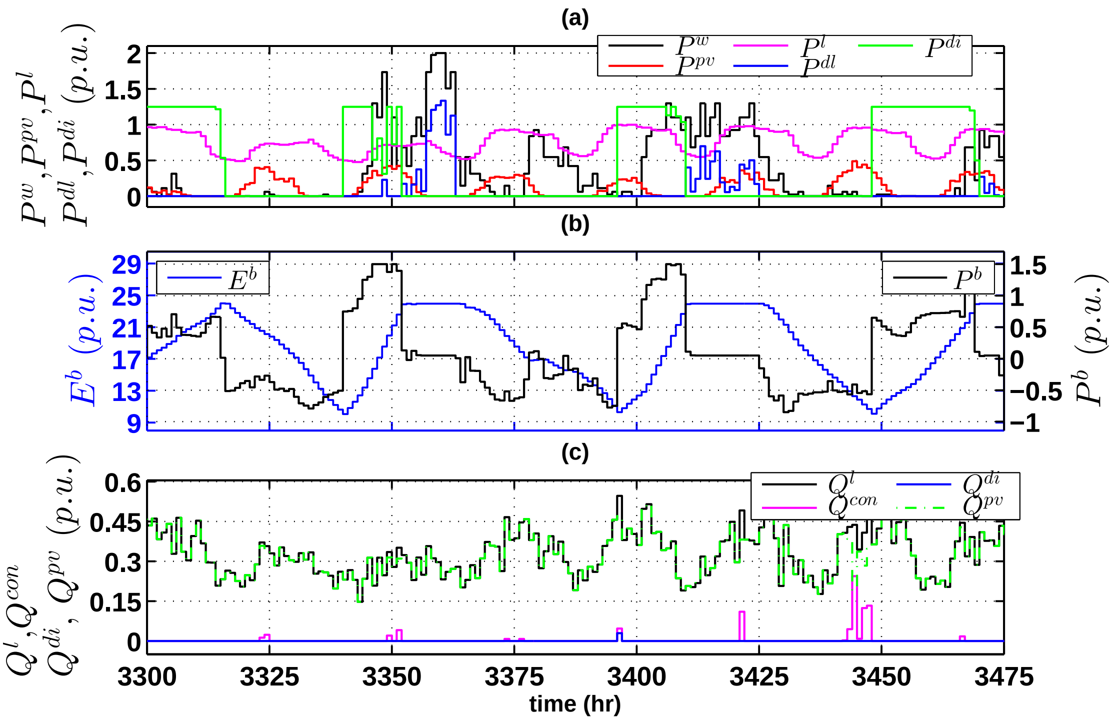

Figure 2.10: Performances measure of the PMS-C by the power and energy behaviors of the IMG components.

The slow decreasing of SOE may enhance the lifespan of the battery bank. Alternately, the charging is faster in the battery than that of discharging.

2.5.6 Comparison of the SOEs of Batteries for the PMSs

Figures 2.12(a), (b) and (c) illustrate respectively the SOEs of battery bank for the PMS-A, PMS-C, and PMS-D. As can be seen in Figure 2.12(a), the SOE of the battery bank for PMS-A remains low from 2900th to 5500th hour due to seasonal variations of wind speed. The magnified plot in Figure 2.12(a) demonstrates that the SOE of the battery bank significantly decreases and reaches below minimum energy level due to self-discharge of the battery bank. The aforementioned situation becomes worse when the renewable power generation continues low (e.g., 1376th to 1475th hour) for a long period after reaching the battery bank at minimum energy level. Thus, the PMS-B and PMS-C utilize the DGS for charging the battery bank. Figure 2.12(b) shows that the SOE of the battery bank does not reach below minimum energy

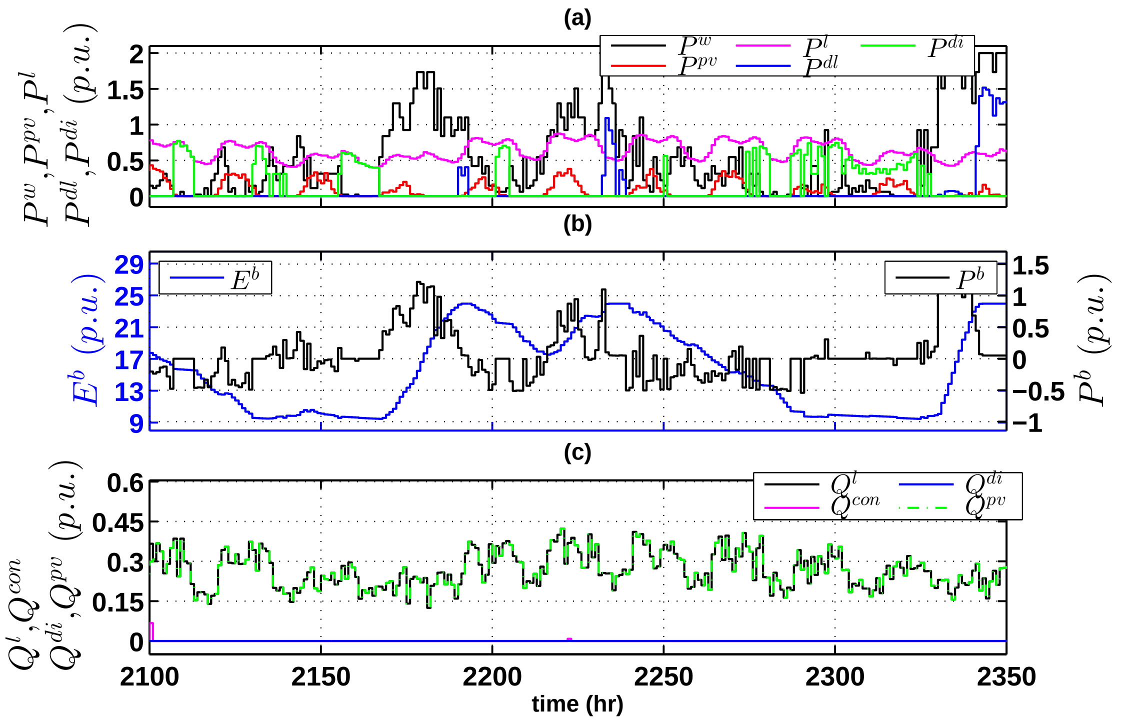

Figure 2.11: Power and energy behaviors of the IMG components for the PMS-D.

level while the SOE of the battery bank frequently touches at maximum energy level of the battery bank. Although, the SOE of the battery bank for the PMS-B is not included for the clarity of the figure, it can be inferred that the SOE of the battery for the PMS-B will not frequently reach at the maximum energy level. The SOE of the battery bank for the PMS-D, shown in Figure 2.12(c), illustrates that the discharge power of the battery bank is low due to delivering power to a low net load demand. Figures 2.12(a) and (c) show that the SOE and self-discharge patterns of the battery bank are similar both for PMS-A and for PMS-D.

2.5.7 Reactive Power Sharing Among in the IMG Components

The reactive powers of the IMG, which is constituted without PVS, are shown in Figures 2.13(a), (b), (c), and (d), for the PMS-A, PMS-B, PMS-C, and PMS-D, respectively. All of the sub-figures of Figure 2.13 illustrate that the PVS reactive power Q^{pv} is zero. Thus, the BESS converter mostly delivers the reactive power Q^{con}. Sometimes, the DGS and BESS share the compensation of the load reactive power. Figure 2.13(a) demonstrates that the load reactive

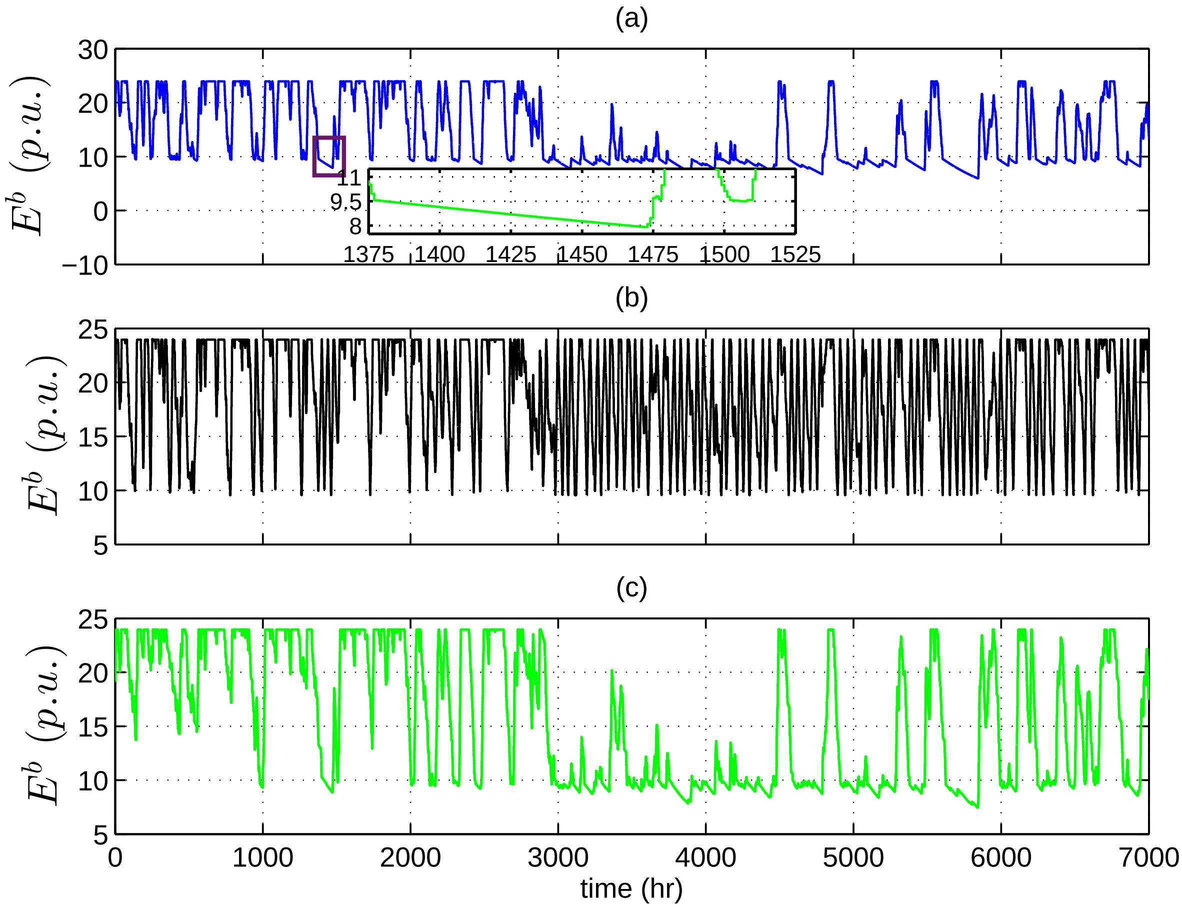

Figure 2.12: SOE of the battery bank for the (a) PMS-A, (b) PMS-C, and (c) PMS-D.

power demand at 2121th hour is 0.45, which is shared by the BESS converter and the DGS; while Figures 2.13(b), (c), and (d) indicate that the reactive powers are mainly delivered from the BESS converter.

2.5.8 Performances Comparison Among the PMSs

The aforementioned studies are presented for few hours of simulation for the clarity of the figures. Thus, Table 2.4 compares the performances of the strategies based on a year round (i.e., 8760 hours) simulation. As Table 2.4 shows, the SOEs of the battery bank stay 3898 hours, 156 hours, 72 hours, and 1143 hours at minimum energy level for PMS-A, PMS-B, PMS-C, and PMS-D, respectively. The number of hours, the SOE of the battery bank stays at minimum level, is significantly low for the PMS-B and PMS-C compare to that of the others.

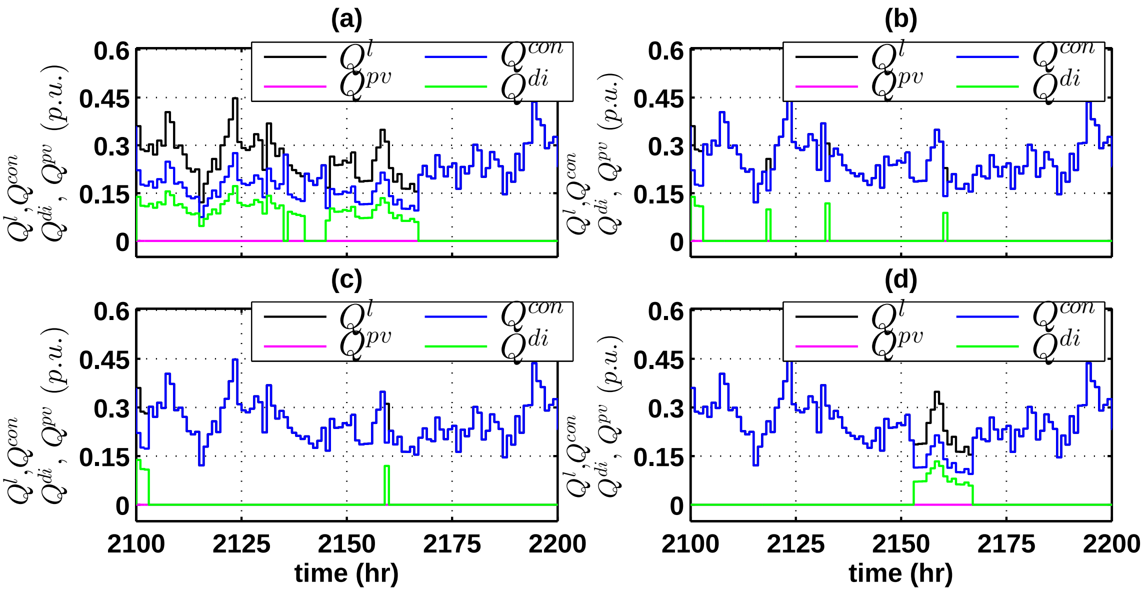

Figure 2.13: Reactive power sharing in the IMG.

The number of hours, the SOE reaches above the 97% of maximum energy level, is the highest for the PMS-C. Consequently, the REP is the lowest and thus the dumping energy is the highest for the PMS-C. Although the DGS is used for charging the battery bank in PMS-B and PMS-C, the number of operating hours for the DGS is low in the strategies due to mostly operating at rated power. Alternately, the DGS operates longer hours by the PMS-A and PMS-D. Moreover, the self discharges of the battery bank for the PMS-A and PMS-D are high. The low operating hours of the DGS signifies low maintenance and operating costs.

2.6 Conclusions

This chapter has modeled four PMSs for an IMG, which is comprised of a DGS, a BESS, and RERs, using flowcharts and has compared the performances of the PMSs upon simulating the IMG. The chapter has presented the insight complexities of the PMSs by including all possible cause-effect relationships, while modeled based on an unknown set of sizes. The impact of reactive power on charging power of the battery bank is demonstrated. The performance analysis, based on a few case studies and long-term simulation, indicates that the PMS-B is apparently

Table 2.4: Performances Comparison Among the PMSs

Observed features	PMS-A	PMS-B	PMS-C	PMS-D
SOE at minimum level	3898 hrs	156 hrs	72 hrs	1143 hrs
SOE above 97% of maximum	1559 hrs	1824 hrs	2506 hrs	1864 hrs
DGS operation	3671 hrs	1763 hrs	1678 hrs	3614 hrs
Renewable energy penetration	69.15%	66.83%	62.62%	66.55%
Dump of energy (kWh)	1183	1375.2	1620.3	1414.5
BESS self discharge	high	low	low	high
DGS operation	variable	rated	rated	variable
Expected lifespan of battery	low	moderate	moderate	low
Expected maintenance cost	high	low	low	high

the best PMS for the IMG. This study further illustrates the impacts of self discharge on the battery bank and compares the SOEs of the battery bank, hours of operation, and start/stop of the DGS. Thus, the study has figured out a few sensitive parameters, which need to be taken into account during system design and feasibility study and has focused that the algorithms of the PMSs that can effectively be utilized for determining the optimal sizes.

Chapter 3

A Single-Objective Optimal Sizing Approach for an IMG

3.1 Introduction

Real-life engineering problems are mostly complex and are generally difficult to optimize by analytical means, i.e., a closed form solution. In Chapter 1, the various optimization problems and the techniques of solving them were discussed. It was also discussed in Chapter 1 that the types of decision variables, the number of objective functions, nonlinearity, constraints, and modality make the optimization problems complex. Thus, the optimal sizing of an islanded microgrid (IMG) is challenging as the problem involves nonlinearity, discrete decision variables, and stochastic parameters. When the decision variables are discrete and the objective functions are implicit, i.e., defined by cause-effect relationship, then an optimization problem prefers a simulation-based technique for the solution.

This chapter proposes a simple and robust algorithm for the optimal sizing of an IMG employing an enumeration technique. The proposed algorithm incorporates the impact of both real and reactive powers on the components sizes of the IMG and involves many decision variables. As multiple simulations are required for optimization, this chapter employs the PMSs of Chapter 2 for simulating the IMG. The algorithm primarily employs the PVS and WPS converters for compensating the load reactive power and it considers the net present value of life-cycle cost (LCC) as an objective function where, LCC is minimized upon maintaining a low loss of power supply probability (LPSP). The algorithm is facilitated for simultaneous optimization of both sizes and the PMSs, also for calculating the REP of the IMG. The effectiveness of the proposed algorithm is evaluated in MATLAB/Simulink environment.

3.2 Renewable Resource and Subsystems Models

This chapter takes into account Figure 2.2 as the study system. The time series models of the renewable resources, i.e., wind speeds and solar irradiations, and the subsystem models of the IMG, i.e., WPS, PVS, battery bank, DGS, and converter, are developed in the following subsections.

3.2.1 Renewable Resource Data Model

The hourly wind speed is modeled by using Weibull probability density function (PDF) [107], which is expressed as

$$f(v_w) = \frac{k}{c_1}\left(\frac{v_w}{c_1}\right)^{k-1}\exp\left\{-\left(\frac{v_w}{c_1}\right)^{k}\right\}, \tag{3.1}$$

where c_1 and k are the scale parameter and the shape parameter, respectively, and v_w is the wind speed. A random variable vector of wind speed v_w, as a time series, is generated in the MATLAB/Simulink environment based on Weibull PDF, while its scale and shape parameters are estimated from historical weather data of wind speed and calculated as,

$$k = \left(\frac{\sigma_w}{\bar{v}_w}\right)^{-1.086} \tag{3.2}$$

$$c_1 = \frac{\bar{v}_w}{\Gamma(1+(1/k))} \tag{3.3}$$

where $\bar{v}_w$ and σ_w respectively signify the mean and standard deviation of the historical wind speed. This chapter considers both the model-based wind speeds and the typical meteorological year (TMY) wind speeds for determining the optimal sizes of the IMG.

Solar resource is the amount of solar radiation that strikes the earth's surface. Irradiation is generally expressed by the average of total radiation on the horizontal surface. In this study, the solar irradiation time series is produced using HOMER software [87], which employs the method described in [108]. The latitude and longitude for an intended site are the required inputs to the HOMER software.

3.2.2 Wind Power Subsystem Model

Two important factors that need to be considered to calculate the output power of a WPS are the wind-speed distribution of the intended site and the power output curve of the wind turbine. A most simplified model for the output power of a wind turbine is

$$P^w = \begin{cases} 0 & \text{if} \quad v_w < V_{ci} \;\text{ or }\; v_w > V_{co} \\ \left(a + bv_w + cv_w^2\right) P^w_{rat} & \text{if} \quad V_{ci} \leq v_w \leq V_r \\ P^w_{rat} & \text{if} \quad V_r \leq v_w < V_{co} \end{cases} \tag{3.4}$$

where V_{ci}, V_r, and V_{co} are the cut-in, rated, and cut-out wind speeds, respectively; v_w and P^w_{rat} respectively signify the wind speed and the rated power of WPS. The coefficients a, b, and c are calculated based on V_{ci} and V_r, as explained in [109]. The values of cut-in wind speed are low for the small-scaled wind turbines.

3.2.3 PV Subsystem Model

The PV subsystem of the study system (see Figure 2.2) is composed of PV arrays, whereas the PV arrays consist of PV modules. In a PV module, the solar cells are connected in series and parallel to obtain the desired voltage and current output. When sunlight strikes a solar cell, the incident energy of sunlight is converted into electrical energy. The performance of a PV module is highly dependant on weather condition, such as temperature and solar irradiance, as well as on the basic PV cell material. Therefore, solar radiation, temperature of the intended site, and type and number of PV modules are required for calculating the output power of a PV array. This chapter adopts the model presented in [104], formulated as

$$P^{pv} = \eta_{pv} \underbrace{A_p N_{pv}}_{P^{pv}_{rat}} \phi_s \{1 - \gamma(T_c - T_{cref})\} \tag{3.5}$$

where η_{pv} is the energy conversion efficiency, A_p is the area of PV modules [m^2], N_{pv} is the number of PV modules in the PV array, ϕ_s is the solar irradiation [$p.u./m^2$], P^{pv}_{rat} is the rated power of the PV array when ϕ_s is the highest, T_c is the PV array temperature [$°C$], T_{cref} is reference temperature under standard test condition (25 $°C$), and γ is the temperature co-efficient (0.005 per $°C$).

3.2.4 Primary Load Power Factor Model

The load power-factor is modeled by the normal distribution PDF, [106], as,

$$f_{X_\theta}(x_\theta) = \frac{1}{\sigma_l \sqrt{2\pi}} \left\{ e^{-\frac{(x_\theta - \mu_l)^2}{2\sigma_l^2}} \right\} \tag{3.6}$$

where X_θ is the Gaussian random variable; the coefficient σ_l and μ_l respectively denote the standard deviation and mean of the load power-factor. The random number x_θ is generated in MATLAB/Simulink utilizing the PDF (3.6).

3.2.5 Primary Load Power Model

A primary load is an electrical demand that the power system must meet at any time according to a given schedule [110]. Though a primary load can be DC, this chapter considers an AC load. Thus, the AC primary load of this study system is decoupled in two components, i.e., the primary load real-power component and primary load reactive-power component. To account for both diurnal and seasonal load variations, the IEEE reliability test system (IEEE-RTS) model, [105], is adopted in this paper for the real power of the primary load. Then the load reactive power [111] is computed as

$$Q^l = P^l \, tan[cos^{-1}(x_\theta)] \tag{3.7}$$

3.2.6 Dump Load Power Model

A dump load absorbs the excess power and is used when the generated power cannot be consumed or stored in the power system network. In this case, the dump load, P^{dl}, is assumed to be a free variable. The cost associated with the dump load is ignored in this paper. This load is characterized by the power rating and the excess power that needs to be dumped during each time step.

3.2.7 BESS Model

The batteries must be of such a collective capacity and power rating that they are capable of meeting the primary-load demand as much as possible during the hours/days of autonomy. The main parameters of a battery bank are the maximum depth of discharge (DOD), rated power, rated energy capacity, per unit cost, and life cycles. The parameters and their effects are deliberately taken into account in the model of the battery bank.

If the rated energy capacity of the battery bank is E^b_{rat}, then the maximum level of energy, E^b_{max}, and minimum level of energy, E^b_{min}, for the battery bank are formulated as,

$$E^b_{max} = 0.98 E^b_{rat} \tag{3.8}$$

$$E^b_{min} = E^b_{rat}(1 - DOD_{max}) \tag{3.9}$$

where DOD_{max} is the maximum depth of discharge.

Owing to diurnal and seasonal variations of solar irradiation, the PV array does not consistently produce the rated power. Therefore, the PVS converter can be utilized for supplying reactive power to the primary load. If the instantaneous real-power output of a PV array is

$P^{pv}(t)$, then the reactive power that the PVS must supply is given by

$$Q^{pv} = \sqrt{(S^{pv}_{con})^2 - (P^{pv})^2} \text{ where } (S^{pv}_{con})^2 \geq (P^{pv})^2 \tag{3.10}$$

where S^{pv}_{con} is the apparent power rating of the PVS converter. When the rated power of the PV array is required to deliver to the PCC, the rated power of the PVS converter is needed to be either greater or equal to the rated power output of the PV array. Thus to keep the PVS cost at minimum, it is assumed that the rated power of the PV array, P^{pv}_{rat}, and the rated power of the PVS converter, S^{pv}_{con}, are equal. When the load reactive-power demand is high, i.e., Q^l is larger than Q^{pv}, then the remaining load reactive power, i.e., $(Q^l - Q^{pv})$, is shared by the BESS and DGS and is controlled by the employed PMS. If the BESS converter delivers reactive power, then the real-power component, P^{con}_{ava}, of the BESS converter is expressed as

$$P^{con}_{ava} = \sqrt{(S^{con}_{rat})^2 - \big(\underbrace{\max\{0, (Q^l - Q^{pv})\}}_{Q^l_{rem}}\big)^2} \tag{3.11}$$

where S^{con}_{rat} is the apparent power rating of the BESS converter, and Q^l_{rem} is the remaining load reactive-power demand. Thus, S^{con}_{rat} must be larger than Q^l_{rem} when the DGS does not run. If the DGS runs to supply real power, the reactive power is shared by the the DGS and BESS, as

$$\begin{aligned} Q^{con} &= \frac{S^{con}_{rat}}{S^{con}_{rat} + S^{di}_{rat}}\big(\underbrace{\max\{0, (Q^l - Q^{pv})\}}_{Q^l_{rem}}\big) \\ Q^{di} &= \frac{S^{di}_{rat}}{S^{con}_{rat} + S^{di}_{rat}}\big(\underbrace{\max\{0, (Q^l - Q^{pv})\}}_{Q^l_{rem}}\big) \end{aligned} \tag{3.12}$$

where Q^{con} and Q^{di} respectively signify the reactive-power components of the DGS and the BESS converter. The variable, S^{di}_{rat}, is the rated apparent-power rating of the DGS. Thus, the maximum amounts of real power that the BESS converter and DGS can deliver are calculated as

$$P^{con}_{ava} = \sqrt{(S^{con}_{rat})^2 - (Q^{con})^2}$$
$$P^{di}_{max} = \sqrt{(S^{con}_{rat})^2 - (Q^{di})^2} \tag{3.13}$$

During the charging process, the power and energy of the battery bank are expressed as

$$P^b_{ava} = \min\left[P^b_{rat}, \max\left(0, \frac{\{E^b_{max} - E^b(t)\}}{\Delta t}\right)\right] \tag{3.14}$$

$$P^b(t) = -\min(P_{sur}, P^b_{ava}, P^{con}_{ava}) \tag{3.15}$$

$$E^b(t + \Delta t) = E^b(t)\,(1 - \delta) - \eta^b_c P^b(t)\Delta t, \tag{3.16}$$

and during the discharging process, the power and energy of the battery bank are expressed as

$$P^b_{ava} = \min\left[P^b_{rat}, \max\left(0, \frac{\{E^b(t) - E^b_{min}\}}{\Delta t}\right)\right] \tag{3.17}$$

$$P^b(t) = \min(P_{def}, P^b_{ava}, P^{con}_{ava}) \tag{3.18}$$

$$E^b(t + \Delta t) = E^b(t)\,(1 - \delta) - \frac{P^b(t)}{\eta^b_d}\Delta t \tag{3.19}$$

where P^b and E^b are the real-power output and stored energy of the battery bank, respectively. The power P_{sur} and P_{def} correspond to the surplus and shortage of renewable generation, respectively; and they are the difference between the aggregated renewable generation and load power. The parameter δ is the self-discharge coefficient of the battery bank, and $\frac{\eta^b_c}{\eta^b_d}$ is the round-trip efficiency of the BESS.

When the minimum charging or discharge time of the battery bank is T_{chr}, then the rated power, P^b_{rat}, of the battery bank can be formulated as

$$P^b_{rat} = \frac{E^b_{max}}{T_{chr}} \tag{3.20}$$

3.2.8 Diesel Generator Subsystem Model

In a low renewable energy penetrated IMG, the main function of the DGS is to maintain the frequency and voltage of the microgrid. Alternately, in a high renewable energy penetrated IMG, both the DGS and the BESS coordinate with each other to maintain the frequency and voltage of the microgrid. Conventional DGS is usually made of a diesel engine coupled with a synchronous generator.

In this chapter, the DGS is modeled with the minimum loading power, rated power, maximum loading power, and fuel consumption. The output power of the DGS maintains a constraint which is expressed as

$$S^{di}_{min} \leq S^{di} \leq S^{di}_{rat}, \tag{3.21}$$

where S^{di}_{min}, S^{di}, and S^{di}_{rat} respectively signify the minimum loading power, output power, and maximum loading power/apparent power rating of the DGS, respectively. However, the PMSs control the operation of the DGS in the IMG and the operation of the DGS can be scheduled to force it on or off at certain times. The DGS sometimes operates at unity power factor, while the load reactive-power demand is supplied by the PVS and BESS converters.

The fuel consumption of the DGS is assumed to be a quadratic function that includes a cost at no-load operation. Thus, F^{di}_c, the fuel consumption $[L/h]$ of the DGS, for a power output of P^{di}, is expressed as [106]

$$F^{di}_c = g_1(P^{di})^2 + g_2P^{di} + g_3P^{di}_{rat} \tag{3.22}$$

where g_1, g_2, and g_3 are the fuel consumption coefficients in L/kW^2h, L/kWh, and L/kWh, respectively. The apparent power rating of the DGS, S^{di}_{rat}, is the same as P^{di}_{rat} at unity power factor operation. The fuel consumption cost in $\$/kWh$ for the DGS is expressed as

$$\beta^{di}_{fl} = \left(g_1P^{di} + g_2 + g_3\frac{P^{di}_{rat}}{P^{di}}\right)c_f \tag{3.23}$$

where the coefficient c_f (in $\$/L$) accounts for the fuel price, the transportation cost, and the inventory holding cost.

3.3 Performance Measurement Models

The reliability evaluation and REP determination models are accounted in this chapter as performance measurement models for the IMG.

3.3.1 Reliability Model

Amongst the reliability indices, the loss of power supply probability (LPSP) is one of the most popular index. Thus, this chapter adopts the LPSP as a reliability measure for the IMG. The LPSP criterion is generally considered a technical criterion in optimal sizing studies. The LPSP is the probability that an insufficient power supply results when the IMG is unable to satisfy the load demand [42]. Alternately, it is the ratio of aggregate power failure time events, i.e., the sum of time the IMG cannot supply the load demand, to the total observed time, calculated as

$$\begin{aligned} LPSP &= \frac{\sum_{t=1}^{N} \text{power failure time}, \Delta t_f \text{ for } (S^{del}(t) < S^{l}(t))}{N} \\ &= \frac{\sum_{t=1}^{N} \{\Delta t_f \text{ for } (P^{del}(t) < P^{l}(t)) \; or \; (Q^{del}(t) < Q^{l}(t))\}}{N}, \end{aligned} \tag{3.24}$$

where N, Δt_f, $S^{del}(t)$, and $S^{l}(t)$ are the total observed hours, the hour of power failure, the output apparent power, and the primary load apparent power, respectively.

3.3.2 Renewable Energy Penetration

Renewable energy penetration (REP) is the ratio of the aggregated delivered energy of RERs to the primary load and the total energy demand of the primary load for a year [112]. Thus, the

REP, γ_{re}, of an IMG which contains both WPS and PVS, is expressed as

$$\gamma_{re} = \frac{(E^{w} + E^{pv} - E^{dl})}{E^{l}} \tag{3.25}$$

where E^{w}, E^{pv}, E^{dl}, and E^{l} are the total energies of WPS, PVS, dump load, and primary load, respectively, for a year. Other than the WPS and PVS, the IMG has employed both the DGS and BESS. Thus, the WPS, PVS, and DGS are the prime energy sources for the primary load, whereas the BESS acts as an intermediate and a dependent resource. Considering a low round-trip conversion loss in the BESS, the REP is alternately formulated as

$$\gamma_{re} = \frac{(E^{l} - E^{di})}{E^{l}} \tag{3.26}$$

where E^{di} is the energy of the DGS for a year and $(E^{l} - E^{di})$ is considered the aggregated delivered energy of the RERs at zero LPSP.

The yearly average energy for a component of the IMG, e.g., for the WPS is calculated as,

$$E^{w} = \int_{\Delta t=1}^{N} P^{w}.dt = \sum_{\Delta t=1}^{N=8760} P^{w}.\Delta t \tag{3.27}$$

In a similar way of (3.27), the aforementioned energies, i.e., the energies for the other components of the IMG are calculated for determining the REP.

3.4 Objective Function

Economic analysis is the most essential criterion for determining the optimal sizes of the IMG. The economic criterion is required to formulate meticulously, while attempting a SOO. The total net present value of the LCC is considered the objective function for this study. The steps of determining the LCC are broadly described in the following subsection.

3.4.1 Economic Model

This economic model predominantly considers the capital, replenishment, operation, maintenance, fuel, and salvage costs of the subsystems. In this analysis, all the cash flows are converted into net present values (NPVs). The factor NPV [107] is calculated as

$$NPV(r_1, N_{lp}) = \frac{(1+r_1)^{N_{lp}} - 1}{r_1(1+r_1)^{N_{lp}}} \tag{3.28}$$

$$r_1 = \frac{1+r_2}{1+r_3} - 1 \tag{3.29}$$

where r_1, r_2, r_3 are the discount rate, interest rate, and inflation rate, respectively; the discount rate is calculated from interest and inflation rates and the parameter N_{lp} is the project life of the IMG. It is assumed that the WPS, PVS and DGS have the same lifespan as the project life. Considering the project life N_{lp}, the cost components of LCC are formulated as follows:

The capital cost, C_c^w, operation and maintenance cost, C_{om}^w, salvage value, C_s^w, and the total cost, C_{tk}^w, of the WPS are calculated as

$$C_{om}^w = \beta_{om}^w P_{rat}^w \bullet NPV(r_1, N_{lp}) \tag{3.30}$$

$$C_s^w = \beta_s^w P_{rat}^w \left(\frac{1+r_3}{1+r_2}\right)^{N_{lp}} \tag{3.31}$$

$$C_{tk}^w = \underbrace{\beta_c^w P_{rat}^w}_{C_c^w} + C_{om}^w - C_s^w \tag{3.32}$$

where β_c^w, β_{om}^w, and β_s^w are the capital cost, operation and maintenance cost, and salvage value of 1 kW WPS, respectively.

Similarly the costs related to the PVS are calculated as

$$C_{tk}^{pv} = \underbrace{\beta_c^{pv} P_{rat}^{pv}}_{C_c^{pv}} + \underbrace{\beta_{om}^{pv} P_{rat}^{pv} \bullet NPV(r_1, N_{lp})}_{C_{om}^{pv}} - \underbrace{\beta_s^{pv} P_{rat}^{pv} \left(\frac{1+r_3}{1+r_2}\right)^{N_{lp}}}_{C_s^{pv}} \tag{3.33}$$

where β_c^{pv}, β_{om}^{pv}, and β_s^{pv} are the capital cost, operation and maintenance cost, and salvage value of 1 kW PVS, respectively; C_c^{pv}, C_{om}^{pv}, C_{sal}^{pv}, and C_{tk}^{pv} respectively signify the capital, operation and maintenance, salvage value, and total costs. The costs related to the PVS have incorporated both the PVS converter cost and the PV array cost.

The capital and replenishment cost, C_c^{con}, operation and maintenance cost, C_{om}^{con}, salvage value, C_s^{con}, and the total cost, C_{tk}^{con}, of the BESS converter are calculated as

$$C_c^{con} = \beta_c^{con} S_{rat}^{con} + \beta_r^{con} S_{rat}^{con} \sum_{i=2}^{N_{pc}} \left(\frac{1 + r_3}{1 + r_2}\right)^{(i-1)N_{con}} \tag{3.34}$$

$$C_{om}^{con} = \beta_{om}^{con} S_{rat}^{con} \bullet NPV(r_1, N_{lp}) \tag{3.35}$$

$$C_s^{con} = \beta_s^{con} S_{rat}^{con} \sum_{i=1}^{(N_{pc}-1)} \left(\frac{1 + r_3}{1 + r_2}\right)^{(i-1)N_{con}} \tag{3.36}$$

$$C_{tk}^{con} = C_c^{con} + C_{om}^{con} - C_s^{con} \tag{3.37}$$

where β_c^{con}, β_{om}^{con}, and β_s^{con} are the capital and replenishment cost, operation and maintenance cost, and salvage value of 1 kVA BESS converter, respectively; N_{pc} is the number of times the converter must be replaced, and N_{con} is the converter lifespan.

The capital cost, C_c^{di}, operation and maintenance cost, C_{om}^{di}, salvage value, C_s^{di}, and the total cost, C_{tk}^{di} of DGS are calculated as

$$C_{om}^{di} = \left\{\beta_{om}^{di} S_{rat}^{di} + \sum_{h=1}^{r_h} \beta_{fl}^{di} P^{di}\right\} \bullet NPV(r_1, N_{lp}) \tag{3.38}$$

$$C_s^{di} = \beta_s^{di} S_{rat}^{di} \left(\frac{1 + r_3}{1 + r_2}\right)^{N_{lp}} \tag{3.39}$$

$$C_{tk}^{di} = \underbrace{\beta_c^{di} S_{rat}^{di}}_{C_c^{di}} + C_{om}^{di} - C_s^{di} \tag{3.40}$$

where β_c^{di}, β_{om}^{di}, and β_s^{di} respectively denote the capital cost, operation and maintenance cost, and salvage value of 1 kVA DGS.

The lifespan of the battery bank and the charge controller is usually shorter than that of the project lifespan. The cost related to battery bank is calculated as

$$C_{tk}^{b} = \underbrace{\beta_c^b E_{rat}^b + \beta_r^b E_{rat}^b \sum_{i=2}^{N_{pb}} \left(\frac{1+r_3}{1+r_2}\right)^{(i-1)N_b}}_{C_c^b} + \underbrace{\beta_{om}^b E_{rat}^b \bullet NPV(r_1, N_{lp})}_{C_{om}^b} \tag{3.41}$$

where β_c^b and β_{om}^b are the capital cost and operation and maintenance cost of 1 kWh battery bank, respectively; N_{pb} denotes the number of times the purchase of battery bank and N_b signifies the battery bank lifespan. However, the parameter N_b varies with the use of the PMS.

An independent charge controller (not shown in Figure 2.1) controls the charging/dischrging of the battery bank. Thus, the cost related to charge controller is calculated as

$$C_{tk}^{chr} = \underbrace{\beta_c^{chr} P_{rat}^b \sum_{i=1}^{N_{pcc}} \left(\frac{1+r_3}{1+r_2}\right)^{(i-1)N_{chr}}}_{C_{cap}^{chr}} + \underbrace{\beta_{om}^{chr} P_{rat}^b \bullet NPV(r_1, N_{lp})}_{C_{om}^{chr}} \tag{3.42}$$

where β_c^{chr} is the capital cost of 1 kW charge controller; N_{chr} and N_{pcc} respectively denote the life cycles and the number of purchases of the charge controller.

The LCC is the total of all the aforementioned costs, expressed as

$$\text{LCC} = (C_{tk}^{w} + C_{tk}^{pv} + C_{tk}^{di} + C_{tk}^{con} + C_{tk}^{chr} + C_{tk}^{b}) \tag{3.43}$$

3.4.2 Problem Formulation

The decision variables of the proposed single objective optimal sizing approach are the rated power of the WPS, P_{rat}^{w}, rated power of the PVS, P_{rat}^{pv}, rated power of the battery bank, P_{rat}^{b}, rated power of the DGS, S_{rat}^{di}, rated power of the BESS converter, S_{rat}^{con}, and rated energy capacity of the battery bank E_{rat}^{b}. Thus, the decision variable vector is expressed as

$$\mathbf{X} = [P_{rat}^{w}\ P_{rat}^{pv}\ S_{rat}^{di}\ E_{rat}^{b}\ S_{rat}^{con}\ P_{rat}^{b}]^T \tag{3.44}$$

Then, the SOO problem is formulated as,

$$\underset{\mathbf{X}}{\text{minimize}} \quad \text{LCC}$$

$$\text{subject to} \quad \text{LPSP} \leq LPSP^{des}$$

$$\sum_{i=1}^{8760} \left(P_i^w + P_i^{pv} + P_i^{di} + P_i^b - P_i^l - P_i^{dl} \right) = 0 \ \text{ and} \tag{3.45}$$

$$\sum_{i=1}^{8760} \left(Q_i^{pv} + Q_i^{di} + Q_i^{con} - Q_i^l \right) = 0 \tag{3.46}$$

$$S_{min}^{di} \leq S^{di} \leq S_{rat}^{di} \tag{3.47}$$

$$E_{min}^b \leq E^b \leq E_{max}^b \tag{3.48}$$

$$P_{rat}^w \geq 0, P_{rat}^{pv} \geq 0, S_{rat}^{di} \geq 0, E_{rat}^b \geq 0, S_{rat}^{con} \geq 0, P_{rat}^b \geq 0 \tag{3.49}$$

where LCC, **X**, and $\mathcal{R}$ respectively signify the objective function, decision variable vector, and feasible region. The aforementioned constraints are taken from the developed mathematical models and they are employed in the algorithm of the PMSs.

3.5 Optimization Algorithm

For determining the optimal sizes of the IMG, the paper employs an enumeration-based SOO approach. The flowchart for the optimization approach is shown in Fig. 3.1, and the steps of the algorithm are as follows:

1. Specify the initial value, final value, and step sizes for the elements of the decision variables.

2. Apply hourly wind speed either from weather data or from model and hourly solar irradiation as shown in Fig. 3.1.

3. Incorporate WPS, PVS, and primary load models so that the hourly wind power and PV power can be produced and compared with load.

4. Utilize the hourly generated powers and loads in the PMSs so that the remaining energy resources and reserves, i.e., the DGS, the BESS, and the dump load can create power balance (see (2.1)).

5. Update the value of LPSP, if there is a shortage of powers in the previous step.

6. Go back to the fourth step and run for 8760 hours in order to calculate yearly LPSP.

7. Go back to the first step if the yearly LPSP does not meet a desired value and discard the configuration.

8. Store the configuration, i.e., the decision variable vector, and the corresponding LPSP, LCC, and γ_{re} when LPSP meet the desired value.

9. Go back to the first step for the next set of decision variable vector.

10. Compare all LCCs.

11. Identify the decision variable vector that provides the lowest LCC, and save the corresponding values of LPSP, LCC, and γ_{re}.

3.6 Simulation Results

The optimal sizing approach for the IMG is evaluated in the MATLAB/Simulink environment. The study system is simulated by hourly average data of a year. The evaluation process employs the parametric values from Tables A.3, A.4, and search spaces from Table 3.1. The hourly average historical wind speed (Figure 3.2(b)) from a Canadian site (Argentia, Newfoundland), and solar irradiation (Figure 3.2(c)) are used in the study. A model-based wind speed time series (Figure 3.2(d)) is also used in the study. Using the data sheet of Siemens solar-module SM110/SM100, the area for 1 p.u. (300 kW) PV array is calculated as 2000 m^2. Taking the peak value of the real load as 350 kW, IEEE-RTS year around real-load (Figure 3.2(a)) is used in the simulation. The hourly average power factor for the load is developed utilizing (3.6)

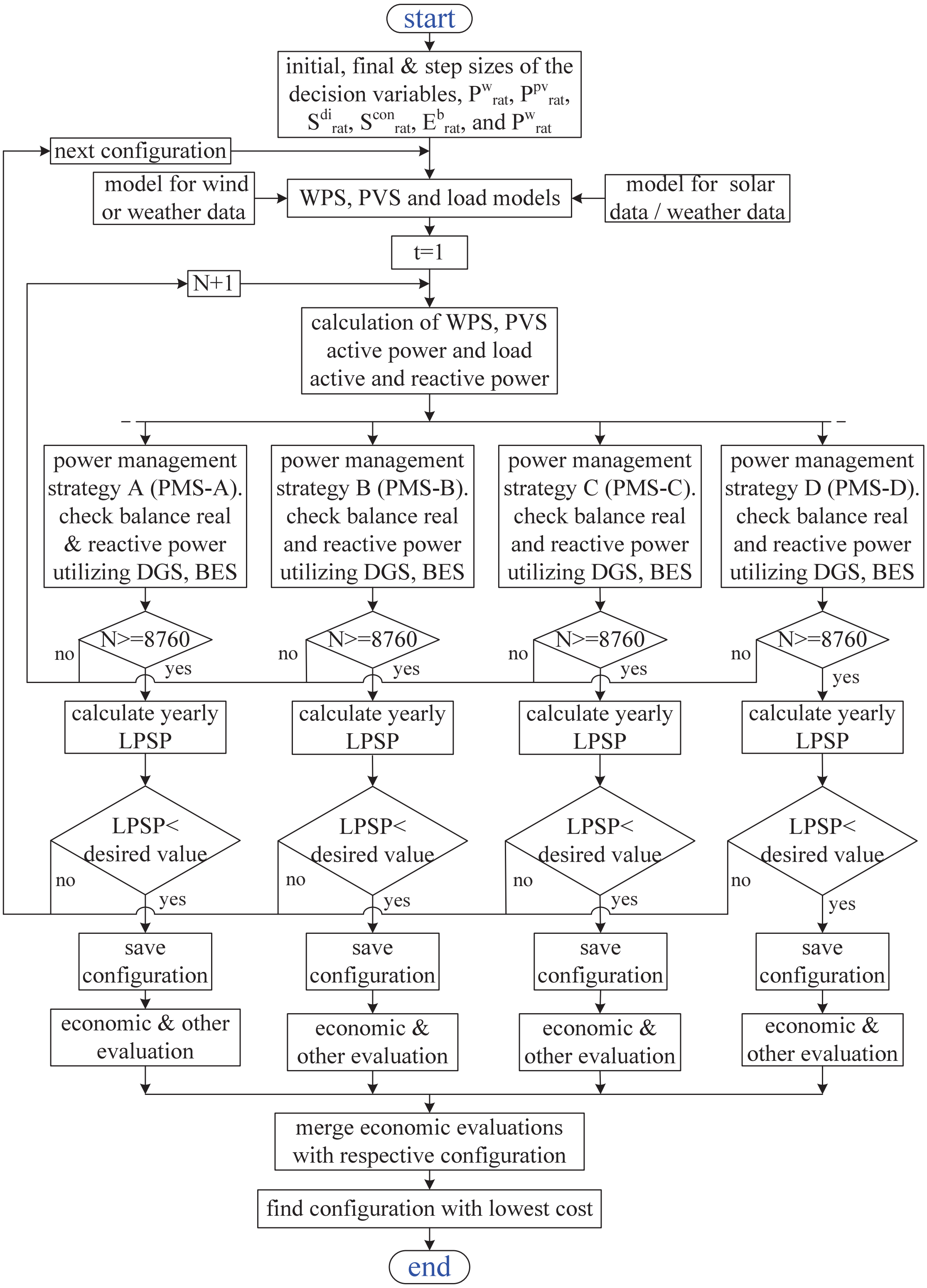

Figure 3.1: Flowchart for the enumeration-based SOO algorithm

with mean value 0.92, and subsequently the load reactive power (Figure 3.2(a)) is constructed by (3.7).

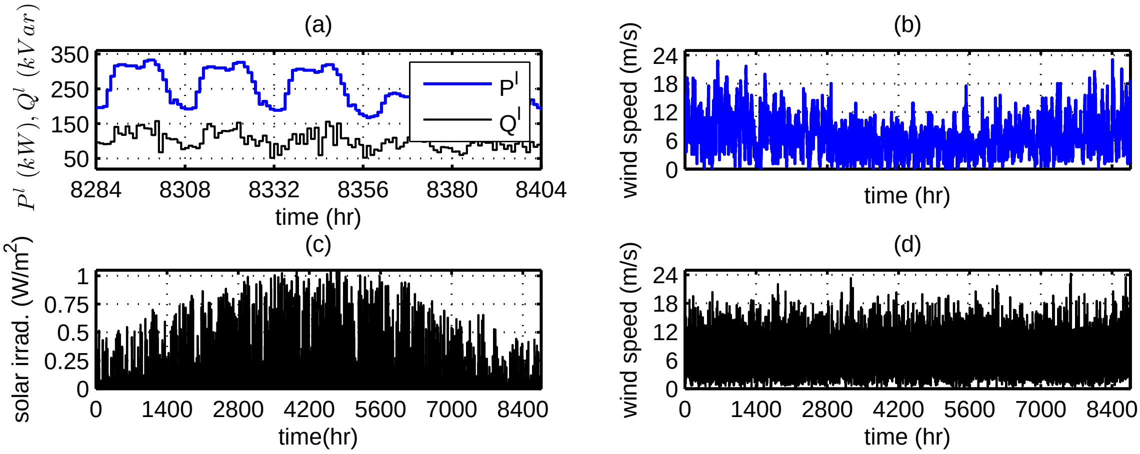

Figure 3.2: Real and reactive load (a), historical wind speed (b), solar irradiation (c), and synthesize wind speed (d)

Table 3.1: Search Space (Decision variable) Ratings for the Components

Components	Unit	Minimum	Step-Size	Maximum
WPS (P^w_{rat})	kW	0	150	900
PVS (P^{pv}_{rat})	kW	0	150	450
BESS (E^b_{rat})	kWh	0	600	3000
DGS (S^{di}_{rat})	kVA	320	80	640
Converter (S^{con}_{rat})	kVA	0	160	640
Charger (P^b_{rat})	kW	$(E^b_{rat})/24$	$(E^b_{rat})/24$	$(E^b_{rat})/6$

3.6.1 Optimal Sizing of the IMG - Case Study by Historical Time Series

This study has been conducted employing both meteorological wind speed time series and HOMER-based solar irradiation time series under severe seasonal and diurnal variations. The first row of Table 3.2 shows the optimal sizes at minimum LCC. A few other combinations of sizes, whose LCCs are slightly above the minimum value, are presented in Table 3.2. As can be seen in Table 3.2, the PMS-B (SOC setpoint) contributes all the recommended sizes. Although the value of γ_{re} at minimum LCC is 54.7%, the REP of the presented solutions varies from 46% to 61%. The values of the rated powers P^{w}_{rat} and P^{pv}_{rat} in Table 3.2 indicate that the REP becomes high when both WPS and PVS present in the sizing combination. The fifth row of Table 3.2 illustrates the aggregate value of the rated powers P^{w}_{rat} and P^{pv}_{rat} (750 kW), which can provide the value of γ_{re} approximate to 60% with 0.5% increase of the LCC than that of the values at minimum LCC.

Table 3.2: Optimal Sizing of the IMG

P^{w}_{rat} kW	P^{pv}_{rat} kW	S^{di}_{rat} kVA	E^{b}_{rat} kWh	S^{con}_{rat} kVA	P^{b}_{rat} kW	LPSP	LCC ($)	γ_{re} (%)	P^{l}_{max} kW	PMS
450	150	400	1200	320	200	0	6205653.81	54.70	350	B
600	0	400	1200	320	200	0	6208714.56	52.57	350	B
450	0	400	1200	320	200	0	6235006.68	46.44	350	B
450	150	480	1200	320	200	0	6235305.15	54.87	350	B
600	150	400	1200	320	200	0	6238748.52	59.97	350	B
600	0	480	1200	320	200	0	6253232.16	52.52	350	B

3.6.2 Impact of Load Reactive-Power Demand on Optimal Sizes

Table 3.3 shows the optimal sizes that are calculated considering only the load real-power demand, i.e., without considering the load reactive-power demand. Thus, the impact of load reactive-power demand on optimal sizes is analyzed comparing the results of Table 3.3 with the results of this case study. The optimal sizes, i.e., the first row of Table 3.2 and that of Table 3.3, are different, though the total power capacities of the RERs remain the same. In Table 3.2, the optimal sizes have included the PVS so that the load reactive-power demand could be shared on priority by the PVS converter. However, the elements of the decision variable vector of Table 3.3 are similar to the second row elements of Table 3.2, while the LCC of the former is lower than that of the later. The LCC becomes high in Table 3.2 due to the requirement of high running hours of DGS such that the load reactive power demand is shared. Considering the aforementioned facts, the optimal sizes and LCC of Table 3.2 can be considered realistic.

Table 3.3: Optimal Sizes of the IMG Without Load Reactive-Power Demand

P^w_{rat} kW	P^{pv}_{rat} kW	S^{di}_{rat} kVA	E^b_{rat} kWh	S^{con}_{rat} kVA	P^b_{rat} kW	LPSP	LCC ($)	γ_{re} (%)	P^l_{max} kW	PMS
600	0	400	1200	320	200	0	6195204.17	52.60	350	B

3.6.3 Optimal Sizing of the IMG - By a Model-based Wind Speed

As can be seen in the first row of Table 3.4, the optimal sizes of the IMG have been determined by utilizing a wind speed time series, which is produced employing the Weibull PDF. The comparison of Tables 3.4 and 3.2 indicates that the optimal sizes of Table 3.4 enhances the value of γ_{re} by 16%, while the LCC is decreased by 13%. The increase of the REP (i.e., γ_{re}) occurs due to not having seasonal variations in the wind speeds and also not having many hours of cut-in or below cut-in wind speeds at stretch in the Weibull PDF-based time series. However, the fourth and sixth columns of Table 3.4 demonstrate that the energy capacity and the rated power of the battery bank are larger than those of Tables 3.2. Consequently, it implies that the more renewable energy is utilized that is also supported by the increased values of γ_{re}. Though the battery bank is large in Table 3.4, the LCC is low due to small operating hours of the DGS.

3.6.4 Global Minima Identification and Impact of the WPS and PVS Sizes on LCC

Figure 3.3 illustrates the impact of the combined sizes of the WPS and PVS on LCC. The minimum values of LCC are calculated, ensuring the LPSP at minimum (i.e., at zero), for various combinations of decision variables where the WPS and PVS sizes are varied systematically. Figure 3.3 shows four convex curves for four different sizes of the PVS. Keeping the PVS size

Table 3.4: Optimal Sizing of IMG Using Wind Speed Model

P^{w}_{rat} kW	P^{pv}_{rat} kW	S^{di}_{rat} kVA	E^{b}_{rat} kWh	S^{con}_{rat} kVA	P^{b}_{rat} kW	LPSP	LCC ($)	γ_{re} (%)	P^{l}_{max} kW	PMS
750	0	400	1800	320	300	0	5393780.62	79.93	350	B
750	0	480	1800	320	300	0	5430651.66	79.41	350	B
600	0	480	1800	320	300	0	5433036.63	72.86	350	B
600	0	400	1800	320	300	0	5440083.68	73.01	350	B
600	150	400	1800	320	300	0	5486722.84	80.92	350	B
750	0	560	1800	320	300	0	5518115.89	78.93	350	B

fixed, the WPS size is varied along with the other decision variables. The curves of Figure 3.3 further demonstrate that the value of LCC is high for a high value of WPS size and the value of LCC goes down with the decrease of WPS size, until a certain size. Figure 3.3 further demonstrates that the value of LCC increases with the very low sizes of WPS, due to high operation costs of the DGS. Figure 3.3 indicates that each curve has its own minimum which is called a local minimum. Thus, the minimum among the four local minimums is determined for identifying the global minimum. It is worthwhile to mention that this global minima resemble the sizes of the first row of Table 3.2.

3.6.5 Impact of Storage-Hour of Battery Bank on LCC

Figure 3.4 demonstrates the relationship between the combinations of sizes of PVS and WPS with LCC for a number of storage-hour battery banks. A large storage-hour battery bank needs more surplus power either from WPS and PVS or from DGS for charging the battery bank. A high hour-storage battery bank ensures the LPSP at minimum. Consequently, the value of LCC increases for the large battery banks, large combination of PVS and WPS sizes, and for large operating costs of the DGS. The increase of battery bank size or battery bank autonomy hour puts the individual curve at the upper position as shown in Figure 3.4. Thus, a large hour-storage battery bank increases the value of LCC. However, the combination of large

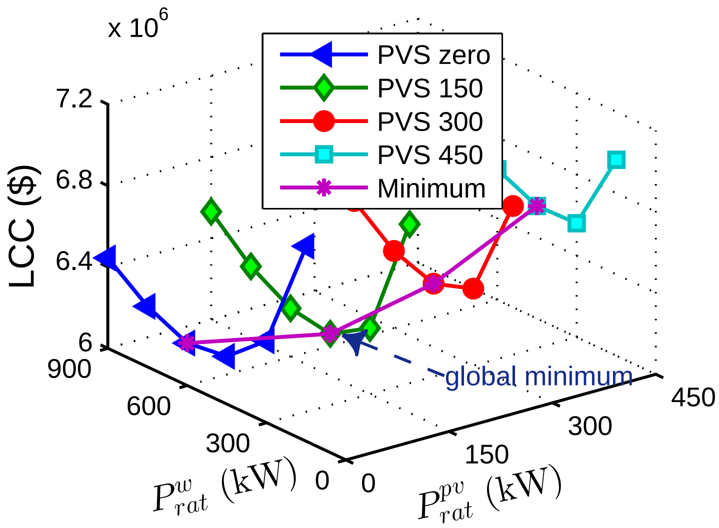

Figure 3.3: Impact of system sizes on LCC

hour-storage battery bank and high sizes of RERs delivers more renewable energy to the IMG.

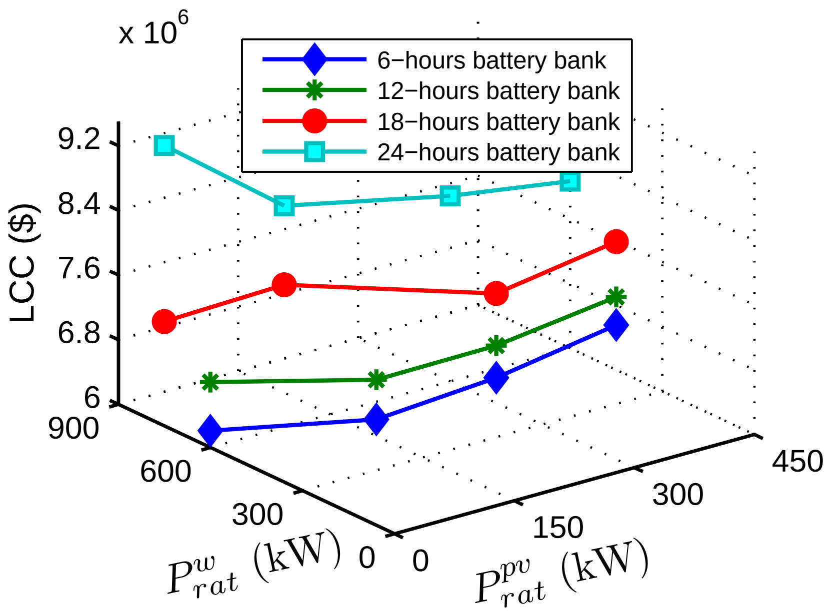

Figure 3.4: Relationship of the LCC and the combination of WPS and PVS sizing with battery bank storage-hour

3.6.6 Impact of Renewable Energy Penetration on LCC

The minimum values of LCC are sorted for every 10% increment of γ_{re}. Figures 3.5(a) and (b) respectively represent the results which are produced by using meteorological time series and Weibull PDF-based time series. Figure 3.5(a) shows that the value of LCC is high at low value of γ_{re} and the LCC decreases with the increases of γ_{re} until the value of γ_{re} reaches 45%. If the minimum value of LCC in Figure 3.5(a) represents a weak minimum, then the values of γ_{re} are assumed to stay between 46% and 60%. The global minimum of LCC provides the value of γ_{re} at exact 54.7% (shown in Table 3.2) which is the mid-value of 46% and 60% shown in Figure 3.5(a). The value of LCC, beyond 60% of γ_{re} in Figure 3.5(a), has increased due to the requirement of a large battery bank. Like above, Figure 3.5(b) demonstrates that the value of γ_{re}, near the weak minimum of LCC, stays between 72% and 84% and the reason for the increased value of γ_{re} is explained earlier. This case study demonstrates that the global minimum of LCC cannot be attained keeping the REP at too low or too high.

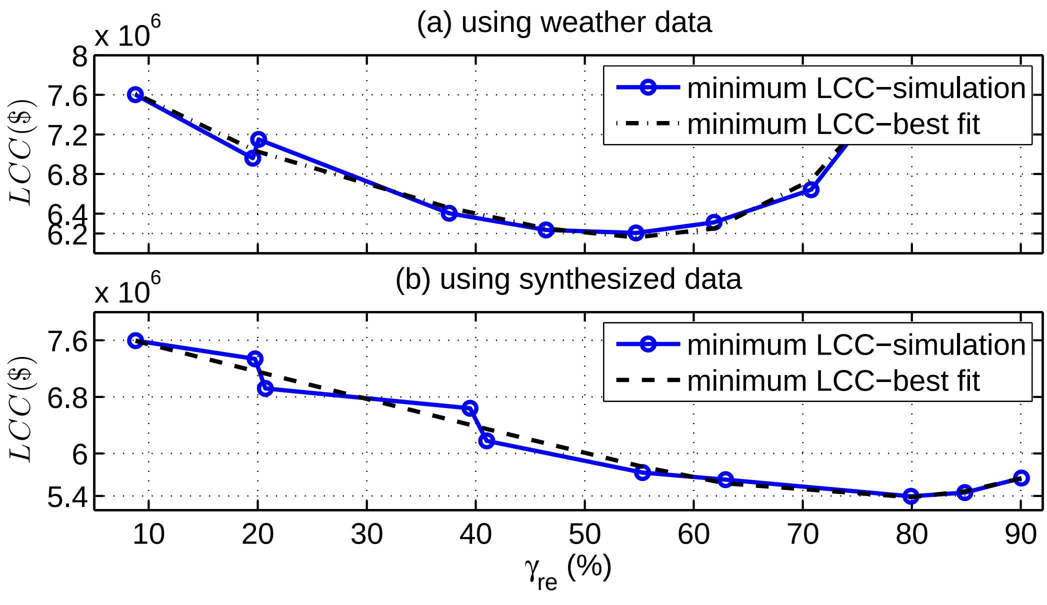

Figure 3.5: The values of γ_{re}% vs the values of LCC

3.6.7 Impact of LPSP on LCC

By employing a meteorological time series, the minimum values of LCC at various combination of sizes are determined for every 2% increment of LPSP. The results along with the best fit curves are presented in Figure 3.6. This study utilizes the rated power of the DGS as 240 kVA so that the simulation of the IMG provides a wide ranges value of LPSP. Figure 3.6 demonstrates that the value of LCC decreases, as expected, continually with the increase of LPSP percentage. The diminishing rate of LCC is not smooth enough due to the effect of other decision variables. Figure 3.6 further illustrates that the value of LCC is high, at zero LPSP, than that of Table 3.2, which is due to large operating costs of the DGS.

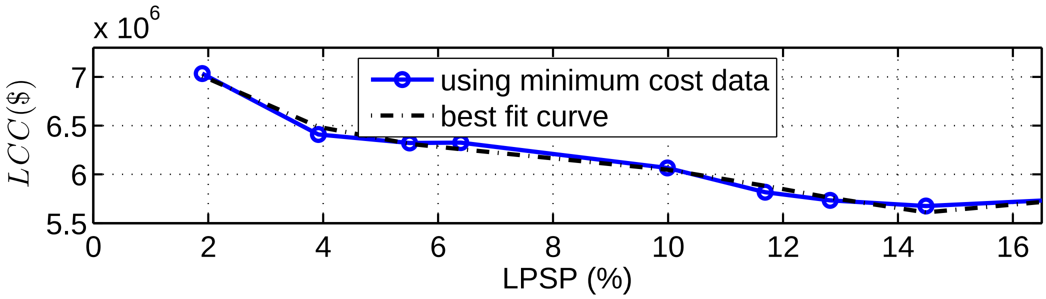

Figure 3.6: LPSP vs. LCC curve

3.6.8 Coefficient of Variation for LCC

The three stochastic variables of this study are wind speed, solar irradiation, and primary load power. It is essential to identify the degree of variations of the LCC in such a stochastic environment. Thus, the coefficient of variations for the LCC, under fifteen realizations of wind speed, is determined. The seventh column of Table C.1 illustrates the global minimum values of LCC for the realizations. Although the average coefficient of variations for wind speeds is 0.527, Table C.1 shows the coefficient of variation for the LCC is only 0.0077. Though the decision variables are widely varied during simulation, the numerous wind-speed realizations provide the same combination of sizes (shown in Table 3.4), i.e., the same decision vector.

3.6.9 Impact of Battery Price on Per Unit Energy Cost

There are varieties of batteries in the markets at various prices. Therefore, a sensitivity study on per unit energy cost for the battery bank capital price is presented in Figure 3.7. The optimal sizes obtained in Table 3.2 are employed for the study. It is expected that the high-priced batteries are better in quality, and thus the lifespan of those batteries are longer. Ten percent increment of battery lifespan is assumed for every \$ 200 of elevated price for battery capital cost (β_c^b). As Figure 3.7 shows, the per unit (kWh) energy costs increase from 16.5 cents to 30.0 cents, if the per unit capital prices of battery bank are elevated from \$ 200 to \$ 2000. The increase of battery bank lifespan reduces the replenishment numbers during project life, and thus the per unit energy costs remain the same at \$ 400 and \$ 500.

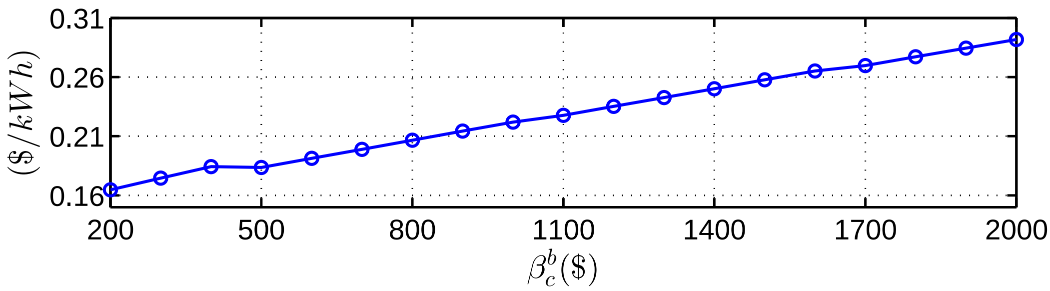

Figure 3.7: Impact of capital cost of batteries on per unit (kWh) energy cost

3.6.10 Comparison of the Proposed Approach with HOMER

To validate the efficacy of the proposed approach, the optimization process for the IMG is replicated in HOMER [87]. Table 3.5 shows the comparison results and indicates that an one step large WPS is suggested by the HOMER while the DGS, BES, and converter sizes of HOMER are lower than those of the proposed approach. The size of the battery bank is slightly higher in the proposed approach due to the remaining marginal difference in the models. The sizes of DGS in the comparison are close whenever we convert the unit kVA into kW by the base power factor. The converter size in the proposed approach is higher than that of HOMER due to taking the converter into account as a reactive power source. Thus, the consideration of reactive power

Table 3.5: Comparison Results of the Proposed Approach with HOMER

Approach	P^{w}_{rat} (kW)	P^{pv}_{rat} (kW)	S^{di}_{rat} –	E^{b}_{rat} (kWh)	S^{con}_{rat} –	P^{b}_{rat} (kW)	LPSP –	LCC ($)	γ_{re} (%)	P^{l}_{max} (kW)	PMS –
Proposed	450	150	400 kVA	1200	320 kVA	200	0	6,205,653	54.70	350	B
HOMER	600	150	350 kW	1140	160 kW	–	0	6,246,003	66	350	CC

provides a realistic optimal sizes. In HOMER, the power rating of battery bank charger cannot be accommodated as a decision variable. Even after the charger cost, the proposed approach provides less LCC than that of HOMER. The REP percentage is high in HOMER because the HOMER method does not dump the extra renewable generation while in the proposed approach the dump load energy is deducted in REP formulation. As all the parameters and few considerations of one approach cannot perfectly fit to the others, a few researchers [55], [57] also observed marginal variations in their comparisons that are also performed in HOMER.

3.7 Conclusions

This chapter has presented a robust single objective optimal sizing approach for an IMG that can be employed in a large off-grid community. It has been shown that the approach is capable of locating the global minimum of LCC upon maintaining a high reliability of power supply in the IMG and it has simultaneously optimized the sizes and PMSs. The comparison results have indicated that the approach has identified realistic optimal sizes due to incorporating the reactive power effect on component sizes. The approach provides a lower cost solution compared to a standard approach and has detected an optimal PMS from four in accordance with HOMER that have employed two. A set of configurations near to minimum value, meeting the desired value of LPSP, is presented in this paper for user judgement and analysis. The impact of seasonal variations of wind speed on optimal sizes has been studied and the results have indicated that a low value of LCC is achieved at a high value of REP when there are no seasonal variations in the wind speed. The approach considers the PVS converter as the prime source of reactive-power supplier and it is assumed that the consideration helps to keep the size of BESS converter at a minimum value. The open-access facility of the output data provides the opportunities for analyzing various impacts on LCC, e.g., the impacts of LPSP and γ_{re} on LCC. A case study has also been conducted to demonstrate the stochastic sensitivity on LCC employing fifteen wind-speed realizations and the results have indicated that the algorithm is robust in the stochastic environment for calculating the minimum value of LCC and thus for determining the optimal sizes of the IMG.

Chapter 4

A Single-Objective Accelerated Optimal Sizing Approach

4.1 Introduction

In Chapter 3, it was shown that the enumeration-based approach can systematically be utilized for optimal sizing of an IMG and the approach ensured to reach at global optimum. The different optimization approaches, especially chronological simulation-based approaches for the optimal sizing of an IMG, were discussed in Chapter 1. By the aforementioned analysis, it was observed that the enumeration and even artificial intelligence-based optimization techniques along with chronological simulation require huge central-processing unit (CPU) times for obtaining the optimum solution. Generally the CPU time increases exponentially with the increased number of decision variables and also depends on the time series data points of the chronological simulation. Thus, an accelerated scheme of sizing optimization for a stand-alone hybrid power system in the context of chronological simulation is a challenging task. The accelerated optimization schemes are not only essential in online optimization but also useful in off-line optimization. An off-line optimization scheme might be used for commercial purposes of optimizing a large number of orders. A sluggish optimization scheme is not only of limited use but consumes substantial working hours. In this chapter, an accelerated optimal sizing approach for the IMG is thus proposed.

The proposed method takes advantage of the improved piecewise aggregate approximation (IPAA) technique [113] in order to reduce the time series data points upon retaining the diurnal and seasonal variations in an acceptable range. Furthermore, a genetic algorithm (GA) technique is used for an efficient searching in the search space. It has shown that the combination of these two techniques substantially accelerates the optimization scheme without significantly deviating the minimum value of the objective function. This chapter has presented the optimization problems without constraining the LPSP and also constraining the LPSP for obtaining the optimal sizes of the IMG. When LPSP is constrained, a penalty function approach is utilized to incorporate the power supply reliability in to the optimization problem. The challenging part of the penalty function approach is the selection of appropriate penalty parameter that is needed to converge the optimization scheme [114]. For that, an adaptive penalty parameter facility for the constrained optimization is utilized. Next, this chapter is going to (see in Section 4.2) review a few chronological simulation-based enumerative and GA optimization methods.

4.2 Complexities in Chronological Simulation and Enumeration-Based Method

Although different optimization techniques, e.g., graphical construction method, probabilistic approach, iterative approach, and artificial intelligence method are demonstrated in the literature for determining the optimal sizes of an IMG, the most of the studies employ chronological simulations such that the dynamic nature of the renewable energy resources (RERs) can be incorporated in the investigations. For the chronological simulations, the most of the researchers have utilized synthesized data of a typical meteorological year (TMY). Others have used either long period time series meteorological data or synthetically generated short-period data for the optimal sizing and feasibility study of a stand-alone hybrid power system [92]. Some optimal sizing methods are developed based on "*worst month*" or "*yearly average monthly*" scenarios. These approaches are neither suitable not accurate for optimal design application due to the stochastic nature of the RERs [115]. As the aforementioned two time series structures cannot retain seasonal variations, diurnal variations, and chronological orders, the time series that is based on hourly average TMY data turns out to be the most popular for the optimal sizing studies. It is worthwhile to mention that the chronological order of the resource data is very important, especially when an energy storage is used in the study system. Thus, most studies of enumeration and/or iterative technique [53, 116–118] have employed chronological data. In the enumerative technique, every point in space is tested systematically and in order. A few researchers utilize GA, along with, chronological simulation utilizing TMY-based time series for determining the optimal sizes of an IMG [62], [78], [119], [120]. The advantage of the GA technique is that the technique does not require to investigate every point in the search space. Figure 4.1 graphically demonstrates the search space options for (a) two decision variables and

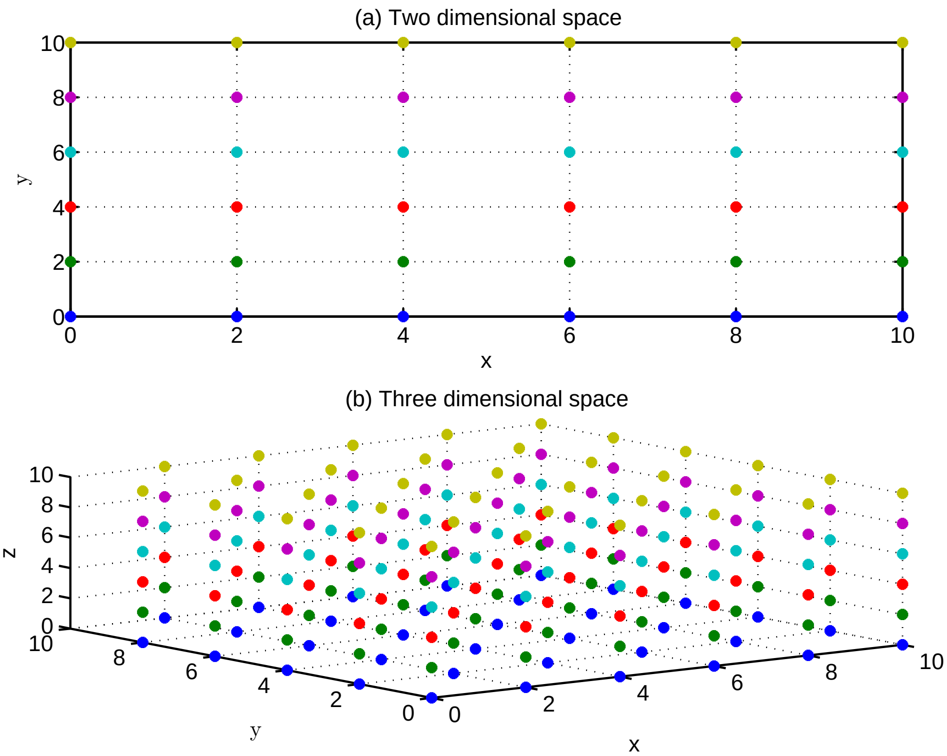

Figure 4.1: Enumeration search space

(b) three decision variables. All the options are required to investigate in the enumeration-based optimization approach. As can be seen in Figures 4.1(a) and (b), the increase of one decision variable exponentially increases the number of search-space points (e.g., 36 to 216).

Each point in space indicates an individual combination of components and the evaluation of each combination is performed by the TMY-based time series. Thus, the computational complexity of an enumeration technique is extreme. The computational complexity can be lessen by incorporating both GA technique that reduces the number of searches in the search space and the IPAA technique that decreases the number of data points. Therefore, the computational complexities lie on both the optimization search technique and on the time series resolution.

4.3 Subsystem Models and Problem Formulation

The main objective of this study is to determine the combination of sizes of WPS, PVS, DGS, battery bank, and BESS converter, i.e., the optimal sizes of the IMG of Section 2.2 in an accelerated way. This chapter takes into account the unit sizes of the components from Table 4.1. As the unit sizes are fixed, i.e., the decision variables are discrete, the optimization problem of this chapter becomes an integer variable problem. Thus, an integer variable GA technique is employed for searching the search space and because of that it is expected to accelerate the optimization scheme compared to enumeration scheme. The following subsections modify the mathematical models that were presented in the subsystems of the study system (Figure 2.1) of Chapter 3.

4.3.1 Non-Dispatchable Power Generation Models

The wind speeds and solar irradiations are site-dependent and they have great impacts on the kilowatt generations. The Section 3.2.2 shows that the WPS output power depends on wind speed and WPS rating, i.e., P_{rat}^{w} of the subsystem. In the enumeration technique of Chapter 3, the step size of the rated power was considered as unit size of the WPS. In the GA technique, the step size cannot be controlled easily during the creation and evaluation process of GA. Therefore, various fractional sizes of component, which are not practical, may come out in the optimum solution when the decision variables are considered continuous. Thus, this chapter introduces an integer variable in equation (4.1) and the power output of the WPS is expressed by two variables as,

$$P^{w} = \begin{cases} 0 & \text{if} \quad v_w < V_{ci} \ \text{ or } \ v_w > V_{co} \\ \left(a + bv_w + cv_w^2\right) K_w \cdot P_{rat}^{w} & \text{if} \quad V_{ci} \leq v_w \leq V_r \\ K_w \cdot P_{rat}^{w} & \text{if} \quad V_r \leq v_w < V_{co} \end{cases} \tag{4.1}$$

where V_{ci}, V_r, and V_{co} are the cut-in, rated, and cut-out wind speeds, respectively; the v_w and P_{rat}^{w} respectively signify the wind speed and the rated power of a single wind turbine. The K_w is the number of wind turbines. The coefficients a, b, and c are calculated based on V_{ci} and V_r, as explained in [109]. The two variables of equation 4.1 are v_w, which is stochastic in nature, and K_w, which is integer in nature, respectively.

For PVS power, this chapter uses the same model, presented in Subsection 3.2.3 by introducing an integer variable K_{pv}, which is expressed as,

$$P^{pv} = \eta_{pv} \underbrace{A_p N_{pv}}_{P_{rat}^{pv}} \phi_s \{1 - \gamma(T_c - T_{cref})\} K_{pv} \tag{4.2}$$

where η_{pv} is the energy conversion efficiency, A_p is the area of a PV module [m^2], N_{pv} is the number of PV module in a PV array, P_{rat}^{pv} is the rated power of the PV array, ϕ_s is the solar irradiation [$p.u./m^2$], T_c is the PV array temperature [$^\circ C$], T_{cref} is the reference temperature under standard test condition [25 $^\circ C$], and γ is the temperature co-efficient [0.005 per $^\circ C$].

4.3.2 Diesel Generator Power and Cost Model

Depending on net load demand and PMS, the DGS output power is either zero or a value that stays between minimum and rated power of a DGS. A DGS generally serves as a reserve power source for an IMG. The DGSs are modeled using minimum loading power level and rated power. The fuel consumption of the DGS is not linear and it is assumed a quadratic function that includes a cost at no-load operation. Thus, the fuel consumption [L/h] of K_{di}

number of DGSs with P^{di} real-power output is approximated as,

$$F_c^{di} = g_1 (P^{di})^2 + g_2 P^{di} + g_3 K_{di} \cdot P_{rat}^{di} \tag{4.3}$$

where g_1, g_2, and g_3 are the fuel consumption coefficients in L/kW^{2}h, L/kWh, and L/kWh, respectively. At unity power factor operation, the apparent power S_{rat}^{di} is the same as P_{rat}^{di} for a DGS. The fuel consumption cost [\$/kWh] for K_{di} number of DGSs is expressed as,

$$\beta_{fl}^{di} = \left(g_1 P^{di} + g_2 + g_3 \frac{K_{di} \cdot P_{rat}^{di}}{P^{di}} \right) c_f \tag{4.4}$$

where c_f is measured [\$/L], and it includes the fuel price, transportation cost, and inventory holding cost. The compression scheme of time series is going to be explained in Subsection 4.3.6 so that the optimal sizing solution can be achieved in an accelerated way. In order to calculate the fuel consumption for the whole year, the equation (4.3) needs to be multiplied by compression factor, i.e., K.

4.3.3 Modified Model of BESS

The BESS model of Section 3.2.7 is modified for this study as follows. During the charging process, the power, $P^b(t)$, and energy, $E^b(t)$, of the battery bank are expressed as,

$$P^b(t) = -\min \left[P_{sur}, \min \left\{ P_{rat}^b, \max \left(0, \frac{K_b \{ E_{max}^b - E^b(t) \}}{\Delta t} \right) \right\}, P_{ava}^{con} \right] \tag{4.5}$$

$$\text{where, } P_{sur} = (P^w + P^{pv} - P^l) > 0$$

$$\text{and } P_{ava}^{con} = \sqrt{\{ (K_{con} S^{con})^2 - (Q^l)^2 \}}$$

$$E^b(t + \Delta t) = E^b(t)\,(1 - \delta) - \eta_c^b P^b(t) \Delta t. \tag{4.6}$$

where P_{rat}^b, S^{con}, and Q^l respectively signify the battery bank charge controller power rating, apparent power rating of BESS converter, and reactive load power compensated by the converter. The parameters δ and η_c^b are self discharge and charging efficiency of the BESS, respectively.

During the discharging process, the power, $P^b(t)$, and energy, $E^b(t)$, of the battery bank are expressed as,

$$P^b(t) = \min\left[P_{def}, \min\left\{P^b_{rat}, \max\left(0, \frac{K_b\{E^b(t) - E^b_{min}\}}{\Delta t}\right)\right\}, P^{con}_{ava}\right] \tag{4.7}$$

$$\text{where } P_{def} = (P^l - P^w - P^{pv}) > 0$$

$$E^b(t + \Delta t) = E^b(t)\,(1 - \delta) - \frac{P^b(t)}{\eta^b_d}\Delta t \tag{4.8}$$

where η^b_d is the discharging efficiency of the BESS. If T_{chr} is the minimum charging or discharging time of the battery bank, then the rated power, P^b_{rat}, of the battery bank is calculated as

$$P^b_{rat} = \frac{K_b \cdot E^b_{rat}}{T_{chr}} \tag{4.9}$$

In order to protect the battery bank from overcharging, this study has assumed the maximum energy level of BESS, E^b_{max}, as 98% of the energy rating of BESS, E^b_{rat}. The apparent power rating, S^{con}_{rat}, of converter attached to the battery bank also need to be multiplied by K_{con}.

4.3.4 Loss of Power Supply Probability

In this study, the reliability model is considered the measure of loss of power supply probability (LPSP). The definition of LPSP of Section 3.3.1 is modified to percentage and expressed as,

$$\begin{aligned} LPSP\% &= \frac{\sum_{t=1}^{N} \text{power failure time}, \Delta t_f \text{ for } (S^{del}(t) < S^l(t)) \cdot 100}{N} \\ &= \frac{\sum_{t=1}^{N} \{\Delta t_f \text{ for } (P^{del}(t) < P^l(t))\ or\ (Q^{del}(t) < Q^l(t))\} \cdot 100}{N} \end{aligned} \tag{4.10}$$

where N, Δt_f , $S^{del}(t)$, and $S^l(t)$ respectively signify the total observed hours, time of power failure, total power output of all the resources, and primary load power demand.

4.3.5 Problem Statement

In this chapter, the small unit numbers of WPS, PVS, DGS, battery bank, and BESS converter are considered as decision variables. Thus, the objective function of the IMG sizing problem is formulated as,

$$\text{LCC} = K_w P^w_{rat} C^w_t + K_{pv} P^{pv}_{rat} C^{pv}_t + K_{di} S^{di}_{rat} C^{di}_t + K_{con} S^{con}_{rat} C^{con}_t + K_b E^b_{rat} C^b_t \tag{4.11}$$

where K_w, K_{pv}, K_{di}, K_b, and K_{con} respectively signify the small unit number of WPS, PVS, DGS, battery bank, and BESS converter. The variables P^w_{rat}, P^{pv}_{rat}, S_{rat}, S^{con}_{rat}, and E^b_{rat} are the rated power of each small unit of WPS, PVS, DGS, BESS converter, and energy capacity of battery bank, respectively. The variables C^w_t, C^{pv}_t, C^{di}_t, C^{con}_t, and C^b_t denote the total net present costs [$/kW] for WPS, PVS, DGS, BESS converter, and battery bank, respectively. The total cost of each unit includes the capital, maintenance, operation, replenishment costs, and salvage value. The decision variable vector of the optimization problem is stated as,

$$\mathbf{X} = [K_w \;\; K_{pv} \;\; K_{di} \;\; K_{con} \;\; K_b]^T \tag{4.12}$$

As the decision variables are discrete (i.e., integer), the problem can be treated as a integer problem. Finally, the optimization problem is defined as

$$\begin{aligned} \underset{\mathbf{X}}{\text{minimize}} \;\; & \text{LCC} \\ \text{subject to} \;\; & LPSP \leq LPSP^{des} \\ & \mathbf{X} \in \mathcal{R} \\ & g_j(\mathbf{X}) \leq 0, j = 1, 2, ..., J \end{aligned} \tag{4.13}$$

where $\mathcal{R}$, $\mathbf{X}$, and $g_j(\mathbf{X})$ respectively signify the feasible region, decision variable vector, and constraints. All the constraints are presented in the mathematical models of the components and are incorporated in the PMSs. The lower bound and the upper bound of the decision variable are respectively expressed as $[K_w^{min}\ K_{pv}^{min}\ K_{di}^{min}\ K_{con}^{min}\ K_b^{min}]^T$ and $[K_w^{max}\ K_{pv}^{max}\ K_{di}^{max}\ K_{con}^{max}\ K_b^{max}]^T$. The parameter LPSP^{des} is the desired percentage of LPSP and can accept a value from 0% to 100%. When the LPSP constrained is not taken into account, the problem is tested under a certain boundary of decision variable. To calculate the LPSP, the PMS-B (from Subsection 2.4.2) is employed to simulate the study system. The simulation scheme of the PMS facilitates the calculation of the fuel consumption of the DGS in every time step. Thus, the LPSP and the fuel consumption cost are the dependent and continuous variables, whereas K_w, K_{pv}, K_{di}, K_{con}, and K_b are integer variables. In this condition, the formulated sizing problem of the IMG can be considered as a mixed-integer programming (MIP) problem. The value of LPSP and the fuel consumption cost at each time step, represented in Subsection 2.4.2, are examples of implicit variables as they are defined by the cause-effect relationship (e.g., "*IF-ELSE*"). Traditional MIP based on binary linear programming or branch and bound can only handle explicit variables, constraints, and objective functions [121]. Thus, this problem cannot be solved by traditional MIP but it is expected to be solved by GA.

4.3.6 Dimensionality Reduction of Time Series

There are many techniques in literature for the dimensionality reduction of a time series. Among them, piecewise aggregate approximation (PAA) is a simple, yet powerful technique for reducing time series data points. This chapter employs an IPAA technique that can retain the statistics of the new time series close to the original one. Dimensionality of a time series $X = x_1, x_2, ...x_n$ of length n is reduced by employing PAA technique. If a new time series is represented by $\bar{X} = \bar{x}_1, \bar{x}_2, ...\bar{x}_N$, then the dimensionality of the transformed time series becomes N, where $1 < N < n$. The ith element of X is calculated as

$$\bar{x}_i = \frac{1}{K} \sum_{j=K(i-1)+1}^{K\cdot i} x_j, \quad \text{where} \quad K = \frac{n}{N} \tag{4.14}$$

where K is the compression ratio. We assume K is an integer, i.e., N is a factor of n. In this representation, the original time series is divided into N segment with equal size. The $\bar{x}_i$ is the mean value of the ith segment in the N dimensional space. The mean value of the segmented data is obtained and the vector of these values is used as a representation of a time series in a new space. As the PAA technique loses the variance feature in each segment, the IPAA method is used [113] to incorporate the variance in the transformed time series. When the variance vector of the transformed time series is represented as $\hat{X} = \hat{x}_1, \hat{x}_2, ...\hat{x}_N$, then the ith variance is expressed as,

$$\hat{x}_i = \sqrt{\frac{1}{K} \sum_{j=K(i-1)+1}^{K \cdot i} (x_j - \bar{x}_i)^2}, \quad \text{where} \quad K = \frac{n}{N} \tag{4.15}$$

where $\hat{x}_i$ is the variance of the ith segment. The new representation of the time series vector can be formed by the ith element as,

$$\tilde{x}_i = \bar{x}_i + \mu \cdot \hat{x}_i, \quad \text{for} \quad \mu \in [-1, 1] \tag{4.16}$$

where $\tilde{x}_i$ is the ith element of a new time series. The values of μ can be generated utilizing uniform PDF. Using the aforementioned process, the new time series of wind power, load demand, and solar irradiation are formulated as,

$$(\tilde{v}_w)_i = (\bar{v}_w)_i + \mu_w \cdot (\hat{v}_w)_i, \quad \text{for} \quad \mu_w \in [-1, 1] \tag{4.17}$$

$$(\tilde{P}_l)_i = (\bar{P}_l)_i + \mu_l \cdot (\hat{P}_l)_i, \quad \text{for} \quad \mu_l \in [-1, 1] \tag{4.18}$$

$$\begin{aligned} (\tilde{\phi}_s)_i &= 0 \;\text{ when }\; (\bar{\phi}_s)_i < T_h \\ &= (\bar{\phi}_s)_i + \mu_s \cdot (\hat{\phi}_s)_i, \quad \text{otherwise} \quad \mu_s \in [-1, 1] \end{aligned} \tag{4.19}$$

where $(\tilde{v}_w)_i, (\tilde{P}_l)_i,$ and $(\tilde{\phi}_s)_i$ respectively signify the ith element of the compressed time series of wind speed, load real power, and solar irradiation. The variables $(\bar{v}_w)_i, (\bar{P}_l)_i,$ and $(\bar{\phi}_s)_i$ represent the mean values of the ith segment of wind speed, load real power, and solar irradiation, respectively.

4.3.7 Penalty Term and Objective Function

In this section, the constraint of LPSP in the optimization problem is dealt with the penalty function approach. The new objective function assigns penalties for violation of the constraints. Thus, the new objective function is expressed as,

$$\begin{aligned} \underset{\mathbf{X}}{\text{minimize}} \quad & \{LCC + R_p(LPSP - LPSP^{des})^2\} \\ \text{subject to} \quad & \mathbf{X} \in \mathcal{R} \\ & g_j(\mathbf{X}) \leq 0, j = 1, 2, ..., J \end{aligned} \tag{4.20}$$

where R_p is the penalty parameter whose purpose is to make the constraint violation, i.e., $(LPSP - LPSP^{des})^2$ as the same order of magnitude of objective function value, i.e., LCC. The values of penalty parameters have great influence on the optimal solution of the objective function. To find out an appropriate penalty parameter, extensive experimentation is required [114]. The inclusion of a penalty term distorts the objective function. When the value of the penalty parameter is small, the distortion is small; but the optimum of fitness may not be near the true constrained optimum. When the penalty parameter is large, the optimum of fitness moves closer to the true optimum, but the distortion may be so large that the fitness may reach artificial local optimal solutions. The situation can be avoided by adaptively adjusting the penalty parameter. If the penalty factors are low, then invalid solutions may survive for some generations. It is observed that the performance of constraint optimization is largely dependent on the penalty parameter values.

4.3.8 Algorithmic Flowchart of the Accelerated Optimization Approach

Figure 4.2 shows the algorithmic flowchart of the proposed accelerated optimization approach. As can be seen from Figure 4.2, the wind speed, solar irradiation, load active power time series are compressed to make new time series. The figure further demonstrates a PMS is utilized to simulate the IMG by the new time series and then GA technique is employed in the proposed approach. For each iteration, an individual from a set of population (different combination of components) is adopted and then chronological time series are utilized for simulating the system employing the PMS in order to determine the yearly LPSP and LCC. The objective function values for the set of population are evaluated and then fitness values are assigned for each of the solutions. When we do not consider the LPSP a constraint, then the LCC is taken as an objective function. While the equation (4.20) is used as objective function when the LPSP is considered a constraint. The detail descriptions of GA operations of Figure 4.2 are described

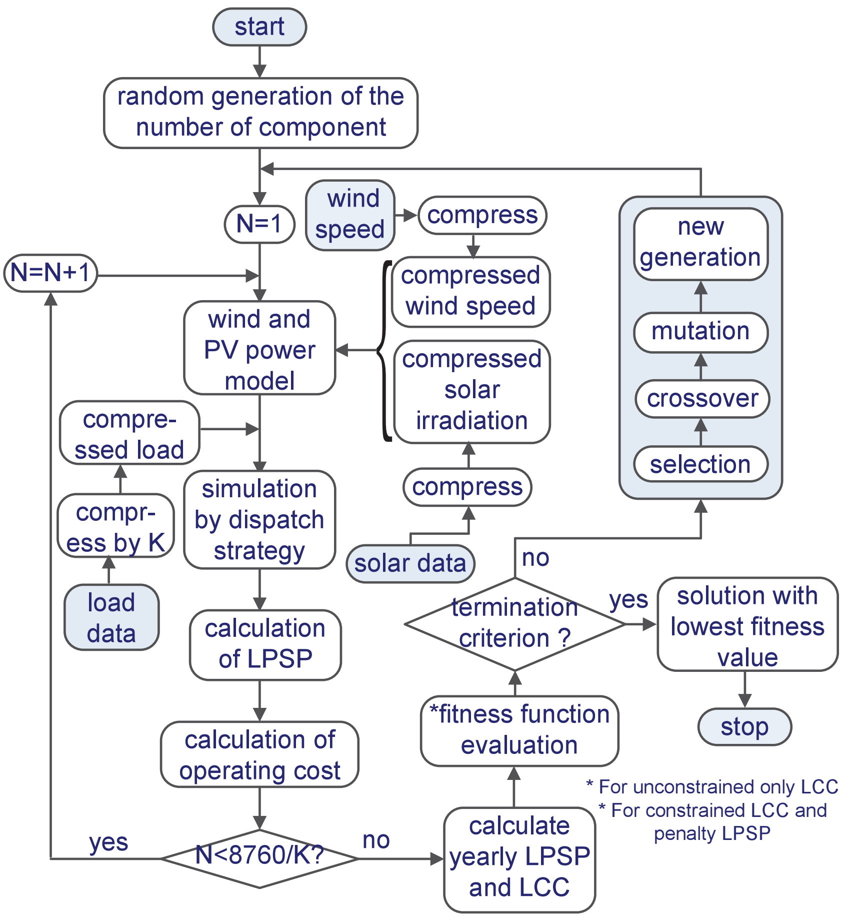

Figure 4.2: Flowchart of the accelerated optimization approach

in Subsection 4.3.9.

4.3.9 Genetic Algorithm

The genetic algorithm (GA) is a method that is based on natural selection. According to the natural selection method, the weak and unfit species within their environment face extinction, consequently, the strong species have a greater opportunity to pass their genes to the next generation. In GA, population is termed as a collection of individual (or chromosome). Alternately, the individual is a solution vector out of the population. The individuals are made of genes, where the genes are normally binary type. The GA schemes do not require gradient information, and they are effective regardless of the nature of the objective functions and constraints. They gather information from previous generations and random numbers to evaluate and improve a population points instead of single point at a time. Thus, GAs can sample the search space widely and efficiently. They have turned out to be powerful search tools for solving numerous optimization problems, especially in the global optimization perspective. Figure 4.3 demonstrates the operations of GA which are explained below.

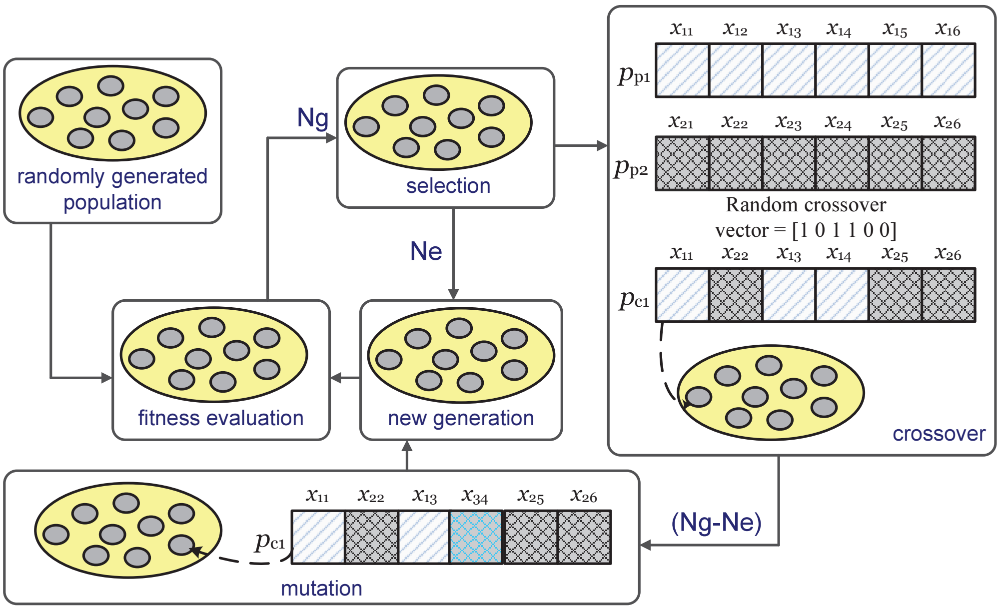

Figure 4.3: Flowchart of GA and operation

1) Initial Population

Figure 4.3 demonstrates at initial, a population of N_g size is randomly generated in the feasible space, encoded in "*double vector*" and then to discrete in case of MIP. The number of individuals, i.e., the population size, remains unchanged throughout the process of GA. The accuracy of the optimal solution depends on both the size of population and the number of generation. The double vector representation instead of binary one is used for chromosome codification to guarantee mutation coherence.

2) Fitness Evaluation

Figure 4.3 further illustrates that each population group is utilized to evaluate the objective function. Then, a value on each individual solution is assigned that gives a measure of the solution quality. The scaling of objective function is done by assigning a rank to each individual solution. In this process, the best individual, i.e., the minimal function value, receives the maximal fitness value with greater chance for survival and vice versa.

3) Selection

After completing the fitness evaluation, individuals from the population are selected pairwise for genetic operations and thus create the offspring/child population. In this study the stochastic uniform probabilistic selection is used in order to attain the individual's selection probability proportional to the individual's fitness. The process ensures that the high quality solutions will be selected many times and become parents of many offsprings. Alternately, the low quality individuals will not contribute much for generating offsprings. Usually the best selection schemes are designed to maintain diverse population. The other selection process that does not take part in the offspring creation process, rather than directly copied to the next generation is called elitism. The elitism scheme preserves the best solutions for the next generation. By introducing elite count, the number of individuals with best fitness values in the current generation are guaranteed to survive to the next generation. Figure 4.3 illustrates that N_e are the number for elite count.

4) Crossover or Recombination

Figure 4.3 shows the crossover step of GA that starts just after selection. Crossover generally produces new individuals in combining the information of two individuals, called parents. The parents are selected based on aforementioned selection process so that the offsprings are expected to inherit good genes. In this study, the scattered crossover is utilized for crossover operation. Figure 4.3 shows the scattered process creates a binary vector and then the process selects the genes from the first and second parents when the vector is a 1 and 0, respectively, in order to diversify genes in the expected offsprings. This crossover scheme is applied iteratively until generating the desired number of offspring. According to the Figure 4.3, if the elitism selection is N_e, the crossover scheme will produce $N_g - N_e$ offsprings.

5) Mutation

The mutation scheme introduces random changes in the genes of the individual. Figure 4.3 shows the changes of gene x_{14} occurs to x_{34} at random. For mutation operation, the gaussian scheme is employed in this study. Generally, mutation fraction is kept at low so that the new individual that is created by mutation, does not very a lot from the original one. It is observed earlier that crossover converges the offsprings to similar type, whereas mutation reintroduces genetic diversity in the individual. Thus, mutation GA helps the search for global optimization [122].

4.4 Results and Discussions

The proposed approach of optimal sizing is evaluated under MATLAB/Simulink environment for two cases (i.e., without considering the LPSP as a constraint and also taking LPSP a constraint) in order to determine optimal sizes of the IMG of Section 2.2 in an accelerated way. The PMS-B of Subsection 2.4.2 is used as a power management strategy for simulating the study system where the unit sizes of the components are taken from Table 4.1. An IEEE reliability test system (IEEE-RTS) load real-power model for yearly peak of 350 kW is developed

Table 4.1: Capacity Ratings of Small Unit Sizes of the Components

Components	Unit	Rating
WPS (P^{w}_{rat})	kW	150
PVS (P^{pv}_{rat})	kW	150
BESS (E^{b}_{rat})	kWh	300
DGS (S^{di}_{rat})	kVA	80
Converter (S^{con}_{rat})	kVA	160

and the dimensionality reduction scheme is applied whenever required. The time series for load reactive-power component is produced utilizing both the power factor model of (3.7) and the compressed time series of load real-power component. Expecting the optimized IMG to be a high REP system, the study system incorporates a dump load by a free slack variable. The battery bank charging/discharing rate is not considered a decision variable. Thus, the battery autonomy hour, T_{chr}, of (4.9) is taken 12 hours in this study. The economic parameters for the study are taken from Table A.3.

First, the time series dimensionality reduction principle of Subsection 4.3.6 is studied. Figures 4.4(a), (b), and (c) graphically represent the effects of dimensionality reduction of wind speed, solar irradiation, and load power, respectively, at a compression ratio equals four, i.e., for K=4. As seen from the figures, it can be presumed that the variances of the newly formed time series decrease, though the mean values of the time series remain unchanged. It can further be observed that the seasonal variations seems very similar to the original data though the diurnal variations seem to decrease at a high compression ratio. Table 4.2 illustrates a comparative study of the descriptive statistics for the wind speed, solar irradiation, and load time series that are compressed based on PAA and IPAA methods and at various compression ratios. Table 4.2 further demonstrates that the mean values of the compressed time series remain the same. However, the standard deviations (SDs) drop more at high compression ratios, though the decreased amounts of SD is less in IPAA than those of PAA. As mentioned earlier, some of the previous studies have used monthly average weather data, weekly average, or typical month hourly data for optimal sizing. These approaches are neither suitable not accurate for

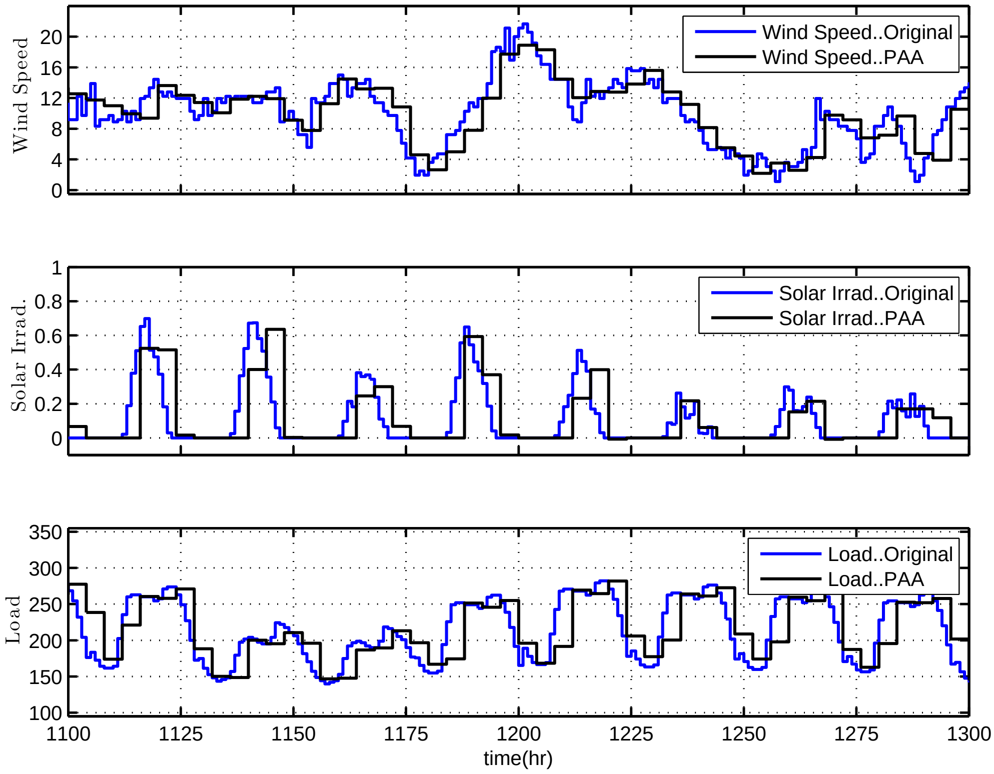

Figure 4.4: Four hourly PAA of (a) wind speed, (b) Solar irra. and (c) load power time series

optimal sizing application due to stochastic nature of the resources [115]. The large number of samples are preferred by the researchers for achieving realistic sizes at the expense of high computational time. Thus, it is also challenging to employ an efficient sampling rate in the optimization scheme of the IMG.

Therefore, the study has used an IPAA for compressing the time series without largely deviating the descriptive statistics. As well, the approach utilizes GA technique for searching the decision space in order to accelerate the optimal sizing process. The GA parameters of the study system are taken from Table 4.3. The proposed approach considers the net present value of the life cycle cost (LCC) as an objective function for one optimization problem and the objective function that augments LCC with a penalty term is used for the other optimization (see 4.20) problem. Before comparing the results of this chapter, the computational complexity in the enumeration technique of the sizing problem of Chapter 3 is explained. Considering the boundary limits and step sizes of the decision variables from Table 3.1, the complete enumer-

Table 4.2: Descriptive Statistics of Various Time Series

Descriptions	Wind			Solar			Load		
	O.D	PAA	IPAA	O.D	PAA	IPAA	O.D	PAA	IPAA
Two hours average									
Mean	7.11	7.11	7.12	0.15	0.15	0.15	215.02	215.02	215.02
SD	3.74	3.66	3.69	0.23	0.23	0.23	49.15	48.64	48.81
Maximum	23.06	22.37	22.16	1.06	1.02	1.02	350.00	348.25	347.75
Range	22.86	22.17	21.96	1.06	1.02	1.02	231.42	229.67	229.17
Median	6.67	6.67	6.67	0.01	0.02	0.02	213.44	213.05	213.32
Four hours average									
Mean	7.11	7.11	7.10	0.15	0.15	0.15	215.02	215.02	215.00
SD	3.74	3.57	3.64	0.23	0.22	0.22	49.15	46.90	47.60
Maximum	23.06	21.39	20.49	1.06	0.94	1.03	350.00	345.63	348.12
Range	22.86	20.83	20.15	1.06	0.94	1.03	231.42	221.57	228.37
Median	6.67	6.67	6.62	0.01	0.04	0.02	213.44	212.31	212.32
Six hours average									
Mean	7.11	7.11	7.11	0.15	0.15	0.15	215.02	215.02	214.84
SD	3.74	3.51	3.61	0.23	0.20	0.21	49.15	45.15	46.17
Maximum	23.06	20.84	21.53	1.06	0.79	0.97	350.00	336.00	343.52
Range	22.86	20.09	20.82	1.06	0.79	0.97	231.42	210.42	224.17
Median	6.67	6.62	6.66	0.01	0.03	0.02	213.44	217.33	215.66
Eight hours average									
Mean	7.11	7.11	7.15	0.15	0.15	0.15	215.02	215.02	215.17
SD	3.74	3.41	3.53	0.23	0.21	0.22	49.15	45.32	46.83
Maximum	23.06	20.45	21.75	1.06	0.88	0.94	350.00	332.06	335.08
Range	22.86	19.62	21.78	1.06	0.88	0.94	231.42	205.50	210.12
Median	6.67	6.67	6.77	0.01	0.06	0.04	213.44	214.54	215.43
Twelve hours average									
Mean	7.11	7.11	7.10	0.15	0.15	0.14	215.02	215.02	214.72
Standard Deviation	3.74	3.29	3.45	0.23	0.10	0.15	49.15	36.95	41.67
Maximum	23.06	19.10	18.97	1.06	0.42	0.76	350.00	315.58	330.86
Range	22.86	17.92	17.94	1.06	0.41	0.76	231.42	176.78	204.43
Median	6.67	6.67	6.61	0.01	0.13	0.09	213.44	213.51	212.58

O.D.-Original Data
PAA-Piecewise Aggregate Approximation
IPAA-Improved Piecewise Aggregate Approximation
S.D.-Standard Deviations

Table 4.3: Used GA Parameters for the Simulation in MATLAB

Parameter	Value	Parameter	Value
Population Size, N_g	30	Selection function	Stochastic uniform
Fitness scaling	Rank	Crossover fraction	0.7
Elitism, N_e	2	Crossover function	Scattered
Max generation	30	Mutation function	Gaussian
Fitness tolerance	10^-3	Mutation Fraction	0.2

ation of the problem requires

$$\underbrace{7}_{WPS} \cdot \underbrace{5}_{PVS} \cdot \underbrace{6}_{BESS} \cdot \underbrace{5}_{DGS} \cdot \underbrace{5}_{con} \cdot \underbrace{4}_{chr} = 2.1 \cdot 10^4 \tag{4.21}$$

nearly $2.1 \cdot 10^4$ evaluation in order to find the optimal sizes. If the battery charger rating was not considered a decision variable, even then, more than five times function evaluation than that of the present approach were required. As a result, the complete enumeration approach required high computational time. Likewise, reference [67] provides an example that requires approximately 362 years for the complete enumeration. In the case studies a comparatively large population size is selected to increase the possibility of convergence to the global minimum. Two elitist children are maintained for each generation to ensure desirable solutions by diversity.

4.4.1 Performances Comparison When LPSP is not Constrained

This case study has been conducted to compare the CPU times of the optimization problem when LPSP is not constrained upon simulating the IMG by TMY-based time series and IPAA-based time series of various compression ratios (see in Figure 4.5). The lower bound and upper bound of the decision vector, $[K_w\ K_{pv}\ K_{di}\ K_{con}\ K_b]$, are accounted as [1 1 0 3 0] and [7 4 5 8 10], respectively. In this study, the lower bound is raised compared to the case study of Section 4.4.2 so that the minimum value of decision vector/objective function does not become zero. By considering the compression ratio (i.e., K) two, Figure 4.5(a) illustrates that the mean value and best value of the objective function convergence smoothly. As can be seen in Figures

4.5(b) and (c), the mean values and best values of the objective functions, for the compression ratios (from 2 to 12), converge without any large deviation compared to the results those are obtained by TMY (i.e., K=1)-based time series simulation. Table 4.4 numerically illustrates the comparisons of the evaluated results. As can be seen from the table, the CPU times, for the IPAA-based time series simulation, vary from 2189.77 s to 489.38 s that are lower than that of TMY-based time series simulation value (3564.28 s). Thus, the CPU times of the IPAA-based time series simulation decrease from 39% to 86% compared with the result of TMY-based time series simulation. Although the average value of the objective function stays around ($5.32e + 06), the best function value for TMY-based time series is ($5.27e + 06) and the same values for the IPAA-based time series mostly remain around $5.33e + 06. It can also be observed that though the objective function values changes slightly, the combination of components, under the range of observed compression ratios, do not change at all. The outcome values of component (i.e., the decision vector is $[3, 1, 0, 3, 0]$) WPS, PVS, converter, DGS, and battery bank are 450 kW, 150 kW, 0 kVA, 240 kVA, and 0 kWh, respectively. The presented results of this study are the best solution of 30 iterations with population size 30. As the number of evaluated function in GA is 930, which is less than 80% of the number of evaluated function of enumeration method (i.e., $6 \times 3 \times 5 \times 5 \times 10 = 4500$), it can be inferred that the CPU time under the proposed approach significantly accelerates (97%) compared to that of enumeration based technique.

Table 4.4: Performance Comparison When LPSP is not Constrained in the Optimization Problem

	K=1	K=2	K=4	K=6	K=8	K=10	K=12
CPU time (s)	3564.28	2189.77	1134.79	853.65	670.90	552.31	489.38
Acceleration	-	38.56%	68.16%	76.04%	81.17%	84.50%	86.27%
Best function value ($)	5.27e+06	5.29e+06	5.30e+06	5.32e+06	5.33e+06	5.35e+06	5.38e+06
No. of functions	930	930	930	930	930	930	930
Component no.	3,1,0,3,0	3,1,0,3,0	3,1,0,3,0	3,1,0,3,0	3,1,0,3,0	3,1,0,3,0	3,1,0,3,0
Generations	30	30	30	30	30	30	30
Population	30	30	30	30	30	30	30

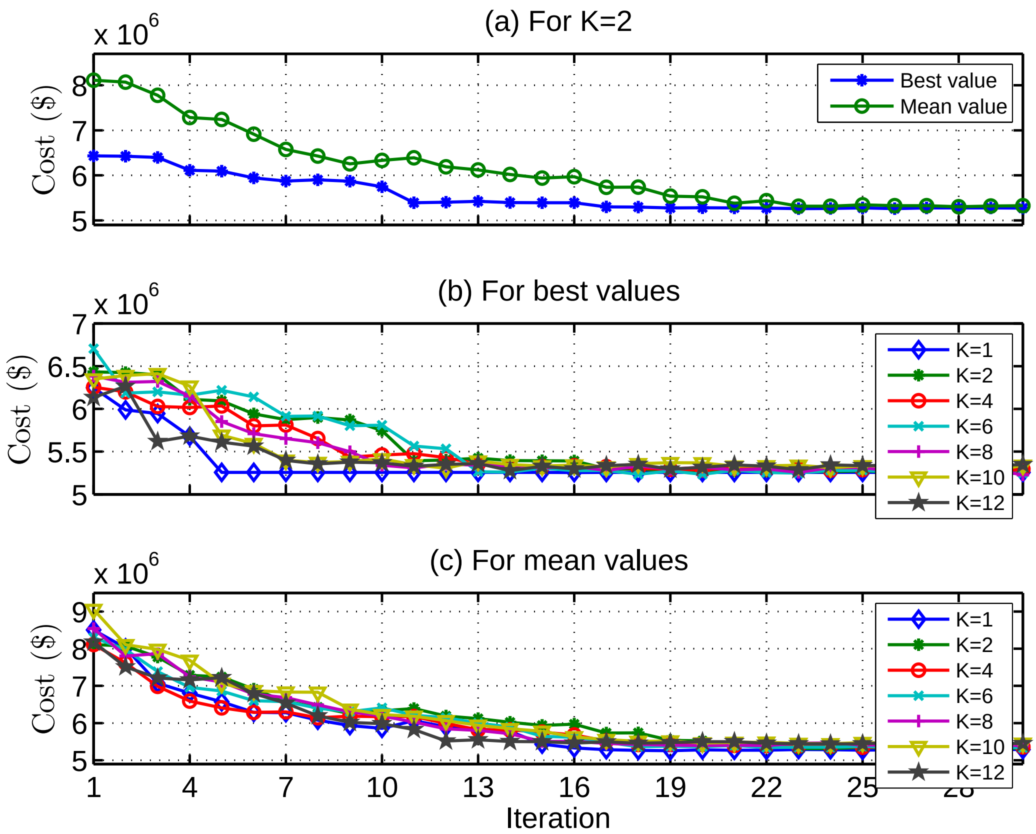

Figure 4.5: Performance comparisons for various compression ratios when LPSP is not constrained in the optimization problem

4.4.2 Performances Comparison When LPSP is Constrained

Most real-life applications are constrained optimization problems and thus this case study is performed for constrained optimization taking $LPSP^{des} = 0$. Figure 4.6 illustrates the convergence of the best values and the mean values for the constrained optimization under TMY-based and the IPAA-based time series simulation. In this case, the lower and upper bounds of the decision variable vector, i.e., $[K_w\ K_{pv}\ K_{di}\ K_{con}\ K_b]$, are taken as [0 0 0 1 0] and [7 4 5 8 10], respectively. The study results are split in Figures 4.6(a) and (b) in order to present neatly. Figure 4.6(a) demonstrates the best values and mean values of the objective function both for TMY-based IPAA-based time series simulation. Table 4.5 numerically compares the obtained results from TMY-based and IPAA-based time series simulations. As can be seen, the CPU times of IPAA-based time series simulation ranges from 496.48 s to 2104.96 s, which are

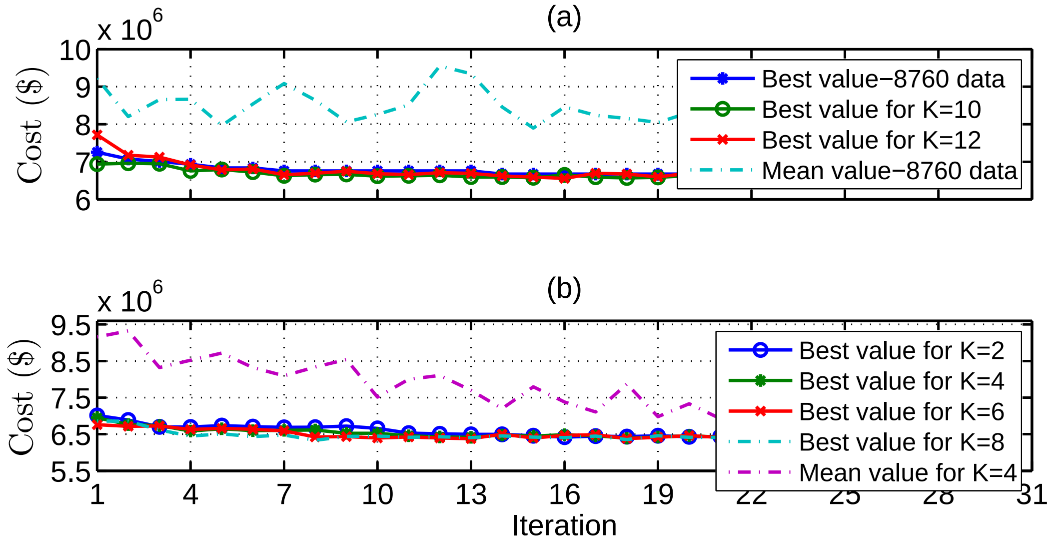

Figure 4.6: Performance comparisons of optimization problem when LPSP is constrained

lower than that of TMY-based time series simulation value (i.e., 3576.95 s). Thus in IPAA-based time series simulation, the optimization is accelerated from 42% to 86% compared with TMY-based time series simulation. The best function value obtained by TMY-based time series simulation is \$6.67$e+06$, where the the same values under IPAA-based simulation ranges from \$6.52$e+06$ to \$6.68$e+06$. As the simulations are performed utilizing GA technique under adaptive penalty factor and in stochastic environment, the combination of components varies slightly. The best set of component sizes, for several observations of simulation both for TMY-based and the IPAA-based time series, is [4, 1, 1, 3, 6], i.e., 600 kW WPS, 150 kW PVS, 160 kVA converter, 240 kVA DGS, and 1800 kWh battery bank are required for a reliable power system. However, the most frequent results of the combination of components are presented in Table 4.5. The close observation of the combination of components inferred that the component combinations vary in a logical way and it have the capability of providing reliable power supply by all the other combinations too. If we compare the results of this case study with the previous case of Table 4.4, it can be inferred that a possible reason for deviation is due to the inclusion of constraints, more specifically for the penalty term. Moreover, owing to the mixed-integer problem, the contribution of penalty term and the constraints value do not change continuously. Therefore, the mean values swing with the change of iteration. The results are the best values, those extracted from 30 iterations with a population size of 30. It is worthwhile to mentioned that the enumeration-based (i.e., $7 \times 4 \times 5 \times 7 \times 10 = 9800$ number of function evaluation) searching for the ranges of the aforementioned decision variable vector requires 90% more function evaluation than that of GA searching (i.e., 930 function evaluation) technique.

Table 4.5: Performance Comparisons When LPSP is Constrained in the Optimization Problem

	K=1	K=2	K=4	K=6	K=8	K=10	K=12
CPU time (s)	3576.95	2104.96	1146.66	818.19	656.22	564.25	496.48
Acceleration	-	41.15%	67.94%	77.13%	81.65%	84.20%	86.12%
Best function value ($)	6.67e+06	6.58e+06	6.52e+06	6.53e+06	6.59e+06	6.61e+06	6.68e+06
No. of functions	930	930	930	930	930	930	930
Components no.	4,1,1,4,5	4,1,1,3,6	4,2,1,3,6	4,1,1,3,6	4,1,1,3,6	3,2,1,3,6	4,1,1,3,6
Generations	30	30	30	30	30	30	30
Population size	30	30	30	30	30	30	30

4.4.3 Impacts of LPSPs on the Convergence and Objective Function

The impacts of numerous desired LPSP values on objective function and on iteration performance are examined by the TMY-based (i.e., K=1 means no compression) and IPAA-based (for K=10) time series. Figures 4.7(a) and (b) illustrate the convergence of the objective function values under different LPSPs for TMY-based and IPAA-based simulations, respectively. Figures 4.7(a) and (b) also demonstrate that the iteration performances and CPU times are independent of LPSPs. As can be seen from the Figure 4.7(a) and (b), the requested high reliability incurs high LCC. For both TMY-based and IPAA-based simulation, when the requested reliability is low (i.e., LPSP is high) the LCC goes down. Table 4.6 shows the objective function values and the combination of components for different LPSP values and for two compression ratios. As can be seen from Table 4.6, whenever the high LPSPs (i.e., low reliability) are requested, not only the LCC values but also the combination of components goes down. It is also observed that the high LPSP values (i.e., low reliability) decrease either DGS unit and/or

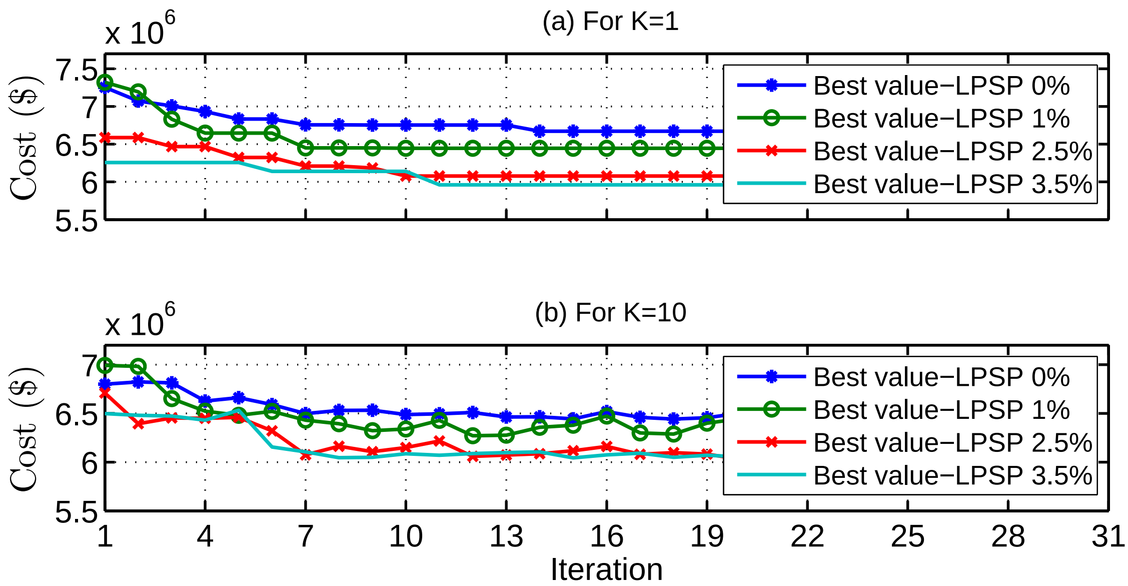

Figure 4.7: Impacts of LPSP values on objective functions and iteration performances under (a) TMY-based (b) IPAA-based time series simulation

battery bank unit in the component combination. As the WPS and PVS provide intermittent power, it is obvious that the DGS and the battery banks are the two important sources that maintain the power supply reliability of the study system. Alternately, the high number of DGS and/or large sizes battery bank can provide a high reliable power system for the remote community.

Table 4.6: Performances Comparison for Various Desired Values of LPSP

Description	K=1		K=10	
LPSP	Final Value	$[K_w\ K_{pv}\ K_{di}\ K_b\ K_{con}]$	Final Value	$[K_w\ K_{pv}\ K_{di}\ K_b\ K_{con}]$
0%	6.66e+06	[4 1 1 4 5]	6.61e+06	[3 2 1 3 6]
1.0%	6.45e+06	[4 2 1 3 5]	6.51e+06	[4 3 1 2 6]
2.5%	6.07e+06	[3 2 1 3 5]	6.29e+06	[4 2 1 2 6]
3.5%	5.96e+06	[4 1 1 3 5]	6.09e+06	[4 2 1 2 5]

4.5 Conclusions

A single-objective optimization approach utilizing both GA technique and IPAA-based time series has been proposed in this chapter such that the optimization process (i.e., CPU times) can significantly be improved compared to the techniques that employ traditional hourly average TMY-based time series. This study has indicated that the compression of hourly average TMY-based time series, i.e., dimensionality reduction of time series, leads to a significant decrease of computational complexity and CPU timing. The searching of decision space using GA has also reduced the CPU times and computational complexities compared to an enumeration-based approach. Thus, it has been observed that this new approach is much faster than that of enumeration and TMY-based time series simulation. As the main objective of this chapter is to achieve an accelerated approach, the optimization problem has employed the power management strategy-B (SOC setpoint) only to simulate the IMG and thus to evaluate the proposed approach. It is worthwhile to mentioned that the PMS-B scheme has used both load real and reactive powers and thus the algorithm has many cause and effect (i.e., *IF-ELSE*) relations. The case studies have indicated that iteration performances and CPU times do not change with the change of LPSP. Alternately, the study has shown that the performances and objective function values depend on the types of optimization problem, i.e., whether the optimization problem is constrained or unconstrained by LPSP. Owing to the changes of statistical characteristics in the time series, small deviations are occurred both in objective function values and in component sizes. If the deviations of objective function values and component sizes are taken into account then the results of hourly average TMY-based time series might deviate to that of high time resolution based simulation, i.e., 30 minutes average or fifteen minute average time series based simulation. Finally, the results have indicated that the computational times, i.e., CPU times are decreased remarkably while the optimality is retained within an acceptable limit. Thus, the approach can be used for designing the large IMGs with huge decision variables in an accelerated way.

Chapter 5

A Bi-objective Optimal Sizing Approach

5.1 Introduction

Two single objective optimal sizing approaches for the IMG were presented in Chapters 3 and 4, respectively. Most of the engineering, financial, and industrial optimization problems are multiobjective where the objective functions generally conflict with each other. For such cases, optimizing a problem to a particular solution with respect to a single objective cannot provide an acceptable result with respect to the other objectives. An acceptable solution for a multiobjective optimization problem (MOP) is to generate a set of trade-off solutions [71], [73].

This chapter proposes an approach that aims to optimize the sizes of the IMG, by employing a bi-objective optimization. The proposed approach benefits from the enumerative search and adaptive weighted sum (AWS) method in order to produce a Pareto front in the objective space where the Pareto front points cannot be identified by the traditional weighted sum (AW) method [123–125]. The AWS method effectively approximates a Pareto front by gradually increasing the number of points on the front. The proposed approach is facilitated to produce well-distributed solution points throughout the Pareto front, even in unexplored regions where the WS method cannot find any solution. The enumerative search scheme of Chapter 3 is employed to simulate the IMG in chronological order so that the objective functions can be evaluated systematically for all possible sizes. First, the WS method is applied and subsequently, the

AWS method is repeatedly employed on the evaluated objective functions. Utilizing the WS method, a Pareto front is developed solving the problem multiple times for different weight combinations. This chapter compares two Pareto fronts that are produced based on both the WS and AWS methods so that the advantages of the AWS method can easily be distinguished.

5.2 Formulation of the Bi-objective Optimization Problem

The definitions of a power system reliability index, LPSP, and a renewable energy penetration (REP), γ_{re}, are given in Subsections 3.3.1 and 3.3.2, respectively. The mathematical representations of LPSP and γ_{re} are subsequently given in equations (3.24) and (3.25). The detailed derivation of LCC for the IMG is performed in Section 3.4. For this study, REP (i.e., γ_{re}) and life-cycle cost (i.e., LCC) of the aforementioned items are considered two independent objective functions, which are expressed as,

$$\begin{aligned} f_1(\mathbf{X}) &= -\gamma_{re} \\ f_2(\mathbf{X}) &= \text{LCC} \end{aligned} \tag{5.1}$$

where $\mathbf{X}$ is a vector of decision variables, which is expressed as,

$$\mathbf{X} = [P^{w}_{rat}\ \ P^{pv}_{rat}\ \ S^{di}_{rat}\ \ E^{b}_{rat}\ \ P^{b}_{rat}\ \ S^{con}_{rat}]^T \tag{5.2}$$

$$= [x_1\ \ x_2\ \ x_3\ \ x_4\ \ x_5\ \ x_6]^T \tag{5.3}$$

where the elements of the decision variable vector (i.e., $\mathbf{X}$) are the sizes of the IMG and for the convenience of mathematical derivation, $[x_1\ \ x_2\ \ x_3\ \ x_4\ \ x_5\ \ x_6]^T$ is presented equivalent to the decision variable vector. The main goal of this chapter is to minimize the LCC and maximize the REP upon maintaining the LPSP a desirable low value. Thus, utilizing the aforementioned individual objective functions (5.1), the bi-objective optimization problem for the

IMG is expressed as,

$$
\begin{aligned}
\underset{\mathbf{X}}{\text{minimize}} \quad & \mathbf{F}(\mathbf{X}) = [f_1(\mathbf{X}) \;\; f_2(\mathbf{X})]^T \\
\text{subject to} \quad & LPSP \leq LPSP^{des} \\
& \mathbf{X} \in \mathcal{R} \\
& g_j(\mathbf{X}) \leq 0, j = 1, 2, ..., J
\end{aligned}
\tag{5.4}
$$

where $\mathbf{F}$ is the objective function vector and LPSP is considered a constraint in the objective space. The lower levels (i.e., $x_{i,ll}$) and upper levels (i.e., $x_{i,ul}$) of the decision variable of vectors constitute the feasible region $\mathcal{R}$ in the decision space. The inequality constraint, $g_j(\mathbf{X})$, is incorporated in the mathematical models and also in PMSs. The increase of γ_{re} requires an utilization of more renewable energy resources (RERs) as well as large battery banks, which incur the escalation of LCC. The increase in REP results in a decrease in greenhouse gas emission. Therefore, it is impossible to improve the value of an objective function without deteriorating the value of the other objective functions. The evaluated Pareto front for the aforementioned objectives will provide the Pareto optimal solutions.

5.3 Flowchart of the Bi-objective Optimization Problem

The algorithmic flowchart of the proposed bi-objective optimization for the IMG is presented in Figure 5.1. As shown in Figure 5.1, an enumerative scheme is employed for selecting the decision variables. The PMSs of Chapter 1 are utilized to simulate the IMG. TMY-based time series of wind speeds and solar irradiations are used for the chronological simulation. The mathematical models of Chapter 3 are used for generating power from the resources and for fulfilling the demand of both real and reactive power of the primary load. The yearly LPSP, economic evaluation, and REP are calculated for each decision vector. When the LPSP (i.e., $f_3(m, 3)$) meets the desired set point, the economic evaluation (i.e., LCC), the REP (i.e., γ_{re}), and the corresponding decision variable vector (*i.e.*, $[x_1 \;\; x_2 \;\; x_3 \;\; x_4 \;\; x_5 \;\; x_6]$) along with the PMS

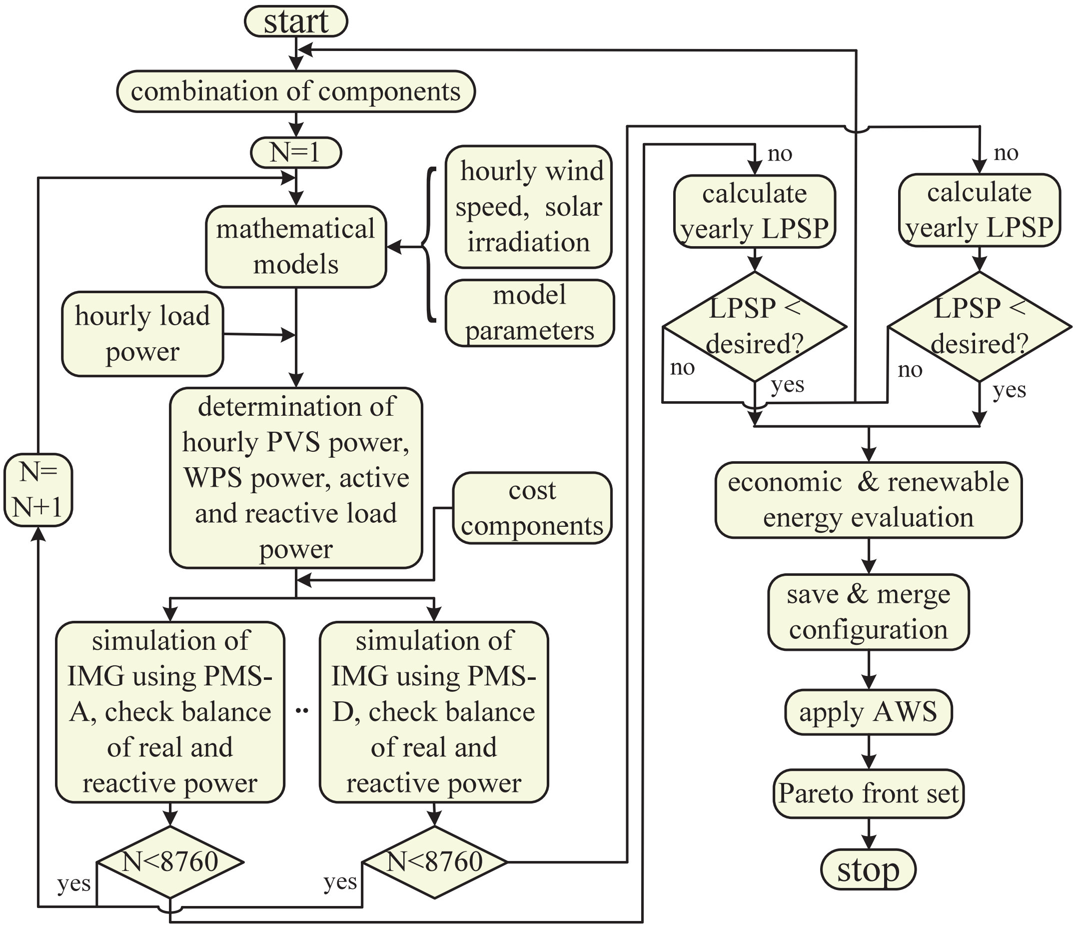

Figure 5.1: Bi-objective optimization flowchart using AWS method.

index (i.e., S) are stored in a matrix, given in (5.5). The process continues until the end of all decision variable vectors, and consequently the number of rows in (5.5) increases. The total evaluated results upon maintaining a low LPSP are stored in the rows of a matrix, $M_{m,10}$, given as,

$$M_{m,10} = \begin{pmatrix} f_{1(1,1)} & f_{2(1,2)} & f_{3(1,3)} & x_{1(1,4)} & x_{2(1,5)} & x_{3(1,6)} & x_{4(1,7)} & x_{5(1,8)} & x_{6(1,9)} & S_{(1,10)} \\ f_{1(2,1)} & f_{2(2,2)} & f_{3(2,3)} & x_{1(2,4)} & x_{2(2,5)} & x_{3(2,6)} & x_{4(2,7)} & x_{5(2,8)} & x_{6(2,9)} & S_{(2,10)} \\ \vdots & \vdots & \vdots & \vdots & \vdots & \vdots & \vdots & \vdots & \vdots & \vdots \\ \vdots & \vdots & \vdots & \vdots & \vdots & \vdots & \vdots & \vdots & \vdots & \vdots \\ f_{1(m,1)} & f_{2(m,2)} & f_{3(m,3)} & x_{1(m,4)} & x_{2(m,5)} & x_{3(m,6)} & x_{4(m,7)} & x_{5(m,8)} & x_{6(m,9)} & S_{(m,10)} \end{pmatrix} \tag{5.5}$$

At the end of Figure 5.1 a block represent the AWS method where the two evaluated objective functions (i.e., $f_{1(m,1)} = -\gamma_{re}$ and $f_{2(m,2)}$ =LCC) are utilized for bi-objective optimization with the initial employment of traditional WS method. By changing the weights, multiple solutions are developed by the WS method. The WS method searches multiple solutions in parallel where weights are not assumed fixed. The results of the WS method are used to calculate the length of the segment that spans the two neighboring solutions. Further refinement is done on the large segments employing the AWS method so that the unexplored regions can be investigated to generate evenly distributed Pareto optimal solutions. As shown in Figure 5.1, all the PMSs are used for simulating the IMG and thus the simultaneous optimization of the sizes and the PMSs is envisaged in this study. Reference [76] has proposed the AWS method for generating Pareto front solutions in (1) convex regions with non-uniform curvature, (2) non-convex regions of non-dominated solutions, and (3) non-convex regions of dominated solutions. In this study, the author takes advantage of the AWS method for the bi-objective problem of the IMG, where the decision variables of the problem are integers and the objective functions are evaluated in the cause effect ("*IF-ELSE*") relationship state. The bi-objective optimization problem does not provide a single-point solution; instead, the scheme provides a trade-off solution set that helps a DM to make a decision. The mathematical explanations and the detailed steps of the AWS method are given in the following subsection.

5.3.1 Adaptive Weighted Sum (AWS) Method for Bi-objective Optimization

The AWS method is a modified form of the WS method. The WS method cannot find some solutions in some regions on the Pareto front where the AWS method designates those regions as a feasible region for sub-optimization. Figure 5.2 illustrates a region where the AWS method is more efficient than that of WS method. Although the normal boundary intersection (NBI) [126] and normal constraint (NC) [127], [128] methods are some other scalarized methods that can find uniform solutions in the Pareto front, the NBI method sometimes obtains non-Pareto solutions and the NC method requires the Pareto filter to remove the dominant solutions [129], respectively. Alternately, the AWS method can produce well-distributed Pareto front points both in the non-convex region and some other unexplored regions. Reference [75] shows that the AWS method can identify well-distributed solutions in the Pareto front for a bi-objective optimization of the continuous variable problem. In this section, mathematical procedures that are described in [75], [76] of the AWS method and the implementing steps at enumeration-based iterative simulation under discrete decision variable cases are described in the following ways.

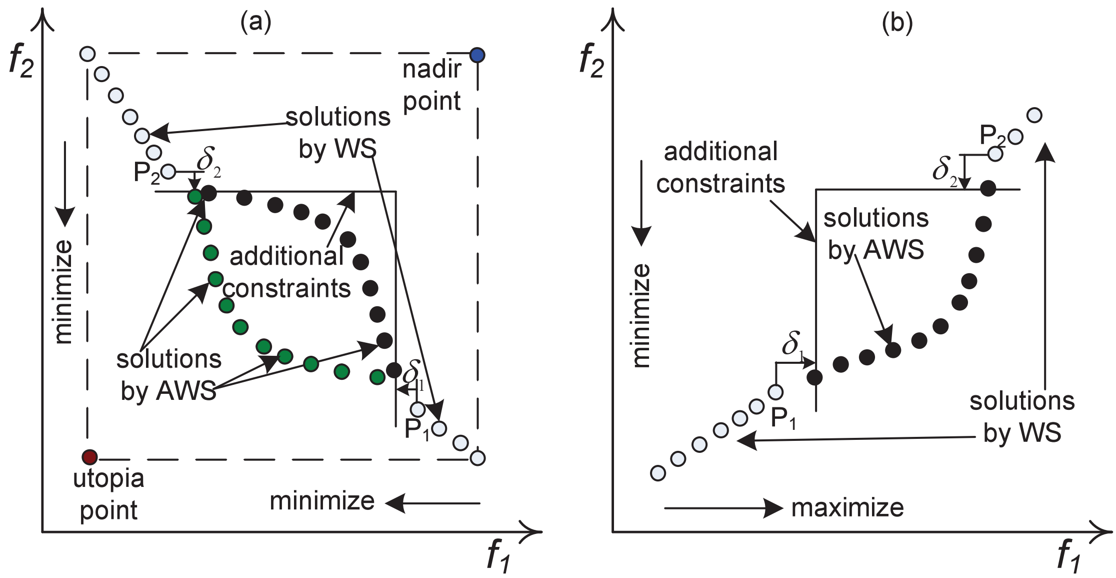

Figure 5.2: AWS method for Pareto front solutions/points of unexplored regions (a) min-min (b) max-min.

- Firstly, it is required to normalize the objective functions. If $\mathbf{X}^{i*}$ is an optimum solution vector of single-objective optimization, i.e., the *ith* objective function f_i, then the Utopia point of $\mathbf{F}^{Utopia}$ is expressed as,

$$\begin{aligned}\mathbf{F}^{Utopia} &= [f_1(\mathbf{X}^{1*})\ f_2(\mathbf{X}^{2*})] \\ &= [\min T_{(:,1)}\ \min T_{(:,2)}] \\ &= [f_1^{Utopia}\ f_2^{Utopia}]\end{aligned} \tag{5.6}$$

The Nadir points f_1^{Nadir} and f_2^{Nadir} are determined as,

$$f_1^{Nadir} = \max\left[f_1(\mathbf{X}^{1*})\ f_1(\mathbf{X}^{2*})\right]$$
$$f_2^{Nadir} = \max\left[f_2(\mathbf{X}^{1*})\ f_2(\mathbf{X}^{2*})\right] \tag{5.7}$$

Then, the Nadir vector, i.e., $\mathbf{F}^{Nadir}$ is expressed as,

$$\mathbf{F}^{Nadir} = \left[f_1^{Nadir}\ f_2^{Nadir}\right] \tag{5.8}$$

The *ith* anchor point $\mathbf{F}^{i*}$ is defined as,

$$\mathbf{F}^{i*} = \left[f_1(\mathbf{X}^{i*})\ f_2(\mathbf{X}^{i*})\right] \tag{5.9}$$

The normalized objective function $\bar{f_i}$ is defined as,

$$\bar{f_i} = \frac{f_i - f_i^{Utopia}}{f_i^{Nadir} - f_i^{Utopia}} \tag{5.10}$$

The Utopia and Nadir points are determined from matrix (5.5) and consequently all the objective function values of (5.5) are normalized.

- Utilizing a small number of divisions, i.e., a large step size of weighting factor, the traditional WS method is applied in the bi-objective problem for determining the Pareto front points. The WS method scalarizes the objective functions and combines the MOP into a single-objective function. Utilizing the two objective functions of the bi-objective optimization problem, the single-objective function is achieved as,

$$F_{tw}(\mathbf{X}) = \{w_1\bar{f_1} + (1 - w_1)\bar{f_2}\}$$
$$\text{and}\ \ w_1 \in [0, 1] \tag{5.11}$$

For all the rows of (5.5) and for a weighting factor, the first two column elements are used in (5.11) to make a single objective column vector. The calculated values of each row are stored in a new matrix, $M_{N(m,11)}$, expressed as,

$$M_{N(m,11)} = \begin{pmatrix} F_{tw(1,1)} & f_{1(1,2)} & f_{2(1,3)} & f_{3(2,4)} & x_{1(2,5)} & \cdots & x_{6(1,10)} & S_{(1,11)} \\ F_{tw(2,1)} & f_{1(2,2)} & f_{2(2,3)} & f_{3(2,4)} & x_{1(2,5)} & \cdots & x_{6(2,10)} & S_{(2,11)} \\ \vdots & \vdots & \vdots & \vdots & \vdots & \ddots & \vdots & \vdots \\ \vdots & \vdots & \vdots & \vdots & \vdots & \ddots & \vdots & \vdots \\ \vdots & \vdots & \vdots & \vdots & \vdots & \ddots & \vdots & \vdots \\ F_{tw(m,1)} & f_{1(m,2)} & f_{2(m,3)} & f_{3(m,4)} & x_{1(m,5)} & \cdots & x_{6(m,10)} & S_{(m,11)} \end{pmatrix} \tag{5.12}$$

The minimum value from the first column of (5.12) is determined and the corresponding row vector is saved in another matrix. Likewise, the single objective minimum values for other weights are calculated and saved to the matrix, which is expressed as,

$$M_{WS(p,11)} = \begin{pmatrix} F^{min}_{tw0(1,1)} & f_{1(1,2)} & f_{2(1,3)} & f_{3(2,4)} & x_{1(2,5)} & \cdots & x_{6(1,10)} & S_{(1,11)} \\ F^{min}_{tw1(2,1)} & f_{1(2,2)} & f_{2(2,3)} & f_{3(2,4)} & x_{1(2,5)} & \cdots & x_{6(2,10)} & S_{(2,11)} \\ \vdots & \vdots & \vdots & \vdots & \vdots & \ddots & \vdots & \vdots \\ \vdots & \vdots & \vdots & \vdots & \vdots & \ddots & \vdots & \vdots \\ \vdots & \vdots & \vdots & \vdots & \vdots & \ddots & \vdots & \vdots \\ F^{min}_{twp(p,1)} & f_{1(p,2)} & f_{2(p,3)} & f_{3(p,4)} & x_{1(p,5)} & \cdots & x_{6(p,10)} & S_{(p,11)} \end{pmatrix} \tag{5.13}$$

The number of rows in (5.13) linearly depends on the number of small divisions in weights, i.e., if three divisions of weights are selected, then three minimum-valued row vectors are generated. While the number of divisions of weights is high, there is no guarantee of generating the same number of minimum-valued row vectors. Therefore, a small number of divisions for the weight w_1 is selected initially for the WS method. The vector consists of second and third column values of (5.13), which are a Pareto optimal points of the Pareto front, which is generated by the WS method.

- In the previous step, there might have been some overlapping solutions. Thus, the overlapping and the nearly overlapping solutions are deleted in this step upon computing the lengths of the segments between all of the neighboring solutions. The length of each segment is determined utilizing Euclidean distance, which is expressed as,

$$D_{el}(\mathbf{X}_1, \mathbf{X}_2) = \sqrt{\sum_{q=1}^{2} \left(f_q(\mathbf{X}_1) - f_q(\mathbf{X}_2) \right)^2} \tag{5.14}$$

where the normalized value of the objective functions (i.e., values from columns two and three) are used to determine the distance between neighbouring solutions. When the Euclidean distances between the solutions are nearly zero, then one of the nearly overlapping solutions is deleted so that only one solution can represent the Pareto front. It is worthwhile to mention that the nearly overlapping distances are measured in the objective space.

- Then an adaptive refinement is conducted. In this case, the numbers of further refinements are identified by comparing the length of segments with the average segment length. More refinements are usually necessary in the larger length. The further refinements are essential in continuous variable problems where the well distributed Pareto front points are obvious. Alternately, all the segments can further be investigated. Whatever the criteria are chosen, the refinements in the neighbouring solution points are done upon imposing additional constraints, expressed (see Figure 5.2) as,

$$\begin{aligned} f_1(\mathbf{X}) &\leq P_1^x - \delta_1 \\ f_2(\mathbf{X}) &\leq P_2^y - \delta_2 \end{aligned} \tag{5.15}$$

- The last two steps are repeated until all the segments become equal length in order to generate evenly distributed Pareto front points. As this problem is based on a discrete variable set, further refinements are done upon running the above two steps by a few iterations.

5.4 Results and Discussion

The effectiveness of the proposed bi-objective optimization approach of this chapter is investigated in the MATLAB/SIMULINK environment. The IMG is choronologically simulated employing the hourly average TMY-based time series. The ranges of decision variables for the first two case studies are taken from Table 5.1. The upper and lower limits of the decision variables are chosen meticulously so that the computational complexity can be kept as small as possible for determining the optimal sizes of the IMG. The decision variables of this problem are integers and the objective functions are related with cause and effect criteria. Thus, this study aims to identify the maximum number of solution points on the Pareto front and to maintain an evenly spread among the solutions. The approach employs the parametric values from Tables A.3. The models for load real and reactive powers of Chapter 3 are used in this study. Both the values of δ_1 and δ_2 in (5.15) are taken 1% of their respective objective function value. One particular decision variable, i.e., the battery charger rating, P^b_{rat}, is kept fixed in each investigation by setting a fixed value of battery bank autonomy hour. However, the battery bank autonomy hour, i.e., T_{chr} has an impact on LCC. Therefore, the battery bank autonomy hours are taken at six hours for one case study and twelve hours for the others. In order to

Table 5.1: Ranges of Decision Variable For Bi-objective Optimization

Components	Unit	Minimum	Step-Size	Maximum
WPS (P^w_{rat})	kW	150	150	900
PVS (P^{pv}_{rat})	kW	0	150	450
BESS (E^b_{rat})	kWh	0	600	3000
DGS (S^{di}_{rat})	kVA	240	80	560
Converter (S^{con}_{rat})	kVA	0	160	640
Charger (P^b_{rat})	kW	$E^b_{rat}/12$	-	$E^b_{rat}/6$

compare the performances, the results of the case studies, both for the WS and AWS methods, are presented in this chapter.

5.4.1 Pareto Fronts at Six Hours of Battery Bank Autonomy

Figures 5.3(a) and (b) are produced by the WS and AWS methods, respectively, and illustrate all the possible values of objective functions and the solutions on the Pareto fronts. As shown in Figure 5.3(a) and in Table C.2 (Appendix C), three trade-off solutions and corresponding decision variable vectors are identified by the WS method because the weighting factor are taken 0.0, 0.50, and 1.0. Figure 5.3(a) further demonstrates that there are many solutions, which are not identified, on the Pareto front. Alternately, Figure 5.3(b) illustrates that the AWS method identifies more solutions (twelve solutions, see in Table C.2) on the Pareto front compared to those of the WS method. Table C.2 illustrates that the LPSP is a constraint and is set to zero in the objective space. Furthermore, Figure 5.3(b) shows that the AWS method

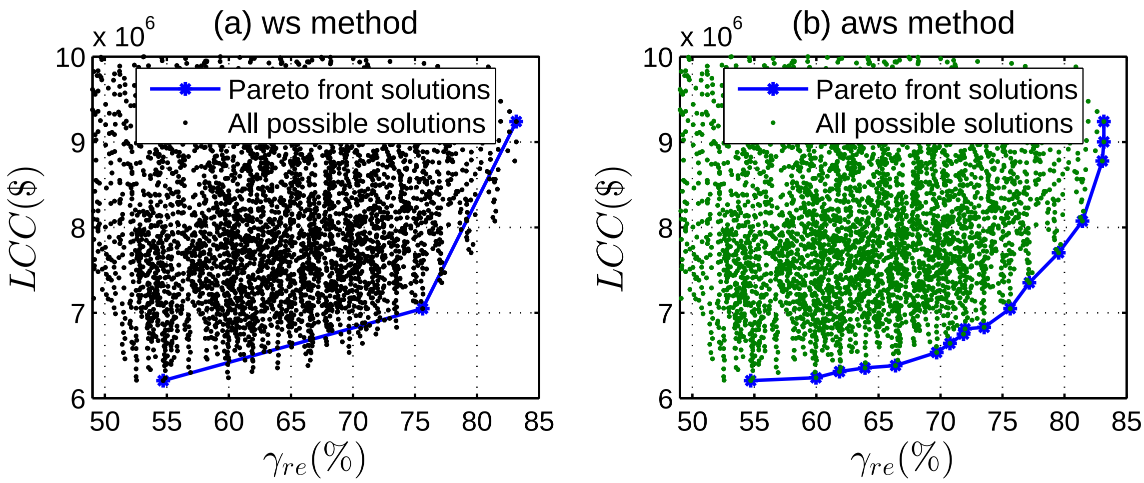

Figure 5.3: Pareto front solutions (a) WS and (b) AWS methods with battery autonomy hour six

can identify some solutions in the unexplored regions, which are formed as either convexes with irregular curvatures or non-convexes. The ranges and step sizes of decision variables of this case study are taken very close to those of the case study of Subsection 3.6.1. Thus, the minimum value of LCC and corresponding optimal decision variable vector of Table C.2

closely matches with those of Subsection 3.6.1 (see Table 3.2). The battery bank size, E^b_{rat}, and battery charging/discharging rate, P^b_{rat}, of Table C.2 indicate that the battery bank autonomy is six hours. The Pareto front of Figure 5.3(b) further demonstrates that the increase of REP soar the LCC. Thus, this bi-objective optimization result shows that one objective function value cannot be improved without deteriorating the other objective function value.

5.4.2 Impact of Weighting Factors and Battery Bank Autonomy Hours on Pareto Fronts

This case study has been conducted to investigate the impacts of battery bank autonomy hour and weighting factors of the WS method on the identified solutions of Pareto front. Considering battery bank autonomy as twelve hours, Figures 5.4(a) and (b) are respectively produced by the WS and AWS methods, where the step size of the weighting factor is 0.50. Therefore, Figure 5.4(a) identifies only three solution points on the Pareto front. While the weighting step size is decreased to 0.25, the WS method can determine five solutions on the Pareto front, as shown in Figure 5.4(c). It has been observed that if the step size of the weighting factor is reduced further, the numbers of solutions on Pareto front do not linearly increase. Moreover, the WS method cannot identify all the solutions on the Pareto front and the situation becomes worse when the Pareto front region is very irregular. However, Figures 5.4(b) and (d) indicate that the AWS method can identify more solutions on the Pareto front than the WS method, though the increasing rate of newly identified solutions in the AWS method, due to the effect of small step size in the weight factor of the WS method, is negligible. It can also be inferred that the longer segments of neighbouring Pareto front points, i.e., the large weighting factors in the WS method, reduce the total computation of the approch. The comparison of Figure 5.4 with Figure 5.3 illustrates that the large hour of battery bank autonomy moves up the LCC on the Pareto front. Therefore, the Pareto front of Figure 5.4 stays in the upper postion compared to that of Figure 5.3. The numerical values of the Pareto front solutions for this study are provided in Tables C.3 and C.4 (Appendix C). Although the increase in battery bank autonomy hour

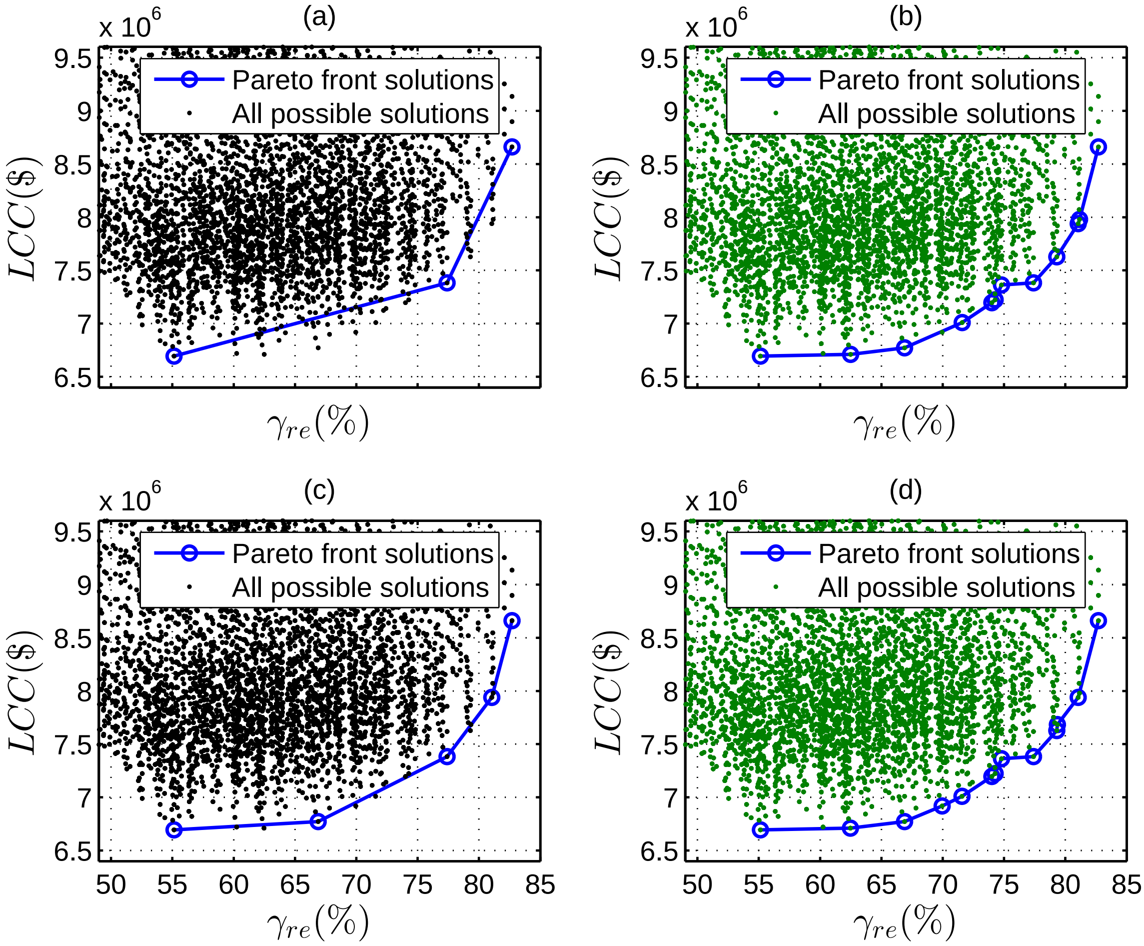

Figure 5.4: Pareto optimal front solutions (a) WS method with large step size of weighting factor (b) AWS method with twelve hours of battery autonomy (c) WS method with small step size of weighting factor and (d) AWS method used the small step size of WS

moderately lifts the LCC, the REP does not grow at the same pace. The close observation of REPs in Tables C.2, C.3, and C.4 reveal that most of the initial solutions in Tables C.2 and C.3 are high. Though a large battery bank is required when more hour of battery bank autonomy is requested, the corresponding charging/discharging rate does not increase at the same rate (see Tables C.3, C.4 and Table C.2); as such the LCC soars due to the requirements of very large battery bank. The aforementined tables show that the PMS-B is the optimized PMS and thus the simultaneous optimizations of the sizes and PMSs are performed.

5.4.3 Impact of LPSPs on Pareto Fronts

This case study has been conducted to investigate the impact of LPSPs on the Pareto fronts. In this case, the battery bank autonomy hour is considered twelve hours. The lower and upper boundaries of the decision variable vector, $[P_{rat}^{w}\ \ P_{rat}^{pv}\ \ E_{rat}^{b}\ \ P_{rat}^{b}\ \ S_{rat}^{di}\ \ S_{rat}^{con}]^T$, for this case study are taken $[0,\ 0,\ 600,\ 50,\ 80,\ 0]^T$ and $[900,\ 450,\ 3000,\ 250,\ 480,\ 480\ ]^T$, respectively. Figure 5.5 shows three Pareto fronts for LPSP of 0%, 2%, and 4%. As can be seen in Figure 5.5, the more reliable the power supply system (i.e., low LPSP) is requested the more the Pareto front moves up due to the high value of LCC. At low REP, the Pareto fronts produced by numerous requested LPSPs are very near to each other due to the sharing operation of the components of the IMG and the sharing operation is performed among the DGS, RERs and BESS. However, Figure 5.5 demonstrates that the Pareto front solutions at high REP and at high LPSPs (i.e., at low reliability) stay at the bottom due to the low value of LCC. To achieve a high REP at low LPSP, more RERs and a large battery bank, which consequently moves up the LCC, are required. Figure 5.5 further demonstrates that the LCC increases sharply at above 80% of REP and for a low LPSP (e.g., LPSP=0%).

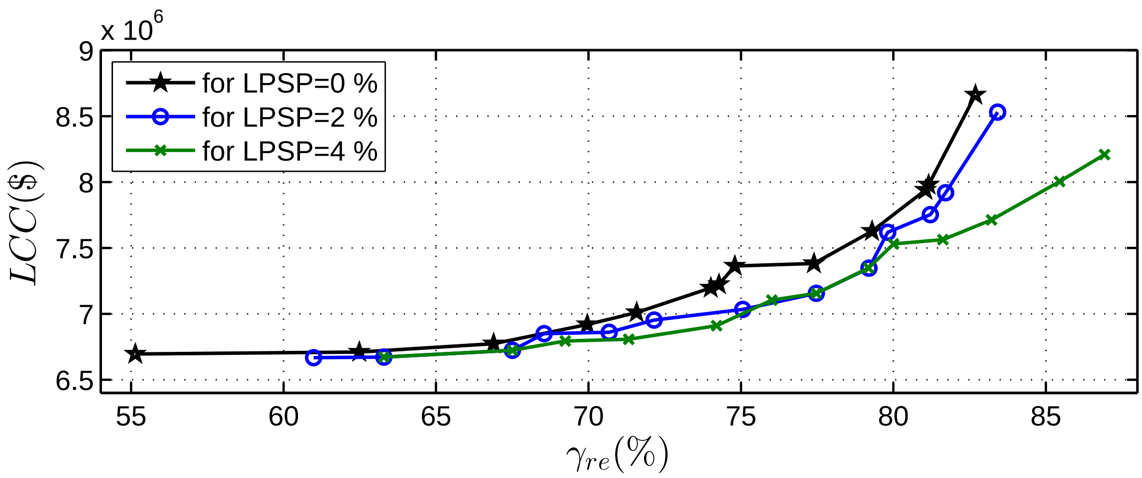

Figure 5.5: Impact of LPSPs on Pareto fronts

5.5 Conclusions

This chapter has proposed a bi-objective optimization approach for generating Pareto fronts and Pareto optimal solutions of the IMG in a discrete decision variable environment. The mathematical model of the bi-objective optimization and the algorithmic flowchart of the approach have also been presented in this chapter. The results of the case studies have indicated that the approach is capable of generating many solution points on the Pareto optimal front. The more Pareto fronts indicate more options available for the decision maker. The comparisons between the traditional WS method and the AWS method have also been demonstrated in this chapter. It is observed that the AWS method has included many solution points that cannot be identified by the WS method and the approach has identified almost evenly distributed solutions. One of the studies has indicated that the global optimum value of Chapter 3 coincides with a solution in the Pareto optimal front of the AWS method. This chapter has further investigated the sensitivity of battery bank autonomy hour and LPSP on Pareto optimal fronts. When two objective functions are involved, the proposed approach can easily be utilized for designing an IMG, along with, optimizing the PMSs based on a Pareto front set.

Chapter 6

A Multiobjective Optimal Sizing Approach

6.1 Introduction

Two single objective optimal sizing approaches for IMGs were discussed in Chapter 3 and Chapter 4, respectively. Subsequently, one bi-objective optimal sizing approach was introduced in Chapter 5. Owing to increased social awareness, real-life engineering problems are encountering pressure to increase the number of objective functions in the optimization problems. The criteria of objective functions include economic criteria (e.g., LCC), reliability (e.g., LPSP), environmental criteria (e.g., greenhouse gas emission/REP), and social criteria (e.g., social acceptance) [85]. An intensive investigation of the IMG reveals that the optimization of the IMG is complex as the problem is composed of several competing objective functions, multiple variables, and a high degree of nonlinearity. When an optimization problem includes (a) multiple objectives, (b) multiple constraints, (c) multiple variables, and (d) a high degree of nonlinearity, the MOP becomes challenging to solve [130]. Generally, the MOO approaches provide the best possible trade-off solutions [131] for a decision maker (DM). The AWS method, which is employed in the bi-objective optimization of Chapter 5, is based on the WS method, a classical technique that converts an MOP into an SOP for each weight. The AWS method imposes constraints in smaller regions for further searching. In the AWS method, the computation of surfaces, i.e., the determination of Pareto patches, becomes difficult with the increased number of objective functions. Many studies [71], [72] support the idea that evolutionary algorithms (EAs) are effective for finding a global optimum solution and also for performing MOO regardless of the nature of the objective function, decision variable, modality, and constraint. Moreover, all the GAs have the ability to deal with non-convex optimization problems, non-differentiable functions, parallel functions, and noisy environments [131], [132]. This chapter proposes a fundamentally robust MOO approach for optimal sizing of the IMG. The proposed approach takes benefit of the non-dominated sorting genetic algorithm-II (NSGA-II) [133] method, as it provides less computational complexity than that of any other GAs. Additionally, the NSGA-II method not only extracts the better fitness of chromosome/ individual but also increases the diversity of the individual in the Pareto optimal set. The approach of this chapter systematically evolves efficient solutions and successively converges to the global Pareto optimal solution.

6.2 Problem Statement

This chapter has considered Figure 2.1 of Section 2.2 as the study system (i.e., the IMG) in order to determine the optimal sizes utilizing the MOO approach. The mathematical models of the subsystems of Figure 2.1 are taken from Section 3.2. Those models include the renewable resources, WPS, PVS, BESS, active and reactive powers of primary load, dump load, and the BESS converter. In order to simultaneously optimize the sizes and PMSs of the IMG, the concept of collaborative optimization of Figure 6.1 is adopted for which one new gene (decision variable) is introduced in each individual (decision variable vector) to represent the PMSs. The value of the new gene determines the PMS and thus only one PMS is required to be employed for simulating the IMG. This scheme is implemented incorporating a few conditional (*IF-ELSE*) statements in the pseudo code of the algorithm. The MOO is generally utilized for determining a set of trade-off solutions when the optimization problem contains multiple

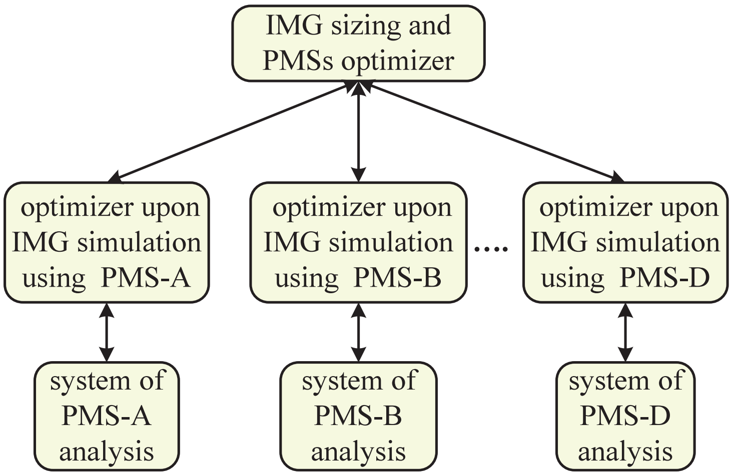

Figure 6.1: Simultaneous optimization of PMSs and sizes

objective functions that usually conflict with each other. The multiobjective optimization problem (MOP) of the study system is formulated considering the following objective functions. The three equations that are described in (3.24), (3.25), and (3.43) are taken as three objective functions, expressed as,

$$f_1(\mathbf{X}) = -\gamma_{re}, f_2(\mathbf{X}) = LCC, f_3(\mathbf{X}) = LPSP \tag{6.1}$$

where $\mathbf{X}$ is an individual/decision variable vector in a population set. The details of the decision variable vector and the MOO formulation are provided in the following subsection.

6.2.1 Decision Variables Vector and MOP Formulation

This chapter has accounted six genes (i.e., decision variables) in each of the individuals (i.e., decision variable vectors) to solve the MOP of the IMG. The MOP is formulated by an objective function vector that is comprised of the aforementioned three different objective functions, along with, the associated constraints. The constraints are expressed in the mathematical models and are incorporated in the flowcharts of the PMSs. The main goals of this MOP are to find (i) a set of solutions as close as possible to the Pareto optimal front and (ii) the solutions should be as diverse as possible. The objective functions and the constraints are dependent on the decision variable vector. The MOP for the IMG is formulated as,

$$\begin{aligned}
\underset{\mathbf{X}}{\text{minimize}}\;\; & \mathbf{F}(\mathbf{X}) = [f_1(\mathbf{X})\; f_2(\mathbf{X})\; f_3(\mathbf{X})]^T \\
\text{subject to}\;\; & \mathbf{X} \in \mathcal{R} \\
& g_j(\mathbf{X}) \leq 0,\; j = 1, 2, ..., J \\
\text{where}\;\; \mathbf{X} & = [P^{w}_{rat}\; P^{pv}_{rat}\; S^{con}_{rat}\; S^{di}_{rat}\; E^{b}_{rat}\; PMS]^T \\
& = [x_1\; x_2\; x_3\; x_4\; x_5\; x_6]^T \in \mathcal{R}
\end{aligned} \tag{6.2}$$

and x_i denotes the value of the ith gene in an individual. The lower bound $l = [l_1\; l_2\; l_3\; l_4\; l_5\; l_6]^T$ and the upper bound $u = [u_1\; u_2\; u_3\; u_4\; u_5\; u_6]^T$ of the decision variable vector define the feasible region (i.e., solution space) and the domain of each decision variable vector is denoted as interval $[l_i\; u_i]$. As expressed earlier, each decision variable is called a gene and each chromosome/individual represents a feasible solution. The variable $\mathbf{F}(\mathbf{X})$ is the objective function vector that is formulated by the three different objective functions.

6.3 Multiobjective Optimization by GA Approaches

The multiobjective optimization approaches can carry optimization of several incommensurable and often competing objectives [132]. The GAs have the ability to search in non-convex, discontinuous, and multi-modal solution spaces and to generate a set of solutions [71] as diverse as possible. Owing to the inclusion of multiple random variable vector (i.e., a set of population), which also facilitate the approache's ability to avoid getting trapped in the solution of a local optima, the GA approaches have gained the abilities to deal with non-convex regions and multi-modal cases. Recently, the parallel implementation of multiobjective GA over multiple processors [134] has been introduced for reducing the execution time. Many researchers [83], [131], [133], [135] have investigated different approaches of MOO based on evolutionary and/or genetic algorithms. The popular approaches for solving an MOP are the (i) aggregation-based approaches, (ii) population-based non-Pareto approaches, and (iii) population -based Pareto approaches [71], [136], [137]. Among the GA-based MOO approaches, the weight-based GA (WBGA) [124] is an aggregation approach, which is an extension of the single-objective optimization, and utilizes various combinations of weights for generating multiple solutions. Another MOO approach, based on GA, is a vector evaluated GA (VEGA) [138], which is the first population-based non-Pareto approach and it has the capacity of easy implementation. Though the approach is based on population, it has not employed diversity preservation and an elitism mechanism. Some approaches, i.e., multiple objective GA (MOGA) [138], niched Pareto GA (NPGA) [139], and non-dominated sorting GA (NSGA) [132], [140] are Pareto-based non-elitist approaches that have utilized diversity mechanisms only. On the other hand, the non-dominated sorting GA-II (NSGA-II) [133], strength Pareto evolutionary algorithm (SPEA) [141], and SPEA2 [142] are some Pareto-based elitist approaches that have employed both diversity and elitism for producing uniform spread in the trade-off solutions. In this study, the NSGA-II is employed due to its reduced computational complexity, i.e., for faster diversity mechanisms and for elitist schemes.

6.4 Algorithmic Flowchart for Solving the MOP of an IMG

Figure 6.2 illustrates a flowchart of the proposed approach that is employed for solving the MOP of an IMG, where the NSGA-II method is utilized. The NSGA-II method is an improved version of NSGA [140] where the former is proposed in reference [133]. As shown in Figure 6.2, a population set is randomly generated first. The flowchart in Figure 6.2 further shows that a chronological simulation of the IMG is performed based on hourly average TMY-based time series and each individual (i.e., a decision variable vector) from the population. The mathematical models and load models of Figure 6.2 are taken from Chapter 3. The sixth gene (decision variable) of an individual denotes the types of PMS and the simulation of the IMG is performed based on that particular PMS. The algorithm of this chapter has accounted in four PMSs and the details of those PMSs are presented in Chapter 2 of this thesis. The determination process of a PMS requires an *IF-ELSE* logic on the value of the sixth gene (decision variable), which is implemented in the PMS block of Figure 6.2. The values of the gene that is responsible for determining the PMSs might be different in different individuals. The IMG is simulated using all the individuals from the population. After producing all the objective functions by the individuals of population, the population is sorted based on non-domination into each front. The first front is completely non-dominant set in the current population. The second front

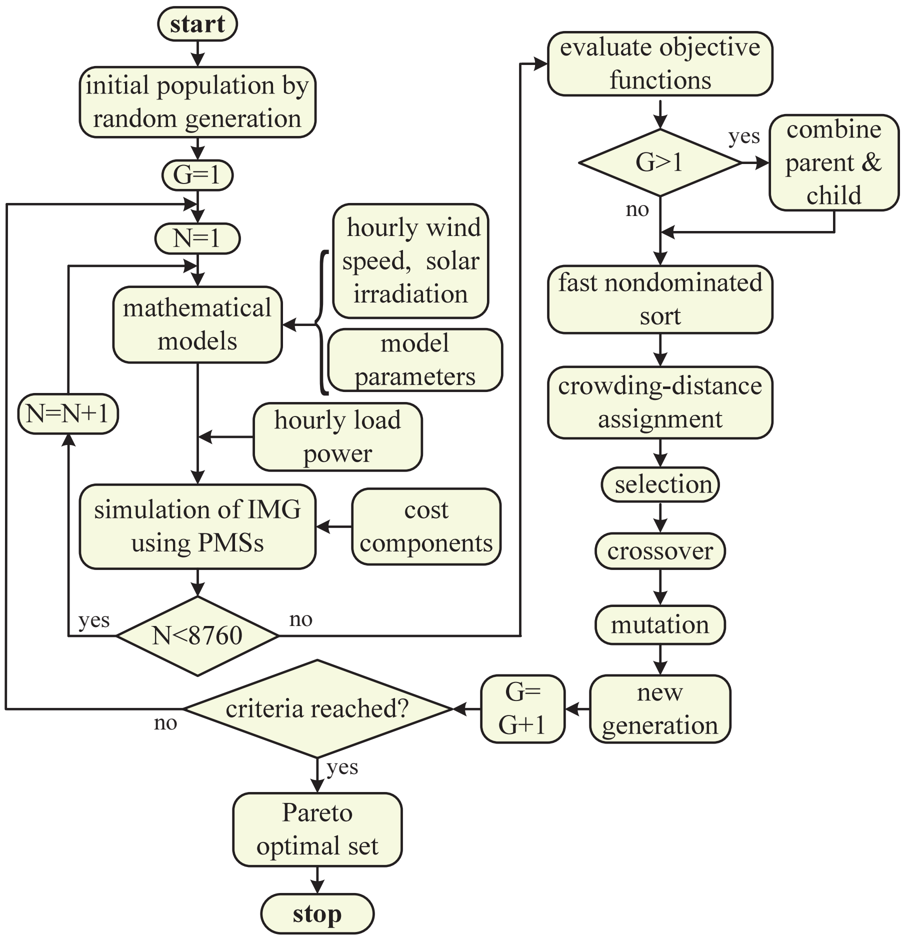

Figure 6.2: Genetic optimization algorithm.

is dominated by only the individual of the first front and the sorting of front continues until the population set becomes null. The individuals in each front are given the same fitness value (e.g., all the individuals of front 1 are assigned fitness 1). Then, crowding distance is calculated for each individual such that better diversity in the population can be generated. After that based on rank and crowding distance, the parents are selected from the population utilizing binary tournament in order to generate offspring. As such, the generation of new population is produced by utilizing the selection, crossover, and mutation operators. If the criteria of stopping in the optimization process is not reached, the generation of the population is continually upgraded by the NSGA-II process where both parent and offsprings are merged after the first generation such that the elitism can be maintained in the front. The process evolves until reaching a stopping criteria. The internal process of NSGA-II [71], [133] is discussed in the following section.

6.5 Non-dominated Sorting Genetic Algorithm-II (NSGA-II)

Generally, multiobjective GA approaches differ with each other based on their fitness assignment, elitism, and diversification mechanism [132]. There are numerous GAs [71], [131], [132], [136] in the literature for solving MOPs. In this chapter, the 'gamultiobj' tool of MATLAB is utilized to get the Pareto optimal solution. However the basic background of 'gamultiobj' tool is a layered classification GA approach, called NSGA-II [133]. It is a Pareto-ranking approach that explicitly utilizes the concept of Pareto non-dominance in evaluating fitness. As the NSGA-II method reduces computational complexity and weakness of the NSGA technique, the basics of the NSGA-II method is described in this section. This basics of NSGA-II expect to facilitate in modifying and improving the quality of the Pareto optimal solutions. Before explaining the main loop of NSGA-II, the mechanisms of sorting, raking, selection, crossover, and mutation in general are described in the following subsections.

6.5.1 Fast Nondominated Sort

This technique is utilized to sort the individuals of initial and successive populations in fronts based on a nondomination criterion, called fast nondominated sort. In this sorting technique, two entities are calculated for each individual. The entities are,

- Domination count, n_p, i.e., the number of individuals that dominate the individual p, and
- S_p, a set of individuals that the individual p dominates.

Then, the steps of nondominated sort approach are described as,

1. For each individual p in main population P, i.e., for $p \in P$, initialize $S_p = \emptyset$ and $n_p = 0$. For each $q \in P$, where $q \neq p$, go to step 2 and then step 3.

2. If p dominates q, i.e., $p \preceq q$ add q to the set S_p, i.e., $S_p = S_p \bigcup q$, otherwise if q dominates p, i.e., $q \preceq p$ set $n_p = n_p + 1$.

3. If $n_p = 0$, i.e., no individual dominates p, set rank of individual p to one and keep p in the first nondominated front F_{r1} (shown in Figure 6.3(a)). Initialize the front counter to one, i.e., $i = 1$.

4. While ith front is empty, i.e., $F_{ri} = \emptyset$, perform the following steps.

5. Initialize $Q = \emptyset$, The set for storing the individuals for $(i+1)$th front. For each individual p in F_{ri} (i.e., $p \in F_{ri}$) and for each individual q in S_p (i.e., $q \in S_p$) set $n_q = n_q - 1$. If $n_q = 0$, keep q in Q, i.e., $Q = Q \bigcup q$

6. Set $i = i + 1$ and $F_{ri} = Q$. Go to step 4.

The graphical representation of the fast nondominated sort utilizing front is shown Figure 6.3(a).

6.5.2 Diversity Preservation

The main target of an MOO is to maintain a good spread in the Pareto optimal solution set. Some GA techniques, (e.g., original NSGA) have employed "*sharing functions*" for maintaining a diversity among the solutions upon assigning values to the sharing parameter. A user estimation is essential for assigning values to the sharing parameter. The performances of the spread depend on the assigned value of the sharing parameter where each of the solutions is required to compare with others. Therefore, the scheme turns out to be computationally intensive. The NSGA-II method does not use sharing parameters and the method utilizes different kinds of density estimations called crowding distance among the solutions.

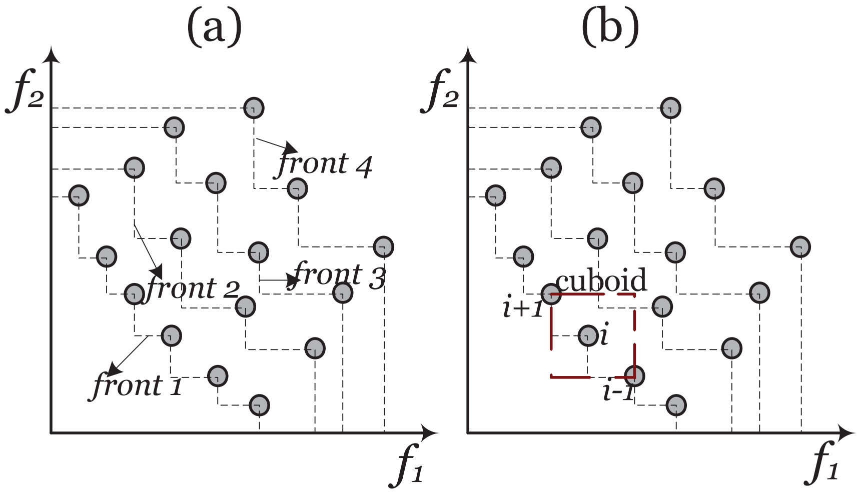

Figure 6.3: (a) Non-dominated sorting of NSGA-II and (b) crowding distance calculation

1) Density Estimation-Crowding Distance

In NSGA-II, the density estimation around a particular solution is performed by calculating an average distance of two points on either side of that particular point along each of the objectives. The crowding distance maintains the measure of population density around a solution. To calculate this distance, first, all objective function values are normalized. Thus, a cuboid is formed around a member, *i*, by taking the nearest neighboring members as vertices, which is shown in Figure 6.3(b). The crowding distance of the *ith* solution in its front is measured by the average side length of the cuboid. The crowding distance computation requires sorting the population according to each objective function in ascending order of magnitude. Then, each objective function of two boundary solutions is assigned an infinite distance value. The other solutions are assigned a distance value equal to the absolute normalized difference in the function values of two adjacent solutions. The main advantage of the crowding distance scheme is that it measures the population density around a solution where the process does not require the sharing parameter. Thus, the crowding distance for each solution in a set $\mathcal{R}_i$ is calculated by the following procedure.

- Determine the number of solutions in $\mathcal{R}_i$, i.e., $l = \mathcal{R}_i$. Then, assign $\mathcal{R}_i[i]_{distance} = 0$ for each *ith* solution in the set.

- The computation of crowding distance requires the sorting of the population. For each objective function of m, sort the solutions in $\mathcal{R}_i$ in ascending order.

- The boundary objective functions are assigned infinity, i.e., assume a large distance for each of the first and the last solutions, i.e., $\mathcal{R}_i[1]_{distance} = \mathcal{R}_i[l]_{distance} = \infty$. Then the adjacent two solutions of the rest are measured in the normalized way. Thus, for the rest of the solutions, i.e., for $i = 2$ to $(l - 1)$, calculate the distance as,

$$\mathcal{R}_i[i]_{distance} = \mathcal{R}_i[i]_{distance} + \frac{\mathcal{R}_i[i+1]_m - \mathcal{R}_i[i-1]_m}{f_m^{max} - f_m^{min}} \tag{6.3}$$

- The total crowding distance is the sum of individual distance values corresponding to each objective. Thus, to find the total crowding distance of a solution, sum the solutions' crowding distance with respect to each other.

where, $\mathcal{R}_i[i]_m$, f_m^{max}, and f_m^{min} represent the *mth* objective function value of the *ith* individual in the set $\mathcal{R}_i$, maximum value, and minimum value of the *mth* objective function, respectively. The crowding distance, $\mathcal{R}_i[i]_{distance}$, is used to select members in a less crowded part of a rank.

2) Crowded Comparison

The crowded comparison of two solutions is performed after assigning the distances to each solution. The crowded-comparison operator guides the selection process at the various stages of the algorithm toward a uniformly spread Pareto front. Every individual, i, in the population has two attributes, which are (1) non-domination rank and (2) crowding distance. Then a partial order comparator is used for a solution to prefer one over another. The smaller value of a distance indicates that the solution is more crowded than the others. The scheme needs either a better rank or a better crowding distance if two solutions stay in the same rank. The crowding comparison operator is highly required when the selection of partial size of population from a particular front is required. In this case usually all the solutions of the front are sorted in descending order and then the operator is utilized.

6.5.3 Tournament Selection

Selection process in GA techniques can be either stochastic or completely deterministic and the process removes the low-quality individuals from the population, while the high-quality individuals are regenerated. Thus, the selection process determines which of the previous solutions should be kept in memory. This selection process drives the algorithm to improve the population and to speed up the convergence rate over the succeeding generations. In NSGA-II, a tournament selection process is suggested for employment. The process is carried out utilizing the aforementioned crowded-comparison operator where the crowding distance measure is used as a tie-breaker and is called crowded tournament selection. Two solutions are randomly selected first. When a solution lies in the same non-dominated front, the solution with higher crowed distance is declared the winner. Otherwise the solution with the lowest rank is selected as all the solutions of first front is ranked 1, and the solutions of second front is ranked 2 and so on. The winner of each tournament (the one with the best fitness) is selected for the crossover. Before going to explain crossover, the elitism in general is described below.

6.5.4 Elitism

Elitism provides a means for reducing genetic drift by ensuring that the best individual(s) is allowed to pass their traits to the next generation. In NSGA-II, the elitism is mainly maintained by combining parent with off-spring and then by nondomination sorting. Other than that, two options, the ‘Pareto fraction’ and ‘distance function’, are used in GA in general to control elitism. The Pareto fraction option limits the number of individuals on the Pareto front and the distance function helps to maintain diversity on a front by favoring those individuals relatively away from the front. Based on the Pareto fraction, the non-dominated individuals from the population are propagated directly to the next generation. The rest of the off-spring are produced by crossover operator. However, the degree of elitism needs to be adjusted properly and carefully because high selection pressure may lead to premature convergence. The scheme maintains elitism by the aforementioned options and generates new diversified populations.

6.5.5 Crossover

The crossover operator is applied to the parent population, which are selected from tournaments. If a new generation length is N_g, there needs to be selected the remaining parents, upon deducting the parents based on crossover fraction, for the crossover operation. Crossover produces a new individual in combining the information of two parents at a time. The most common approach for performing crossover is the one-cut point method. There are also multi-cut point method for crossover. The cut point position on a genetic string is randomly determined. Although the default crossover function in MATLAB 'gamultiobj' is intermediate, the mathematical representation of binary crossover, taken from [143], is expressed as,

$$(p_c)_{1,m} = \frac{1}{2}\Big[\{1-\beta_m\}(p_p)_{1,m} + \{1+\beta_m\}(p_p)_{2,m}\Big] \tag{6.4}$$

$$(p_c)_{2,m} = \frac{1}{2}\Big[\{1+\beta_m\}(p_p)_{1,m} + \{1-\beta_m\}(p_p)_{2,m}\Big] \tag{6.5}$$

where $(p_c)_{i,m}$ is the ith child with mth component, $(p_p)_{1,m}$ is the selected parent and $\beta_m \geq 0$ is a sample from a random number, which is generated by a density function given as,

$$(p_p)_\beta = \frac{1}{2}(\eta_c + 1)\beta^{\eta_c}, \text{ if } 0 \leq \beta \leq 1 \tag{6.6}$$

$$(p_p)_\beta = \frac{1}{2}(\eta_c + 1)\frac{1}{\beta^{\eta_c} + 2}, \text{ if } \beta > 1 \tag{6.7}$$

The distribution is obtained from a uniformly sampled random number u between $(0, 1)$. η_c is the distribution index for the crossover.

6.5.6 Mutation

Mutation alters the individuals with a low probability of survival. Although the default mutation function in MATLAB 'gamultiobj' is adaptive feasible, the mathematical representation of polynomial mutation, taken from [143], is expressed as,

$$(p_c)_m = (p_p)_m + ((p_p)_k^u - (p_p)_m^l)\delta_m \tag{6.8}$$

where $(p_c)_m$ and $(p_p)_m$ respectively signify the child population and the parent population. The $(p_p)_m^u$ and $(p_p)_m^l$ are the upper bound and the lower bound, respectively, for the parent population. The parameter, δ_m, is a small variation that is calculated from polynomial distribution, expressed as,

$$\delta_m = (2r_m)^{\frac{1}{\eta_m+1}} - 1, \text{ if } r_m < 0.5 \tag{6.9}$$

where r_m is a uniformly sampled random number between $(0, 1)$ and η_m is the mutation distribution index.

6.5.7 Main Loop of NSGA-II and Summary

After the random generation of first parent population set, they are processed based on nondomination sort, ranking assignment of the front, tournament selection, crossover, and mutation in order to create off-springs. In the next iteration, the parent and off-springs are merged together such that an elitism can be maintained. After combining, the size of population will be twice of the original size. Next the total population is sorted according to nondomination. Now, the solutions belonging to the first front can be considered the best solutions in the combined population. If the size of the first front is lower than the first generation size, all the solutions from the first front will be chosen for the new population. The remaining members of the population are chosen from subsequent nondomination fronts in order of their ranking. In such a way to choose population from the fronts exactly original population size, the individuals of the last front are sorted using the crowded-comparison operator in descending order and choose the best solutions needed to fill all population slots. Thus, the new population is now used for selection, crossover, and mutation in order to create next generation off-spring. Considering all the aforementioned schemes, the NSGA-II algorithm is briefly expressed as,

- Set the ranges of design variables, the parameters of NSGA-II and then initialize the population.
- For every individual in a population, calculate the values of all (m) objective functions.
- Rank the solutions in the population using the non-domination criteria.
- Perform selection using the crowding distance binary tournament selection operator.
- Perform crossover and mutation to generate offspring population.
- Combine the parent and child populations.
- Replace the parent population by the best members of the combined population. If the termination criterion is not met, evolve operation.
- Output the first non-dominated front of the final population.

6.6 Results and Discussion

To demonstrate the effectiveness of the proposed MOO approach, several case studies have been conducted in the MATLAB software environment. This chapter has used the study system of Figure 2.1 to determine the optimal sizes of the IMG by employing this approach. In this approach, the maximum charging/discharging rate of battery bank has not been accounted a decision variable, but rather, it has been formulated as a fixed value for each case study by building a relationship with battery bank autonomy hour to its capacity. Thus, a few sensitivity analyses have been performed based on the battery bank autonomy hour. However, in this chapter a new decision variable has been introduced for the PMSs. The value of the new variable (gene) selects the PMS to simulate the IMG. Thus, the approach has simultaneously optimized the sizes and the PMSs of the IMG. For the sake of theoretical analysis, the case studies of this chapter have been conducted based on real-valued decision variables. The MOO

Table 6.1: Multiobjective GA Parameters

Parameter	Value	Parameter	Value
Population Size	60	Selection function	Tournament
Population Type	Double vector	Crossover fraction	0.7
Creation Function	Custom	Crossover function	Intermediate
Max generation	30	Mutation function	Adaptive feasible
Fitness tolerance	10^{-4}	Pareto Fraction	0.35
Creation function	Uniform	Distance measure function	Distance crowding

of this study has aimed to minimize two objective functions (i.e., LCC and LPSP) and maximize one objective function, γ_{re} (i.e., minimize -γ_{re}) upon employing the algorithm of Figure 6.2 and the NSGA-II method. Contrary to a single-objective optimization, the solution of the MOP is not a single point but a set of solutions known as the Pareto optimal solution. Any solution in this set is optimal as no improvement of any solution can be made without worsening at least one of them. The case studies of this chapter have investigated the impacts of the decision variable range on Pareto optimal solutions; subsequently, the impacts on the Pareto front are extended for the DGS lower bounds and for the battery bank autonomy hours. Other than the case study in Subsection 6.6.4, the rest have been conducted considering six hours of battery bank autonomy. The values of LPSP in the result of the case studies have been converted into hours instead of percentages (%). To do so, the yearly LPSP percentage is multiplied by 8760 hours. The parameters for the approach are taken from Table 6.1, which are mostly default values of 'gamultiobj'. The per unit costs and other parameter values are taken from Tables A.2 and A.4 (Appendix A). In this chapter, the base values for P^{w}_{rat}, P^{pv}_{rat}, S^{con}_{rat}, S^{di}_{rat}, and E^{b}_{rat} are 300 kW, 300 kW, 320 kVA, 320 kVA, and 300 kWh, respectively.

6.6.1 Pareto Front and Solution using a Wide Range of Population

Figures 6.4(a), (b), (c), and (d) respectively show the Pareto fronts for the three objective functions, γ_{re} versus LCC, γ_{re} versus LPSP, and LPSP versus LCC for a wide range (bound) of populations, i.e., for a large feasible region. The lower and upper bounds of an individual (i.e., a decision variable vector), in p.u., are taken as [0, 0, 0, 0.25, 0, 0] and [6.0, 4.0, 3.0, 3.0, 12, 2] respectively. This case study has been conducted considering six hours of battery bank autonomy. Figures 6.4(a), (c), and (d) illustrate that the values of LPSP vary from 0 to 8760 hours due to adopting the wide range of decision variable vectors. As shown in Figures 6.4(a) and (d), the LCC decreases from $\$10^7$ to $\$10^6$ while the LPSP reaches from a low value (i.e., zero) to its high value (i.e., 8760 hours). Although the values of LPSP that are shown in Figures 6.4(a) and (d) increase to 8760 hours, the values of LCC remain large due to the selection of the marginal component sizes (especially DGS size) where the configuration consisting of the component sizes cannot supply the full amount of primary load demand at every hours of a year. Figure 6.4(b) indicates that the γ_{re} varies from 20% to around 90%. It can be estimated that the further wide range of populations, especially the large WPS, PVS, and huge BESS sizes, might contribute to increase REP, i.e., γ_{re} to reach 100%. Figure 6.4(b) further demonstrates that the LCC increases with the increase of γ_{re} mainly due to the selection of a large battery bank and RER. Figure 6.4(c) illustrates a Pareto front for γ_{re} and LPSP where the LPSP decreases with the increase of γ_{re} and the phenomenon might not occur if the DGS could be operated at a lower cost. Thus, the analysis of the Pareto fronts indicates that a low value of LCC cannot be achieved at a low value of LPSP and a high value of γ_{re}. Therefore, one objective function cannot be made better without worsening any of the other objective functions. Despite multiple solutions in Pareto front, only one solution is required where the choice of the solution depends on the demand of a user. Thus, the trade-off solutions (i.e., the Pareto optimal set and Pareto front) in numerical values are provided in Table C.5 (Appendix C). Table C.5 indicates that there are a significant number of solutions that have large values of LPSP. The Pareto front solutions that contain too large values of LPSP cannot be the solution of interest for a DM. Thus, a random choice of a wide range of populations not only generates unwanted solutions, but also needs a large CPU time in order to evaluate more meaningful solutions, which can be achieved either by increasing the generation number or by increasing the population size of a generation.

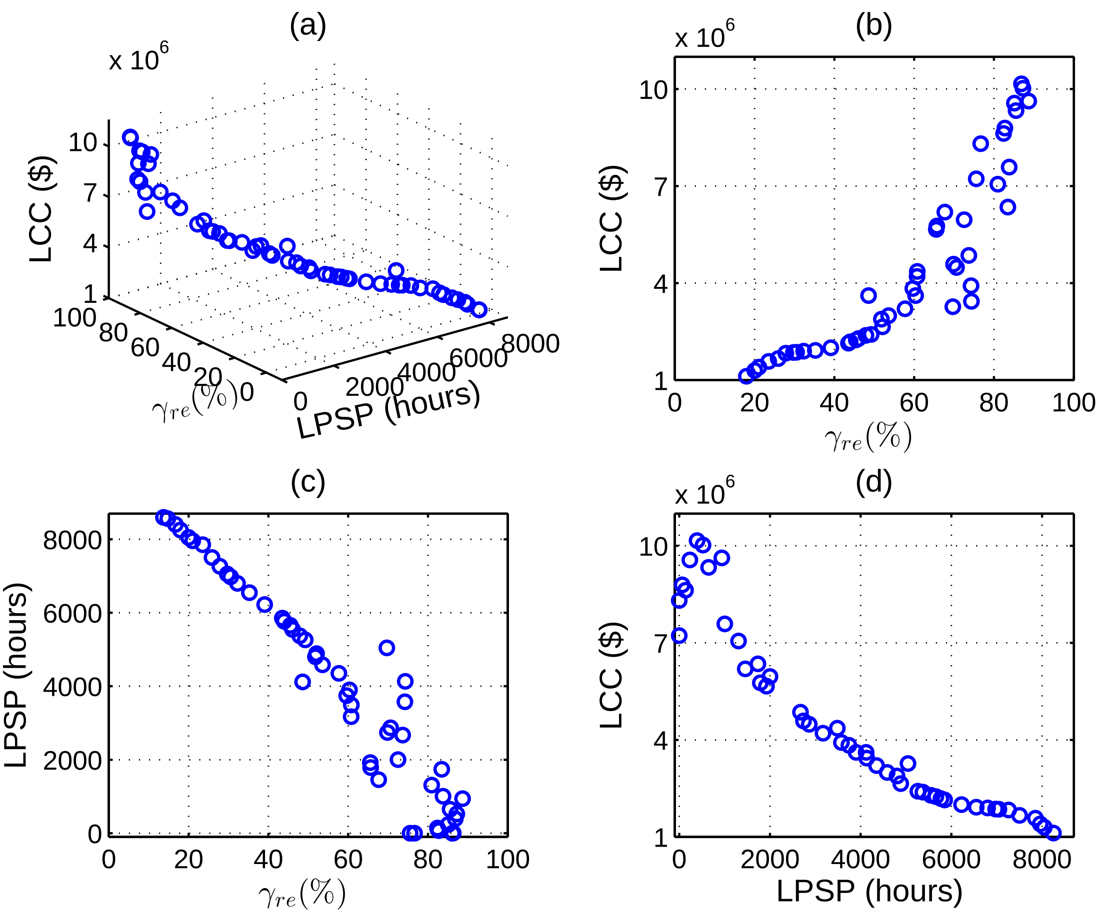

Figure 6.4: Using NSGA-II, Pareto front solutions for (a) three objectives (3D), (b) percentage of REP vs LCC, (c) percentage of REP vs LPSP, and (d) LPSP vs. LCC at wide range of population.

6.6.2 Pareto Front and Solution using a Narrow Range of Population

The Pareto fronts of the case study in Subsection 6.6.1 indicate that the values of LPSP widely vary. The values of LPSP that remain above a couple of hundred hours might not have any practical implication for many IMG. Therefore, this case study is conducted for a narrow range of populations with six hours of battery bank autonomy. Figure 6.5 demonstrates the Pareto fronts, which are produced using a narrow bound of individuals (decision variable vectors) in a population. The lower bound and the upper bound of an individual in p.u. are respectively [0, 0, 0, 1.0, 0, 0] and [3, 1.5, 2, 2, 10, 2], which are the same as that of the case study of Subsection 3.6.1. Figure 6.5(a) represents a Pareto front in a three dimensional space where all

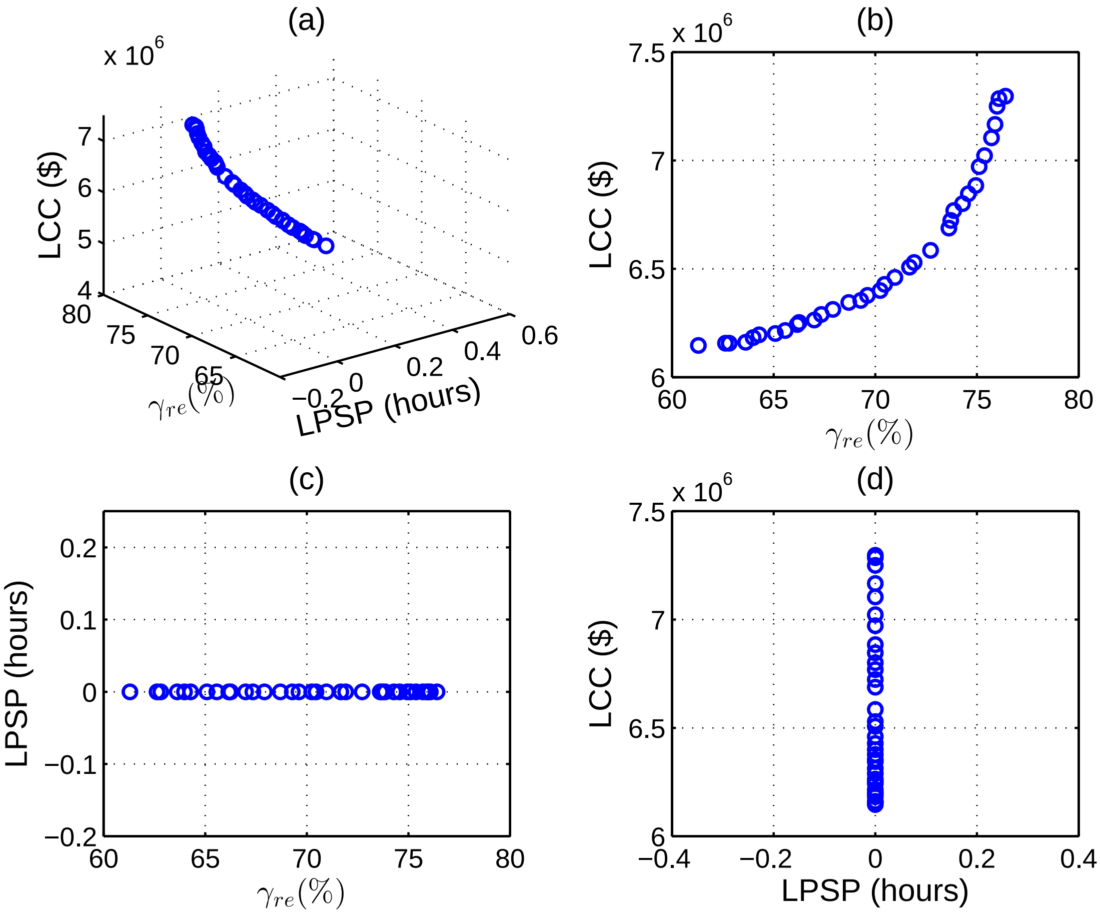

Figure 6.5: Pareto front solutions for (a) three objectives (3D), (b) percentage of REP vs LCC, (c) percentage of REP vs LPSP, and (d) LPSP vs LCC.

three objective functions are utilized. Figures 6.5(b), (c), and (d) respectively signify the two dimensional Pareto fronts, i.e., γ_{re} versus LCC, γ_{re} versus LPSP, and LPSP versus LCC. As can be seen in Figures 6.5(c) and (d), the values of LPSP remain zero while the γ_{re} and LCC vary. The outcome values of LPSP to zero means the reliability of the power supply is ensured in the design while the value of LCC soars with the increase of γ_{re}. Despite the existence of multiple Pareto front solutions, only one solution is required and the choice of the solution depends on DM's requirement. Thus, the trade off solutions (i.e., the Pareto optimal set) for this case study at ensured reliability of power supply are presented in Table C.6 (Appendix C). As the decision variable range of this study is similar to that of case study 3.6.1, the value of LCC at 61% of γ_{re} in Table C.6 is \$6, 146, 122.00, which is close to the minimum value of LCC that is obtained in the case study of Subsection 3.6.1. However, the calculated value of γ_{re} in Subsection 3.6.1 is lower than that of Table C.6 and the lower value of LCC in this case has resulted due to adopting real valued decision variables. It is worthwhile to mention that the consideration of taking the lower bound of DGS as 1.0 p.u., i.e. 320 kVA, drops down the LPSP to zero. There might be some projects where a very high reliability of power supply is not required. Thus, a sensitivity study on LCC and LPSP by the DGS lower bound is required.

6.6.3 Impact of Lower Bounds of DGS Size on Pareto Fronts

The case studies of Subsections 6.6.1 and 6.6.2 have been conducted by putting restriction on the lower bounds of the DGS size as 0.25 p.u. and 1.0 p.u., respectively. The results of the studies have indicated that the lower bounds of the DGS size significantly affect the Pareto optimal fronts. Therefore, a few more case studies have been investigated considering numerous values of lower bounds for the DGS size. Figure 6.6 compares two Pareto fronts that are generated for 0.50 p.u. and 0.65 p.u. of the lower bounds of the DGS size. In Figures 6.6(a) and (d), two Pareto fronts are presented where the values of LCC and LPSP are \$$3e10^6$ and 6000 hours, respectively. If we compare the values of LPSP that is shown in Figure 6.6) with the highest value of Subsection 6.6.1, it is observed that a 0.25 p.u. increase of the lower bound of the DGS size decreases the LPSP value by 2500 hours. Although the Pareto fronts in Figures 6.6(a) and (d) are overlapping with each other, the Pareto front that is generated at the lower bound of the DGS size for 0.65 p.u. provides low LPSP values in the solutions. Therefore, the higher value of the lower bound of DGS size provides more reliable power supply (i.e., low LPSP) system. Figures 6.6(b) and (c) respectively represent the Pareto fronts for γ_{re} versus LCC and γ_{re} versus LPSP where they distinctively distinguish the impacts of the lower bounds of the DGS size on LCC and γ_{re}. Figure 6.6(b) illustrates that the Pareto front, produced at 0.65 p.u. of the lower bound for the DGS, is in the top of the other; it signifies that a high LCC is required to achieve the same REP. Alternately, the aforementioned result implies that the operation of the DGS at some combination of sizes is expensive. Figure 6.6(c) demonstrates two Pareto fronts for γ_{re} versus LPSP, where the Pareto front, produced at 0.65 p.u. of the lower level for the DGS, stays at the bottom of the other. Thus, the solutions of Figure 6.6(c) indicate that the high lower bound of the DGS size promotes power supply reliability, i.e., the value of LPSP decreases. In this comparison, the lower and upper bounds of other individuals than the DGS size, are kept fixed. Like Figure 6.6, Figure 6.7 demonstrates the comparison of the Pareto

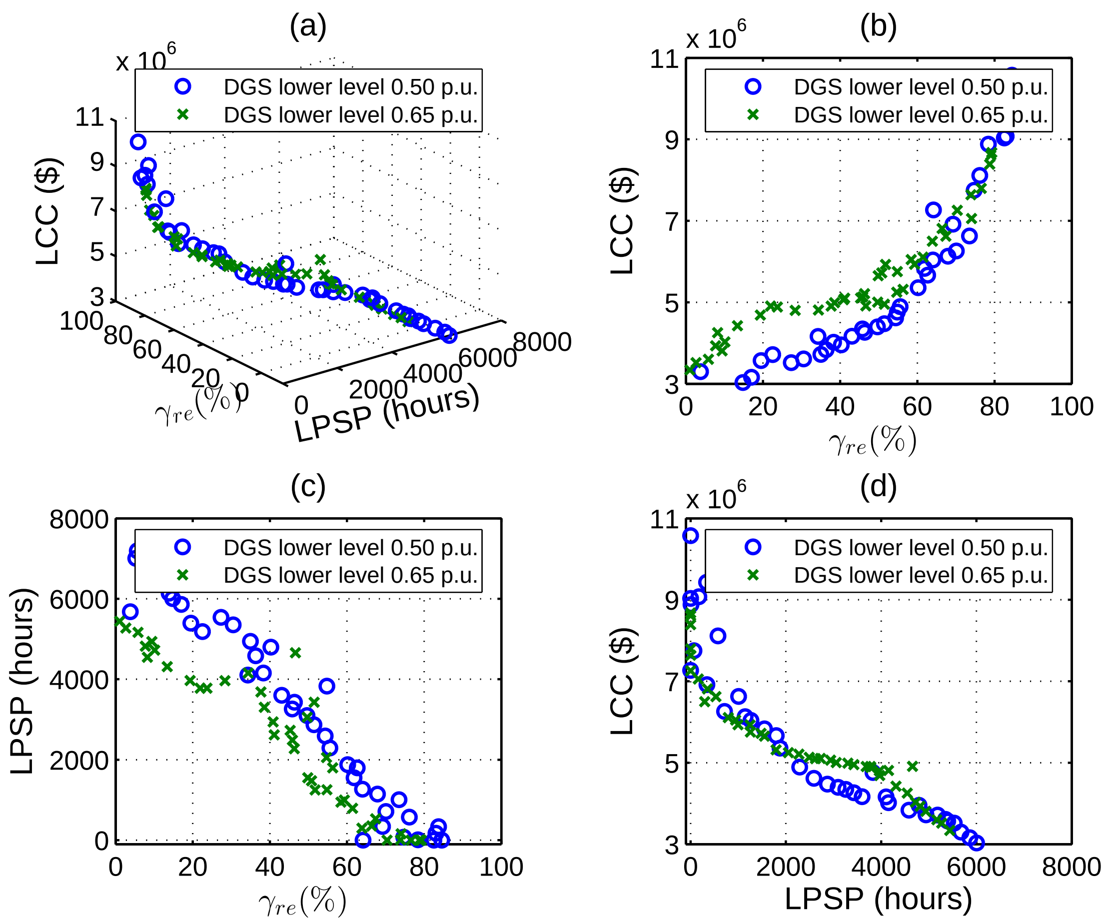

Figure 6.6: DGS lower level impacts on Pareto fronts for (a) three objectives (3D), (b) percentage of REP vs LCC, (c) percentage of REP vs LPSP, and (d) LPSP vs LCC.

fronts that are generated by considering the lower bounds of the DGS as 0.75 p.u. and 0.85 p.u.. As shown in Figure 6.7(a), (c), and (d), the LPSP values are remarkably low in the Pareto front (green curve), which is generated considering the lower bound of the DGS size as 0.85 p.u., though the LPSP values for the 0.75 p.u. lower bound of the DGS are within reasonable values. Again Figure 6.7(c) shows that the increase in the DGS lower bounds increases the reliability (i.e., low LPSP) at the cost of REP. The comparison of Figure 6.6(c) and Figure 6.7(c) further demonstrates that the higher the lower bounds of DGS are, the more reliable the power supply systems are. The numerical values of the Pareto optimal solutions (i.e., Pareto optimal set and Pareto front) for the aforementioned case studies are given in Tables C.7 and C.8 (Appendix C). Considering the values of LPSP in Figure 6.7 and judging the rationality of power supply reliability for remote community applications, a good spread Pareto optimal solution can be generated for the IMG by taking the lower bound of the DGS size, in p.u., within 0.75 to 0.85.

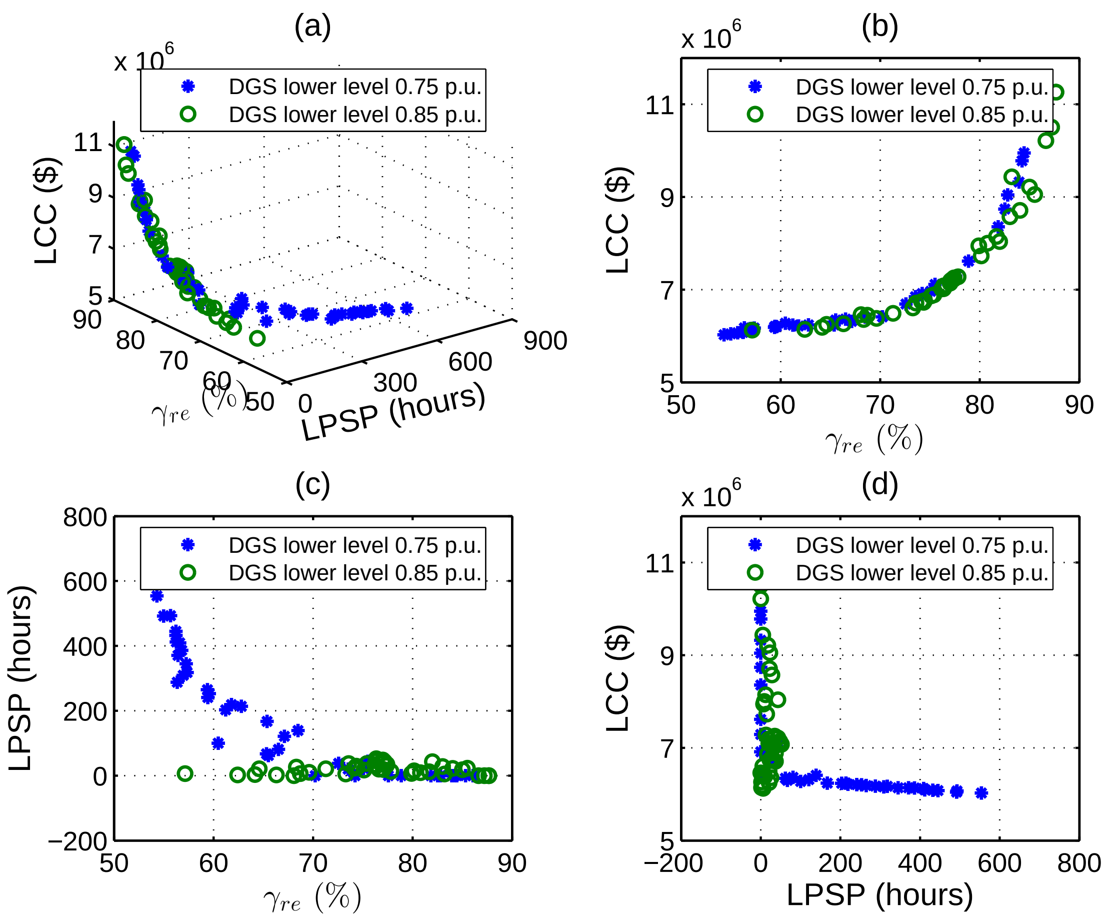

Figure 6.7: DGS lower level impacts on Pareto fronts for (a) three objectives (3D), (b) percentage of REP vs LCC, (c) percentage of REP vs LPSP, and (d) LPSP vs LCC.

6.6.4 Impact of Battery Bank Autonomy Hours on Pareto Fronts

This case study investigates the impacts of battery bank autonomy hours on Pareto fronts. The battery bank autonomy hours are considered 6, 12, 18, and 24 for this case study. The lower and upper bounds of an individual (decision variable vector) in p.u. are taken as [0, 0, 0, 0.9, 0, 0] and [6.0, 4.0, 3.0, 3.0, 12, 2], respectively. Figures 6.8(a), (b), (c), and (d) respectively signify the Pareto fronts of the three objectives, γ_{re} versus LCC, γ_{re} versus LPSP, and LPSP versus LCC with the aforementioned battery bank autonomy hours. Figures 6.8(a) and (b) distinctively demonstrate that the Pareto fronts that are produced based on six hours of battery bank autonomy remain at the lowest level compared to the others. It signifies that the LCCs are minimal in the Pareto fronts. Figures 6.8(a), (b), (c), and (d) further demonstrate that the values of LPSPs in the Pareto fronts, generated based on six hours of battery bank autonomy hour, are near to zero due to the requirement of a small autonomy hour battery bank. Figures 6.8(a) and (b) further illustrate that the LCCs in the Pareto fronts are high for the large hours of battery bank autonomy due to the requirement of a large size battery bank. As shown in Figures 6.8(c) and (d), the LPSPs are high at low γ_{re} for the large hours of battery bank autonomy. The aforementioned situation occurs due to maintaining a small capacity battery bank at large hours of autonomy, i.e., the discharging rate is low. In the above situation, the DGS size is also kept low in order to maintain a low LCC. The marginal sizes of DGS as well as the low discharge (i.e., high hours of battery bank autonomy) rate of battery bank cannot fulfill the net primary load demand in all hours of a year. Therefore, if we request a highly reliable power (i.e., low LPSP) system with large hours of battery bank autonomy, we have to spend more, i.e., the LCC will increase. Although it has been expected that the γ_{re} will be high at large hours of battery bank autonomy, the γ_{re} does not reach a high value because the LCC is kept at a lower limit without increasing the capacity of the battery bank.

6.7 Conclusions

In this chapter, the optimal sizing design of the IMG has been investigated by adopting an MOO approach upon generating Pareto optimal solutions (i.e., the Pareto front and Pareto optimal set) where the NSGA-II technique has been utilized as a prime tool. The proposed MOO approach has simultaneously provided the optimal solutions of the sizes and the PMSs. This approach

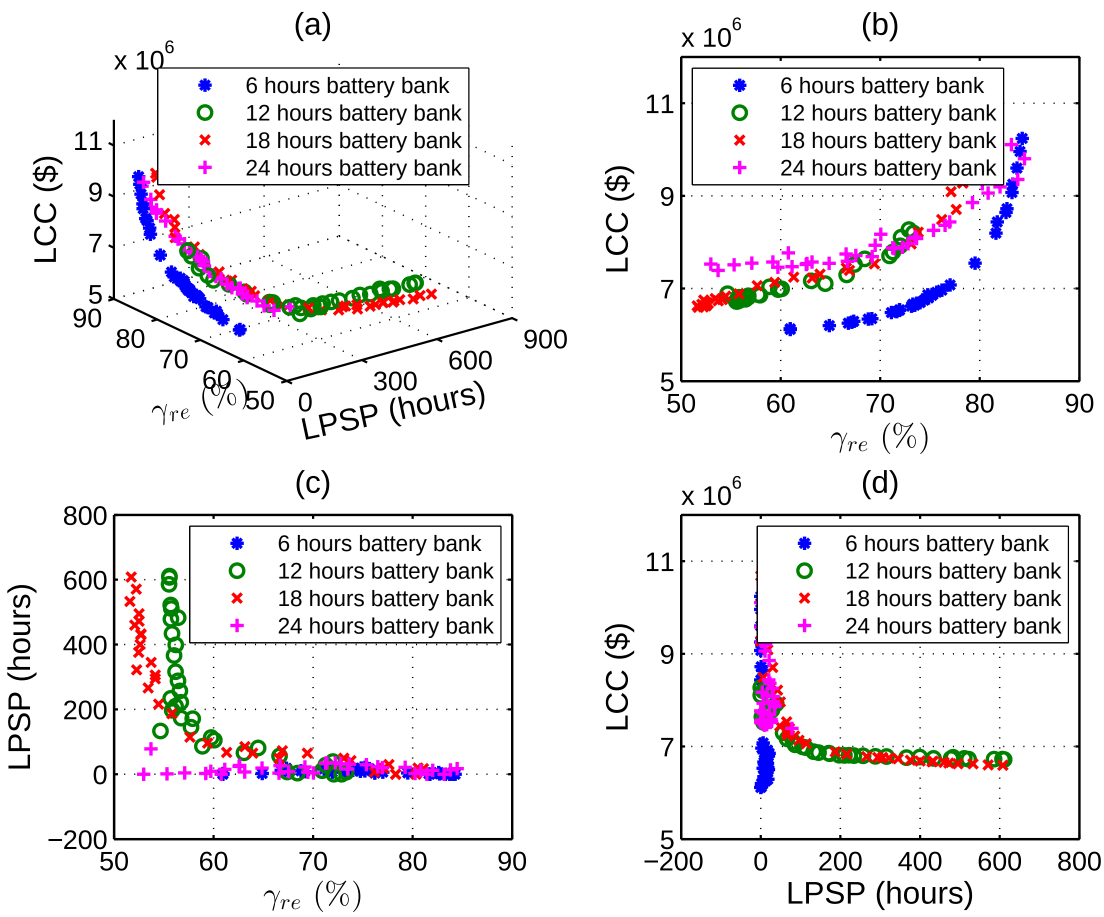

Figure 6.8: Impact of battery bank autonomy hours on Pareto fronts for (a) three objectives (3D), (b) Percentage of REP vs LCC, (c) percentage of REP vs LPSP, and (d) LPSP vs LCC.

fundamentally differs with the other similar types of research on how the PMSs have been optimized, i.e., the way a gene (design variable) for the PMSs has been accommodated in the design. From the designer's and the DM's point of view, the reliability of power supply and LCC have critically been affected by the optimal sizes of the IMG. Thus, the impacts on Pareto fronts by the ranges of population, the lower bound of the DGS size, and the battery bank autonomy hours have been analyzed and then presented the results in this chapter. The studies have demonstrated that a meaningful and a good spread Pareto front points can be achieved with the appropriate choices of the range of decision variable vector. The results also have demonstrated that the surge of LCC occurs with the increase of REP. As such, it can be inferred that it would be too expensive to achieve a 100% REP-based IMG due to the requirement of a very large BESS. The essentiality of the DGS in the IMGs has been emphasized by the case studies, otherwise; a very large BESS has to be added in the configuration to get both a high reliability and a large REP IMG. The betterment of an objective function cannot be done without deteriorating any of the other two objective functions. Considering the aforementioned criteria, Pareto optimal solutions (Pareto front and Pareto optimal set) have been presented in this chapter so that a DM can select a solution from the trade-off set.

Chapter 7

Conclusions and Future Work

7.1 Conclusions

In Canada, remote communities are presently witnessing and expecting an increased number of hybrid power systems (namely RER-based IMGs) in order to cost effectively and reliably fulfill their electricity demands. Around the world and in Canada, random integration of RERs into a remote community microgrid initially assumes benefits, but after a certain time the financial losses and/or reliability of power supply issues force the integration of those RERs to be abandoned. An appropriate design of an IMG is thus a prerequisite for the survival of a project. The RERs are intermittent and have both diurnal and seasonal variations. The design of the IMG under this situation demands chronological simulations to include the dynamic behaviors of the RERs. Power supply reliability, LCCs, environmental factors, and social issues are a few concerns in designing the IMG. Thus, the optimum design of an IMG in connection to sizing depends on many factors and expects to include many objective functions and constraints. The optimal sizing designs are performed in such a way that the approaches can fulfill both technical and economical criteria. The choice of optimal sizing approach is also a trade-off matter and depends on many factors, e.g., the size of a project, customer needs, and social factors etc. Considering the aforementioned issues, this thesis has modified a few PMSs to simulate the IMG and proposed few single and multiobjective optimal sizing approaches based on the chronological simulation. The conclusions of this thesis are listed as follows:

- The long-term simulation of an IMG is required for analyzing the performances. Moreover, the simulation of an IMG is an initial step for the optimization study. Thus, Chapter 2 has shown the modification and flowcharts of four PMSs upon considering primary load real- and reactive-power components. The main contribution of the chapter is the consideration of load reactive power and providing the PV converter on priority to compensate that reactive power when the PV converter is assumed built-in with the PVS. Various simulation studies have been performed under the employment of the modified PMSs, and subsequently the performances of these PMSs have been compared.

- It is essential to figure out a global optimum value of LCC for determining the optimal sizes of the IMG. Thus employing LCC as an objective function, an enumeration-based robust SOO approach has been discussed in Chapter 3. The approach is facilitated to simultaneously optimize the sizes and the PMSs. A few main contributions of the chapter are (1) the incorporation of load reactive power effects on component sizes (e.g., converter size) and on the calculation of LPSPs, (ii) the development of detailed mathematical models for LCC, (iii) the assurance of reaching in a global optimum, (iv) the open access facility of the data, which can be used for further analysis on REP and LPSP, and (v) the inclusion of more decision variables. As wind speed is unpredictable and highly intermittent, a case study has been demonstrated to investigate the sensitivity of the approach on stochastic behavior of wind speed. Although the optimization approach is based on a single objective, a few analyses have been performed to investigate the impacts of REP and LPSP on LCC.

- The CPU time of the optimization process is another important factor for both off-line and on-line optimization. Chapter 4 of this thesis has presented an accelerated SOO approach for both a constrained and an unconstrained objective functions. It has been shown that the proposed approach can accelerate the optimization process, i.e., the CPU timing by more than 80% compared to the traditional approach without significantly deviating the value of LCC. An adaptive penalty parameter scheme has been introduced for handling the constraints of optimization. This chapter has incorporated the sensitivity analysis of LPSP on LCC.

- As real-life engineering problems contain more than one objective function, Chapter 5 of this thesis has discussed a bi-objective optimal sizing approach for the IMG based on the AWS method. The Pareto optimal fronts that have been generated utilizing both the WS and AWS methods are compared. It has been discussed that the AWS method can include more solution points than those of the WS method. Moreover, the AWS method can generate evenly spread solutions in the Pareto optimal front. The use of AWS method for bi-objective optimization of the IMG, in the context of integer variable environment, seems the first attempt. This chapter has also included the sensitivity analysis of LPSP on Pareto fronts.

- Finally, the thesis has discussed an MOO approach in Chapter 6 by employing an elitist NSGA-II technique. The three dimensional Pareto optimal front and the transformed two dimensional Pareto optimal fronts have been presented so that the DMs can make decisions based on the trade-off solutions. The sensitivity studies of the range of decision variable vectors, the DGS lower bounds, and battery bank autonomy hour on Pareto fronts have been presented in this study.

In all of the approaches, the integration of BESS is presented where the energy storage is often cited as a facilitating and essential component for the IMG in order to integrate the stochastic generation. Figure 7.1 illustrates the organization of this thesis and can be used for choosing an approach for optimizing an IMG that can be used in a large off-grid community.

7.2 Future Work

The following points are suggested for future work:

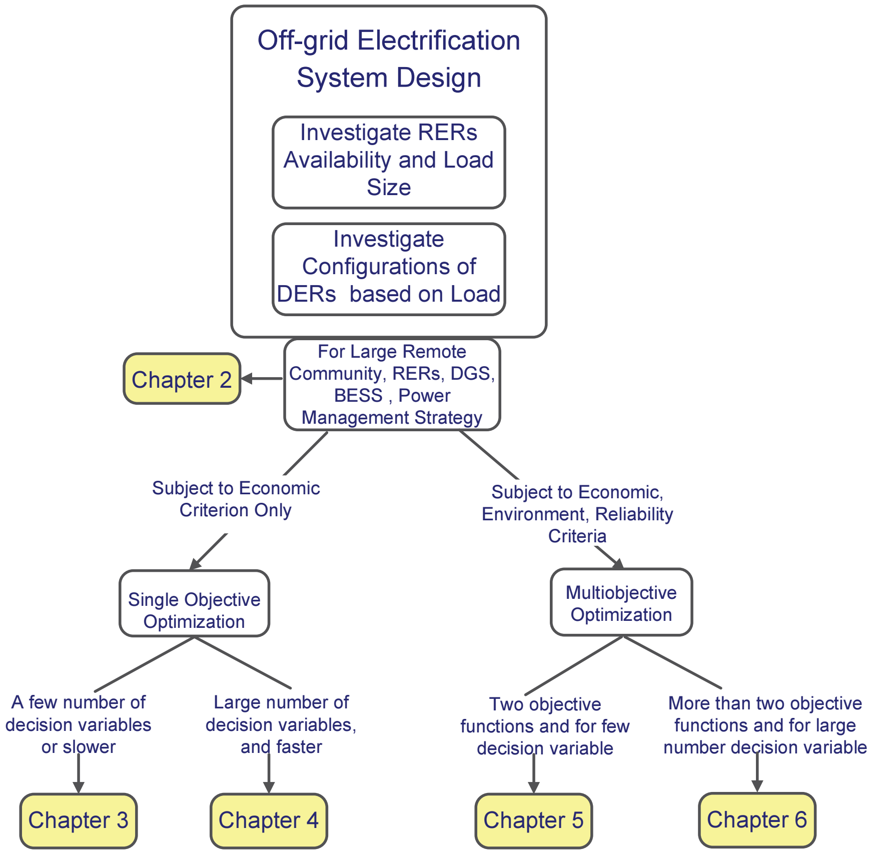

Figure 7.1: Procedure to decide the approach for optimization.

- The development of a procedure/tool for combining the MOO and the multi-criteria decision making (MCDM) so that a DM can make a rational decision that would be supported by the analysis. The MOOs are giving special emphasis only to generating diverse Pareto optimal solutions. Numerous methods [144], e.g., hierarchy process, fuzzy TOPSIS (technique for ordering preference by similarity to ideal solutions), preference ranking organization method for enrichment evaluation (PROMETHEE), and elimination and choice translating reality (ELECTRE) are available for analyzing the Pareto optimal fronts. The appropriate investigation of MCDM on the Pareto optimal front will help to explain the reasons for supporting a particular option. Thus, the work on decision making upon combining MOO and MCDM has yet to be a good research area.

- The development of a user friendly and versatile optimization software program utilizing all the proposed approaches of this thesis. It is envisaged that the software program will have all the capabilities of choosing the optimization types, objective functions, and techniques to perform the optimal sizes of an IMG. More elaborately, the software program will have the flexibility of performing both SOO and MOO utilizing robust and accelerated approaches.

- The extension of the research can be done on the optimal topology of DERs and/or integration of other DERs for the IMG. Nowadays, hydrogen energy storage is gaining popularity as a long-term storage solution and a provider of hydrogen gas used as fuel. Moreover, pumped hydro storage has been used for load leveling in grid connected systems. Thus, the cost effectiveness and environmental benefits of integrating other DERs, e.g., a hydrogen energy storage or pumped hydro storage, in IMG for enhancing REP and thus for eliminating the DGS can be investigated.

- The utilization of the proposed approaches in a pilot/field project. The optimal sizing approaches of this thesis could further be validated by applying them in the project.

- The extension of the research can be done by investigating the impact of high load variations on LCC for the islanded communities.

- Stochastic optimization approaches and stochastic impacts [145], [146] can further be incorporated upon utilizing a stochastic model of RER, especially in the purview of the MOO environment.

Appendix A

Economic and System Parameters for Optimization

Table A.1: Critical Load, P_d, Determination Parameters for PMS-D

Parameter	Values [87, 100, 101, 106]	Comments
g_1	0.00012 L/kW^{2}h	equation (2.8)
g_2	-0.011 L/kWh	equation (2.8)
g_3	0.16 L/kWh	equation (2.8)
P_{rat}^{di}	300 kW	equation (2.8)
Fuel price, c_f	1 $/L	equation (2.9)
C_{mh}^{di}	0.11 $/h for 1 kWh	equation (2.10)
c_c^b/E_{rat}^b	400 $/kWh	equation (2.12)
C_{mh}^b	0.05 $/h for 1 kWh	equation (2.12)
DOD_{eqc}	1100 cycles	equation (2.14)

Table A.2: Simulation Parameters

Simulation Parameters	Values [83, 87, 110]
WPS rating	600 kW
PV power rating	150 kW
Diesel generator rating	320 kVA
Inverter rating	640 kVA
BESS capacity rating	7.2 MWh
BESS power rating	450 kW
Base power	300 kW
Base power factor	0.9
Base BESS discharge time	1 hr
Base BESS capacity	300 kWh
Efficiency of PV system (η_{pv})	15%
Cut-in wind speed	3.5 m/s
Rated wind speed	12 m/s
Cut-out wind speed	23 m/s
Period under observation	8760 hrs
BESS minimum level E_{min}	40%
BESS SOC level E_{soc}	60%
Initial BESS SOC	80% of rated
Self discharge of battery	0.2% per hour
Efficiency of inverter (discharging)	95%
Efficiency of rectifier (charging)	95%

Table A.3: Economic Parameters for System Optimization

Components [1, 5, 83, 87, 110]	Size	Capital Cost (β_c) (\$)	Replacement Cost (β_r) (\$)	O & M Cost (β_{om}) (\$)	Salvage Value (β_s) (\$)	Life Span (Yrs)
WPS	1 kW	2000	1800	$30/yr$	300	20
PVS	1 kW	3500	3000	$10/yr$	400	20
BESS	1 kWh	200	180	$4/yr$	-	5
DGS	1 kVA	600	400	$60/yr$	100	20
Converter	1 kVA	800	700	$10/yr$	-	10
Charge controller	1 kW	100	80	$2.0/yr$	-	10

Table A.4: Data For Simulation

System Parameters	values [83, 87, 110]
Project life, (N_{pl})	20 yrs
Interest rate, (r_2)	10%
Escalation rate, (r_3)	7%
Efficiency of PV system (η_{pv})	15%
Cut-in wind speed, (V_{ci})	3.5 m/s
Rated wind speed, (V_r)	12 m/s
Cut-out wind speed, (V_{co})	23 m/s
Period under observation (N)	8760 hrs
Storage DOD_{max}	60%
Initial BESS SOE	80% of rated
Self discharge of battery (δ)	0.2% per hour
Efficiency of inverter (discharging) (η_d)	95%
Efficiency of rectifier (charging) (η_c)	95%
Diesel fuel price incl. transportation, (c_f)	1.1 $/L
Minimum BESS discharge time (T_c)	6 hrs
Base real power	300 kW
Base power factor	0.9
Base BESS charging/discharging time	1 hr
Base BESS capacity	300 kWh

Appendix B

Terminologies of MOO and Pareto Optimality Theory

B.1 Basic Concepts and Terminology on MOO and Pareto Optimality Theory

In MOP there is no single point solution like in SOO, it is necessary to determine a set of points that all fit a predetermined definition for an optimum. Thus, a solution to MOP is more of a concept than a definition. The basics of MOO and Pareto optimality theory are taken from [73], [131], [147], [148], [149], which are listed below:

B.1.1 Pareto Dominance

Pareto dominance is used to compare and rank the decision variable vector. If all objective functions are for minimization, a feasible solution or a decision variable vector $\mathbf{X} = [x_1, ..., x_n]^T \in \mathcal{R}$ is said to dominate another decision variable vector $\mathbf{Y} = [y_1, ..., y_n]^T \in \mathcal{R}$, which is denoted by $\mathbf{X} \preceq \mathbf{Y}$, if and only if $\mathbf{F}(\mathbf{X})$ is partially less than $\mathbf{F}(\mathbf{Y})$ which is expressed as,

$$\begin{aligned} &\forall\, i \in \{1, ..., n\}\,, F_i(\mathbf{X}) \le F_i(\mathbf{Y}) \\ &\wedge \exists\, j \in \{1, ..., n\} : F_j(\mathbf{X}) < F_j(\mathbf{Y}) \end{aligned} \tag{B.1}$$

Alternately when all objective functions are for maximization, a feasible solution or a decision variable vector $\mathbf{X} = [x_1, ..., x_n]^T \in \mathcal{R}$ is said to dominate another decision variable vector $\mathbf{Y} = [y_1, ..., y_n]^T \in \mathcal{R}$, which is denoted by $\mathbf{X} \ge \mathbf{Y}$, if and only if $\mathbf{F}(\mathbf{X})$ is partially greater than $\mathbf{F}(\mathbf{Y})$ which is expressed as,

$$\begin{aligned} &\forall\, i \in \{1, ..., n\}, F_i(\mathbf{X}) \ge F_i(\mathbf{Y}) \\ &\wedge \exists\, j \in \{1, ..., n\} : F_j(\mathbf{X}) > F_j(\mathbf{Y}) \end{aligned} \tag{B.2}$$

Thus in general, $\mathbf{X}$ dominates $\mathbf{Y}$ in the Pareto sense means that $\mathbf{F}(\mathbf{X})$ is better than $\mathbf{F}(\mathbf{Y})$ (or $\mathbf{F}(\mathbf{X})$ no worse than $\mathbf{F}(\mathbf{Y})$) for all objectives and there is at least one objective function for which $F_i(\mathbf{X})$ is strictly better than $F_i(\mathbf{Y})$.

B.1.2 Pareto Optimality

A solution is said to be Pareto optimal if and only if there does not exist another solution that dominates it, i.e., the solution is not dominated by any other solution in the solution space. Mathematically, a solution $\mathbf{X} \in \mathcal{R}$ is said to be Pareto optimal with respect to $\mathcal{R}$ if and only if there is no $\mathbf{Y} \in \mathcal{R}$ for which $\mathbf{F}(\mathbf{Y}) = [F_1(\mathbf{Y}), ..., F_k(\mathbf{Y})]^T$ dominates $\mathbf{F}(\mathbf{X}) = [F_1(\mathbf{X}), ..., F_k(\mathbf{X})]^T$, e.g., in a maximization context $\mathbf{F}(\mathbf{Y}) \ge \mathbf{F}(\mathbf{X})$ for all, and $F_i(\mathbf{Y}) > F_i(\mathbf{X})$ for at least one. A solution belongs to the Pareto set if there is no other solution that can improve at least one of the objectives without degradation any other objective. The corresponding objective vector is called a *Pareto dominant vector*, or *non-dominated vector*. All Pareto optimal points in a Pareto dominant vector lie on the boundary of the feasible objective space.

B.1.3 Weakly Pareto Optimality

A point, $\mathbf{X} \in \mathcal{R}$, is weakly Pareto optimal iff there does not exist another point, $\mathbf{Y} \in \mathcal{R}$, such that $\mathbf{F}(\mathbf{Y}) < \mathbf{F}(\mathbf{X})$. In other words, a point is weakly Pareto optimal if there is no other point that improves all of the objective functions simultaneously. All Pareto optimal points are weakly Pareto optimal, but all weakly Pareto optimal points are not Pareto optimal.

B.1.4 Properly Pareto Optimal

A point, $\mathbf{X} \in \mathcal{R}$, is properly Pareto optimal if it is Pareto optimal and there is some real number $M > 0$ such that for each $F_i(\mathbf{Y})$ and each $\mathbf{Y} \in \mathcal{R}$ satisfying $F_i(\mathbf{Y}) < F_i(\mathbf{X})$, there exists at least one $F_j(\mathbf{Y})$ such that $F_j(\mathbf{X}) < F_j(\mathbf{Y})$ and $\frac{F_i(\mathbf{X}) - F_i(\mathbf{Y})}{F_j(\mathbf{Y}) - F_j(\mathbf{X})} \leq M$

B.1.5 Pareto Optimal Set

The set of all feasible non-dominated solutions in $\mathcal{R}$ is referred to as the Pareto optimal set. For a given multiobjective problem (MOP), $\mathbf{F}(\mathbf{x})$, the Pareto optimal set, $\mathcal{P}^*$, is defined as:

$$\mathcal{P}^* := \{\mathbf{X} \in \mathcal{R} \mid \neg \, \exists \, \mathbf{Y} \in \mathcal{R} \, \mathbf{F}(\mathbf{Y}) \preceq \mathbf{F}(\mathbf{X})\}$$

Pareto optimal solutions are those solutions within the decision space whose corresponding objective vector components cannot be all simultaneously improved. These solutions are also termed *non-inferior*, or *admissible*, or *efficient* solutions, within the entire set named as Pareto set (shown in Figure B.1) which is represented by $\mathcal{P}^*$. Their corresponding objective vectors are termed *non-dominated*; selecting a vector(s) from the vector set (the Pareto front set $\mathcal{PF}^*$), shown in Figure B.1, implicitly indicates acceptable Pareto optimal solutions or decision variables.

B.1.6 Pareto Front

It is also called Pareto optimal front. For a given MOP, $\mathbf{F}(\mathbf{x})$, and Pareto optimal set, $\mathcal{P}^*$, the Pareto front (shown in Figure B.1) is defined as:

$$\mathcal{PF}^* := \{\mathbf{f} = \mathbf{F}(\mathbf{X}) \mid \mathbf{X} \in \mathcal{P}^*\}$$

When plotted in objective space, the non-dominated vectors are collectively known as Pareto front. Again, $\mathcal{P}^*$ is a subset of some solution set. Its evaluated objective vectors form $\mathcal{PF}^*$, of which each is non-dominated with respect to all objective vectors produced by evaluating every possible solution in $\mathcal{R}$.

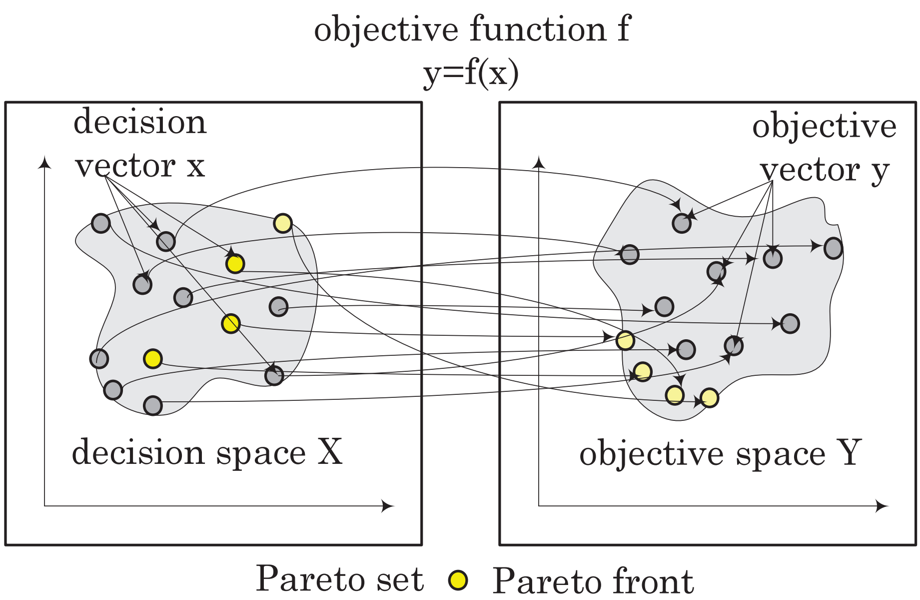

Figure B.1: Relation between decision space and objective space

B.1.7 Feasible Region/ Feasible Set

The region over which the optimization is to be performed. It is a subset of the n-dimensional space. Feasible region is also called decision space or search space. The feasible set $\mathbf{X}_f$ is defined as the set of decision vectors **X** that satisfy the constraints $g(\mathbf{X})$:

$$\mathbf{X}_f = \{\mathbf{X} \in \mathcal{R} | g(\mathbf{X}) \leq 0\}$$

B.1.8 Objective Space/ Feasible Criterion Space

The image of $\mathbf{X}_f$, i.e., the feasible region in the objective space, is denoted as $\mathbf{Y}_f = f(\mathbf{X}_f) = \cup_{\mathbf{X} \in \mathbf{X}_f} \{f(\mathbf{X})\}$

Appendix C

Numerical Results-Long Tables

Table C.1: Coefficient of Variation for Fifteen Realization

P^{w}_{rat} (kW)	P^{pv}_{rat} (kW)	S^{di}_{rat} (kVA)	E^{b}_{rat} (kWh)	S^{con}_{rat} (kVA)	P^{b}_{rat} (kW)	LCC ($)
750	0	400	1800	320	300	5422068.3
750	0	400	1800	320	300	5444637.5
750	0	400	1800	320	300	5404287.1
750	0	400	1800	320	300	5347300.2
750	0	400	1800	320	300	5377818.1
750	0	400	1800	320	300	5485004.7
750	0	400	1800	320	300	5488850.7
750	0	400	1800	320	300	5443199.6
750	0	400	1800	320	300	5423494.9
750	0	400	1800	320	300	5406147.8
750	0	400	1800	320	300	5492351.7
750	0	400	1800	320	300	5391799.9
750	0	400	1800	320	300	5429918.0
750	0	400	1800	320	300	5455259.2
750	0	400	1800	320	300	5399858.6
			Coefficient of variations = 0.0077			

Table C.2: Pareto Optimal Set and Pareto Front for Both WS and AWS Methods at Six Hours of Battery Autonomy

P_{rat}^{w}	P_{rat}^{pv}	S_{rat}^{di}	E_{rat}^{b}	P_{rat}^{b}	S_{rat}^{con}	LPSP	LCC	γ_{re}	PMS
(kW)	(kW)	(kVA)	(kWh)	(kW)	(kVA)		($)	(%)	
Pareto (set and front) solutions by WS method									
450	150	400	1200	200	320	0	6205653.29	54.70	PMS-B
900	450	400	1200	200	320	0	7048015.85	75.62	PMS-B
900	450	400	3000	500	640	0	9237692.50	83.17	PMS-A
Pareto (set and front) solutions by AWS method									
450	150	400	1200	200	320	0	6205653.29	54.70	PMS-B
600	150	400	1200	200	320	0	6238747.91	59.97	PMS-B
450	300	400	1200	200	320	0	6311286.82	61.86	PMS-B
750	150	400	1200	200	320	0	6354271.45	63.92	PMS-B
600	300	400	1200	200	320	0	6381527.96	66.38	PMS-B
750	300	400	1200	200	320	0	6534827.29	69.70	PMS-B
600	450	400	1200	200	320	0	6641968.81	70.77	PMS-B
900	300	400	1200	200	320	0	6750843.97	71.86	PMS-B
900	300	480	1200	200	320	0	6812117.54	71.98	PMS-B
750	450	400	1200	200	320	0	6829919.34	73.52	PMS-B
900	450	400	1200	200	320	0	7048015.85	75.62	PMS-B
900	450	400	1800	300	320	0	7352752.91	77.16	PMS-B
900	450	400	2400	400	320	0	7702732.27	79.52	PMS-B
900	450	400	3000	500	320	0	8074581.57	81.44	PMS-B
900	450	400	3000	500	320	0	8778119.27	83.04	PMS-A
900	450	400	3000	500	480	0	9001319.56	83.17	PMS-A
900	450	400	3000	500	640	0	9237692.50	83.17	PMS-A

Table C.3: Pareto Optimal Optimal Set and Pareto Front for Both WS and AWS Methods at Twelve Hours of Battery Autonomy

P^{w}_{rat}	P^{pv}_{rat}	S^{di}_{rat}	E^{b}_{rat}	P^{b}_{rat}	S^{con}_{rat}	LPSP	LCC	γ_{re}	PMS
(kW)	(kW)	(kVA)	(kWh)	(kW)	(kVA)		($)	(%)	
Pareto (set and front) solutions by WS method									
450	150	400	1800	150	160	0	6694459.28	55.14	PMS-B
750	450	400	2400	200	320	0	7382179.55	77.40	PMS-B
900	450	400	3000	250	320	0	8660596.86	82.69	PMS-A
Pareto (set and front) solutions by AWS method									
450	150	400	1800	150	160	0	6694459.28	55.14	PMS-B
450	300	400	1800	150	160	0	6710742.89	62.48	PMS-B
600	300	400	1800	150	160	0	6772381.80	66.89	PMS-B
600	450	400	1800	150	160	0	7008835.97	71.58	PMS-B
750	450	400	1800	150	160	0	7195703.81	74.01	PMS-B
600	450	400	2400	200	320	0	7223521.82	74.28	PMS-B
900	300	400	2400	200	320	0	7363121.17	74.80	PMS-B
750	450	400	2400	200	320	0	7382179.55	77.40	PMS-B
900	450	400	2400	200	320	0	7627358.56	79.30	PMS-B
900	450	400	3000	250	320	0	7939005.95	81.05	PMS-B
900	450	480	3000	250	320	0	7979186.27	81.15	PMS-B
900	450	400	3000	250	320	0	8660596.86	82.69	PMS-A

Table C.4: Pareto Optimal Set and Pareto Front for Both WS and AWS Methods at Twelve Hours of Battery Autonomy and Small Weighting Step Size in WS

P^{w}_{rat}	P^{pv}_{rat}	S^{di}_{rat}	E^{b}_{rat}	P^{b}_{rat}	S^{con}_{rat}	LPSP	LCC	γ_{re}	PMS
(kW)	(kW)	(kVA)	(kWh)	(kW)	(kVA)		(\$)	(%)	
Pareto (set and front) solutions by WS method									
450	150	400	1800	150	160	0	6693788.58	55.14	PMS-B
600	300	400	1800	150	160	0	6772381.77	66.89	PMS-B
750	450	400	2400	200	320	0	7382179.55	77.40	PMS-B
900	450	400	3000	250	320	0	7939005.95	81.05	PMS-B
900	450	400	3000	250	320	0	8660596.86	82.69	PMS-A
Pareto (set and front) solutions by AWS method									
450	150	400	1800	150	160	0	6693788.58	55.14	PMS-B
450	300	400	1800	150	160	0	6710762.07	62.48	PMS-B
600	300	400	1800	150	160	0	6772381.77	66.89	PMS-B
750	300	400	1800	150	160	0	6918507.68	69.96	PMS-B
600	450	400	1800	150	160	0	7008853.31	71.58	PMS-B
750	450	400	1800	150	160	0	7195717.89	74.01	PMS-B
600	450	400	2400	200	320	0	7223521.82	74.28	PMS-B
900	300	400	2400	200	320	0	7363121.17	74.80	PMS-B
750	450	400	2400	200	320	0	7382179.55	77.40	PMS-B
900	450	400	2400	200	320	0	7627358.56	79.30	PMS-B
750	450	400	3000	250	320	0	7683054.29	79.35	PMS-B
900	450	400	3000	250	320	0	7939005.95	81.05	PMS-B
900	450	400	3000	250	320	0	8660596.86	82.69	PMS-A

Table C.5: Pareto Optimal Solutions (i.e., the Pareto Optimal Set and Pareto Front) at Wide Range of Population

γ_{re} (%)	LCC ($)	$LPSP$	P^{w}_{rat} (kW)	P^{pv}_{rat} (kW)	S^{con}_{rat} (kVA)	S^{di}_{rat} (kVA)	E^{b}_{rat} (kWh)	PMS
76	7223113	0	737	565	393	411	1305	1.42
9	580265	8760	32	67	70	90	71	0.57
62	580330	8760	32	67	70	90	71	1.07
52	2644777	4886	535	52	106	93	250	0.40
17	989279	8402	89	60	78	90	78	0.55
28	1831874	7264	174	53	85	93	79	0.39
46	2283614	5547	416	46	91	92	80	0.33
30	1855409	7051	193	45	87	93	80	0.36
81	7058733	1309	747	735	286	139	926	1.03
32	1894905	6801	216	46	88	92	49	0.36
31	1857708	6977	200	46	87	92	73	0.36
84	7586804	1007	1181	628	320	146	1025	1.03
87	10026591	524	1346	1166	458	160	1259	1.36
46	2245582	5658	393	56	79	91	78	0.41
15	855480	8562	73	64	91	91	70	0.55
35	1919679	6549	245	49	86	91	25	0.37
49	2413002	5261	491	46	91	92	80	0.33
89	9626345	940	1372	1093	528	128	1143	1.35
60	3613739	3901	598	203	81	103	142	0.42
71	4482121	2868	633	196	77	135	254	1.15
60	3829781	3742	811	47	100	106	438	0.60
82	8629788	141	1284	642	506	230	1273	1.35
44	2138828	5852	368	46	89	92	57	0.34
9	567933	8760	34	60	71	90	76	0.96
21	1401085	7960	123	54	81	91	79	0.47
18	1115128	8252	100	54	75	91	80	0.59
49	3610818	4120	462	38	152	133	392	0.76
24	1575063	7854	116	103	45	90	74	0.76
48	2382854	5374	454	49	90	92	80	0.37
77	8312871	0	792	927	204	396	1125	0.61
61	4360641	3488	596	196	258	109	325	0.99
86	9336937	650	1145	1131	367	157	1079	1.24
58	3203546	4352	577	146	52	92	154	0.76
20	1297658	8051	115	55	77	91	61	0.51
14	762161	8594	72	51	76	90	79	0.94
26	1666007	7505	158	55	78	91	5	0.45
86	11164439	2	1661	1177	622	320	1340	1.14
74	3919076	3576	645	119	126	110	536	1.13
39	2000109	6225	291	49	87	91	80	0.44
74	3434934	4133	539	165	72	102	182	1.12
85	9566143	236	1478	933	364	198	1083	1.09
66	5761775	1787	804	212	208	157	473	0.64
66	5662266	1922	864	172	210	152	567	0.92
52	2880934	4801	483	89	98	99	129	0.82
70	4585182	2739	614	196	78	138	356	1.14
44	2183981	5769	367	53	87	92	74	0.36
83	8795988	68	1221	772	443	252	1289	1.40
74	4856773	2673	747	194	220	129	473	1.11
73	5958177	2003	888	417	245	125	446	0.98
54	2994646	4585	527	93	86	102	128	0.60
83	6348529	1737	887	609	162	115	748	1.05
70	3266363	5043	320	123	123	98	769	1.10
68	6196658	1458	816	212	230	152	1185	0.85
87	10165404	393	1346	1175	463	170	1269	1.48
86	11124983	0	1661	1177	582	400	1340	1.14
61	4204427	3172	598	212	41	133	157	0.42

Table C.6: Pareto Optimal Solutions (i.e., the Pareto Optimal Set and Pareto Front) at Narrow Range of Population

γ_{re} (%)	LCC ($)	$LPSP$	P^{w}_{rat} (kW)	P^{pv}_{rat} (kW)	S^{con}_{rat} (kVA)	S^{di}_{rat} (kVA)	E^{b}_{rat} (kWh)	PMS
64	6161131	0	518	290	205	416	1114	PMS-B
66	6215447	0	581	297	204	416	1114	PMS-B
74	6769044	0	864	403	212	446	1097	PMS-B
72	6528900	0	767	370	210	432	1131	PMS-B
69	6344586	0	691	314	207	423	1123	PMS-B
69	6354493	0	671	343	205	422	1128	PMS-B
71	6459990	0	741	352	210	425	1122	PMS-B
70	6377412	0	696	334	208	426	1134	PMS-B
75	6972094	0	869	422	238	499	1398	PMS-B
73	6585678	0	764	403	211	431	1122	PMS-B
63	6156148	0	485	289	212	419	1121	PMS-B
66	6252421	0	588	312	204	421	1118	PMS-B
76	7250297	0	870	433	379	469	1608	PMS-B
75	7022801	0	870	426	242	547	1395	PMS-B
67	6263537	0	623	306	206	418	1129	PMS-B
70	6428408	0	758	324	212	429	1128	PMS-B
74	6723535	0	802	427	219	432	1189	PMS-B
75	6846635	0	866	410	233	455	1314	PMS-B
74	6801231	0	856	425	218	434	1136	PMS-B
75	6884729	0	855	427	242	464	1327	PMS-B
76	7286024	0	870	432	372	546	1592	PMS-B
66	6242642	0	585	311	204	420	1117	PMS-B
76	7297223	0	869	433	298	610	1675	PMS-B
65	6200997	0	581	284	206	417	1125	PMS-B
64	6195268	0	548	287	206	420	1119	PMS-B
76	7166416	0	870	428	371	477	1516	PMS-B
64	6182372	0	524	296	205	419	1114	PMS-B
74	6687801	0	815	415	210	431	1120	PMS-B
61	6146122	0	446	293	205	418	1117	PMS-B
63	6156318	0	491	291	205	419	1117	PMS-B
76	7104221	0	860	425	336	469	1540	PMS-B
67	6289607	0	626	314	211	429	1127	PMS-B
68	6313041	0	656	312	206	422	1119	PMS-B
72	6507439	0	766	359	209	430	1130	PMS-B
70	6399767	0	725	321	212	421	1240	PMS-B

Table C.7: Numerical Results for the Impact on Pareto Front for DGS Lower Level at 0.50 p.u. and 0.65 p.u.

DGS 0.5 *p.u.*									DGS 0.65 *p.u.*								
γ_{re}	LCC	$LPSP$	P^{w}_{rat}	P^{pv}_{rat}	S^{con}_{rat}	S^{di}_{rat}	E^{b}_{rat}	PMS	γ_{re}	LCC	$LPSP$	P^{w}_{rat}	P^{pv}_{rat}	S^{con}_{rat}	S^{di}_{rat}	E^{b}_{rat}	PMS
(%)	($)		(p.u.)	(p.u.)	(p.u.)	(p.u.)	(p.u.)	*	(%)	($)		(p.u.)	(p.u.)	(p.u.)	(p.u.)	(p.u.)	*
64.2	7.27E+06	0.0	2.2	0.9	0.9	1.1	1.4	1.3	23.7	4.88E+06	3779.0	0.6	0.0	0.0	0.7	0.2	0.8
3.8	3.29E+06	5676.0	0.1	0.0	0.2	0.6	0.5	0.5	9.4	3.81E+06	4936.0	0.2	0.0	0.1	0.7	0.2	0.9
5.2	2.19E+06	7005.0	0.1	0.1	0.3	0.5	0.5	0.5	49.7	5.00E+06	3056.0	1.3	0.0	0.3	0.7	0.3	1.0
22.5	3.72E+06	5186.0	0.5	0.1	0.2	0.5	0.3	0.3	5.8	3.60E+06	5168.0	0.1	0.0	0.1	0.7	0.2	0.9
5.6	1.96E+06	7192.0	0.1	0.1	0.2	0.5	0.4	0.4	79.0	8.61E+06	0.0	4.5	2.1	0.7	1.6	2.6	1.1
10.1	2.59E+06	6493.0	0.2	0.1	0.2	0.5	0.3	0.3	51.5	4.95E+06	3427.0	1.4	0.0	0.3	0.7	0.3	1.0
30.5	3.61E+06	5350.0	0.7	0.1	0.1	0.5	0.2	0.2	45.8	5.13E+06	2489.0	1.6	0.0	0.4	0.7	0.3	0.8
46.4	4.26E+06	3427.0	1.4	0.1	0.3	0.5	0.7	0.3	10.1	4.03E+06	4722.0	0.2	0.0	0.1	0.7	0.3	0.7
54.4	4.62E+06	2589.0	2.1	0.2	0.4	0.5	0.5	0.4	67.4	6.62E+06	531.0	2.4	1.0	0.4	0.7	1.0	1.0
84.6	1.06E+07	0.0	3.6	3.3	3.0	1.4	4.2	0.4	78.7	8.39E+06	0.0	4.5	2.0	0.7	1.4	2.5	1.1
36.3	3.84E+06	4583.0	0.9	0.1	0.2	0.5	0.3	0.8	34.4	4.81E+06	4153.0	0.9	0.0	0.1	0.7	0.3	1.0
14.8	3.03E+06	6004.0	0.3	0.1	0.2	0.5	0.2	0.3	76.6	7.79E+06	0.0	3.8	1.7	0.6	1.3	2.5	1.1
55.6	4.89E+06	2290.0	2.2	0.2	0.4	0.6	1.0	0.3	58.4	6.05E+06	945.0	2.2	0.2	0.4	0.7	1.3	1.0
27.3	3.52E+06	5536.0	0.6	0.1	0.1	0.5	0.4	0.4	61.4	6.11E+06	792.0	2.3	0.4	0.4	0.7	1.8	1.0
73.5	6.63E+06	1008.0	1.9	1.9	0.5	0.6	2.5	0.3	37.7	4.91E+06	3686.0	1.1	0.0	0.2	0.7	0.2	0.9
74.7	7.75E+06	73.0	2.7	1.6	0.9	0.9	2.4	0.4	54.7	5.25E+06	2052.0	1.8	0.0	0.4	0.7	0.3	1.1
83.8	9.43E+06	336.0	3.3	3.1	2.5	0.7	3.6	0.4	8.2	4.26E+06	4546.0	0.2	0.0	0.3	0.7	0.2	0.9
60.2	5.36E+06	1877.0	2.0	0.3	0.5	0.6	0.5	1.0	45.3	5.11E+06	2728.0	1.5	0.0	0.3	0.7	0.2	0.8
76.2	8.11E+06	573.0	3.2	3.0	0.4	0.6	0.4	0.4	40.9	5.06E+06	2938.0	1.2	0.0	0.3	0.7	0.3	0.8
69.2	6.92E+06	342.0	2.3	1.4	0.5	0.7	2.4	0.6	63.9	6.50E+06	297.0	2.2	0.8	0.4	0.8	1.9	1.0
19.5	3.57E+06	5396.0	0.4	0.0	0.2	0.5	0.3	0.6	13.4	4.42E+06	4313.0	0.3	0.0	0.2	0.7	0.3	1.0
17.0	3.16E+06	5862.0	0.4	0.1	0.2	0.5	0.3	0.4	19.3	4.69E+06	3968.0	0.5	0.0	0.1	0.7	0.2	0.9
61.8	5.83E+06	1551.0	2.4	0.6	0.5	0.6	0.7	0.6	56.3	5.32E+06	1796.0	1.9	0.0	0.4	0.7	1.8	1.0
51.5	4.47E+06	2871.0	1.9	0.1	0.4	0.5	0.6	0.5	46.3	5.21E+06	2274.0	1.6	0.0	0.4	0.7	0.3	0.8
40.3	3.96E+06	4797.0	1.1	0.1	0.2	0.5	0.6	0.3	49.8	5.65E+06	1552.0	1.7	0.2	0.4	0.7	0.2	0.9
49.7	4.39E+06	3097.0	1.6	0.2	0.2	0.5	0.4	0.4	51.7	5.93E+06	1249.0	1.6	0.2	0.4	0.7	1.0	1.0
83.1	9.07E+06	172.0	3.3	2.5	2.5	0.8	4.1	0.4	59.3	5.93E+06	997.0	2.1	0.3	0.4	0.7	1.8	1.1
43.1	4.17E+06	3601.0	1.2	0.1	0.3	0.5	0.8	0.4	50.8	5.72E+06	1478.0	1.8	0.2	0.4	0.7	0.3	0.8
70.1	6.26E+06	711.0	2.4	1.1	0.4	0.6	2.2	1.3	1.1	3.34E+06	5441.0	0.0	0.0	0.1	0.7	0.2	0.7
78.4	8.88E+06	10.0	2.9	2.5	1.7	1.0	2.6	0.4	38.6	4.99E+06	3302.0	1.1	0.0	0.3	0.7	0.3	1.0
62.7	5.67E+06	1798.0	1.7	1.1	0.5	0.5	1.0	0.5	79.3	8.68E+06	0.0	4.6	2.1	0.7	1.6	2.6	1.1
35.0	3.72E+06	4942.0	0.9	0.1	0.2	0.5	0.2	0.4	70.4	7.26E+06	0.0	3.3	1.0	0.6	1.3	2.0	1.1
13.9	2.94E+06	6137.0	0.3	0.1	0.2	0.5	0.4	0.4	73.9	7.64E+06	6.0	3.5	1.6	0.5	1.0	2.0	1.0
67.9	6.13E+06	1144.0	2.2	1.2	0.3	0.6	1.3	0.4	28.3	4.80E+06	3962.0	0.7	0.0	0.1	0.7	0.2	1.0
45.8	4.35E+06	3259.0	1.4	0.1	0.3	0.5	0.4	0.5	2.6	3.52E+06	5271.0	0.1	0.0	0.1	0.7	0.2	0.7
34.3	4.16E+06	4103.0	0.8	0.1	0.3	0.5	0.5	0.3	41.2	5.10E+06	2620.0	1.2	0.0	0.4	0.7	0.3	1.0
7.5	2.37E+06	6781.0	0.1	0.1	0.2	0.5	0.5	0.4	7.7	3.93E+06	4821.0	0.2	0.0	0.1	0.7	0.2	0.8
64.0	6.04E+06	1267.0	2.6	0.6	0.5	0.6	1.8	0.6	74.0	7.05E+06	160.0	3.4	1.3	0.6	0.8	2.4	1.0
82.5	9.03E+06	0.0	3.0	2.8	1.2	1.2	4.2	0.3	46.6	4.91E+06	4657.0	1.6	0.0	0.1	0.7	0.2	0.9
11.3	2.71E+06	6375.0	0.2	0.1	0.2	0.5	0.4	0.4	22.0	4.91E+06	3777.0	0.5	0.0	0.1	0.7	0.3	0.8
38.3	4.02E+06	4155.0	1.0	0.1	0.2	0.5	0.5	0.4	54.8	5.75E+06	1255.0	2.0	0.0	0.4	0.7	1.9	1.1
54.8	4.76E+06	3827.0	2.2	0.2	0.1	0.6	1.0	0.3	66.4	6.81E+06	354.0	2.3	1.0	0.5	0.8	1.0	1.1

* For (PMS column value ≥ 0 and < 0.5), then PMS-A
For (PMS column value ≥ 0.5 and < 1.0), then PMS-C
For (PMS column value ≥ 1 and < 1.5), then PMS-B
For (PMS column value ≥ 1.5 and ≤ 2.0), then PMS-D

Table C.8: Numerical Results for the Impact on Pareto Front with DGS Lower Level at 0.75 p.u. and 0.85 p.u.

DGS 0.75 *p.u.*									DGS 0.85 *p.u.*								
γ_{re}	LCC	$LPSP$	P^{w}_{rat}	P^{pv}_{rat}	S^{con}_{rat}	S^{di}_{rat}	E^{b}_{rat}	PMS	γ_{re}	LCC	$LPSP$	P^{w}_{rat}	P^{pv}_{rat}	S^{con}_{rat}	S^{di}_{rat}	E^{b}_{rat}	PMS
(%)	($)		(*p.u.*)	(*p.u.*)	(*p.u.*)	(*p.u.*)	(*p.u.*)	*	(%)	($)		(*p.u.*)	(*p.u.*)	(*p.u.*)	(*p.u.*)	(*p.u.*)	*
74.2	6.91E+06	0.0	3.1	1.4	0.5	1.1	3.1	1.2	68.1	6.46E+06	0.0	2.2	1.1	0.6	1.2	3.1	1.2
56.4	6.17E+06	288.0	2.1	0.2	0.5	0.8	2.9	1.2	68.3	6.36E+06	26.0	2.3	1.0	0.6	1.0	3.4	1.1
67.1	6.31E+06	121.0	2.2	1.0	0.5	0.9	3.0	1.2	64.2	6.18E+06	3.0	2.0	0.8	0.6	1.1	3.8	1.1
81.8	8.35E+06	0.0	4.6	2.1	0.7	1.4	4.2	1.4	66.3	6.26E+06	2.0	2.1	1.0	0.6	1.1	3.7	1.2
59.4	6.19E+06	265.0	2.1	0.4	0.5	0.8	3.1	1.3	81.7	8.15E+06	12.0	3.6	2.5	0.7	1.0	4.5	1.2
56.2	6.08E+06	445.0	2.1	0.1	0.5	0.8	2.9	1.2	75.1	6.87E+06	17.0	3.0	1.5	0.6	1.0	3.5	1.2
75.1	6.96E+06	22.0	3.3	1.3	0.5	0.9	3.7	1.3	76.4	7.02E+06	30.0	3.3	1.5	0.6	0.9	3.8	1.1
85.3	1.10E+07	0.0	4.9	3.5	2.2	2.2	4.8	1.4	84.0	8.71E+06	22.0	3.5	2.7	0.8	1.0	4.2	0.4
84.0	9.32E+06	0.0	4.6	3.1	0.7	1.5	4.2	1.4	73.3	6.60E+06	5.0	2.6	1.4	0.6	1.0	3.7	1.2
54.3	6.02E+06	554.0	2.0	0.1	0.5	0.8	2.8	1.2	77.8	7.27E+06	13.0	3.5	1.7	0.6	1.0	3.9	1.2
60.5	6.27E+06	100.0	2.2	0.4	0.5	0.9	3.2	1.3	83.0	8.57E+06	28.0	3.5	2.6	0.6	0.9	3.8	0.5
61.8	6.21E+06	219.0	2.1	0.6	0.5	0.8	3.0	1.2	77.1	7.19E+06	19.0	3.6	1.5	0.6	1.0	3.7	1.1
65.4	6.24E+06	167.0	2.2	0.8	0.5	0.8	3.0	1.2	69.6	6.38E+06	10.0	2.4	1.1	0.6	1.0	3.5	1.1
66.5	6.36E+06	81.0	2.4	0.8	0.5	0.9	3.0	1.2	57.1	6.13E+06	6.0	1.5	0.7	0.6	1.1	3.5	1.1
55.0	6.04E+06	492.0	2.0	0.1	0.5	0.8	2.8	1.2	87.7	1.13E+07	0.0	5.9	3.5	0.9	1.9	4.9	0.5
55.7	6.07E+06	493.0	2.1	0.1	0.5	0.8	2.8	1.2	73.6	6.71E+06	37.0	2.9	1.2	0.6	0.9	3.8	1.1
56.8	6.13E+06	386.0	2.1	0.2	0.5	0.8	2.9	1.2	85.5	9.05E+06	23.0	4.3	2.7	0.7	1.0	4.3	0.5
57.3	6.14E+06	345.0	2.1	0.2	0.5	0.8	3.0	1.2	76.2	7.01E+06	33.0	3.3	1.4	0.6	0.9	3.8	1.1
59.6	6.20E+06	253.0	2.1	0.4	0.5	0.8	3.1	1.3	85.0	9.21E+06	18.0	4.0	3.0	0.6	1.0	4.0	0.4
56.9	6.16E+06	309.0	2.1	0.2	0.5	0.8	3.0	1.2	74.2	6.74E+06	23.0	2.9	1.3	0.6	0.9	3.6	1.2
61.2	6.23E+06	203.0	2.1	0.6	0.5	0.8	2.9	1.2	87.2	1.05E+07	0.0	5.4	3.3	0.7	1.5	4.5	0.5
56.2	6.09E+06	432.0	2.1	0.1	0.5	0.8	2.9	1.2	87.7	1.13E+07	0.0	5.9	3.5	0.9	1.9	4.9	0.5
65.3	6.30E+06	67.0	2.2	0.8	0.5	0.9	3.2	1.2	76.4	7.08E+06	52.0	3.4	1.4	0.6	0.9	3.8	1.1
62.8	6.24E+06	214.0	2.1	0.7	0.5	0.8	2.9	1.2	77.0	7.14E+06	48.0	3.3	1.4	0.6	0.9	4.8	1.0
78.9	7.61E+06	0.0	4.3	1.5	0.7	1.3	3.7	1.3	76.4	7.08E+06	45.0	3.3	1.4	0.6	0.9	4.4	1.0
72.6	6.69E+06	38.0	2.3	1.6	0.6	0.9	3.7	1.3	86.6	1.02E+07	0.0	4.7	3.4	0.7	1.5	4.5	0.5
57.4	6.17E+06	318.0	2.1	0.2	0.5	0.8	3.0	1.3	77.4	7.25E+06	35.0	3.5	1.4	0.6	0.9	4.7	1.1
70.2	6.41E+06	0.0	2.2	1.2	0.7	1.3	4.0	1.2	76.6	7.09E+06	20.0	3.3	1.5	0.6	1.0	3.9	1.1
59.4	6.21E+06	241.0	2.1	0.4	0.5	0.8	3.0	1.3	77.4	7.22E+06	31.0	3.4	1.6	0.6	0.9	4.0	1.1
56.6	6.12E+06	409.0	2.1	0.2	0.5	0.8	2.8	1.2	80.8	8.00E+06	9.0	3.6	2.5	0.6	1.0	4.0	1.1
56.4	6.14E+06	371.0	2.0	0.2	0.5	0.8	2.9	1.2	74.4	6.72E+06	29.0	2.9	1.3	0.6	0.9	3.7	1.1
73.5	6.84E+06	20.0	3.4	1.0	0.7	1.0	3.7	1.3	82.0	8.04E+06	43.0	3.4	1.8	0.7	0.9	4.8	0.5
82.5	8.74E+06	0.0	3.9	2.7	1.0	1.7	4.6	1.3	68.7	6.45E+06	6.0	2.9	0.7	0.6	1.1	3.5	1.1
84.4	9.95E+06	0.0	4.9	2.9	1.8	1.8	4.6	1.4	80.1	7.73E+06	15.0	3.4	2.2	0.7	0.9	4.3	1.0
82.8	9.04E+06	0.0	4.7	2.3	1.3	1.8	4.3	1.4	71.3	6.49E+06	21.0	2.4	1.2	0.6	1.0	3.9	1.1
65.5	6.34E+06	62.0	2.2	0.8	0.6	0.9	3.7	1.2	79.9	7.94E+06	7.0	2.9	2.8	0.6	1.0	4.1	1.0
68.5	6.41E+06	139.0	2.5	0.9	0.5	0.8	3.1	1.2	77.2	7.21E+06	43.0	3.0	1.8	0.7	0.9	4.0	1.1
75.5	7.11E+06	44.0	3.5	1.4	0.6	0.9	2.9	1.2	74.5	6.76E+06	25.0	2.8	1.4	0.6	0.9	3.8	1.1
56.3	6.09E+06	412.0	2.1	0.1	0.5	0.8	2.9	1.3	64.6	6.25E+06	21.0	1.7	1.1	0.6	1.0	3.4	1.1
84.3	9.78E+06	0.0	4.6	2.9	1.8	1.8	4.6	1.4	75.4	6.89E+06	37.0	3.1	1.4	0.6	0.9	3.8	1.1
86.1	1.11E+07	0.0	5.0	3.5	2.3	2.3	5.1	1.3	83.2	9.43E+06	5.0	5.4	2.7	0.7	1.0	4.3	0.7
77.6	7.29E+06	0.0	3.3	1.8	0.7	1.2	3.8	1.3	62.4	6.14E+06	2.0	1.8	0.8	0.7	1.1	3.7	1.4

* For (PMS column value ≥ 0 and < 0.5), then PMS-A
For (PMS column value ≥ 0.5 and < 1.0), then PMS-C
For (PMS column value ≥ 1 and < 1.5), then PMS-B
For (PMS column value ≥ 1.5 and ≤ 2.0), then PMS-D

Table C.9: Numerical Results for the Impacts on Pareto Front with Battery Bank Autonomy of Six andTwelve Hours

Battery Bank Autonomy Hour 6 hrs									Battery Bank Autonomy Hour 12 hrs								
γ_{re}	LCC	$LPSP$	P^{w}_{rat}	P^{pv}_{rat}	S^{con}_{rat}	S^{di}_{rat}	E^{b}_{rat}	PMS	γ_{re}	LCC	$LPSP$	P^{w}_{rat}	P^{pv}_{rat}	S^{con}_{rat}	S^{di}_{rat}	E^{b}_{rat}	PMS
(%)	($)		$(p.u.)$	$(p.u.)$	$(p.u.)$	$(p.u.)$	$(p.u.)$	*	(%)	($)		$(p.u.)$	$(p.u.)$	$(p.u.)$	$(p.u.)$	$(p.u.)$	*
81.6	8.19E+06	1.0	4.1	2.4	0.7	1.1	3.9	1.1	72.1	8.11E+06	0.0	2.5	2.2	0.5	1.2	1.6	1.4
79.5	7.55E+06	4.0	3.7	1.9	0.7	1.0	4.0	1.2	55.5	6.72E+06	586.0	2.3	0.3	0.1	0.9	0.1	0.1
66.8	6.25E+06	12.0	2.1	1.0	0.6	1.0	3.6	1.1	55.6	6.72E+06	607.0	2.3	0.3	0.1	0.9	0.1	0.1
72.0	6.54E+06	18.0	2.5	1.2	0.7	1.0	3.8	1.2	55.7	6.74E+06	478.0	2.3	0.3	0.1	0.9	0.1	0.1
68.8	6.34E+06	10.0	2.2	1.1	0.6	1.0	3.8	1.2	54.7	6.88E+06	133.0	2.1	0.3	0.2	1.0	0.1	0.1
81.7	8.43E+06	0.0	4.3	2.4	0.8	1.3	4.0	1.3	72.0	7.92E+06	39.0	2.5	2.2	0.2	0.9	1.0	0.9
67.2	6.27E+06	7.0	1.9	1.2	0.6	1.0	3.6	1.2	66.6	7.29E+06	56.0	2.3	1.3	0.3	0.9	0.7	0.5
74.8	6.79E+06	19.0	2.6	1.6	0.6	1.0	3.8	1.1	57.9	6.85E+06	171.0	2.4	0.4	0.1	0.9	0.2	0.3
73.2	6.61E+06	13.0	2.5	1.4	0.6	1.0	3.7	1.2	56.6	6.80E+06	257.0	2.3	0.4	0.1	0.9	0.1	0.1
73.7	6.68E+06	14.0	2.6	1.5	0.6	1.0	3.8	1.1	56.2	6.77E+06	399.0	2.3	0.3	0.1	0.9	0.2	0.3
77.0	7.07E+06	6.0	3.0	1.7	0.7	1.0	3.9	1.2	56.2	6.78E+06	316.0	2.3	0.3	0.1	0.9	0.1	0.1
71.1	6.48E+06	16.0	2.3	1.3	0.6	1.0	3.7	1.2	55.7	6.80E+06	234.0	2.3	0.3	0.2	0.9	0.1	0.1
82.6	8.64E+06	5.0	4.4	2.5	1.0	1.0	4.0	1.2	57.7	6.87E+06	145.0	2.3	0.5	0.1	0.9	0.1	0.1
84.3	1.02E+07	0.0	5.0	2.7	2.7	1.7	4.6	1.4	56.8	6.84E+06	173.0	2.3	0.4	0.2	0.9	0.1	0.2
75.2	6.85E+06	21.0	2.8	1.6	0.6	1.0	3.8	1.1	68.4	7.64E+06	3.0	2.6	1.4	0.3	1.1	1.2	0.7
67.3	6.29E+06	18.0	1.9	1.1	0.6	1.0	3.7	1.2	72.9	8.27E+06	0.0	2.7	2.3	0.5	1.2	1.5	1.4
74.0	6.69E+06	12.0	2.7	1.4	0.6	1.0	3.7	1.2	73.3	8.20E+06	6.0	2.6	2.3	0.5	1.0	1.3	1.4
69.2	6.35E+06	8.0	2.1	1.2	0.6	1.0	3.8	1.1	56.7	6.81E+06	222.0	2.3	0.4	0.1	0.9	0.1	0.1
83.7	9.60E+06	0.0	4.8	2.7	1.9	1.6	4.4	1.4	59.8	6.97E+06	113.0	2.5	0.5	0.1	0.9	0.5	0.3
74.8	6.86E+06	9.0	3.1	1.4	0.7	1.0	3.8	1.2	55.6	6.72E+06	611.0	2.3	0.3	0.1	0.9	0.1	0.1
71.9	6.53E+06	6.0	2.3	1.4	0.6	1.0	3.7	1.2	55.9	6.81E+06	197.0	2.2	0.3	0.2	0.9	0.1	0.2
75.7	6.92E+06	17.0	2.9	1.6	0.6	1.0	3.8	1.1	56.0	6.76E+06	366.0	2.3	0.3	0.1	0.9	0.1	0.1
83.2	9.07E+06	0.0	4.6	2.8	1.1	1.1	4.0	1.4	56.2	6.80E+06	210.0	2.3	0.4	0.2	0.9	0.1	0.1
64.9	6.20E+06	2.0	1.8	1.0	0.6	1.1	3.6	1.2	60.1	6.99E+06	105.0	2.3	0.7	0.1	0.9	0.1	0.3
60.9	6.13E+06	2.0	1.7	0.8	0.6	1.1	3.5	1.1	67.4	7.52E+06	7.0	2.6	1.2	0.3	1.1	1.0	0.7
82.7	8.72E+06	1.0	4.4	2.7	0.8	1.1	4.0	1.3	58.9	7.03E+06	86.0	2.3	0.5	0.2	0.9	0.3	0.1
73.3	6.66E+06	8.0	2.4	1.6	0.6	1.0	3.8	1.2	71.3	7.79E+06	28.0	2.4	2.0	0.4	1.0	1.1	0.4
83.3	9.25E+06	0.0	4.7	2.6	1.4	1.6	4.2	1.3	55.8	6.74E+06	511.0	2.3	0.3	0.1	0.9	0.1	0.1
74.4	6.74E+06	14.0	2.7	1.5	0.6	1.0	3.8	1.2	55.7	6.72E+06	522.0	2.3	0.3	0.1	0.9	0.1	0.1
73.5	6.63E+06	17.0	2.5	1.4	0.6	1.0	3.7	1.2	63.1	7.16E+06	66.0	2.5	0.8	0.2	0.9	0.5	0.7
76.2	6.96E+06	3.0	2.9	1.7	0.6	1.1	3.7	1.2	56.5	6.77E+06	483.0	2.4	0.3	0.1	0.9	0.2	0.1
60.9	6.11E+06	0.0	1.7	0.8	0.6	1.2	3.6	1.1	70.9	7.70E+06	11.0	2.6	1.6	0.5	1.0	1.2	1.1
84.0	9.96E+06	0.0	4.8	2.7	2.3	1.8	4.6	1.3	64.5	7.10E+06	81.0	2.3	1.1	0.1	0.9	0.4	0.2
75.2	6.87E+06	10.0	2.8	1.6	0.6	1.0	3.9	1.1	55.8	6.74E+06	434.0	2.3	0.3	0.1	0.9	0.1	0.2
71.7	6.50E+06	19.0	2.5	1.2	0.6	1.0	3.8	1.2	56.4	6.79E+06	288.0	2.3	0.4	0.1	0.9	0.1	0.1

* For (PMS column value ≥ 0 and < 0.5), then PMS-A
For (PMS column value ≥ 0.5 and < 1.0), then PMS-C
For (PMS column value ≥ 1 and < 1.5), then PMS-B
For (PMS column value ≥ 1.5 and ≤ 2.0), then PMS-D

Table C.10: Numerical Results for the Impacts on Pareto Front with Battery Bank Autonomy of Eighteen and Twenty-four Hours

Battery Autonomy Hour 18 hrs									Battery Autonomy Hour 24 hrs								
γ_{re}	LCC	$LPSP$	P^{w}_{rat}	P^{pv}_{rat}	S^{con}_{rat}	S^{di}_{rat}	E^{b}_{rat}	PMS	γ_{re}	LCC	$LPSP$	P^{w}_{rat}	P^{pv}_{rat}	S^{con}_{rat}	S^{di}_{rat}	E^{b}_{rat}	PMS
(%)	($)		$(p.u.)$	$(p.u.)$	$(p.u.)$	$(p.u.)$	$(p.u.)$	*	(%)	($)		$(p.u.)$	$(p.u.)$	$(p.u.)$	$(p.u.)$	$(p.u.)$	*
78.3	9.28E+06	0.0	4.2	2.5	0.9	1.1	2.2	1.3	60.8	7.77E+06	0.0	1.7	0.8	0.4	1.1	3.9	1.3
59.4	7.13E+06	96.0	2.3	0.6	0.4	0.9	0.6	0.2	53.0	7.53E+06	0.0	2.1	0.1	0.5	1.2	3.0	1.4
52.5	6.62E+06	495.0	2.2	0.1	0.4	0.9	0.7	0.3	81.5	9.58E+06	0.0	2.6	2.5	0.8	1.2	9.2	0.3
66.9	7.39E+06	72.0	2.7	1.0	0.4	0.9	0.8	0.4	80.3	9.26E+06	2.0	2.6	2.1	0.9	1.1	8.8	0.4
63.2	7.22E+06	85.0	2.4	0.8	0.4	0.9	0.6	0.3	76.5	8.36E+06	23.0	2.6	1.9	0.4	1.0	5.5	0.5
51.7	6.59E+06	608.0	2.2	0.0	0.4	0.9	0.7	0.1	73.7	8.08E+06	31.0	2.5	1.8	0.4	1.0	3.6	0.4
52.1	6.66E+06	460.0	2.1	0.1	0.4	0.9	0.7	0.2	80.8	9.06E+06	11.0	2.9	1.8	0.7	1.0	9.5	0.4
52.7	6.67E+06	430.0	2.2	0.1	0.4	0.9	0.7	0.3	83.8	9.35E+06	13.0	3.6	2.0	0.5	0.9	9.2	0.3
52.3	6.75E+06	322.0	2.1	0.1	0.4	0.9	0.7	0.2	66.7	7.59E+06	26.0	2.2	1.1	0.3	1.0	2.8	1.1
52.7	6.68E+06	433.0	2.2	0.1	0.4	0.9	0.7	0.3	64.9	7.54E+06	19.0	2.2	0.9	0.3	1.0	2.9	1.2
81.1	1.04E+07	17.0	3.6	3.1	2.6	1.0	3.2	0.5	59.7	7.46E+06	9.0	2.1	0.5	0.2	1.0	2.7	1.1
80.3	1.07E+07	0.0	3.7	3.2	2.7	1.2	3.2	0.4	75.4	8.26E+06	29.0	2.7	1.9	0.5	0.9	4.0	0.4
76.2	8.49E+06	6.0	3.4	2.2	0.6	1.0	2.1	1.1	55.3	7.51E+06	1.0	1.9	0.4	0.3	1.1	2.8	1.3
52.6	6.68E+06	400.0	2.2	0.1	0.4	0.9	0.7	0.2	53.7	7.39E+06	78.0	1.9	0.2	0.3	1.1	2.8	1.3
54.1	6.76E+06	294.0	2.3	0.1	0.4	0.9	0.6	0.3	66.6	7.75E+06	3.0	2.2	1.1	0.4	1.1	2.9	0.4
80.6	9.78E+06	19.0	3.6	2.8	1.9	0.9	3.2	0.4	72.2	7.89E+06	35.0	2.4	1.6	0.3	1.0	3.4	0.3
54.5	6.83E+06	216.0	2.3	0.2	0.4	0.9	0.6	0.2	62.6	7.52E+06	24.0	2.0	0.8	0.3	1.0	2.9	1.2
55.8	6.88E+06	187.0	2.4	0.2	0.4	0.9	0.7	0.3	61.1	7.47E+06	15.0	2.1	0.7	0.2	1.0	2.7	1.1
77.6	8.71E+06	30.0	3.1	2.7	0.4	0.9	2.4	0.3	82.0	9.19E+06	12.0	3.0	2.1	0.6	1.0	8.8	0.3
51.6	6.62E+06	533.0	2.1	0.1	0.4	0.9	0.7	0.2	72.8	7.96E+06	32.0	2.6	1.6	0.4	0.9	3.3	0.4
57.6	7.06E+06	114.0	2.2	0.4	0.4	0.9	0.7	0.3	73.5	8.11E+06	16.0	2.9	1.4	0.5	1.0	4.3	0.4
53.7	6.73E+06	345.0	2.3	0.1	0.4	0.9	0.7	0.3	77.0	8.43E+06	20.0	2.7	1.7	0.4	1.0	6.1	0.3
73.1	7.96E+06	49.0	3.2	1.8	0.6	0.9	1.0	0.3	70.0	8.17E+06	4.0	2.6	1.4	0.5	1.1	3.6	0.6
73.8	8.21E+06	42.0	2.6	2.3	0.5	0.9	1.6	0.4	69.2	7.69E+06	22.0	2.2	1.4	0.3	1.0	2.8	1.1
69.4	7.53E+06	65.0	2.6	1.5	0.4	0.9	0.9	0.2	83.2	1.01E+07	0.0	3.2	2.6	1.2	1.3	9.5	0.5
77.1	9.09E+06	18.0	3.2	2.3	1.7	1.0	2.5	0.4	59.2	7.57E+06	2.0	2.0	0.6	0.3	1.1	2.8	1.3
61.3	7.24E+06	67.0	2.2	0.8	0.4	0.9	0.7	0.2	71.3	7.88E+06	34.0	2.3	1.6	0.4	0.9	3.0	0.4
64.0	7.31E+06	65.0	2.4	0.9	0.4	0.9	0.8	0.4	63.1	7.57E+06	7.0	2.0	0.9	0.3	1.1	2.8	1.3
52.2	6.60E+06	571.0	2.2	0.0	0.4	0.9	0.7	0.3	71.4	7.86E+06	35.0	2.5	1.5	0.4	0.9	3.3	0.4
66.6	7.44E+06	48.0	2.5	1.2	0.4	0.9	0.7	0.5	69.5	7.93E+06	6.0	2.4	1.1	0.4	1.0	7.6	1.2
53.4	6.78E+06	266.0	2.2	0.1	0.4	0.9	0.7	0.2	67.5	7.71E+06	8.0	2.1	1.3	0.3	1.0	3.1	1.0
78.3	9.28E+06	0.0	4.2	2.5	0.9	1.1	2.2	1.3	62.6	7.54E+06	27.0	2.1	0.7	0.3	1.0	3.0	1.1
52.5	6.70E+06	376.0	2.1	0.1	0.4	0.9	0.7	0.3	57.1	7.55E+06	4.0	2.0	0.4	0.4	1.0	2.8	1.2
54.2	6.76E+06	306.0	2.3	0.1	0.4	0.9	0.6	0.3	84.5	9.80E+06	17.0	3.1	2.7	0.8	1.0	8.9	0.3
52.5	6.64E+06	472.0	2.2	0.1	0.4	0.9	0.7	0.3	79.3	8.85E+06	21.0	3.0	1.6	0.8	1.0	8.5	0.4

* For (PMS column value ≥ 0 and < 0.5), then PMS-A
For (PMS column value ≥ 0.5 and < 1.0), then PMS-C
For (PMS column value ≥ 1 and < 1.5), then PMS-B
For (PMS column value ≥ 1.5 and ≤ 2.0), then PMS-D

Bibliography

[1] M. Arriaga, C. A. Cañizares, and M. Kazerani, "Renewable energy alternatives for remote communities in Northern Ontario, Canada," *IEEE Trans. on Sustainable Energy*, vol. 4, no. 3, pp. 661–670, Jul. 2013.

[2] L. Freris and D. Infield, *Renewable Energy in Power Systems*. John Wiley & Sons, 2008.

[3] T. Senjyu, D. Hayashi, A. Yona, N. Urasaki, and T. Funabashi, "Optimal configuration of power generating systems in isolated island with renewable energy," *Renewable Energy*, vol. 32, no. 11, pp. 1917–1933, Sep. 2007.

[4] N. Duić and M. da Graça Carvalho, "Increasing renewable energy sources in island energy supply: case study Porto Santo," *Renewable and Sustainable Energy Reviews*, vol. 8, no. 4, pp. 383–399, Aug. 2004.

[5] M. J. Khan and M. T. Iqbal, "Pre-feasibility study of stand-alone hybrid energy systems for applications in Newfoundland," *Renewable Energy*, vol. 30, no. 6, pp. 835–854, May 2005.

[6] B. Wichert, "PV-diesel hybrid energy systems for remote area power generation-a review of current practice and future developments," *Renewable and Sustainable Energy Reviews*, vol. 1, no. 3, pp. 209–228, Sep. 1997.

[7] M. A. Elhadidy and S. M. Shaahid, "Parametric study of hybrid (wind+ solar+ diesel) power generating systems," *Renewable Energy*, vol. 21, no. 2, pp. 129–139, Oct. 2000.

[8] F. A. Bhuiyan and A. Yazdani, “Energy storage technologies for grid-connected and off-grid power system applications,” in *Proc. IEEE Electrical Power Engineering Conf. (EPEC)*, pp. 303–310.

[9] S. Vazquez, S. M. Lukic, E. Galvan, L. G. Franquelo, and J. M. Carrasco, “Energy storage systems for transport and grid applications,” *IEEE Trans. on Industrial Electronics*, vol. 57, no. 12, pp. 3881–3895, Dec. 2010.

[10] K. C. Divya and J. Østergaard, “Battery energy storage technology for power systemsan overview,” *Electric Power Systems Research*, vol. 79, no. 4, pp. 511–520, Apr. 2009.

[11] NRCan, “Wind and storage demonstration in a first nations community, cowessess first nation,” http://www.nrcan.gc.ca/energy/science/programs-funding/2056, Nov. 2011, [Online: accessed 7-June-2014].

[12] J. Driesen and F. Katiraei, “Design for distributed energy resources,” *IEEE Power and Energy Magazine*, vol. 6, no. 3, pp. 30–40, May 2008.

[13] P. Lundsager, H. Bindner, N.-E. Clausen, S. Frandsen, L. H. Hansen, and J. C. Hansen, *Isolated Systems with Wind Power*. Wiley, 2005.

[14] T. M. Weis and A. Ilinca, “The utility of energy storage to improve the economics of wind-diesel power plants in Canada,” *Renewable Energy*, vol. 33, no. 7, pp. 1544–1557, Jul. 2008.

[15] T. Ackermann *et al.*, *Wind Power in Power Systems*. Wiley, 2005.

[16] NRCan, “Status of Remote/Off-Grid Communities in Canada,” http://publications.gc.ca/collections/collection_2013/rncan-nrcan/M154-71-2013-eng.pdf, Aug. 2011, [Online: accessed 3-June-2014].

[17] J. G. McGowan, J. F. Manwell, and S. R. Connors, “Wind/diesel energy systems: review of design options and recent developments,” *Solar Energy*, vol. 41, no. 6, pp. 561–575, 1988.

[18] H. Ibrahim, J. Lefebvre, J. F. Methot, and J. S. Deschenes, "Numerical modeling wind-diesel hybrid system: Overview of the requirements, models and software tools," in *Proc. IEEE Electrical Power and Energy Conference (EPEC)*. IEEE, 2011, pp. 23–28.

[19] M. Falahi, K. Butler-Purry, and M. Ehsani, "Dynamic reactive power control of islanded microgrids," *IEEE Trans. on Power Systems*, vol. 28, no. 4, Nov. 2013.

[20] R. C. Bansal, "Automatic reactive-power control of isolated wind-diesel hybrid power systems," *IEEE Trans. on Industrial Electronics*, vol. 53, no. 4, pp. 1116–1126, Aug. 2006.

[21] D. E. Olivares, C. A. Canizares, and M. Kazerani, "A centralized energy management system for isolated microgrids," *IEEE Trans. on Smart Grid*, vol. -, no. -, pp. 1116–1126, Dec. 2013.

[22] G. Fay, K. Keith, T. Schwoerer, and et. al, "Alaska isolated wind-diesel systems: performance and economic analysis," *prepared for Alaska Energy Authority and Denali Commission*, June 2010.

[23] H. Ghoddami, M. B. Delghavi, and A. Yazdani, "An integrated wind-photovoltaic-battery system with reduced power-electronic interface and fast control for grid-tied and off-grid applications," *Renewable Energy*, vol. 45, pp. 128–137, Sep. 2012.

[24] C. Dennis Barley and C. Byron Winn, "Optimal dispatch strategy in remote hybrid power systems," *Solar Energy*, vol. 58, no. 4-6, pp. 165–179, Oct.-Dec. 1996.

[25] M. Ashari and C. V. Nayar, "An optimum dispatch strategy using set points for a photovoltaic (pv)-diesel-battery hybrid power system," *Solar Energy*, vol. 66, no. 1, pp. 1–9, May 1999.

[26] R. Dufo-Lopez and J. L. Bernal-Agustín, "Design and control strategies of PV-diesel systems using genetic algorithms," *Solar Energy*, vol. 79, no. 1, pp. 33–46, Jul. 2005.

[27] F. Valenciaga and P. F. Puleston, "Supervisor control for a stand-alone hybrid generation system using wind and photovoltaic energy," *IEEE Trans. on Energy Conversion*, vol. 20, no. 2, pp. 398–405, June 2005.

[28] C. Wang and M. H. Nehrir, "Power management of a stand-alone wind/photovoltaic/fuel cell energy system," *IEEE Trans. on Energy Conversion*, vol. 23, no. 3, pp. 957–967, Sep. 2008.

[29] E. I. Vrettos and S. A. Papathanassiou, "Operating policy and optimal sizing of a high penetration res-bess system for small isolated grids," *IEEE Trans. on Energy Conversion*, vol. 26, no. 3, pp. 744–756, Sep. 2011.

[30] B. Zhao, X. Zhang, J. Chen, C. Wang, and L. Guo, "Operation optimization of standalone microgrids considering lifetime characteristics of battery energy storage system," *IEEE Trans. on Sustainable Energy*, vol. 4, no. 4, pp. 934–943, Oct. 2013.

[31] R. Billinton and Bagen, "Evaluation of different operating strategies in small stand-alone power systems," *IEEE Trans. on Energy Conversion*, vol. 20, no. 3, pp. 654–660, Sep. 2005.

[32] J. M. Lujano-Rojas, C. Monteiro, R. Dufo-López, and J. L. Bernal-Agustín, "Optimum load management strategy for wind/diesel/battery hybrid power systems," *Renewable Energy*, vol. 44, pp. 288–295, Aug. 2012.

[33] Y. Ohsawa, S. Emura, and K. Arai, "Optimal operation of photovoltaic/diesel power generation system by neural network," in *Proc. Neural Networks to Power Systems*. IEEE, 1993, pp. 99–103.

[34] F. Katiraei and C. Abbey, "Diesel plant sizing and performance analysis of a remote wind-diesel microgrid," in *Proc. IEEE Power Engineering Soc. General Meeting*, 2007, pp. 1–8.

[35] D. Ipsakis, S. Voutetakis, P. Seferlis, F. Stergiopoulos, and C. Elmasides, “Power management strategies for a stand-alone power system using renewable energy sources and hydrogen storage,” *International Journal of Hydrogen Energy*, vol. 34, no. 16, pp. 7081–7095, Aug. 2009.

[36] T. Zhou and B. François, “Energy management and power control of a hybrid active wind generator for distributed power generation and grid integration,” *IEEE Trans. on Industrial Electronics*, vol. 58, no. 1, pp. 95–104, Jan. 2011.

[37] B. S. Borowy and Z. M. Salameh, “Methodology for optimally sizing the combination of a battery bank and pv array in a wind/pv hybrid system,” *IEEE Trans. on Energy Conversion*, vol. 11, no. 2, pp. 367–375, Jun. 1996.

[38] S. H. Karaki, R. B. Chedid, and R. Ramadan, “Probabilistic performance assessment of autonomous solar-wind energy conversion systems,” *IEEE Trans. on Energy Conversion*, vol. 14, no. 3, pp. 766–772, Sep. 1999.

[39] R. Chedid and Y. Saliba, “Optimization and control of autonomous renewable energy systems,” *International Journal of Energy Research*, vol. 20, no. 7, pp. 609–624, Jul. 1996.

[40] S. H. El-Hefnawi, “Photovoltaic diesel-generator hybrid power system sizing,” *Renewable Energy*, vol. 13, no. 1, pp. 33–40, Jan. 1998.

[41] W. D. Kellogg, M. H. Nehrir, G. Venkataramanan, and V. Gerez, “Generation unit sizing and cost analysis for stand-alone wind, photovoltaic, and hybrid wind/pv systems,” *IEEE Trans. on Energy Conversion*, vol. 13, no. 1, pp. 70–75, Mar. 1998.

[42] H. Yang, Z. Wei, and L. Chengzhi, “Optimal design and techno-economic analysis of a hybrid solar-wind power generation system,” *Applied Energy*, vol. 86, no. 2, pp. 163–169, Feb. 2009.

[43] A. Kaabeche, M. Belhamel, and R. Ibtiouen, "Sizing optimization of grid-independent hybrid photovoltaic/wind power generation system," *Energy*, vol. 36, no. 2, pp. 1214–1222, Feb. 2011.

[44] Z. Iverson, A. Achuthan, P. Marzocca, and D. Aidun, "Optimal design of hybrid renewable energy systems (hres) using hydrogen storage technology for data center applications," *Renewable Energy*, vol. 52, pp. 79–87, Apr. 2013.

[45] R. Belfkira, L. Zhang, and G. Barakat, "Optimal sizing study of hybrid wind/pv/diesel power generation unit," *Solar Energy*, vol. 85, no. 1, pp. 100–110, 2011.

[46] T. Markvart, "Sizing of hybrid photovoltaic-wind energy systems," *Solar Energy*, vol. 57, no. 4, pp. 277–281, Oct. 1996.

[47] G. Tina, S. Gagliano, and S. Raiti, "Hybrid solar/wind power system probabilistic modelling for long-term performance assessment," *Solar Energy*, vol. 80, no. 5, pp. 578–588, May 2006.

[48] R. Kaiser, D. U. Sauer, A. Armbruster, G. Bopp, and H. G. Puls, "New concepts for system design and operation control of photovoltaic systems," in *Proc. European Photovoltaic Solar Energy Conf.*, 1997.

[49] R. S. Garcia and D. Weisser, "A wind-diesel system with hydrogen storage: Joint optimisation of design and dispatch," *Renewable energy*, vol. 31, no. 14, pp. 2296–2320, Jan. 2006.

[50] R. Chedid and S. Rahman, "Unit sizing and control of hybrid wind-solar power systems," *IEEE Trans. on Energy Conversion*, vol. 12, no. 1, pp. 79–85, Mar. 1997.

[51] A. R. Prasad and E. Natarajan, "Optimization of integrated photovoltaic–wind power generation systems with battery storage," *Energy*, vol. 31, no. 12, pp. 1943–1954, Sep. 2006.

[52] S. Ashok, "Optimised model for community-based hybrid energy system," *Renewable Energy*, vol. 32, no. 7, pp. 1155–1164, Jun. 2007.

[53] H. Yang, L. Lu, and W. Zhou, "A novel optimization sizing model for hybrid solar-wind power generation system," *Solar Energy*, vol. 81, no. 1, pp. 76–84, Jan. 2007.

[54] S. Diaf, M. Belhamel, M. Haddadi, and A. Louche, "Technical and economic assessment of hybrid photovoltaic/wind system with battery storage in Corsica island," *Energy Policy*, vol. 36, no. 2, pp. 743–754, Feb. 2008.

[55] R. W. Wies, R. A. Johnson, A. N. Agrawal, and T. J. Chubb, "Simulink model for economic analysis and environmental impacts of a pv with diesel-battery system for remote villages," *IEEE Trans. on Power Systems*, vol. 20, no. 2, pp. 692–700, May 2005.

[56] H. Belmili, M. Haddadi, S. Bacha, M. F. Almi, and B. Bendib, "Sizing stand-alone photovoltaic-wind hybrid system: Techno-economic analysis and optimization," *Renewable and Sustainable Energy Reviews*, vol. 30, pp. 821–832, Feb. 2014.

[57] L. Xu, X. Ruan, C. Mao, B. Zhang, and Y. Luo, "An improved optimal sizing method for wind-solar-battery hybrid power system," *IEEE Trans. on Sustainable Energy*, vol. 4, no. 3, pp. 692–700, Jul. 2013.

[58] A. Kaabeche and R. Ibtiouen, "Techno-economic optimization of hybrid photovoltaic/wind/diesel/battery generation in a stand-alone power system," *Solar Energy*, vol. 103, pp. 171–182, May 2014.

[59] C. Protogeropoulos, B. J. Brinkworth, and R. H. Marshall, "Sizing and techno-economical optimization for hybrid solar photovoltaic/wind power systems with battery storage," *International Journal of Energy Research*, vol. 21, no. 6, pp. 465–479, May 1997.

[60] C. Lavania, S. Rao, and E. Subrahmanian, "Reducing variation in solar energy supply through frequency domain analysis," *IEEE Trans. on Systems*, vol. 6, no. 2, pp. 196–204, June 2012.

[61] M. R. Aghamohammadi and H. Abdolahinia, "A new approach for optimal sizing of battery energy storage system for primary frequency control of islanded microgrid," *International Journal of Electrical Power & Energy Systems*, vol. 54, pp. 325–333, Jan. 2014.

[62] E. Koutroulis, D. Kolokotsa, A. Potirakis, and K. Kalaitzakis, "Methodology for optimal sizing of stand-alone photovoltaic/wind-generator systems using genetic algorithms," *Solar Energy*, vol. 80, no. 9, pp. 1072–1088, Sep. 2006.

[63] D. Feroldi and D. Zumoffen, "Sizing methodology for hybrid systems based on multiple renewable power sources integrated to the energy management strategy," *International Journal of Hydrogen Energy*, vol. 39, pp. 8609–8620, 2014.

[64] J. Wang and F. Yang, "Optimal capacity allocation of standalone wind/solar/battery hybrid power system based on improved particle swarm optimisation algorithm," *IET Renewable Power Generation*, vol. 7, no. 5, pp. 443–448, Mar. 2013.

[65] P. Paliwal, N. P. Patidar, and R. K. Nema, "Determination of reliability constrained optimal resource mix for an autonomous hybrid power system using particle swarm optimization," *Renewable Energy*, vol. 63, pp. 194–204, Mar. 2014.

[66] O. Ekren and B. Y. Ekren, "Size optimization of a pv/wind hybrid energy conversion system with battery storage using simulated annealing," *Applied Energy*, vol. 87, no. 2, pp. 592–598, Feb. 2010.

[67] Y. A. Katsigiannis, P. S. Georgilakis, and E. S. Karapidakis, "Hybrid simulated annealing-tabu search method for optimal sizing of autonomous power systems with renewables," *IEEE Trans. on Sustainable Energy*, vol. 3, no. 3, pp. 330–338, Jul. 2012.

[68] G. C. Seeling-Hochmuth, “A combined optimisation concet for the design and operation strategy of hybrid-pv energy systems,” *Solar Energy*, vol. 61, no. 2, pp. 77–87, Aug. 1997.

[69] M. Kalantar and S. M. Mousavi G, “Dynamic behavior of a stand-alone hybrid power generation system of wind turbine, microturbine, solar array and battery storage,” *Applied energy*, vol. 87, no. 10, pp. 3051–3064, Oct. 2010.

[70] Y. A. Katsigiannis and P. S. Georgilakis, “Optimal sizing of small isolated hybrid power systems using tabu search,” *Journal of Optoelectronics and Advanced Materials*, vol. 10, no. 5, pp. 1241–1245, May 2008.

[71] A. Konak, D. W. Coit, and A. E. Smith, “Multi-objective optimization using genetic algorithms: A tutorial,” *Reliability Engineering & System Safety*, vol. 91, no. 9, pp. 992–1007, Sep. 2006.

[72] M. Fadaee and M. A. M. Radzi, “Multi-objective optimization of a stand-alone hybrid renewable energy system by using evolutionary algorithms: a review,” *Renewable and Sustainable Energy Reviews*, vol. 16, no. 5, pp. 3364–3369, Jun. 2012.

[73] R. T. Marler and J. S. Arora, “Survey of multi-objective optimization methods for engineering,” *Structural and Multidisciplinary Optimization*, vol. 26, no. 6, pp. 369–395, Apr. 2004.

[74] I. Das and J. E. Dennis, “A closer look at drawbacks of minimizing weighted sums of objectives for Pareto set generation in multicriteria optimization problems,” *Structural and Multidisciplinary Optimization*, vol. 14, no. 1, pp. 63–69, Aug. 1997.

[75] I. Y. Kim and O. L. De Weck, “Adaptive weighted-sum method for bi-objective optimization: Pareto front generation,” *Structural and Multidisciplinary Optimization*, vol. 29, no. 2, pp. 149–158, Feb. 2005.

[76] ——, "Adaptive weighted sum method for multiobjective optimization: a new method for pareto front generation," *Structural and Multidisciplinary Optimization*, vol. 31, no. 2, pp. 105–116, Feb. 2006.

[77] R. Dufo-Lopez and J. L. Bernal-Agustin, "Multi-objective design of pv–wind–diesel–hydrogen–battery systems," *Renewable energy*, vol. 33, no. 12, pp. 2559–2572, Dec. 2008.

[78] H. Yang, W. Zhou, L. Lu, and Z. Fang, "Optimal sizing method for stand-alone hybrid solar-wind system with lpsp technology by using genetic algorithm," *Solar Energy*, vol. 82, no. 4, pp. 354–367, Apr. 2008.

[79] A. Maheri, "Multi-objective design optimisation of standalone hybrid wind-pv-diesel systems under uncertainties," *Renewable Energy*, vol. 66, pp. 650–661, Jun. 2014.

[80] X. Pelet, D. Favrat, and G. Leyland, "Multiobjective optimisation of integrated energy systems for remote communities considering economics and co¡ sub¿ 2¡/sub¿ emissions," *International Journal of Thermal Sciences*, vol. 44, no. 12, pp. 1180–1189, Dec. 2005.

[81] J. P. Vazhayil and R. Balasubramanian, "Optimization of indias electricity generation portfolio using intelligent pareto-search genetic algorithm," *International Journal of Electrical Power & Energy Systems*, vol. 55, pp. 13–20, Feb. 2014.

[82] S. Avril, G. Arnaud, A. Florentin, and M. Vinard, "Multi-objective optimization of batteries and hydrogen storage technologies for remote photovoltaic systems," *Energy*, vol. 35, no. 12, pp. 5300–5308, Dec. 2010.

[83] L. Wang and C. Singh, "Multicriteria design of hybrid power generation systems based on a modified particle swarm optimization algorithm," *IEEE Trans. on Energy Conversion*, vol. 24, no. 1, pp. 163–172, Mar. 2009.

[84] A. T. D. Perera, R. A. Attalage, K. K. C. K. Perera, and V. P. C. Dassanayake, "A hybrid tool to combine multi-objective optimization and multi-criterion decision making in designing standalone hybrid energy systems," *Applied Energy*, vol. 107, pp. 412–425, Jul. 2013.

[85] M. Alsayed, M. Cacciato, G. Scarcella, and G. Scelba, "Multicriteria optimal sizing of photovoltaic-wind turbine grid connected systems," *IEEE Trans. on Energy Conversion*, vol. 28, no. 2, pp. 370–379, Jun. 2013.

[86] "Hybrid2, available: http://www.ceere.org/rerl/projects/software/hybrid2/."

[87] "Homer (the hybrid optimization model for electric renewables), available: http://www.nrel/gov/homer."

[88] "ihoga, http://www.unizar.es/rdufo/hoga-eng.htm."

[89] "Retscreen, available: http://www.retscreen.net/."

[90] "Transys, available: http://www.trnsys.com/."

[91] "Insel, available: http://www.insel.eu."

[92] W. Zhou, C. Lou, Z. Li, L. Lu, and H. Yang, "Current status of research on optimum sizing of stand-alone hybrid solar–wind power generation systems," *Applied Energy*, vol. 87, no. 2, pp. 380–389, Feb. 2010.

[93] J. L. Bernal-Agustín and R. Dufo-López, "Simulation and optimization of stand-alone hybrid renewable energy systems," *Renewable and Sustainable Energy Reviews*, vol. 13, no. 8, pp. 2111–2118, Oct. 2009.

[94] S. Sinha and S. S. Chandel, "Review of software tools for hybrid renewable energy systems," *Renewable and Sustainable Energy Reviews*, vol. 32, pp. 192–205, Apr. 2014.

[95] K. M. Knight, S. A. Klein, and J. A. Duffie, "A methodology for the synthesis of hourly weather data," *Solar Energy*, vol. 46, no. 2, pp. 109–120, 1991.

[96] R. Billinton, H. Chen, and R. Ghajar, “Time-series models for reliability evaluation of power systems including wind energy,” *Microelectronics Reliability*, vol. 36, no. 9, pp. 1253–1261, Sep. 1996.

[97] M. Üner and A. İleri, “Typical weather data of main Turkish cities for energy applications,” *International Journal of Energy Research*, vol. 24, no. 8, pp. 727–748, Jun. 2000.

[98] Z. Qingyuan, J. Huang, and L. Siwei, “Development of typical year weather data for Chinese locations,” *ASHRAE Transactions*, vol. 108, no. 2, pp. 1063–75, Jun. 2002.

[99] H. Yang and L. Lu, “Study of typical meteorological years and their effect on building energy and renewable energy simulations,” *ASHRAE Transactions*, vol. 110, no. 2, pp. 424–431, 2004.

[100] J. Zhu, *Optimization of Power System Operation*. Wiley-IEEE Press, 2009.

[101] B. L. J. S. Drouilhet and et El, “A battery life prediction method for hybrid power applications,” 1997.

[102] “http://climate.weatheroffice.gc.ca/,” accessed Nov. 2012.

[103] F. A. Bhuiyan and A. Yazdani, “Reliability assessment of a wind-power system with integrated energy storage,” *IET Renewable Power Generation*, vol. 4, no. 3, pp. 211–220, May 2010.

[104] D. J. Lee and L. Wang, “Small-signal stability analysis of an autonomous hybrid renewable energy power generation/energy storage system part i: time-domain simulations,” *IEEE Trans. on Energy Conversion*, vol. 23, no. 1, pp. 311–320, Mar. 2008.

[105] P. M. Subcommittee, “IEEE reliability test system,” *IEEE Trans. on Power Apparatus and Systems*, vol. PAS-98, no. 6, pp. 2047–2054, Nov. 1979.

[106] T. K. Saha and D. Kastha, "Design optimization and dynamic performance analysis of a stand-alone hybrid wind-diesel electrical power generation system," *IEEE Trans. on Energy Conversion*, vol. 25, no. 4, pp. 1209–1217, Dec. 2010.

[107] G. M. Masters, *Renewable and Efficient Electric Power Systems*. Hoboken, NJ: Wiley-IEEE Press, 2004.

[108] J. A. Duffie and W. A. Beckman, "Solar engineering of thermal processes," *NASA STI/Recon Technical Report A*, vol. 81, p. 16591, 1980.

[109] P. Giorsetto and K. F. Utsurogi, "Development of a new procedure for reliability modeling of wind turbine generators," *IEEE Trans. on Power Apparatus and Systems*, vol. PAS-102, no. 1, pp. 134–143, Jan. 1983.

[110] J. A. Martinez, F. De León, A. Mehrizi-Sani, M. H. Nehrir, C. Wang, and V. Dinavahi, "Tools for analysis and design of distributed resourcespart ii: Tools for planning, analysis and design of distribution networks with distributed resources," *IEEE Trans. on Power Delivery*, vol. 26, no. 3, pp. 1653–1662, Jul. 2011.

[111] M. H. Ahmed, K. Bhattacharya, and M. M. A. Salama, "Probabilistic distribution load flow with different wind turbine models," *IEEE Trans. on Power Systems*, vol. 28, no. 2, pp. 1540–1549, May 2013.

[112] T. Ackermann, "Wind power in power systems," *Wind Engineering*, vol. 30, no. 5, pp. 447–449, 2006.

[113] C. Guo, H. Li, and D. Pan, "An improved piecewise aggregate approximation based on statistical features for time series mining," in *Knowledge Science, Engineering and Management*. Springer, 2010, pp. 234–244.

[114] K. Deb, "An efficient constraint handling method for genetic algorithms," *Computer Methods in Applied Eechanics and Engineering*, vol. 186, no. 2, pp. 311–338, Jun. 2000.

[115] D. B. Nelson, M. H. Nehrir, and C. Wang, "Unit sizing and cost analysis of stand-alone hybrid wind/pv/fuel cell power generation systems," *Renewable Energy*, vol. 31, no. 10, pp. 1641–1656, Aug. 2006.

[116] S. Diaf, D. Diaf, M. Belhamel, M. Haddadi, and A. Louche, "A methodology for optimal sizing of autonomous hybrid pv/wind system," *Energy Policy*, vol. 35, no. 11, pp. 5708–5718, Nov. 2007.

[117] J. K. Kaldellis, "Optimum autonomous wind-power system sizing for remote consumers, using long-term wind speed data," *Applied Energy*, vol. 71, no. 3, pp. 215–233, Mar. 2002.

[118] H. Lund, "Large-scale integration of optimal combinations of pv, wind and wave power into the electricity supply," *Renewable Energy*, vol. 31, no. 4, pp. 503–515, Apr. 2006.

[119] Y. A. Katsigiannis, P. S. Georgilakis, and E. S. Karapidakis, "Genetic algorithm solution to optimal sizing problem of small autonomous hybrid power systems," in *Artificial Intelligence: Theories, Models and Applications*. Springer, 2010, pp. 327–332.

[120] T. Senjyu, D. Hayashi, N. Urasaki, and T. Funabashi, "Optimum configuration for renewable generating systems in residence using genetic algorithm," *IEEE Trans. on Energy Conversion*, vol. 21, no. 2, pp. 459–466, Jun. 2006.

[121] Y. Y. Hong and R. C. Lian, "Optimal sizing of hybrid wind/pv/diesel generation in a stand-alone power system using markov-based genetic algorithm," *IEEE Trans. on Power Delivery*, vol. 27, no. 2, pp. 640–647, Apr. 2012.

[122] D. E. Goldberg *et al.*, *Genetic Algorithms in Search, Optimization, and Machine Learning*. Addison-Wesley Reading Menlo Park, 1989.

[123] L. Zadeh, "Optimality and non-scalar-valued performance criteria," *IEEE Trans. on Automatic Control*, vol. 8, no. 1, pp. 59–60, Jul. 1963.

[124] P. Hajela and C. Y. Lin, "Genetic search strategies in multicriterion optimal design," *Structural Optimization*, vol. 4, no. 2, pp. 99–107, Spring 1992.

[125] T. Murata, H. Ishibuchi, and H. Tanaka, "Multi-objective genetic algorithm and its applications to flowshop scheduling," *Computers & Industrial Engineering*, vol. 30, no. 4, pp. 957–968, Sep. 1996.

[126] I. Das and J. E. Dennis, "Normal-boundary intersection: A new method for generating the pareto surface in nonlinear multicriteria optimization problems," *SIAM Journal on Optimization*, vol. 8, no. 3, pp. 631–657, Aug. 1998.

[127] A. Messac, A. Ismail-Yahaya, and C. A. Mattson, "The normalized normal constraint method for generating the Pareto frontier," *Structural and Multidisciplinary Optimization*, vol. 25, no. 2, pp. 86–98, Jul. 2003.

[128] A. Messac and C. A. Mattson, "Normal constraint method with guarantee of even representation of complete pareto frontier," *AIAA Journal*, vol. 42, no. 10, pp. 2101–2111, Oct. 2004.

[129] E. Filatovas and O. Kurasova, "A decision support system for solving multiple criteria optimization problems," *Informatics in Education*, no. 10, pp. 213–224, 2011.

[130] D. Du and D. Simon, "Complex system optimization using biogeography-based optimization," *Mathematical Problems in Engineering*, vol. 2013, pp. 1–18, Oct. 2013.

[131] C. A. C. Coello, D. A. Van Veldhuizen, and G. B. Lamont, *Evolutionary Algorithms for Solving Multi-objective Problems*. Springer, 2002.

[132] K. Deb *et al.*, *Multi-objective Optimization Using Evolutionary Algorithms*. John Wiley & Sons Chichester, 2001.

[133] K. Deb, A. Pratap, S. Agarwal, and T. Meyarivan, "A fast and elitist multiobjective genetic algorithm: NSGA-II," *IEEE Trans. on Evolutionary Computation*, vol. 6, no. 2, pp. 182–197, Apr. 2002.

[134] D. A. Van V., J. B. Zydallis, and G. B. Lamont, "Considerations in engineering parallel multiobjective evolutionary algorithms," *IEEE Trans. on Evolutionary Computation*, vol. 7, no. 2, pp. 144–173, Apr. 2003.

[135] E. Zitzler, M. Laumanns, and S. Bleuler, "A tutorial on evolutionary multiobjective optimization," in *Metaheuristics for Multiobjective Optimisation*. Springer, 2004, pp. 3–37.

[136] C. M. Fonseca, P. J. Fleming *et al.*, "Genetic algorithms for multiobjective optimization: Formulation discussion and generalization," in *ICGA*, vol. 93, 1993, pp. 416–423.

[137] C. M. Fonseca and P. J. Fleming, "An overview of evolutionary algorithms in multiobjective optimization," *Evolutionary Computation*, vol. 3, no. 1, pp. 1–16, 1995.

[138] J. D. Schaffer, "Multiple objective optimization with vector evaluated genetic algorithms," in *Proc. International Conf. on Genetic Algorithms*, 1985, pp. 93–100.

[139] J. Horn, N. Nafpliotis, and D. E. Goldberg, "A niched pareto genetic algorithm for multiobjective optimization," in *Proc. IEEE Conf. on Evolutionary Computation*, 1994, pp. 82–87.

[140] N. Srinivas and K. Deb, "Muiltiobjective optimization using nondominated sorting in genetic algorithms," *Evolutionary computation*, vol. 2, no. 3, pp. 221–248, Fall 1994.

[141] E. Zitzler and L. Thiele, "Multiobjective evolutionary algorithms: a comparative case study and the strength Pareto approach," *IEEE Trans. on Evolutionary Computation*, vol. 3, no. 4, pp. 257–271, Nov. 1999.

[142] E. Zitzler, M. Laumanns, and L. Thiele, "Spea2: Improving the strength pareto evolutionary algorithm," 2001.

[143] A. Seshadri, "A fast elitist multiobjective genetic algorithm: Nsga-ii," *MATLAB Central*, 2006.

[144] S. D. Pohekar and M. Ramachandran, "Application of multi-criteria decision making to sustainable energy planninga review," *Renewable and Sustainable Energy Reviews*, vol. 8, no. 4, pp. 365–381, Aug. 2004.

[145] J. C. Spall, *Introduction to Stochastic Search and Optimization: Estimation, Simulation, and Control*. John Wiley & Sons, 2005.

[146] K. Marti, *Stochastic Optimization Methods*. Springer, 2005.

[147] P. Ngatchou, A. Zarei, and M. A. El-Sharkawi, "Pareto multi-objective optimization," in *Proc. Intelligent Systems Application to Power Systems Conf.*, 2005, pp. 84–91.

[148] S. V. Papaefthymiou and S. A. Papathanassiou, "Optimum sizing of wind-pumped-storage hybrid power stations in island systems," *Renewable Energy*, vol. 64, pp. 187–196, Apr. 2014.

[149] E. Zitzler, *Evolutionary Algorithms for Multiobjective Optimization: Methods and Applications*. Shaker Ithaca, 1999.

Curriculum Vitae

Name:	Faruk Bhuiyan
Post-Secondary Education and Degrees:	Western University London, Ontario, Canada 2009 - 2014, Ph. D. in Electrical Engineering University of Western Ontario London, ON 2007 - 2009, M.E.Sc. in Electrical Engineering. Bangladesh University of Engineering and Technology (BUET) Dhaka, Bangladesh 1988 - 1993, B.Sc. in Electrical and Electronic Engineering.
Honours and Awards:	• Natural Science and Engineering Research Council (NSERC), CGS D, 2011-2013 • Ontario Graduate Scholarship (OGS), 2010-2011 • First Award for the best presentation in the Western Graduate Symposium, 2011 • BUET Merit Scholarship, 1989-1990
Related Work Experience:	• Research and Teaching Assistant, Western University (UWO), 2007-2014 • Senior Engineer, Karnaphuli Fertilizer Company (KAFCO), Bangladesh, 1997-2006 • Engineering Officer, Beximco Textile Limited, Bangladesh, 1995-1997 • Optical Mark Reader Engineer, BUET Computer Center, Bangladesh, 1994

Publications:

Peer-Reviewed Journals

1. F.A. Bhuiyan, A. Yazdani, and S.L. Primak, "An Optimal Sizing Approach for an Islanded Microgrid," *IET Renewable Power Generation*, RPG-2013-0416, accepted Jun. 30, 2014.

2. F.A. Bhuiyan, A. Yazdani and S.L. Primak "Modeling, Simulation, and Performance Analysis of Power Management Strategies for an Islanded Microgrid", *International Journal of Energy Science (IJES)*, vol. 3, no. 6, pp. 383-394, Dec. 2013.

3. F.A. Bhuiyan and A. Yazdani, "Reliability Assessment of a Wind-Power System with Integrated Energy Storage," *IET Renewable Power Generation*, vol. 4, no. 3, pp. 211-220, May 2010.

4. F.A. Bhuiyan and A. Yazdani, "Multi-Mode Control of a DFIG-Based Wind-Power Unit for Remote Applications," *IEEE Trans. on Power Delivery*, vol.24, no. 4, pp. 2079-2089, Oct. 2009.

Referred Conference

1. F.A. Bhuiyan and A. Yazdani, "Energy Storage Technologies for Grid-Connected and Off-Grid Power System Applications," *IEEE Electric Power and Energy Conference, EPEC*, pp. 333-340, Oct. 2012.

Under Preparation

- Two journal papers are under preparation based on Chapter 4 and Chapter 5 of the thesis.